

Bangor University

DOCTOR OF PHILOSOPHY

Functional molecular wires and devices

Wierzchowec, Piotr

Award date:
2008

Awarding institution:
Bangor University

[Link to publication](#)

General rights

Copyright and moral rights for the publications made accessible in the public portal are retained by the authors and/or other copyright owners and it is a condition of accessing publications that users recognise and abide by the legal requirements associated with these rights.

- Users may download and print one copy of any publication from the public portal for the purpose of private study or research.
- You may not further distribute the material or use it for any profit-making activity or commercial gain
- You may freely distribute the URL identifying the publication in the public portal ?

Take down policy

If you believe that this document breaches copyright please contact us providing details, and we will remove access to the work immediately and investigate your claim.

Download date: 10. Apr. 2024

Functional Molecular Wires and Devices

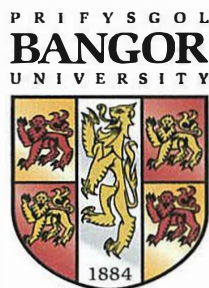
A thesis submitted to the
Bangor University
in candidature for the

Degree of
Philosophiæ Doctor

by

Piotr Wierzchowicz

Supervisor: Professor Geoffrey J. Ashwell



School of Chemistry
Prifysgol Bangor / Bangor University

2008



This thesis is dedicated in memory of my father

Leszek Wierzchowiec
(04/07/1948 – 30/12/2004)

Acknowledgements

First of all, I would like to thank Professor Geoffrey J. Ashwell for giving me the opportunity to do the PhD, and to the Engineering and Physical Sciences Research Council for my funding. I am grateful to all my colleagues from the Nanomaterials Group, especially Dr Anne Whittam and Dr Wayne Tyrrell for help and advice. I am grateful to Professor Ian R. Gentle and Dr Barry J. Wood for the use of XPS facilities and Kym Ford for help with analysis. I would also like to thank Dr Christopher M. Finch and Dr Ian R. Grace for supporting my experimental analysis with theoretical calculations.

Finally and most importantly thanks to Gosia and my family for love and support, and all my friends who made the last three years such an unforgettable time for me.

Abstract

This research considers the requirements for molecular electronics to be a realistic complement to silicon electronics. Results of the studies presented here clearly show that simple molecular components can be used for creating complex structures on solid substrates *via* self-assembly, followed by a series of *in-situ* reactions. Electrical properties of these systems may be finely tuned by the incorporation of appropriate functional units into their core structures during the synthetic process, or by structural modification of previously self-assembled molecular wires. A variety of such molecular systems were sampled and their specific structural and electronic properties were investigated. Implantation of electron-donating and electron-accepting units into π -conjugated systems resulted in exceptional current rectifying molecular wires. A rectification ratio of *ca.* 44 at ± 1 V was obtained for a system with a sequence of two electron-donating elements and two electron-accepting units linked with π -conjugated spacers. Much higher rectification, of *ca.* 200 at ± 1 V was observed for a dual-layer organic structure containing densely packed self-assembled cationic molecular wires, coupled with anionic molecules of an adlayer. The technique of *in-situ* synthesis has also led to the successful formation of a previously designed molecular wire across a *ca.* 3.6 nm gap of a prefabricated skeleton electrode structure. Electrical measurements on this junction have revealed large molecule-induced currents, relative to the residual current through the empty device. The current – voltage profiles of this molecular junction matched those from STM studies of self-assembled films on planar substrates and were consistent with theoretical calculations. Moreover, a novel method for a precise and reliable estimation of the current flow asymmetry through STM probed films is presented, and applied to the rectification measurements. This technique was based on a statistical approach to the analysis of the current – voltage characteristics and was registered at various STM tip – molecule separations.

List of physical constants

Symbol	Constant	Value
R	Gas constant	$8.314 \text{ J K}^{-1} \text{ mol}^{-1}$
N_A	Avogadro's number	$6.022 \times 10^{23} \text{ molecules mol}^{-1}$
h	Planck's constant	$6.626 \times 10^{-34} \text{ J s}$
e	Electron charge	$1.602 \times 10^{-21} \text{ C}$
m_e	Electron Mass	$9.109 \times 10^{-31} \text{ kg}$
k_B	Boltzmann's constant ($= R \times N_A^{-1}$)	$1.381 \times 10^{-23} \text{ J K}^{-1}$

List of contents

Acknowledgements	i
Abstract	ii
List of physical constants	iii
List of contents	iv
1. Introduction	1
1.1. Silicon electronics	1
1.2. Technological progress	2
1.3. Fundamental limitations of silicon technology	3
1.4. Molecular electronics	4
1.5. Aims	5
2. Background and literature	7
2.1. Molecular self-assembly	7
2.1.1. Solid surfaces – structure and reactivity	8
2.1.2. Mechanism and kinetics of thiol self-assembly on gold	10
2.1.3. Structure of self-assembled films on gold	13
2.2. Selected techniques for monolayer characterisation	20
2.2.1. X-ray photoelectron spectroscopy	20
2.2.2. Quartz crystal microbalance	23
2.3. Scanning tunnelling microscopy and spectroscopy	25
2.3.1. Operation	26
2.3.2. Tunnelling current	27
2.3.3. Electronic transmission through molecules	30
2.3.4. Tip – molecule – substrate junction formation	35
2.3.5. Current rectifying properties of molecular systems	39

3. Experimental	46
3.1. Components for the experiments	46
3.2. Studied systems	48
3.3. Synthesis of molecules	53
3.4. Preparation of gold substrates	54
3.4.1. Gold on quartz crystal	54
3.4.2. Atomically flat gold on mica	54
3.4.3. Gold on crystalline graphite	55
3.5. Preparation of molecular structures on gold	55
3.5.1. AT molecular wires	56
3.5.2. PeMP systems	57
3.6. Molecular wires inside nano-sized electrode gap	58
3.7. Analytical methods	61
3.7.1. Identification and characterisation of new materials	61
3.7.2. Quartz crystal microbalance	62
3.7.3. X-ray photoelectron spectroscopy	63
3.7.4. Scanning probe microscopy and spectroscopy	64
3.7.5. Electrical testing of molecular junctions inside silicon platform	67
3.7.6. Molecular modelling	69
4. Results and discussion	70
4.1. Structural studies of AT systems	70
4.1.1. Synthesised azomethines	70
4.1.2. Self-assembly and interfacial reactions – QCM	75
4.1.3. Self-assembly and interfacial reactions – XPS	79
4.1.4. Molecular geometry and arrangement	82
4.1.5. Summary of AT systems preparation	84

4.2. Structural studies of PeMP systems	86
4.2.1. Self-assembly and interfacial reactions – QCM	86
4.2.2. Self-assembly and interfacial reactions – XPS	89
4.2.3. Summary of PeMP systems preparation	92
4.3. Electronic properties of AT systems	93
4.3.1. Statistical studies on I - V characteristics	94
4.3.2. Rectifying behaviour of functionalised SAMs	117
4.3.3. Electron transport through two-terminal AT molecular wires	123
4.3.4. Summary of electronic properties of AT systems	130
4.4. Electronic properties of PeMP systems	132
4.4.1. Electron transport through two-terminal PeMP molecular wires	132
4.4.2. Rectifying behaviour of modified PeMP SAMs	142
4.4.3. Summary of electronic properties of PeMP systems	145
5. Conclusions	146
6. Reference list	148

1 Introduction

Molecular electronics is currently recognised as a key-element of technological progress in the near future. Interest from the world's leading electronics manufacturers in organic electronic devices is increasing rapidly. The market for organic light emitting diodes (OLEDs), organic thin-film transistors (TFTs) and other organic electronics is set to grow 70 % each year, reaching *ca.* \$20 billion in 2012, according to industry analysis firm NanoMarkets LC ¹. Commercialisation of organic electronics, and the continuous increase in investments in this technology, clearly highlights the need for further academic research. The requirement for miniaturisation naturally leads to the development of new, better materials. For example; solution-processable molecular materials promise larger, cheaper and more efficient displays, flexible thin-film transistors and many improvements for other electronic applications. The natural continuation of this trend is towards single molecule electronics. The new molecular materials, techniques for studying their properties and ideas how to achieve the desired level of miniaturisation are studied in this thesis.

1.1 Silicon electronics

The invention of the transistor, together with the development of an integrated circuit manufacturing method, led to the production of low-dimension electronic devices. Soon afterwards, continuous progress in electronics began. This has been stimulated by the reduction of transistor dimensions and increasing complexity of integrated circuits. At the very beginning of this process, in 1965, Gordon Moore predicted that the number of transistors on a computer chip would double every 18 to 24 months, whilst its price would remain relatively stable ². Today, one can see that his prophecy has been fulfilled and will hold, at least during the next few years. This will be possible due to the replacement of silicon dioxide dielectrics and polysilicon elements of gate electrodes with high-permittivity (high-k) insulators and metallic gates, and also with the

implementation of a tri-gate transistor architecture. A combination of these three improvements will significantly reduce leakage power, which is the crucial problem relating to current field-effect transistors (FETs) and should enable a decrease in transistor size down to 32 nm before the end of this decade ^{3,4}. It is likely that the application of a three-dimensional (3D) transistor array on microchips will be the last big innovation in silicon technology. According to recent announcements of a leading processor manufacturer, specialists in the field have already overcome technological problems of producing such structures and demonstrated the first 3D microchip ⁵.

1.2 Technological progress

Huge progress in electronics would not have been possible without the invention of photolithography and related techniques. Apart from the bulk material imperfections and energy dissipation effects, optical lithography limitations have always been the major technological barrier. Evaluation of this method is naturally strongly dependant on the light source applied. Treating this problem briefly: the lower the wavelength of electromagnetic radiation – the lower the dimensions of the final product. Current 65 nm transistor technology uses 193 nm argon-fluoride excimer lasers, the application of which can be extended for manufacturing another generation of microchips. This is going to be possible due to the invention of immersion lithography. This technique leads to an increase of the effective numerical aperture of lenses by using water, or any other fluid with high refractive index and low absorption at certain wavelength, being exposed between the lens and the photoresist during irradiation. This solution guarantees higher optical resolution compared to the standard technique. Additionally, this provides greater depth of focus than traditional air lithography because of the smaller phase of light change upon crossing the lens – medium and the medium – photoresist interfaces. Another innovative technique currently being tested by leading chip manufacturers is the extreme ultra-violet lithography (EUV) using a 13.5 nm wavelength. As the dimensions of devices can not be extended far below the wavelength of the light applied, this technology is probably going to be the most economical replacement for the 193 nm

system. There is also electron-beam lithography (EB), which is regarded as a complementary technique to the optical method. EB is more precise than EUV, but too slow to be used alone. Other techniques, such as X-ray and non-optical nanolithography methods, are currently out of range for commercial applications due to economical reasons.

1.3 Fundamental limitations of silicon technology

A variety of methods for nano-scale manufacturing are available and their potential is enormous. This is why the long-term future of electronics should be considered as being dependent on limitations of matter, principles of thermodynamics, quantum mechanics and electromagnetics, rather than technological barriers⁶⁻⁹. However, (from the point of view of this thesis) more important are the limitations of the currently used silicon technology and their impact on the progress of nanotechnologies, molecular electronics in particular. Many attempts have been made to assess the critical size limits of silicon-based electronic devices¹⁰⁻¹⁵, but this is still a non-trivial task considering the high number of variables. Undoubtedly, a reduction in transistor dimensions without any radical innovations will not significantly improve the efficiency of electronic devices. Miniaturisation of these devices has already become more than just a simple scaling of their components. Evolution in the applied materials and their architecture is becoming more and more distinctive^{16,17}. However, there are currently no practical ideas for effective miniaturisation to progress beyond the next decade. Transistor dimensions, according to the International Technology Roadmap for Semiconductors¹⁸, will approach an electron wavelength where quantum effects will start to dominate their performance. These effects have already been found to cause serious problems, since the silicon dioxide gate reached a thickness of 1.2 nm. This distance is sufficiently low for intensive electron tunnelling to occur. To attain the proper functional characteristic of the transistors, the gate silicon dioxide needs to be replaced by high-k insulators. There are other important limitations: the discrete character of dopant atoms should be maintained for the proper operation of devices, and the power dissipation

problem, which is associated with electron scattering and leakage mechanisms^{6,19-21}. It is highly probable that the next few years will be crucial for settling the matter of silicon technology limitations; the economic factors may be solved by physics. This could be an opportunity for revolutionary solutions involving the integration of silicon technology with functional molecular components.

1.4 Molecular electronics

Many devices and techniques have been proposed as possible alternatives to silicon technology. The potential of the most feasible structures: carbon nanotube FETs, resonant tunnelling diodes, single-electron transistors, quantum cellular automata, and others have been widely reviewed in the literature^{16,22,23}. At present, molecular electronics is one of the most promising alternatives for current materials and solutions. In 1974, A. Aviram and M.A. Ratner mentioned the first visionary idea that organic molecules might act as diodes²⁴. Soon after they presented the theoretical concept of a molecular rectifier²⁵, initiating studies on molecular electronics. This resulted in the discovery of a wide range of molecular rectifiers, wires, switches and other nano-scale devices. At the very beginning, due to the lack of sophisticated analytical techniques, the practical research into molecular electronics was focused on macroscopic electrical and electro-optical features of bulky organic materials. Many solutions that originated from this early stage have already found practical applications, for example: photocopiers, piezo-electric transducers, liquid crystal displays, the aforementioned OLEDs, TFTs and others. Nowadays, taking full advantage of the latest achievements of nano-scale microscopy, spectroscopy, nano-manipulation techniques and powerful computers, it is possible to study the properties of single molecules. Synthetic chemistry has also made enormous progress, as the preparation of various complex functional structures has been widely demonstrated²⁶⁻³¹. More and more organic components, which can be used for building molecular electronic systems, have become commercially available. The variety of the demonstrated structures has led to novel ideas for the architecture of future molecular electronic circuits³²⁻³⁴. However, the present strategy

is based on the adaptation of molecular functional elements into the architectural concept of current inorganic devices. Building hybrid silicon – organic FETs, compatible with existing technology, would be more beneficial than a complete replacement of the manufacturing processes, required to apply unconventional solutions.

1.5 Aims

The research work presented in this thesis was inspired by the so-called bottom-up approach for manufacturing the next generation of logic elements for electronic devices. This idea is based on creating functional elements, or even complete devices, from small molecular components using the principles of chemistry and self-assembly. It is strongly believed that the investigated concepts and solutions will provide advancements in nano-science. The major technological challenge of molecular electronics is to find efficient techniques of placing molecules in circuits, providing good electrical contacts and mechanically stable junctions. Improvement in this field, by developing a method of positioning molecular wires inside predefined silicon-based skeleton structures, which can be mass-produced, was one of the objectives of this project. The other aim was to investigate methods for the *in-situ* functionalisation of the molecular wires in order to achieve specific conducting properties and rectifying behaviour of these structures. Two different methods, which might be useful for further technological applications, were studied. Examining the electronic properties of the molecular structures at different stages of their modification, and by comparing features of the converted systems with those of the prototypical structures are also essential for understanding the mechanisms of electronic transport.

Experimental studies on small molecular systems are complex. Therefore, both structural analysis and electrical probing, supported by theoretical modelling, are necessary to obtain a broad data set for describing the investigated processes. For this purpose, three major techniques were employed, among other supportive methods. For studying the composition and molecular arrangement of molecular layers on gold-coated substrates, the following techniques were found to be useful: X-ray

photoelectron spectroscopy (XPS), quartz crystal microbalance (QCM) and scanning tunnelling microscopy (STM). Measuring conductivity of the investigated molecular junctions and current-flow asymmetry through the chemisorbed molecular wires required the incorporation of scanning tunnelling spectroscopy (STS) as a major tool available for nano-probing.

2 Background and literature

The most important subjects, regarding the described research work, are reviewed in this chapter. First of all, molecular self-assembly is described in Section 2.1, with special attention paid to the adsorption of thiols onto gold substrates. Recent discoveries, including the mechanism and kinetics of the adsorption process and structural properties of self-assembled monolayers (SAMs), are discussed. The theoretical background of physicochemical properties of surfaces and molecules is given where necessary. The major experimental techniques for the structural studies are presented in Section 2.2. The last part, Section 2.3, contains a description of STM with a brief discussion of the tunnelling process, mechanisms of electronic transmission mediated by molecules, current rectification and methods of molecular junction formation using STM.

2.1 Molecular self-assembly

Pioneering research by Zisman *et al.* in the 1940's³⁵ revealed physisorption of surfactants on clean metal substrates. It was demonstrated that specific molecules tended to form dense monolayers, the physicochemical properties of which were different from those observed for bare substrates. For many years this publication received a limited level of interest. This was mainly due to a lack of experimental techniques for studying molecular-scale structures and processes. This has been gradually changing since 1983, when Nuzzo and Allara³⁶ observed the chemisorption of alkanethiolates on gold, a phenomenon which turned out to be very important for nano-scale science. Formation of densely packed and highly oriented monolayers of thiols were later reported on silver^{37,38}, copper³⁸⁻⁴⁰, mercury^{41,42}, iron^{43,44}, gallium arsenide⁴⁵, and indium phosphide⁴⁶ surfaces. Further experiments have also revealed chemisorptive character of other combinations of molecular head groups and substrates^{47,48}. However, because of the low reactivity of gold with the surrounding atmosphere, it has been the most widely

used substrate for molecular self-assembly. Thus, thiolate monolayers on gold still remain the most studied area of interest.

2.1.1 Solid surfaces – structure and reactivity

Understanding the physicochemistry of solid surfaces is necessary for designing molecules that are capable of forming SAMs and for effective control of the deposition of these molecules. The molecules for self-assembly usually require crystalline surfaces in order to form highly ordered SAMs over a large substrate area. Most metals form face-centered cubic (fcc) lattices during crystallisation onto other substrates. Unreconstructed surfaces of the fcc materials, and adsorption places on fcc [111] surfaces are presented in Fig. 2.1.1-1. These ideal crystallographic structures of the surfaces, which reflect atomic arrangement in the bulk of the solid, are thermodynamically unstable. As each of the surface atoms has at least one unbound site, the clean surfaces of solid materials have a natural susceptibility to bind chemical species, minimising surface free energy. Most metallic and semiconductive surfaces undergo oxidation when exposed to air. The lack of strong chemisorption of air particles onto flat gold substrates, opposite to the formation of strong sulfur – gold bonds, mean that this metal is the prime substrate used for molecular self-assembly.

The parameter, called heat of adsorption (ΔH_{ads} , or adsorption enthalpy), which is defined as the energy required to break an adsorbate – surface bond, is typically used for evaluating the stability of the adsorbed moieties. This allows one to distinguish covalent bonding from other, weaker, adsorbate – surface attractive interactions, which are generally termed as physisorption. The bonding formation between surface atoms and adsorbate is normally followed by a reconstruction of the outer layer of surface atoms, which additionally increases stability of the adsorbed adlayer⁴⁹. The total binding energy of the adlayer is also intensified by lateral inter-adsorbate attractive interactions.

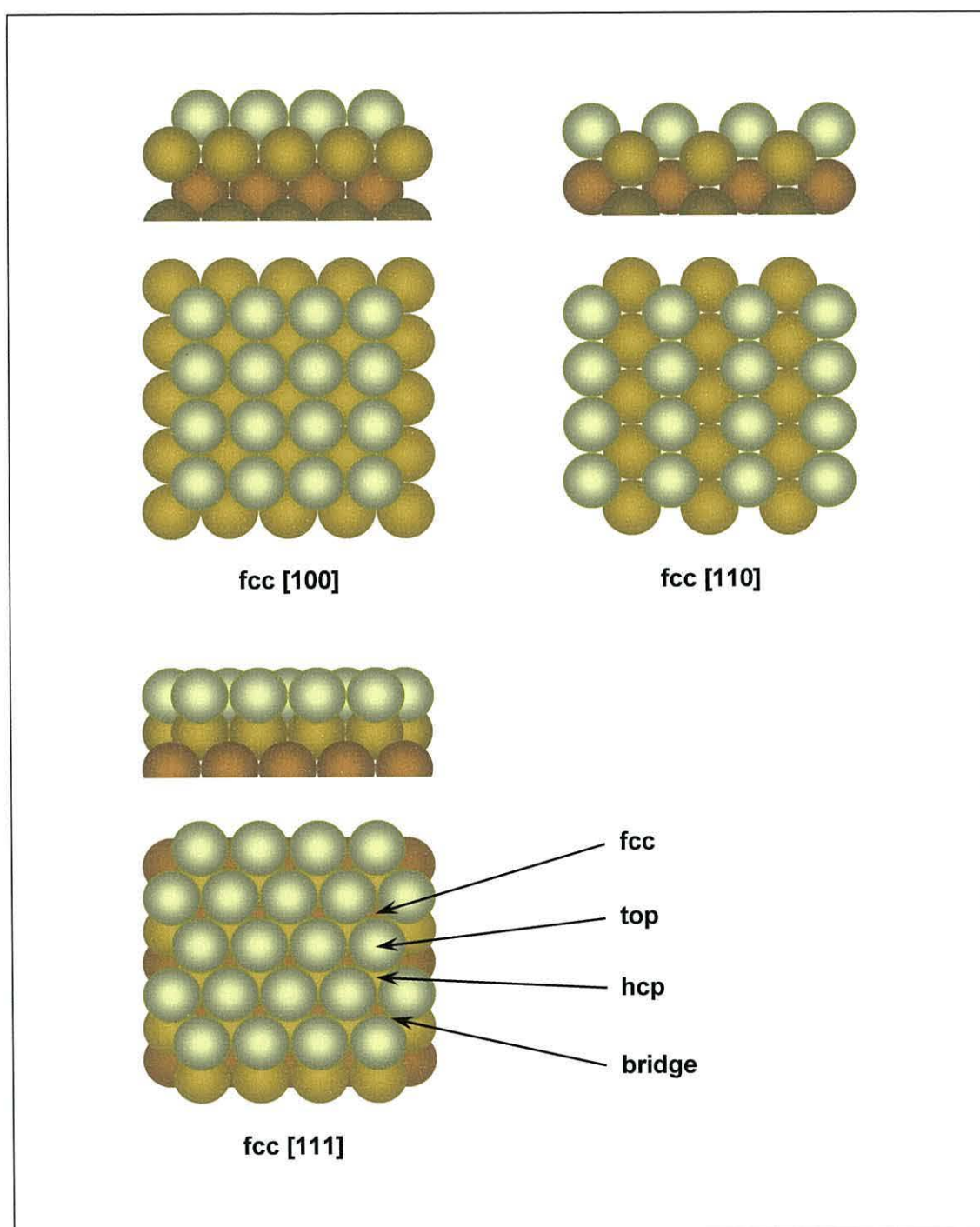


Fig. 2.1.1-1 Unreconstructed surfaces of the fcc materials ⁴⁹; adsorption sites denoted for fcc [111] surface.

Detailed studies have proven physisorption ($\Delta H_{ads} < 60$ kJ/mol) of such impurities as water, oxygen and carbon monoxide onto flat gold surfaces at room temperature⁵⁰⁻⁵⁷. It was found that amounts of O₂, CO, NO and adsorption enthalpies of these moieties on solid surfaces increased with surface roughness^{58,59}. Rates of molecular self-assembly were also expected to be limited by the presence of these impurities. Although, experiments have shown that thiol-terminated molecules are capable of displacing small physisorbed molecules of adventitious materials from the flat surfaces of noble metals⁵⁴. This is highly important, as these surfaces are practically never free of impurities.

Adsorption of particles from a vaporous surrounding medium onto freshly formed surfaces is very fast, and typically lasts nanoseconds under normal conditions. Considering the ideal model, where each molecule striking a surface becomes permanently bound, the time (t) required to passivate the solid material at given temperature (T) and pressure (P), in order to obtain optimal surface concentration of the particles, is given by the equation:

$$t = \frac{\sigma \sqrt{2 \pi M R T}}{N_A P} \quad \text{Eqn 2.1.1-1}$$

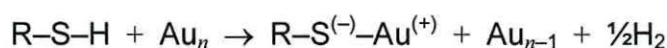
In this equation, σ is surface coverage and M is average molar weight of the gaseous species. Self-assembly from solution takes longer, as it is determined mainly by a diffusion of molecules through a liquid. Additional phenomena, such as intermolecular interactions, co-adsorption and desorption, also affect the duration of the surface coverage process.

2.1.2 Mechanism and kinetics of thiol self-assembly on gold

Several approaches have been made to determine the nature of thiol self-assembly onto gold^{48,60-62}. Various experimental techniques have proved that these molecules, after deprotonation at the gold surface, form highly energetic, covalent S–Au bonds with some ionic character⁶³⁻⁶⁹. The measured value of chemisorption enthalpy varied for different experiments, however, it is generally agreed that ΔH_{ads} slightly exceeds 120 kJ/mol⁷⁰⁻⁷².

In fact, the effective binding energy was significantly higher due to lateral interactions, which consolidated the monolayer and contributed to the total adsorption enthalpy. This also varied for different molecules; for example, van der Waals forces between the alkyl chains of the neighbouring molecules add $\Delta H_{ads} \approx 6$ kJ/mol per each methylene segment to a total value of $\Delta H_{ads}^{70,73}$.

The mechanism of self-assembly has been considered as an oxidative addition of the S–H bond to the gold surface, followed by reductive elimination of the hydrogen⁶⁵:



The fate of a hydrogen atom from the thiol after deprotonation remains uncertain. Desorption of molecular hydrogen seems to be the most feasible mechanism of its loss in the deoxygenated environment^{65,74,75}. This is consistent with the theoretical prediction that hydrogen cleavage is energetically favoured when a path for formation of molecular hydrogen is provided^{69,76}. In the presence of oxygen, the oxidative conversion of H_2 to H_2O or H_2O_2 may occur^{74,77}. Experiments also revealed desorption of alkenethiolates, although the mechanism of this process was not a reversal of the adsorption presented above. This was mainly due to the lack of hydrogen in the system. Strong interactions between the self-assembled molecules may lead to partial desorption of the thiolates as disulfides^{66,72,78-80}. In pure solvent, this was a spontaneous process, which occurred until a solvent-dependant equilibrium for the molecule – substrate interface was reached.

Kinetics of this reaction are not fully understood, mainly because it is a multi-phenomenon process, strongly dependent on the individual features of molecules and substrates, as well as on reaction environment. However, several empirical formulae have been successfully applied in order to match experimental data to theoretical predictions^{72,81-85}. The simplest example, and the most frequently referenced, is the Langmuir model of adsorption, which describes a time-dependent function of surface coverage, $\Theta(t)$:

$$\Theta(t) = 1 - e^{-ck_L t} \quad \text{Eqn 2.1.2-1}$$

Here, c and k_L are concentration of the adsorbate and rate constant of the adsorption process respectively. There are no environmental limitations, desorption from the surface and intermolecular interactions are included in this formula. These assumptions, in most cases, are very far from describing the real behaviour of molecules during deposition, especially for self-assembly from solution. Environmental and thermodynamic conditions should affect the adsorption in a similar manner as for any other chemical reaction. Moreover, for the deposition from solution, these factors can control the process by influencing the diffusion of molecules through a solvent. Thus, mainly temperature^{86,87} and solvent nature^{82,88} determine reaction kinetics, especially at the initial stage of self-assembly and when the concentration of the compound in solution is low. For this reason, a diffusion-limited Langmuir model was proposed⁸⁵:

$$\Theta(t) = 1 - e^{-ck_{LD}\sqrt{t}} \quad \text{Eqn 2.1.2-2}$$

Here, k_{LD} is rate constant of the diffusion-limited adsorption. When the mean inter-adsorbate distance decreases below 1 nm during the self-assembly process, mutual interactions between molecules start to influence ordering, favouring certain adsorbate configurations over others. The initially adsorbed molecules rearrange analogously to the well-known phase transition phenomena in the bulk of a material. At this stage of self-assembly the structural ordering, the packing density and kinetics of the adsorption depend strongly on the shape and size of molecules, and the character of intermolecular interactions (see Section 2.1.3). If these interactions are relatively strong, as in the case of long-chain alkenethiols, much more significant deviations from Langmuir kinetics should be observed^{61,83}.

2.1.3 Structure of self-assembled films on gold

SAMs of *n*-alkanethiol molecules have been the most commonly studied for the investigation of surface arrangement. The characteristic simple structure of these molecules, small cross-section, alkyl chain flexibility and lateral interactions can affect the formation of various surface phases. The conditions associated with self-assembly have also been found to strongly determine the structure of SAMs, when deposited from solution. The concentration of adsorbate^{86,89}, temperature^{86,87} and nature of the solvent⁹⁰⁻⁹² are important for controlling the density of packing and the amount of structural defects. Surface crystallography and surface free energy distribution, favouring particular bonding sites over others, are also very important factors in the structural arrangement of thiolates.

Exact localisation of the attachment site of sulfur elements in the crystalline surface lattice is highly problematic. In the case of deposition onto Au(111), which is the natural structure of evaporated and annealed gold films, there are four (major) possible adsorption sites (see Fig. 2.1.1-1). However, there is no agreement which configuration is the most stable, as contradictory results have been obtained. Density functional theory (DFT) calculations have consistently indicated the local energy minima for adsorption in the high coordinated sites⁹³⁻⁹⁹. On the other hand, experimental results have suggested an on-top position to be more likely^{68,100-103}. The most recent studies have provided new evidence that the real structure of the gold – molecule interface could be more complex than previously expected. The structure of this interface is probably strongly dependent on dynamic processes taking place during adsorption. According to one of the novel theories, molecules in a monolayer may occupy two different adsorption sites, even if one of these positions is energetically less favorable¹⁰⁴⁻¹⁰⁶. It is highly probable, for steric reasons, that the molecules primarily physisorb at on-top sites and then diffuse to other available places. This process would be strongly affected by the crystalline structure of gold surfaces and the presence of other molecules, especially chain – chain interactions between them. Occupation of the different sites in such a case would be determined by trapping a fraction of the molecules in place. This is less favourable for separated molecules, but acts as sufficiently stable binding sites when

the thiolate molecules formation is sufficiently dense. This concept provides a better explanation of the observed geometries of the molecular arrangement in these systems, compared to the one-site model. A separate theory, based on STM observations and DFT calculations, has also been developed ¹⁰⁷. This new model considers a strong reconstruction of the gold surface upon self-assembly, and the possibility of lifting gold atoms from the lattice by adsorbed molecules (see Fig. 2.1.3-1). A dynamic equilibrium has been found for the system, where each adsorbed molecule was bound to a gold atom from the crystalline surface lattice and additionally to a lifted adatom, which was shared with other neighbouring molecules. Thiol radicals could also be bound to the surface *via* a single adatom situated in a hollow site (fcc or hcp) ^{68,108}. Effectively, the interface would be characterised by large atomic roughness with both adatoms and vacancies. Such interfaces have actually been proven to exist *via* X-ray diffraction measurements supported by molecular dynamic simulations ¹⁰⁹. Other indirect evidence ^{110,111} has also supported this theory.

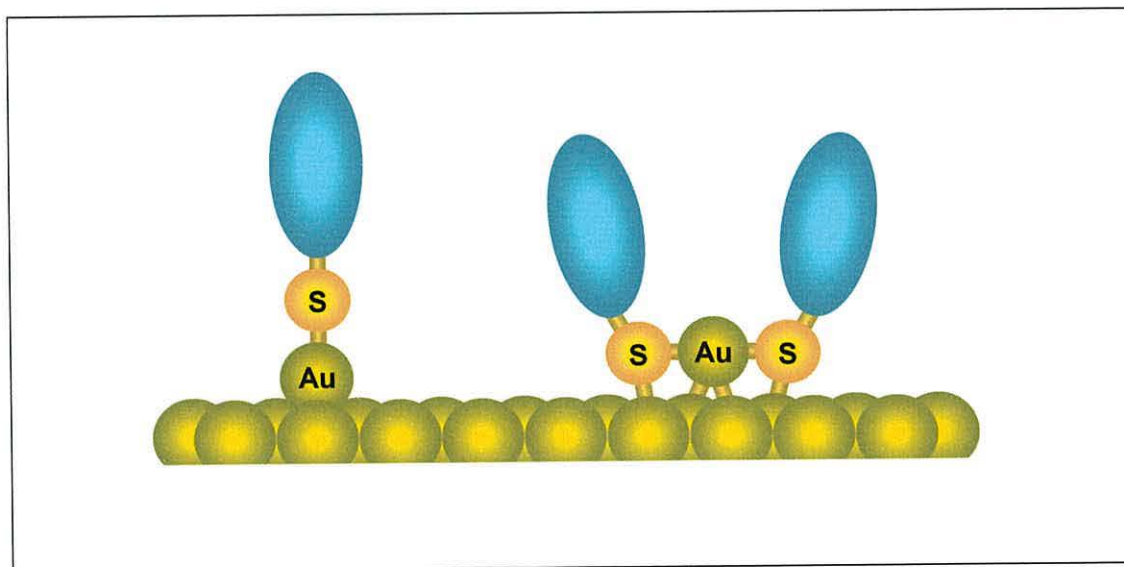


Fig. 2.1.3-1 Schematic model of thermodynamically optimal ways of thiolate sulfur attachment to Au(111) surface *via* lifted gold adatoms, according to M. Yu ¹⁰⁸ (left) and P. Maksymovych model ¹⁰⁷ (right); S element can be bound to gold *via* Au adatom situated in fcc or hcp site (left), or can be attached directly to Au(111) near on-top position, and share Au adatom, lifted to bridge site, with S of other molecule (right).

As previously stated, adsorbed thiulates are dynamic systems and undergo transformations whilst reaching equilibrium conditions. These changes can be observed as surface phase transitions of the formed adsorbate complexes and modifications of the initial crystallography of the monolayers¹¹¹⁻¹¹³. At low coverage, separate molecules are free to diffuse to neighbouring sites of similar local potential minima upon thermal fluctuations. Such a phase is known as a lattice gas. If the intermolecular interactions are sufficiently strong, molecules tend to group into, so-called, domains, or islands¹¹²⁻¹¹⁶. They can also form lying-down configurations, which have been observed as striped phases of *n*-alkanethiolate SAMs with an area per molecule of 0.54 – 0.83 nm² (see Fig. 2.1.3-2). Ordering of the aforementioned forms demonstrate a balance between the crystallography of surfaces, surface – molecule interactions, and lateral interactions between molecules. At higher coverage, other (more or less organised) forms can be observed. If the packing density is high, but molecular formation is highly disordered, the adsorbate is usually referred to as a two-dimension liquid phase. The presence of this phase is common for the shortest-chain *n*-alkanethiolates ($n \leq 6$)¹¹⁷, where interactions between molecules are weak. The liquid phase has also been observed for other structures at higher temperatures¹¹⁸. For cases of extremely dense packing, the structure develops a unit cell that repeats periodically across the surface.

Generally, thiol groups of molecules comprising SAMs tend to adopt the arrangement of elemental sulfur on a particular metal substrate¹¹⁹⁻¹²¹. For the deposition onto Au(111), the metal – sulfur interaction drives the assembly to the limiting case, where the gold surface is covered by a ($\sqrt{3} \times \sqrt{3}$) R30° overlayer of thiulates (see Fig.2.1.3-2). However, there is also a secondary ordering corresponding to a $2\sqrt{3} \times 3$ superlattice, that is traditionally referred to as *c* (4×2). These structures have been extensively studied and the results of which have been reviewed by several authors^{48,61,106,122-124}. In both configurations, the distance between alkyl chains of neighbouring molecules was *ca.* 0.5 nm, and the average area occupied per molecule was *ca.* 0.215 nm². FT-IR studies have indicated that a mean tilt angle of alkyl chains from the surface normal was *ca.* 20 – 40° and with a mean twist angle about the molecular axis of *ca.* 50 – 55°^{38,71,89,118,125,126}. Both vary with the chains length and nature of the terminal groups.

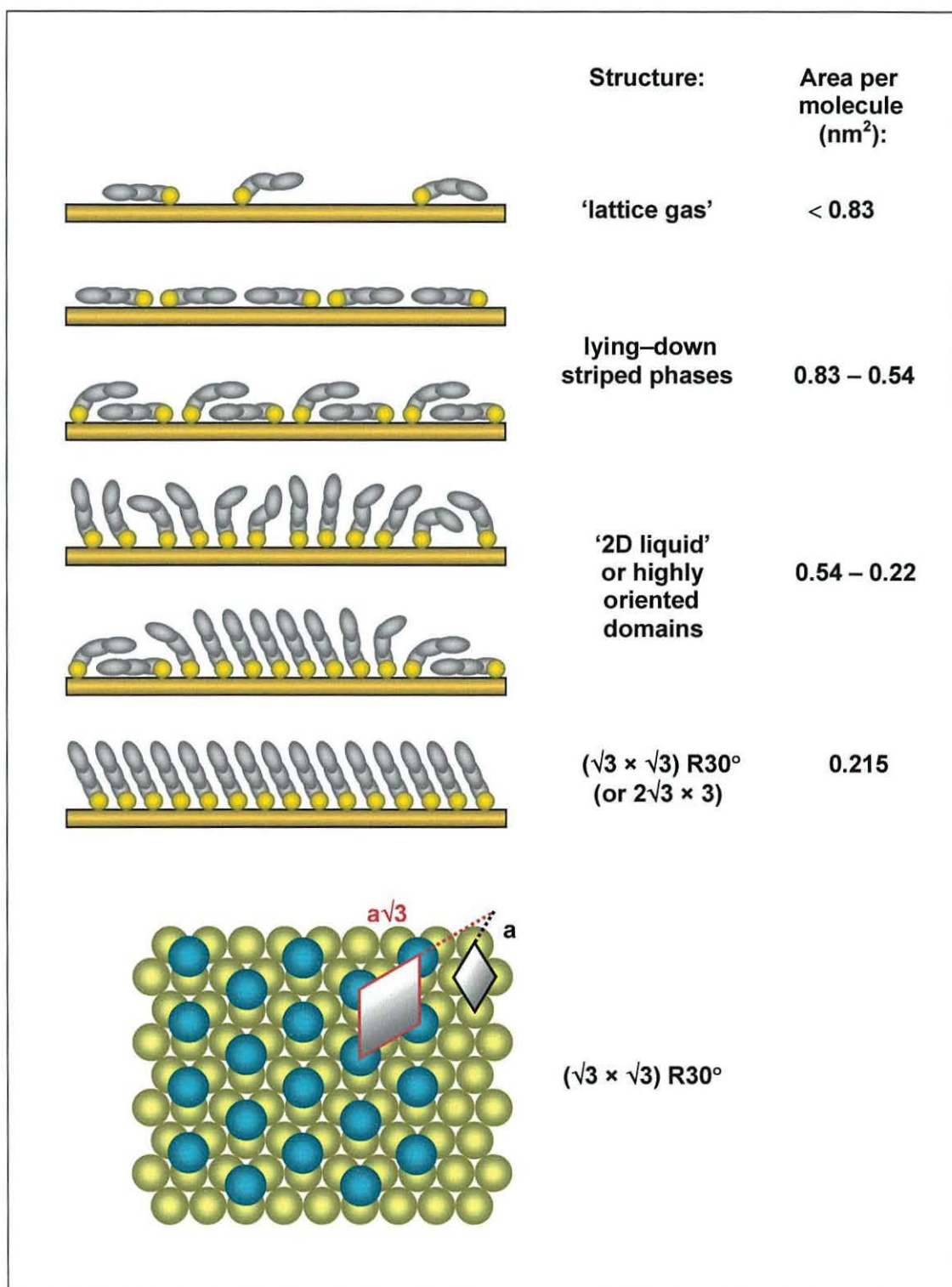


Fig. 2.1.3-2 Schematic representation of *n*-alkanethiolate structures on Au(111) ⁶¹.

Formation of the uniform hexagonal ($\sqrt{3} \times \sqrt{3}$) R30° phase is conditioned by the rule of the highest possible packing. On the other hand, the process of transformation of this phase to the $2\sqrt{3} \times 3$ structure, and the arrangement of molecules in such monolayers, remains unsolved. There seems to be more than one molecular configuration compatible with this unit cell (see Fig. 2.1.1-4). There are also two major theories explaining different surface orientations of the self-assembled molecules. The first considers the coexistence of two different binding sites ¹⁰⁵. The second suggests the presence of two different configurations of molecular attachment at the equivalent binding sites in such a way that the alkyl chains are perpendicular to each other ¹²⁷. The studies of long alkanethiols ($n > 12$) have revealed that the ($\sqrt{3} \times \sqrt{3}$) R30° lattice was predominantly formed at room temperature. The phase transition to the $2\sqrt{3} \times 3$ structure for these molecules occurs upon annealing. For short-chain alkanethiols, the domains of the $2\sqrt{3} \times 3$ structure were found to dominate at room temperature ¹²⁵.

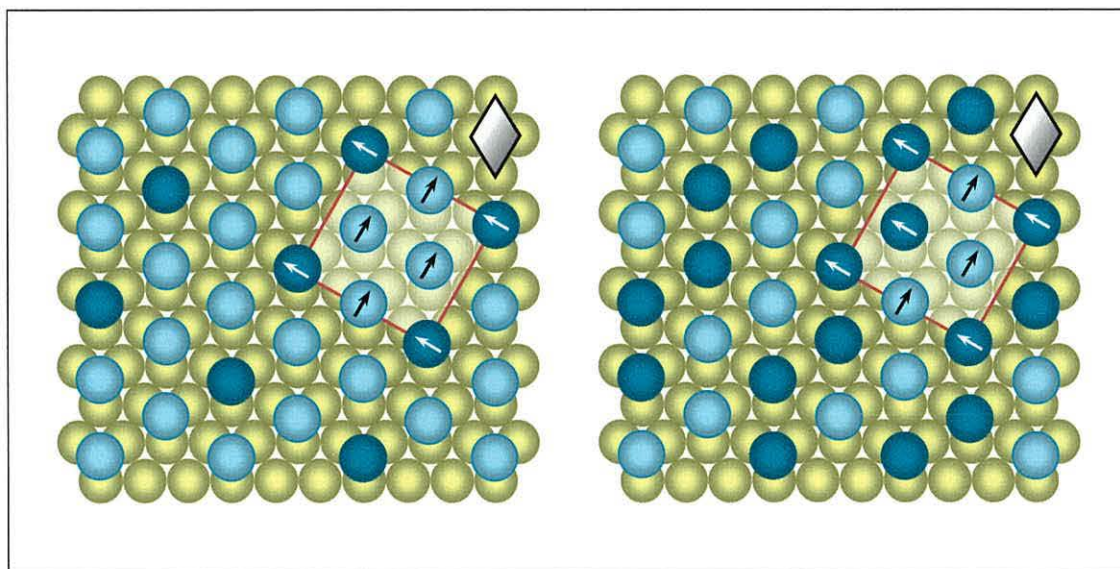


Fig. 2.1.1-4 Schematic diagram of $2\sqrt{3} \times 3$ adlayer structure presenting two different ways of molecular orientation ¹⁰⁶; molecules are tilted or shifted as indicated (arrows); unit cells of the gold substrate (black rhombus) and the adlayer (red rectangle) are also denoted.

There is also strong evidence of striped phases of the short-chain homologues developing a unit cell of $p \times \sqrt{3}$, ($4 \leq p \leq 10$), which were observed after annealing¹²⁸ or after long term storage^{117,129}. Experiments suggest that molecules forming these dense phases have a stand-up configuration, which is in contrast to the laying-down structures observed for the intermediate stages of deposition. Molecules are believed to form highly ordered linear domains. This behaviour could be a consequence of partial desorption of a small fraction of molecules from the monolayer.

Aromatic thiols, except short one-ring systems, also tend to form highly oriented and dense SAMs¹³⁰. However, in the case of the phenyl-based molecules, stronger interactions of these systems with substrates, greater stiffness of their backbone structure and steric hindrance all have a strong impact on the monolayers growth and the final molecular arrangement¹³¹⁻¹³³. It has also been found that the degree of ordering increased with the number of phenyl rings¹³⁰ and varied depending on the nature of the terminal group¹³³. Additionally, a higher number of phenyl rings in the thioaromatic molecules, causing stronger intermolecular interactions, resulted in a less inclined orientation of these molecules in respective SAMs¹³¹. The tilt angles from the surface normal also varied among thioaromatic molecules with different terminal groups¹³⁴. However, their inclination was generally smaller than that found for *n*-alkanethiolates, which reflects the fact that the cross-section of thioaromatic molecules is larger than the cross-section of alkanethiols. Thus, the lateral interactions did not induce a large tilt.

Linear oligoarylenes [$\text{C}_6\text{H}_5-(\text{C}_6\text{H}_4)_n-\text{SH}$] generally exhibit the $(\sqrt{3} \times \sqrt{3})$ R30° lattice of the S elements attachment to Au(111) surfaces, when a limiting mass coverage for the standing-up phase is achieved. However, the higher cross-section of the phenyl rings compared to the alkyl chains leads to the $(2\sqrt{3} \times \sqrt{3})$ R30° lattice of the molecular backbone structure, with a herringbone phenyl plane arrangement in the monolayer^{133,135}. A less dense highly-ordered standing-up phase was also observed for monolayers of these molecules⁹². On the other hand, incorporation of the methyl terminal group, resulted in the $(\sqrt{3} \times \sqrt{3})$ R30° lattice with a larger amount of structural defects, which may be due to conformational changes towards increasing the steric hindrance^{132,136}. Such a mismatch of the two-dimensional lattice of molecular adlayers and Au(111) structure usually results in domains of the $(\sqrt{3} \times \sqrt{3})$ R30° lattice surrounded by other less ordered phases.

A different, atypical molecular arrangement, incompatible with the crystalline gold structure, was observed for conjugated arylthiols $[\text{C}_6\text{H}_5-(\text{C}\equiv\text{C}-\text{C}_6\text{H}_4)_n-\text{SH}]$ ¹³⁷. Their arrangement is similar to the herringbone structure of oligoarylenes, revealing a $(2\sqrt{3} \times \sqrt{3}) \text{R}30^\circ$ superlattice, but a mismatch of the molecular adlayer structure and the crystalline gold lattice underneath occurs. The new rectangular unit cell containing two molecules was proposed for this system (see Fig. 2.1.1-5). Such a monolayer consists of molecular rows being oriented $\pm 5^\circ$ with respect to the three $\langle 121 \rangle$ directions of the Au(111) lattice. According to this model, molecules must occupy two different sites of the gold lattice (attachment *via* lifted Au adatom is not considered here).

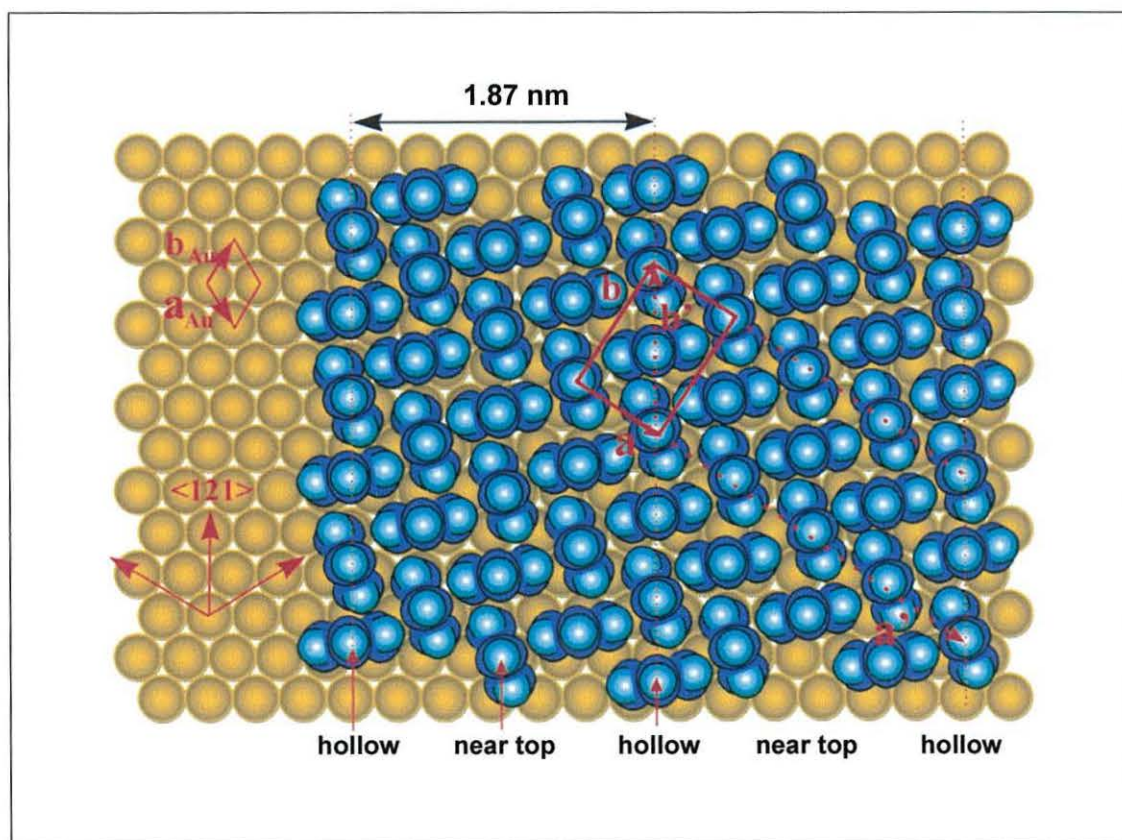


Fig. 2.1.1-5 Schematic diagram of the proposed $(2\sqrt{3} \times \sqrt{3}) \text{R}30^\circ$ arrangement for 4,4'-bis(phenylethynyl)benzenethiolates on Au(111); crystallographic directions, unit cells and hypothetical sites for sulfur attachment are indicated (source: G. Yang *et al.* ¹³⁷).

2.2 Selected techniques for monolayer characterisation

Nowadays, there is a vast number of complementary experimental techniques for characterisation of SAMs available. Vibration and electron spectroscopies, probe microscopy, diffraction methods, and many others can be distinguished. Recently, C. Vericat *et al.*¹²² have comprehensively reviewed these techniques. Undoubtly, STM is one of the most versatile and frequently applied tools for determining the structural properties of SAMs. However, because of another unique ability of STM, which is studying electronic properties of molecular systems, this technique has been reviewed separately (see Section 2.3). This section describes the two techniques, which have been used by the author in order to find an average density of arrangement and chemical composition of molecular films.

2.2.1 X-ray photoelectron spectroscopy

Being classed as a kind of photoemission spectroscopy (PES), XPS, sometimes called ESCA (electron spectroscopy for chemical analysis) is one of the most powerful methods of elemental surface analysis. It provides both qualitative and quantitative information about surface composition (except for hydrogen and helium) of the top *ca.* 1 – 20 nm of any material, which is stable in ultrahigh vacuum. Moreover, it enables acquisition of valuable information about the chemical bonding and electronic structures of a studied material. Its most sophisticated version, angle resolved X-ray photoelectron spectroscopy (ARXPS), is also used for depth composition profiling¹³⁸⁻¹⁴¹.

Theoretical background

XPS was developed in the mid-1960s by K. Siegbahn and his research group¹³⁸. This technique is based on the photoelectric effect outlined in 1905 by Einstein¹³⁸. According to his concept, photons interact with atomic orbital electrons. In the absence of electron scattering, there is total and complete transfer of the incident photon's energy to the electron. Ejection of an electron occurs when the photon energy ($h\nu$) is at

least equal to the binding energy (E_b) of the electron. The kinetic energy (E_k) of such a photoelectron is:

$$E_k \cong h\nu - E_b \quad \text{Eqn 2.2.1-1}$$

Generally, an XPS instrument measures the number of electrons of different E_k , ejected from a sample, and calculates E_b values for the core atomic orbital of each element in the sample. This gives rise to a characteristic set of peaks at specific binding energies in the photoelectron spectrum. The position of peaks in the energy scale reveals the qualitative nature of the sample, and a determination of intensities of the separate peaks enables quantitative analysis.

The physical description of the photoelectric effect, given by Eqn 2.2.1-1, where E_b is simply a reference to the vacuum level, defined as zero energy, is a simplified case of the energy balance of a real XPS experiment. Thus, this applies to separated molecules in a gas phase only. In typical experiments, the detected E_b values need to be corrected by the sample work functions (ϕ^S), surface charge energies, electronic structure relaxation effects, and other instrumental energy losses, including those on the radiation emitter¹³⁸ (the last three were entirely denoted as E_{loss}):

$$E_b^S = h\nu - E_k - \phi^S - E_{loss} \quad \text{Eqn 2.2.1-2}$$

In such a case, core electron binding energy, denoted as E_b^S , is referenced to the Fermi level of the sample.

Instrumentation and operation

A typical XPS instrument consists of an X-ray gun, a monochromator, a sample mounting assembly in a vacuum chamber, an analyser and a detector¹⁴² (see Fig. 2.2.1-1). The X-ray gun is a source of X-ray radiation (Al $K\alpha$, or Mg $K\alpha$). The radiation is obtained when high-energy electrons, emitted by a filament and accelerated by high tension between a filament and an Al or Mg anode face, bombard the anode. They knock out electrons from core orbitals of anode atoms. Created holes are filled with electrons from an upper orbital, and excess energy is emitted in the form of X-ray photons.

Although X-ray emission is dominated by the sharp, intensive and well-defined $K\alpha_1$ and $K\alpha_2$ peak doublet, there are other less intensive satellite peaks, and so called white radiation, which need to be filtered out for rigorous analysis of thin-layer organic materials. This is achieved by X-ray diffraction through quartz crystals mounted to a toroidal glass substrate, according to the Bragg condition, and also the Roland Circle design, this is to simultaneously focus the monochromated radiation on a sample.

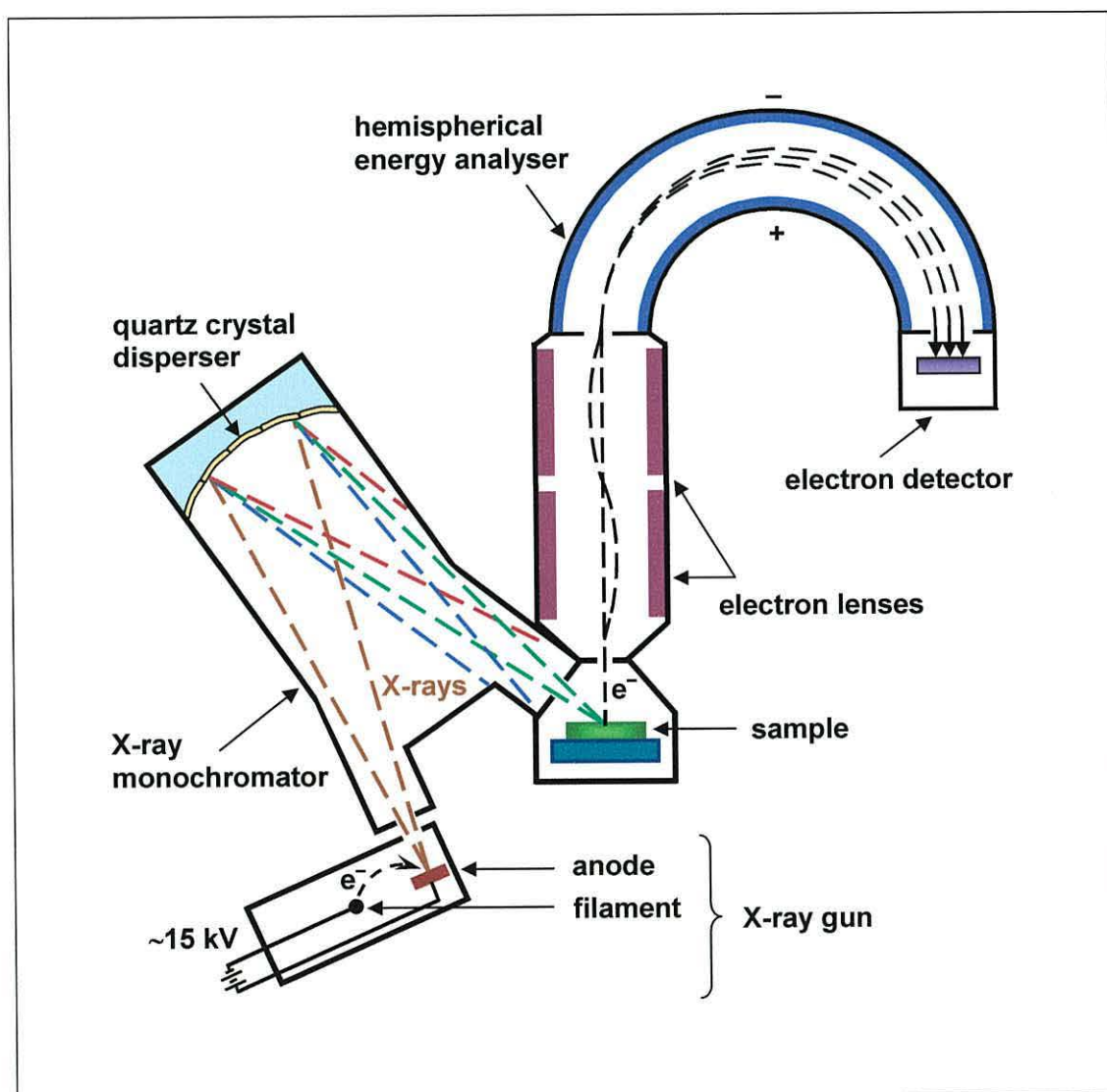


Fig. 2.2.1-1 Schematic of XPS analysis with major components of the instrumentation, according to the description given in the reference cited ¹⁴².

Electrons ejected from the sample are focused onto the hemispherical analyser entrance slit by a set of electrostatic lens units. Electrostatic fields are established to only allow electrons of a given energy, *i.e.* pass energy (*PE*), to reach the detector slits. Electrons of a specific initial E_k are measured by setting voltages for the electrostatic lens system. This focuses photoelectrons of the required initial energy, and retards their velocity so that their kinetic energy (after passing through the lens system) matches the *PE* of the hemispherical analyser. To record a spectrum over a range of initial excitation energies it is necessary to scan the voltages applied to these lenses. The value of *PE* also needs to be adjusted to meet experimental requirements. The higher values of *PE* give stronger signals but lower energy resolution, and *vice versa*: lower values give higher energy resolution but weaker signal intensities¹³⁸.

2.2.2 Quartz crystal microbalance

Compared to other techniques for studying the self-assembly process and monolayer properties, QCM is a relatively simple and cheap method. It is commonly applied for monitoring adsorption kinetics of organic and inorganic moieties in both gaseous and liquid environments¹⁴³⁻¹⁴⁵. It is very useful for determining an average packing density of thiolate SAMs^{66,84}, and can also be adopted for recognition of molecules on functional monolayers^{146,147}.

In the late 1950's G. Sauerbrey¹⁴⁸, based on his previous experiments, proposed a device that was capable of ultra-sensitive mass measurements. He found that changes in vibration frequency (Δf) of a piezoelectric crystal, oscillating in an applied electric field, were directly proportional to the mass of adsorbate (Δm) attached to the surface of the crystal. The formula describing this relation for measurements performed in air is:

$$\Delta m = -\Delta f \frac{A \sqrt{\rho_q \mu_q}}{2 f_0^2} \quad \text{Eqn 2.2.2-1}$$

In this equation, A is the active vibrating area, ρ_q is the density of quartz, μ_q is the shear modulus of quartz and f_0 is the resonant frequency of the quartz resonator.

A typical model of a QCM for the studies of molecular self-assembly processes is shown in Fig. 2.2.2-1. It consists of a thin wafer of quartz and gold electrodes, evaporated on the two major faces of the crystal.

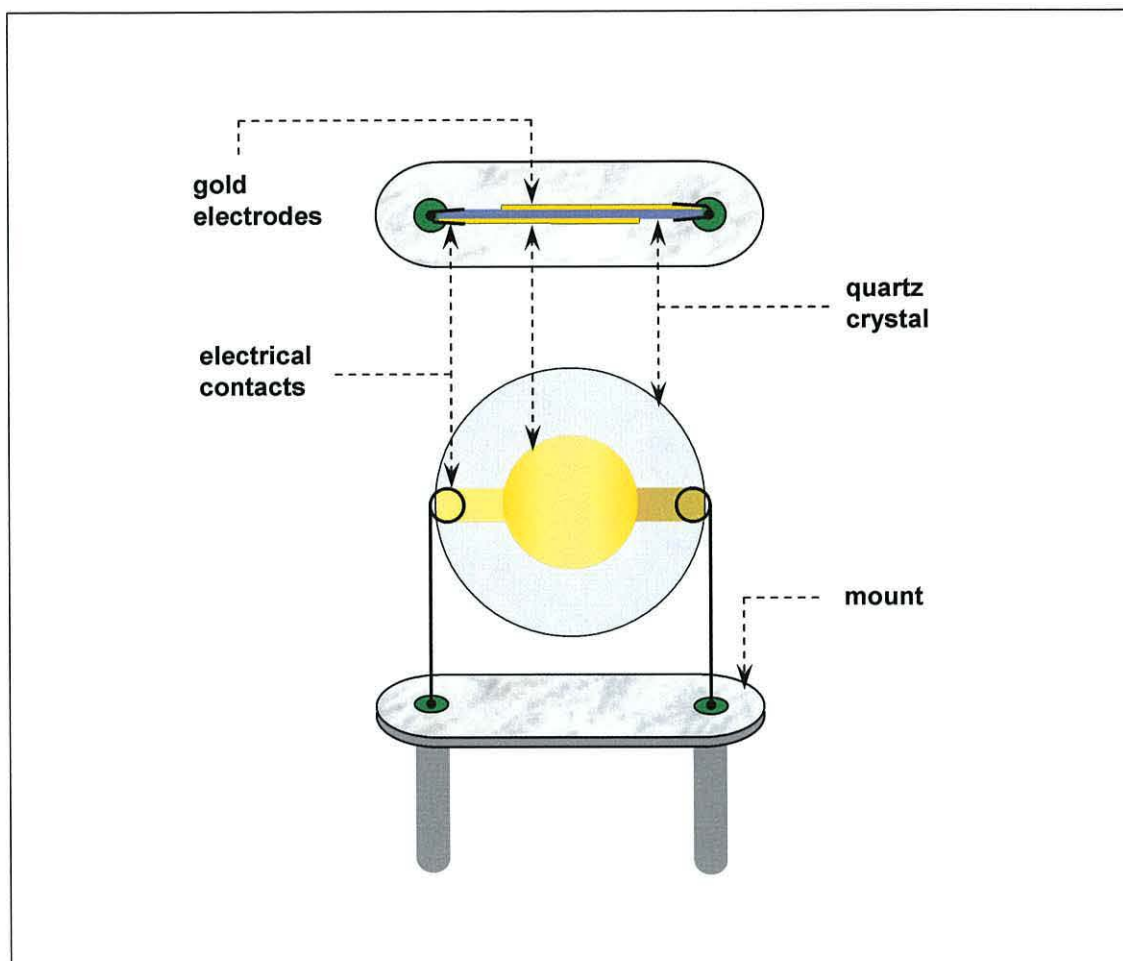


Fig. 2.2.2-1 Pattern of a standard QCM: top and side views.

Measurements of Δm , indicating the adsorption of molecules on both electrodes of the sensor, as a function of deposition time, enable one to obtain the kinetic parameters of the process. Moreover, this data contains information about structural properties of the molecular adlayers. These are revealed by converting Δm into the total number of molecules (N) self-assembled onto the electrodes:

$$N = \frac{\Delta m N_A}{W} \quad \text{Eqn 2.2.2-2}$$

Here; N_A is the Avogadro constant, and W is the molecular weight of the compound. The average area occupied by a single molecule at each stage of the deposition can now be easily calculated by dividing the area of the two gold electrodes ($2A$) by N , which gives:

$$\text{area/molecule} = \frac{2A W}{\Delta m N_A} \quad \text{Eqn 2.2.2-3}$$

These data are useful for the control of molecular packing and for comparison with other experimental results in order to deduce geometric configurations of thiolates in densely packed arrangements.

2.3 Scanning tunnelling microscopy and spectroscopy

STM was developed in 1981 by IBM scientists: G. Binnig and H. Rohrer^{149,150}. The general idea behind it was relatively simple: to probe the structure of surfaces or adlayers by applying small bias voltages between the surface and an atomically sharp metal tip. The tip scans across the surface detecting the variation in the current flow and responds to these changes. It was the first technique, which enabled visualisation of the nanometer-scale topography of metals, semiconductors and superconductors¹⁵¹. It has been an irreplaceable tool for studying adsorbed atoms, molecules and various biological systems both separately and together. Experiments have also shown that it can be used to manipulate atoms and molecules on a surface¹⁵², to probe the electrical properties of the above-mentioned systems¹⁵³ and to investigate other local features of adsorbed structures. This invention was quickly followed by the development of a whole family of related techniques, which may be classified in the general category of scanning probe microscopy (SPM).

2.3.1 *Operation*

STM has two modes of operation: constant-height and constant-current mode. The second, also called a topographic mode, is the most suitable for a vast majority of applications. To maintain the constant-current condition at a selected set-point current and bias voltage, a feedback loop is employed. It corrects the tip – sample separation distance according to the local changes in sample conductivity or topography. These changes are analysed in real-time by a control unit and displayed on a screen. The constant-height mode can be applied only to the small-area/high-resolution scans of atomically flat surfaces, since any structural defects can result in the tip crashing into the surface. Fine movement of the tip in all three dimensions is controlled by piezoelectric elements, these enable tip position adjustment with a precision higher than 0.01 nm. Unfortunately, an equivalent resolution of surface images is not achievable due to environmental noise: vibrations of STM elements and imaged moieties in particular. Resonant vibrations of the piezoelectric elements are the major source of instrumental noise. This can be reduced by appropriate tuning of operational parameters of the STM unit. Other disruptive effects are induced by the operational environment. These acoustic and thermal vibrations of the surrounding atmosphere can, however, be minimised by using acoustic attenuators and environmental hoods for low-temperature measurements.

A separate mode of the same instrument, which performs surface scans at constant bias voltage, can be applied to detect current response at varying electric field at a fixed position of the tip above a sample. This method enables the study of electronic properties of materials in a similar way to optical spectroscopy, which provides information about the molecular electronic structure excited by photons with selected energies. Thus, this electrical probing technique is referred to as scanning tunnelling spectroscopy (STS). It is typically employed for studying current transmission through molecular systems and various quantum phenomena affecting this process, and to measure conductivity of temporarily formed molecular junctions. It is also used as a method of molecular vibration analysis, analogically to the optical infrared spectroscopy. This technique of measuring molecular vibrational modes operates on

the same principles as inelastic electron tunnelling spectroscopy (IETS), and thus it is sometimes called STS-IETS¹⁵⁴.

2.3.2 Tunnelling current

STM-STs operate on a fundamental effect of quantum mechanics. Under an applied voltage (V) electrons tunnel through a small gap ($d < 1$ nm) between a sample and an STM tip. The tunnelling current (I_{tun}) originates from the wave nature of electrons and can be estimated using the standard quantum physical approach. A situation, where a space-dependent wave function $\Psi(x)$ of a single electron with energy E , penetrate a one-dimensional square barrier is shown in Fig. 2.3.2-1. The solution of the Schrödinger equation for this model situation shows an exponential decay of the wave function in this classically forbidden region:

$$\Psi(d) = \Psi(0) e^{-2\pi \frac{\sqrt{2m_e(\phi-E)}}{h} d} \quad \text{Eqn 2.3.2-1}$$

Here, ϕ is the height of the barrier. Considering this equation to be valid for electrons tunnelling between the sample and the STM tip under a small bias voltage, when the shape of the barrier is still approximately rectangular ($eV \ll \phi$, where ϕ can be treated as an average of the sample and the tip work functions), and also taking into account the local density of states (LDOS) of the sample (ρ_{surf}) and the tip (ρ_{tip}) at Fermi level (E_F):

$$I_{tun} \propto V \rho_{surf} \rho_{tip} e^{-4\pi \frac{\sqrt{2m_e(\phi-E)}}{h} d} \quad \text{Eqn 2.3.2-2}$$

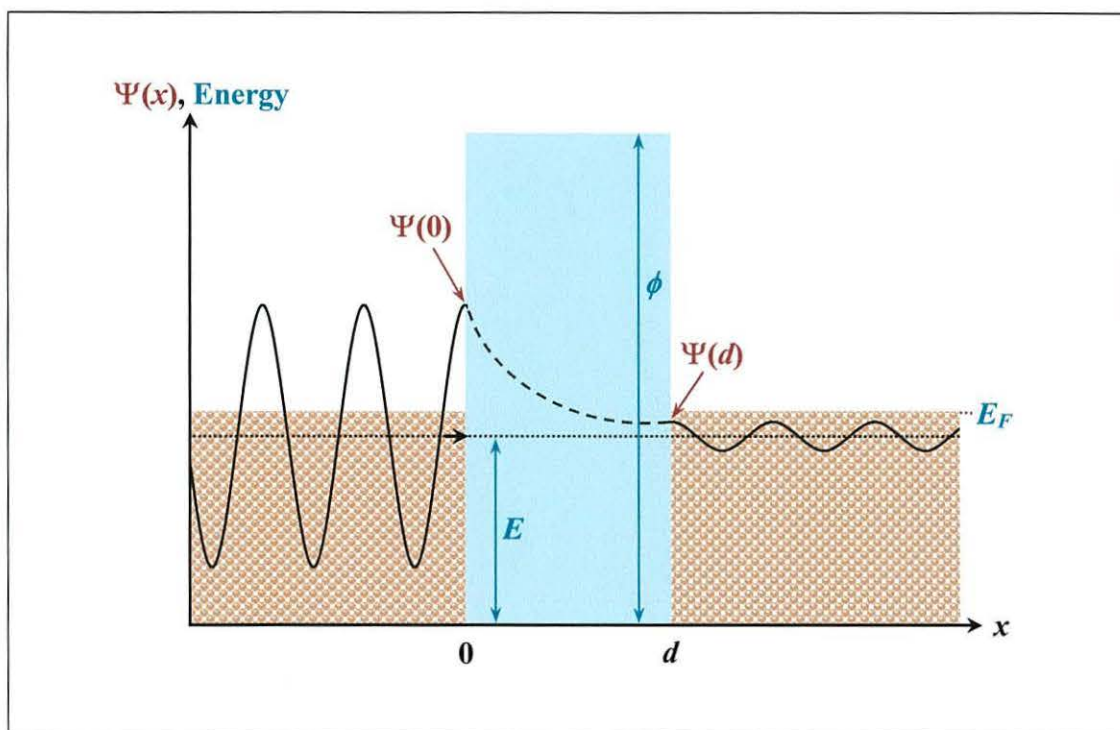


Fig. 2.3.2-1 Wave function $\Psi(d)$, for an electron with kinetic energy E penetrating a thin potential barrier of height ϕ and width d , illustrating the tunnel effect.

For better accuracy of the I_{tun} description, a more complex formula needs to be applied. It should consider the shape of the barrier and the spectral density of surface states of the sample $[\rho_{surf}(E)]$ and the tip $[\rho_{tip}(E)]$, which overlap within the energy range of the tunnelling regime. The first satisfactory quantitative treatment of tunnelling current for a real STM experiment (currently the most commonly referenced) which became a prototype for other, more sophisticated theories, was proposed in 1983 by J. Tersoff and D.R. Hamann^{155,156}. One of the important aspects of their approach was the localisation of $\rho_{tip}(E)$ in the centre of a model probe with a spherical apex. This enabled the determination of a surface – tip distance to be *ca.* 0.6 nm for a gold surface, and predicted the resolution of their instrument to be *ca.* 0.5 nm. The simplified version of their formula by N.D. Lang¹⁵⁷, for $k_B T \ll eV \ll \phi$ conditions, describing the tunnelling current at a fixed location (\vec{r}), under V (which is considered to affect the Fermi levels of both electrodes equally by $\pm \frac{1}{2} eV$) is:

$$I_{tun}(\vec{r}, V) = \frac{8\pi^2 e}{h} \int_{E_F - \frac{1}{2}eV}^{E_F + \frac{1}{2}eV} \rho_{surf}(\vec{r}, E + E_F^{surf} \pm \frac{1}{2}eV) \rho_{tip}(\vec{r}, E + E_F^{tip} \mp \frac{1}{2}eV) M(\vec{r}, E, V) dE$$

Eqn 2.3.2-3

In this equation, $M(\vec{r}, E, V)$ is the tunnelling probability determined by the matrix element, which according to J. Bardeen¹⁵⁸, includes all possible states of electron wave function inside the barrier. For the simplest model case, shown in Fig. 2.3.2-2, the calculated tunnelling probability is:

$$M(\vec{r}, E, eV) = e^{-4\pi \frac{\sqrt{2m_e(\langle\phi\rangle - E + \frac{1}{2}eV)}}{h} d}$$

Eqn 2.3.2-4

When the barrier shape and/or tunnelling conditions differ from this model example, $M(\vec{r}, E, V)$ becomes very complex as matching of the wave function in different regions is required¹⁵⁹.

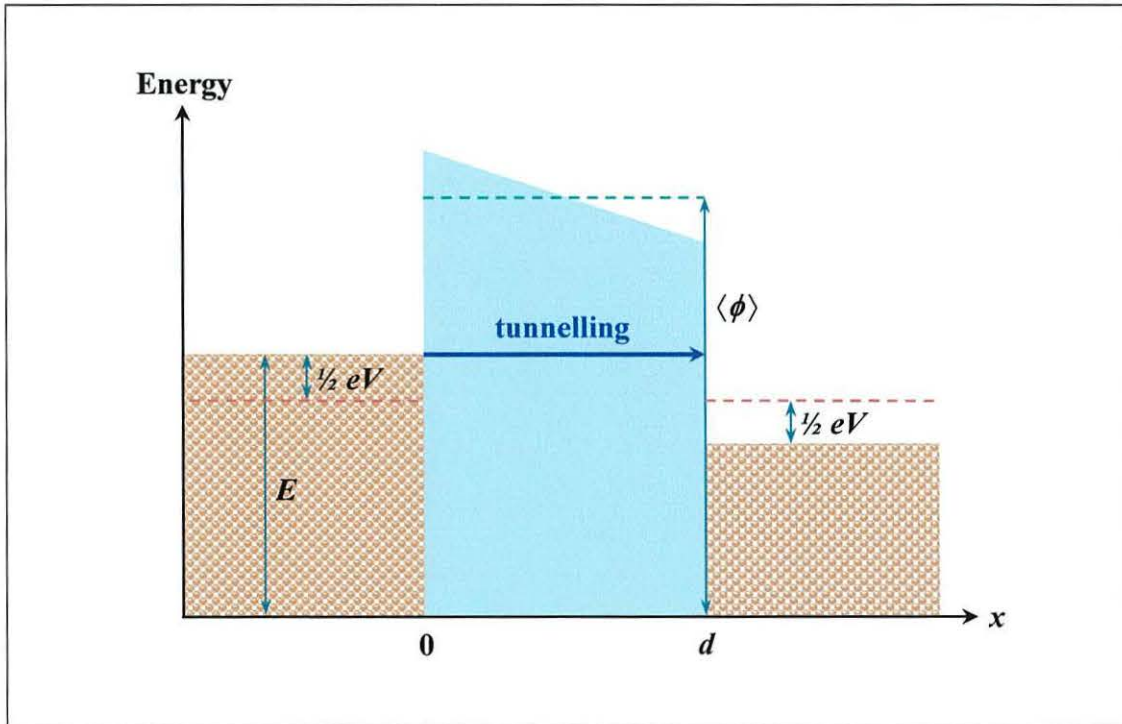


Fig. 2.3.2-2 Energy diagram for the electron tunnelling through the model barrier under applied bias voltage.

The Tersoff and Hamann approach provides a qualitative interpretation of the STM images and good explanation of the tunnelling current between the tip and the metallic surface. On the other hand, since the realistic geometry and the atomistic structure of the tip and its complex interaction with the sample are not included in this model, more strict theories have been successively developed¹⁶⁰⁻¹⁶³. However, this simple picture demonstrates basic principles of STM operation and points out the most important facts, which are:

- 1) the tunnelling current exponentially decreases with an increase in the tip – sample separation distance;
- 2) the barrier shape strongly influences the tunnelling current;
- 3) STM senses LDOS as a function of the tunnelling electrons energy, rather than the real topography of surfaces.

2.3.3 Electronic transmission through molecules

Inserting a molecule into an empty space between an STM tip and a substrate significantly affects the electron tunnelling process, as the incorporated electronic states of the molecule cause a substantial modification of the barrier shape. It has a strong impact on the theoretical description of the electronic transmission, since precise information about the electronic structure of the molecule as well as the electronic coupling (wave function mixing) between electrodes and this molecule are required. The methodology of determining the electronic transmission through such molecular junctions is similar to the Tersoff – Hamann approach. However, the transmission probability is calculated from a more general Hamiltonian matrix – the Green's function matrix^{164,165}. This element carries all the information about the electronic structure of the molecule, including the coupling between discrete molecular orbitals and continuous bands of the electronic structure of the substrate, and can be resolved numerically using DFT. The transmission function $[T(E)]$, obtained from these computations, can be applied directly for calculating the conductance $[G(E)]$ or

current – voltage characteristics from the formula given by R. Landauer¹⁶⁶. For single-molecule conductivity:

$$G(E) = \frac{2e^2}{h} T(E) \quad \text{Eqn 2.3.3-1}$$

Considering the definition of the conductivity, this equation can be converted to the following form, which is useful for I - V characteristic calculations:

$$I(V) = \frac{2e}{h} \int_{E_F - \frac{1}{2}eV}^{E_F + \frac{1}{2}eV} T(E) dE \quad \text{Eqn 2.3.3-2}$$

Ballistic transport

According to Eqn 2.3.3-1, the highest possible value of the one-dimensional systems conductivity is achieved when $T(E)$ reaches unity. The value of such a perfect transfer of electrons from one electrode to the other through a point contact is referred to as the conductance quantum unit (g_0), and is defined as:

$$g_0 \equiv \frac{2e^2}{h} = (12.9 \text{ k}\Omega)^{-1} \quad \text{Eqn 2.3.3-3}$$

This quantity was observed for the electronic transmission through single atoms, or short strands of atoms, trapped between an STM tip and a sample^{167,168}. Such transfer of electrons was called the ‘ballistic transport’, as it occurs when a mean free path of electrons in a medium, through which the electrons travel, is bigger than the distance between the electrodes.

Quasi-ballistic electron transport was proven to exist in short carbon nanotubes¹⁶⁹⁻¹⁷¹, which were stiff enough to prevent most vibrations from coupling with other electrons, and thus could act as ‘electron waveguides’. A similar effect might be theoretically allowed in molecular materials with completely delocalised electronic structure along the main axis of the molecule, and in the absence of vibronic coupling,

which could provide complete electronic transparency of such systems. However, up to now there have been no ideas for creating molecular structures, which would be capable of transmitting electrons, according to this model. Thus, the transparency of molecular materials is commonly accepted to be lower than one, and molecular wires should be considered as partial guides for electron exchange, rather than materials supporting a permanent flux of electrons.

Superexchange

Recent observations of molecular junctions strongly suggest that the typical mechanism of electron transport through these systems is tunnelling^{172,173}. This is to be expected, assuming that the Fermi level is approximately in the middle, between the highest occupied molecular orbital (HOMO) and the lowest unoccupied molecular orbital (LUMO) of neutral molecules, which are separated by a gap of *ca.* 1.5 – 8 eV (see Fig. 2.3.3-1). This means that any molecular level is usually beyond external electrons access. This is because a sufficient amount of energy can not be transferred to the electrons without damaging the molecule, given that the energy required for breaking the gold – thiolate bond is not much higher than 1.2 eV. However, even if the Fermi energy of the electrodes is a significant energetic distance away from resonance with any molecular state, and the electrons do not physically reside on the molecule during the transfer, the presence of these states and the strength of the molecule – electrode coupling play an important role by lowering the effective barrier for tunnelling. Such a molecule-mediated electronic transmission is usually referred to as superexchange in order to distinguish this process from the typical through-vacuum tunnelling¹⁷⁴⁻¹⁷⁶.

Considering the exponential dependence of the geometric parameters on the tunnelling probability (see Eqn 2.3.2-4), a simple description of the superexchange phenomenon can be given based on Eqn 2.3.3-1 and 2.3.3-3. According to these equations, the molecular off-resonant conductivity is:

$$G = g_0 e^{-\beta L} \quad \text{Eqn 2.3.3-4}$$

Here, L is the length of the molecule and β is the tunnelling decay constant, which is related to the effective height of a tunnelling barrier and is obtained straight from distance dependent STM measurements of the molecular conductivity. The values of β have been estimated for various structures (see Fig. 2.3.3-1) using different techniques. This parameter has generally been proven to decrease with higher conjugation of π -type orbitals, which results in smaller HOMO – LUMO gaps¹⁷⁷⁻¹⁸⁵. The other important issue concerning Eqn 2.3.3-4, which should be pointed out here, is the total independence of the superexchange process on temperature. This, in fact, was observed for molecular junctions of *n*-alkanethiols¹⁷².

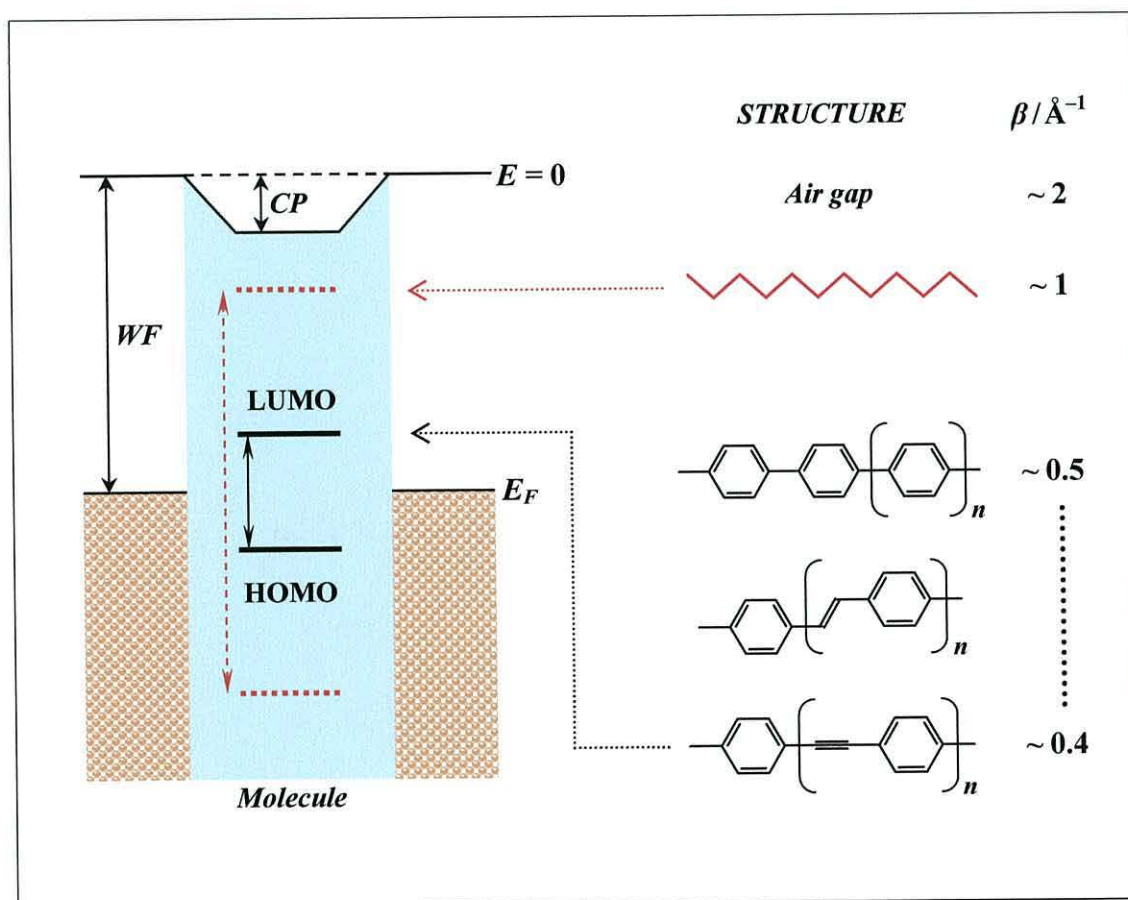


Fig. 2.3.3-1 Schematic differences in the energy level separation of frontier molecular orbitals and the values of β , which were typically observed for the exemplary structures¹⁷⁷⁻¹⁸⁵; CP is a contact potential and WF is an electrode work function; the effect of strong coupling is presented ($CP \gg 0$).

The significance of molecule – electrode coupling was also confirmed by demonstrating much higher transmissions for chemisorbed than physisorbed contacts¹⁸⁶⁻¹⁸⁹. The strength of this coupling, especially distinctive for chemisorbed contacts, magnified the contributions from the contact potential (*CP*) in lowering the barrier for tunnelling¹⁶⁴, which was denoted in the energy diagram in Fig. 2.3.3-1. This has a strong impact on STM experiments, as the conductivity of singly bound thiolate is always more than an order of magnitude lower than that of a doubly bound equivalent¹⁸⁶. Thus, spontaneous chemical bonding between the terminal atom of the STM tip and the thiol group of a dithiol molecule, mono-attached to a substrate, results in a strong and a rapid increase in observed current response at a constant bias voltage (see Section 2.3.4).

Activated transport

The analysis presented above has shown that, for the neutral saturated molecules, it is practically impossible to achieve a model of electron transport that permits a population of molecular orbital states. However, as shown in Fig. 2.3.3-1, such transport is probable for high-conjugated aromatic systems with a small HOMO – LUMO gap when a sufficiently high bias voltage is applied. This creates drastically different conditions for electron flow through the junction, as they can physically reside on the molecule for considerably long enough to be affected by molecular dynamic events. A molecule is capable of trapping excess charge injected from the electrode, until it gains additional energy to escape from a local energy minima on the molecular chain. This is why such a sequential process is called activated transport, or simply hopping¹⁹⁰, although there are other types of activated mechanisms distinguished in the literature apart from hopping¹⁹¹. The basic characterisation of the conductance for activated electron transport over the potential barrier, the averaged height of which is described by Δ , is given by the following dependence:

$$G \propto N^{-\eta} e^{-\frac{\Delta}{k_B T}} \quad \text{Eqn 2.3.3-5}$$

In this formula, η is a numerical parameter in the range $1 < \eta < 2$, depending on the hopping conditions^{185,192,193}. It is significant that the hopping conductance is only a weak function of molecular length, represented by the number of electron trapping sites, N . Contrary to superexchange, the activated transport is also a function of temperature, as it strongly depends on thermal processes affecting local electronic structure of the molecules.

Superexchange and hopping do not exclude each other, but may both be present within one system if the bridge state is sufficiently low in energy and its reorganisation energy is high^{194,195}. The activated transport is expected to dominate for the longer high-conjugated molecules, as the HOMO – LUMO gap is smaller, due to the effect of broadening molecular levels.

2.3.4 Tip – molecule – substrate junction formation

Despite the availability of precise nano-scale manipulation and testing techniques it is still very difficult to contact molecules in the desired manner for electrical measurements. The most problematic task is the formation of symmetrical junctions for testing the electrical response of the molecules under optimal geometry conditions. Thus, the statistical approach, based on nano-probing techniques such as STM-STS, remains the most reliable form of studying the conductive properties of molecular junctions.

There are two different methods of measuring single-molecule conductivity of self-assembled molecules using STM-STS that have been reported in the literature: the first by B. Xu and N.J. Tao¹⁶⁸, and the second by W. Haiss *et al.*¹⁹⁶. The Xu – Tao technique was originally demonstrated for electrical current measurements in liquid environments, but its adaptation to air conditions was also shown by W. Haiss *et al.*^{197,198}. Both methods have been focused on temporal spontaneous trapping of symmetrical molecules between substrate and STM tip, and detecting current response at a constant bias voltage. The terminal parts of these molecules are required to reveal sufficient affinity to gold in order to provide strong coupling to both electrodes simultaneously, when the tip – sample separation distance reaches a sufficiently low value. In order to

estimate the conductivity of a molecular system the difference in the current flow through the strongly coupled two-terminated molecules and the weakly coupled system, after the Au–S bond breaking, are compared. Thus, these methods are generally referred to as the STM-STS break junction techniques. The difference between them is in the practical realisation of the break junction experimental idea.

I-s STS

The first technique was called *I-s* STS as it was based on the measurements of current *vs.* relative distance (*s*) in the direction perpendicular to the substrate. In the Xu – Tao approach the STM tip was repeatedly brought into and out of contact with a gold substrate in a solution containing the sample molecules of 4,4'-bipyridine. Primarily, when the tip was retracted, the conductance decreased stepwise, with each step occurring preferentially at an integer multiple of g_0 (see Fig. 2.3.4-1a, plot A). This indicated a sequential breaking of monoatomic gold nanowire connections formed by gold atoms lifted from the substrate by the tip. When the tip was sufficiently far from the surface and all the atomic chains were broken, a new sequence of steps in a lower conductance regime appeared. This was associated with the presence of the studied molecules in the formed junctions (see Fig. 2.3.4-1a, plot C). In the absence of the molecules in the solvent, no low-conductive peaks were registered (see Fig. 2.3.4-1a, plot E). This approaching – retracting procedure was repeated until a clear statistical picture of the measured effect was obtained, as shown in Fig. 2.3.4-1a (plots: B, D and F). The highest peak observed at the lowest value of conductivity in the histogram (D in Fig. 2.3.4-1a) was assigned as a response of a single molecule in the junction. Other peaks at higher values indicated the presence of a higher number of molecules in the junction.

To study the conductive properties of self-assembled molecules, especially in dense arrangement, the initial contact of a substrate with the tip is not necessary. Instead, the tip can be lowered to a certain distance above the surface (s_0), which is found to be close enough to attach a molecule to the tip (see Fig. 2.3.4-1b) ¹⁹⁸. The further statistical analysis is exactly the same as presented by Xu and Tao.

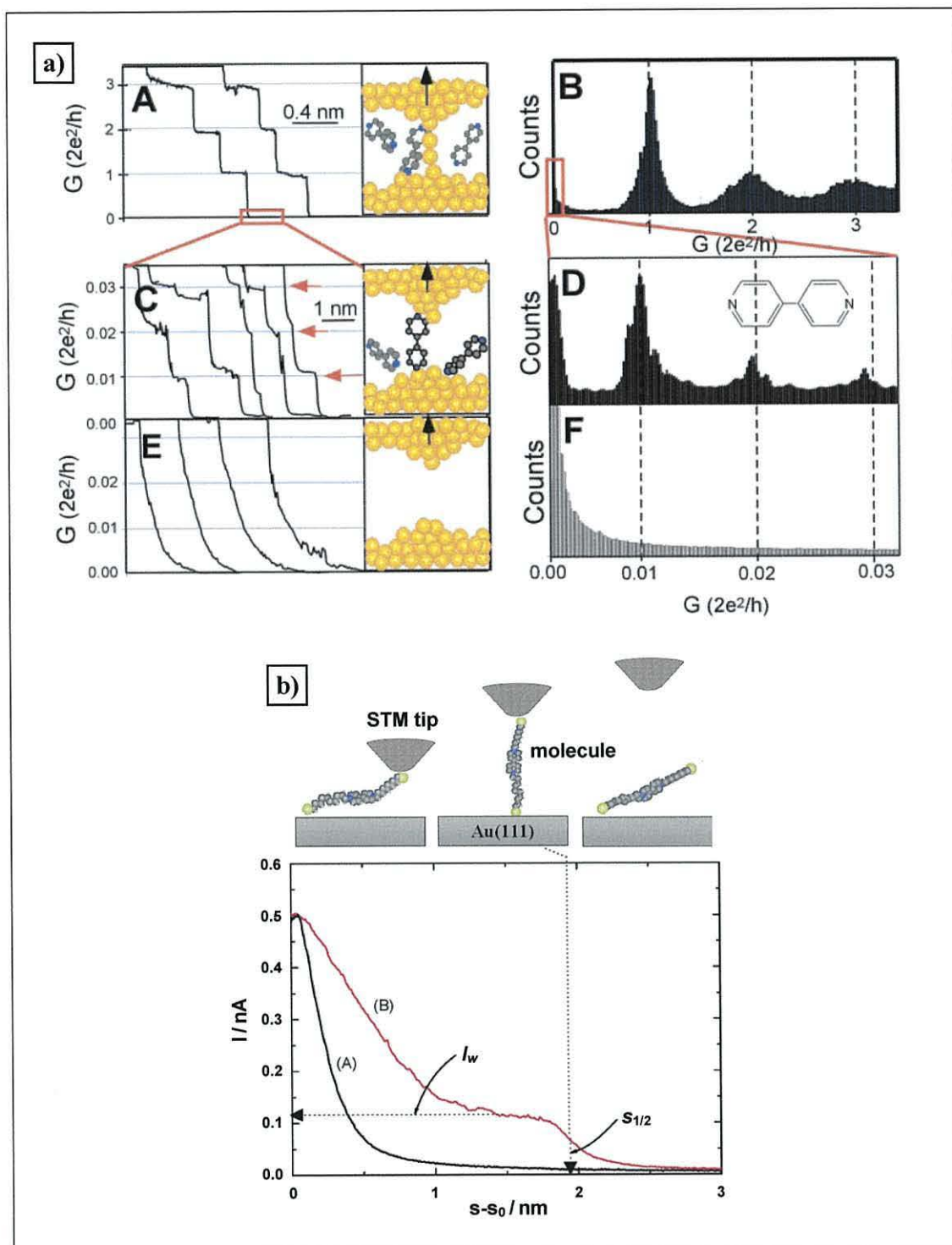


Fig. 2.3.4-1 a) G - s curves and histograms of 1000 G - s (I - s) measurements from Xu and Tao experiment described in the text (source: B. Xu and N.J. Tao¹⁶⁸).
 b) Typical I - s curve (red) observed by Haiss for viologen dithiol molecules in comparison to the exponential decay curve (black) for a clean substrate; I_w characterises conductivity of the junction (source: W. Haiss *et al.*¹⁹⁸).

***I-t* STS**

Another technique developed by Haiss¹⁹⁶, called *I-t* STS, enabled estimation of current flow through single molecules by using the STS constant-height operational mode. In this experiment, the abrupt changes in current response were monitored at constant bias voltage, when an STM tip was kept at very low altitude above a substrate. As a slow thermal drift of the tip occurs at room temperature, a small area of the sample can be scanned without any corrections of the tip – substrate separation made by the feedback loop during such an experiment. When the tip approached the molecule, a temporal junction could be formed, which was observed as a current jump in the *I-t* characteristics (see Fig. 2.3.4-2). A statistically significant amount of current jumps was further evaluated from appropriate histograms according to the procedure described for *I-s* experiments.

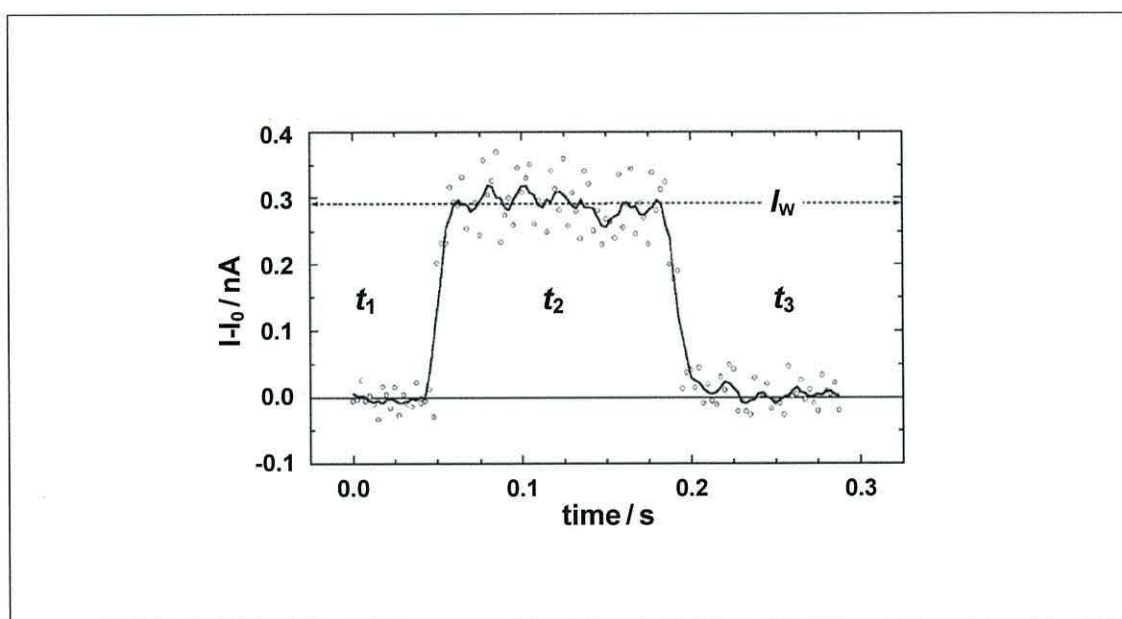


Fig. 2.3.4-2 Typical current jump recorded by Haiss for 1,8-octanedithiol molecule¹⁹⁶ at constant bias $V = 0.3$ V; original experimental data were indicated by circles; I_w characterises conductivity of the junction.

2.3.5 Current rectifying properties of molecular systems

Asymmetrical distribution of the frontier electron orbitals of a molecule in a junction may be represented as a difference in the current flow, depending on the direction of the applied electric field. It is manifested in the I - V characteristics as asymmetry in the scans taken between the value of the bias voltage applied in one direction (negative bias) and the equivalent value at opposite bias (positive bias). Despite different origins, the above mentioned effect mimics that observed for current rectification in solid-state p-n junctions, and is referred to as molecular rectification. In the case of a molecular junction, this phenomenon originates from an asymmetrical distribution of functional groups, characterised by different ionisation potentials and electron affinities, or an asymmetrical coupling of the molecule to the electrodes.

In order to quantify the current asymmetry (rectification), the asymmetry ratio (AR) can be defined:

$$AR = \left| \frac{I(V_n)}{I(V_m)} \right| \quad \text{where : } \begin{cases} V_n = -V_m \\ |V_n| > |V_m| \end{cases} \quad \text{Eqn 2.3.3-5}$$

This parameter has been conventionally assigned for current detected at $V_{n,m} = \pm 1\text{V}$, although this is not a rule and so the value of voltage at which AR was calculated is given.

Aviram and Ratner theory of molecular rectification

The concept presented in 1974 by Aviram and Ratner²⁵ was a pioneering idea of an appropriate matching of electron-rich and electron-poor components in order to obtain a specific distribution of the frontier molecular orbitals. This would facilitate or hinder current flow depending on the electrode polarisation. It was concluded that a molecule containing a strongly electron-donating subunit with HOMO electrons at an energy close to E_F of the electrodes in steady state, and an electron-accepting segment with a low-lying LUMO, would be the most effective rectifier. These two parts need to be isolated by a spacer, which is capable of preventing charge redistribution from donor

to acceptor along the molecule. A model structure, which in theory has the most desired features, together with a simplified energy diagram is shown in Fig. 2.3.5-1. In the molecule proposed by Aviram and Ratner (see the black core structure in Fig. 2.3.5-1) the electron-donating and electron-accepting subunits are separated by a saturated triple σ -electron bridge. This spacer should guarantee sufficient isolation of the frontier molecular orbitals and provide a rigid linkage for both active parts of the system.

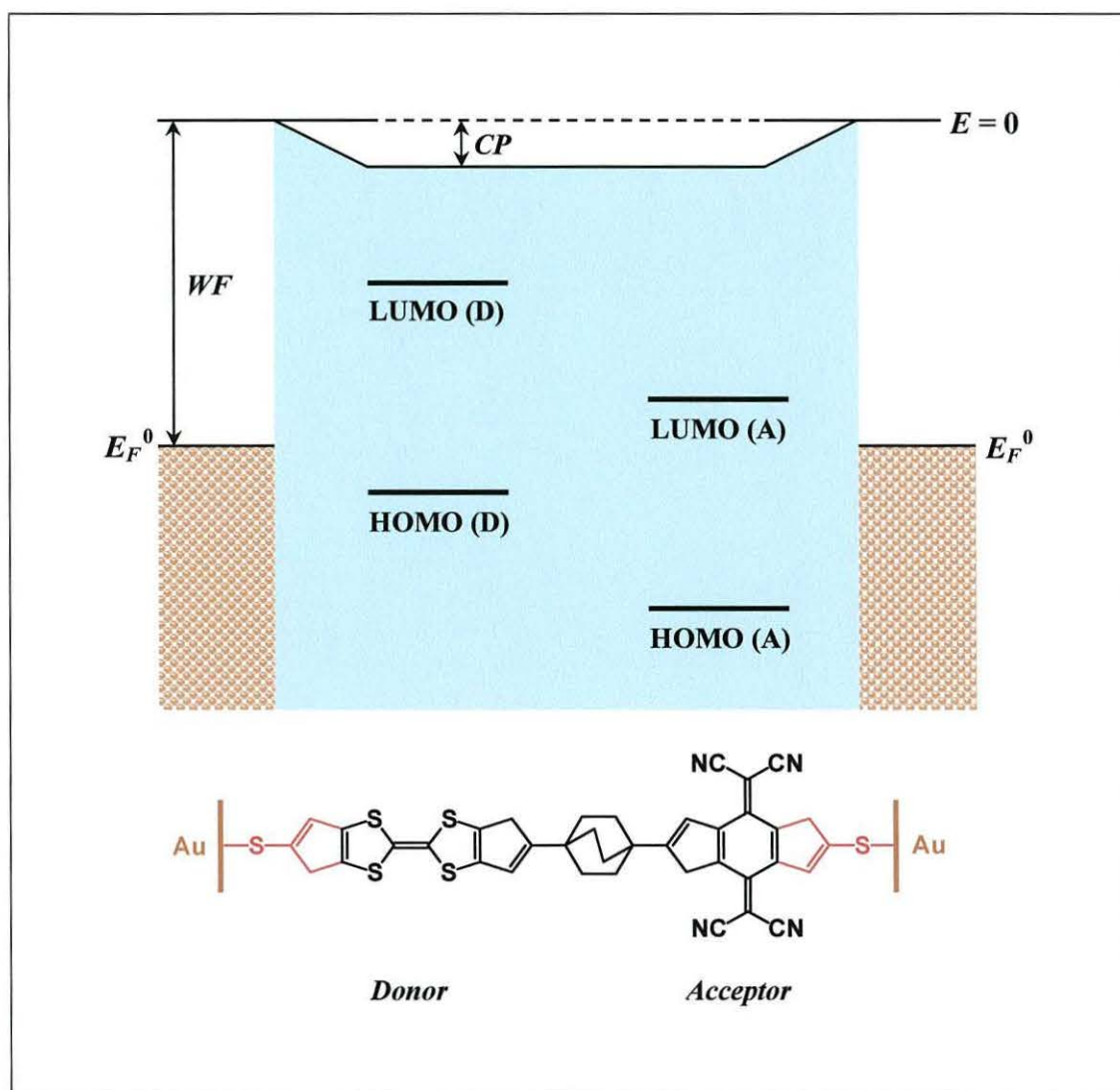


Fig. 2.3.5-1 Simplified energy diagram of the Aviram-Ratner molecular rectifier and the proposed structure of a molecular device.

A schematic description of the rectification process in the Aviram-Ratner molecule is shown in Fig. 2.3.5-2. The top diagram presents electron transfer in the favorable direction, where lower external bias is required. The electron passes the potential barrier on the molecule – electrode contact, when E_F^2 is brought into resonance with the LUMO (A). At the same time, an electron from the HOMO (D) tunnels to the left electrode when the E_F^1 is low enough to accept this electron. The empty space on HOMO (D) can now be filled by the electron, which temporarily occupies LUMO (A), and approaches the left electrode. On the other hand, if the equivalent bias is applied in the reverse direction, the molecular orbitals are far from any resonances with the Fermi energy of the electrodes, and thus there should be no current observed. As shown in the bottom diagram of Fig. 2.3.5-2, much higher external bias is needed in order to enable resonant electron transfer through the junction, according to the abovementioned mechanism.

Due to chemical synthesis limitations, the electrical properties of the proposed Aviram – Ratner molecule have never been verified. Many substitutes, containing donating and accepting subunits separated by single σ -electron spacers, were synthesised and investigated. These attempts were reviewed by one of the pioneers of these studies, R.M. Metzger¹⁹⁹. However, there has been no meaningful rectification found for these molecules. The most successful experimental manifestations of the molecular rectification phenomenon were initiated in 1990 by G.J. Ashwell *et al.*²⁰⁰ and their observation of such an effect in physisorbed molecules, with π -electron bridges instead of σ -electron spacers. It was found that the Aviram – Ratner theory would still be applicable if the twist along the π -bridge was sufficiently high to prevent overlapping of the π -orbitals of donating and accepting components. Since then, many different systems have been proposed and investigated, although most of the values of AR reported in the literature have not exceeded 20 at ± 1.5 V²⁰¹. This changed in 2005, when G.J. Ashwell and A. Mohib²⁰² measured rectification of 50 – 150 at ± 1 V for the self-assembled Au|Au- σ -(A)- π -(D) type molecular monolayer contacted with an Au STM tip (see Fig. 2.3.5-3). The torsion angle between aromatic rings of the donating and the accepting subunits of this molecule was reported to be 61°. This angle was high enough to provide the sufficient isolation of the frontier molecular orbitals of the donors and the acceptors.

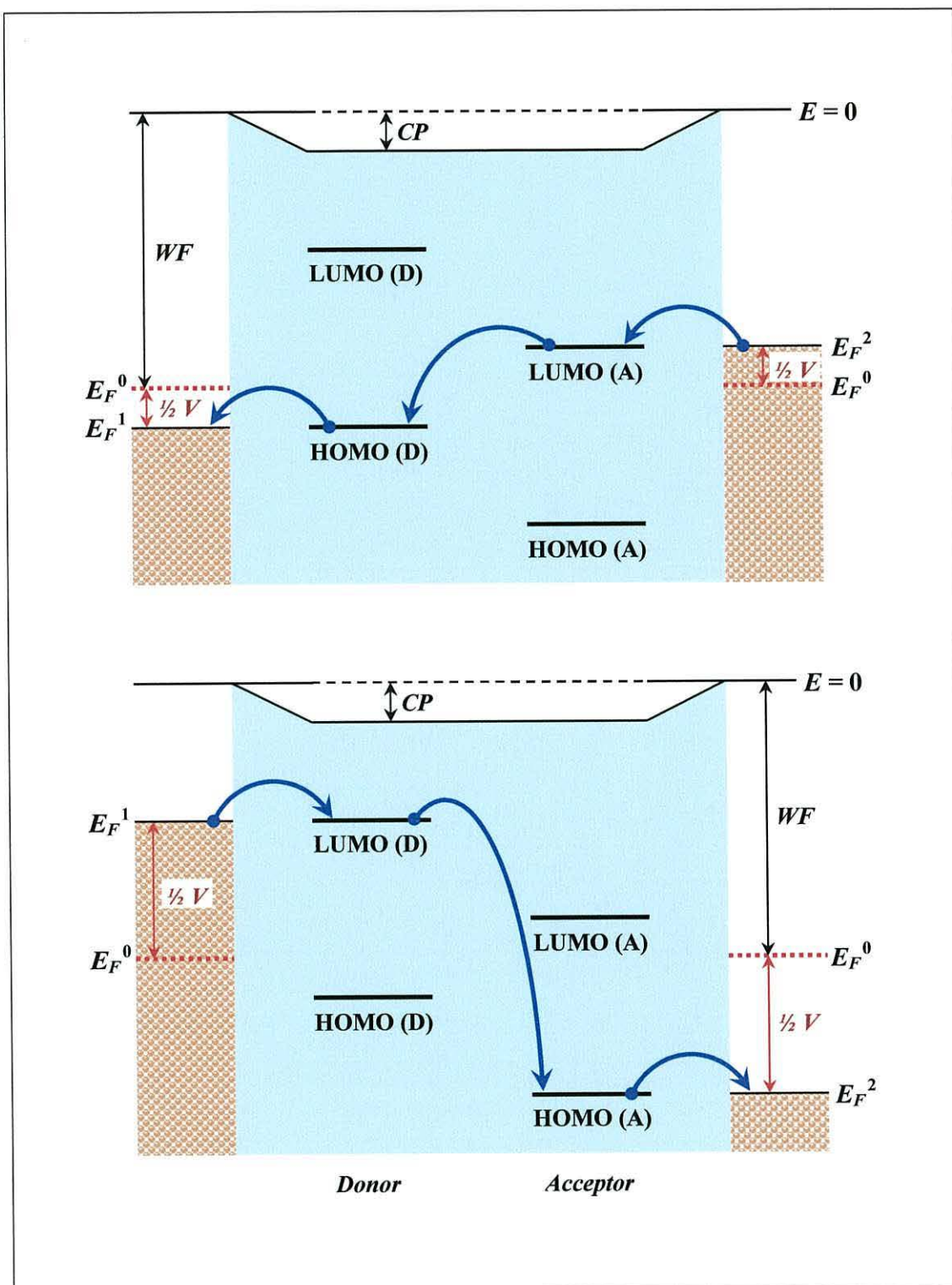


Fig. 2.3.5-2 Schematic description of the rectification process according to the Aviram and Ratner theory; electron transfer was indicated by the blue arrows.

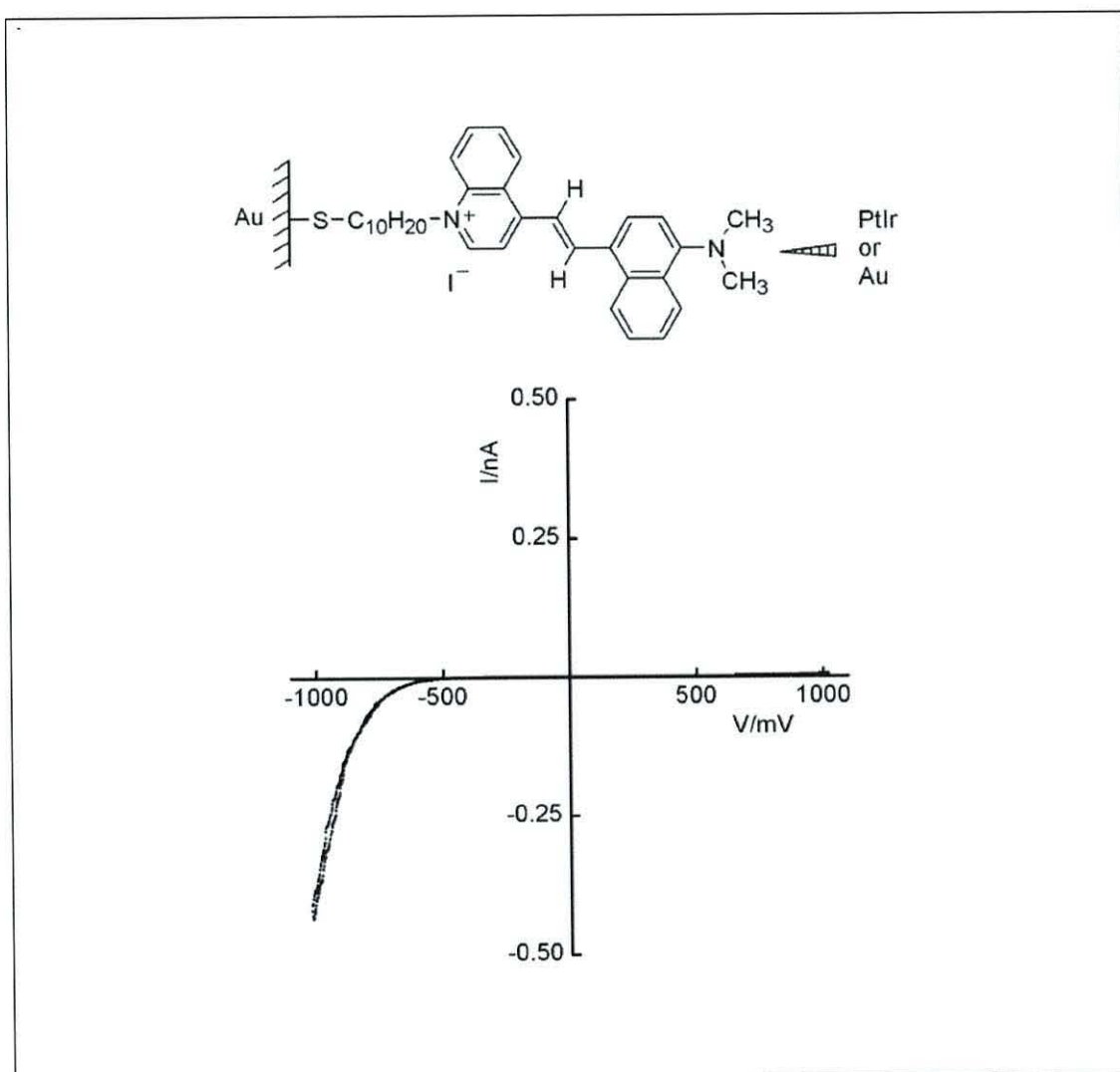


Fig. 2.3.5-3 I - V characteristic observed by Ashwell and Mohib²⁰² for the presented $\text{Au} | \text{Au}-\sigma-(\text{A})-\pi-(\text{D})$ molecular rectifier; the higher current corresponds to electron flow from the substrate to the contacting tip.

Major concerns and other theoretical explanations of molecular rectification

There has been much scepticism about the origin of rectification since the first experimental observations of this effect were reported. The very first criticisms arose from experimental imperfections:

- 1) application of easily oxidisable substrates; this results in a Schottky barrier which can dominate the electron transport between the electrodes^{200,203};
- 2) usage of different materials for substrates and top contacts, which introduces asymmetry from the difference in electron work functions of these electrodes;
- 3) electron work function variations, which depend on surface roughness: smoother surfaces yield lower work functions due to the higher uniformity of the charge distribution⁴⁹;
- 4) geometrical differences of substrate surfaces and probing STM tip, which affect the electrical field between these electrodes: the field is stronger nearer the sharp tip than close to the flat sample, and so the current is larger when the tip is negatively biased relating to the substrate²⁰⁴.

The two first concerns have not been the case for the most recent experiments, as the gold-coated substrates and gold probing tips are commonly applied. However, the last two effects can not be overcome, but they should not induce current asymmetries higher than 10 at ± 1 V for atomically sharp tips, according to the analysis provided in the cited literature²⁰⁴. Due to geometrical reasons, this effect decreases as the tip approaches the sample.

Much scepticism was also directed towards the explanation of the rectification that was said to be due to molecular effects. The major uncertainty concerned geometry of the molecular rectifier itself, a spatial distribution of the frontier molecular orbitals in particular. Molecules with long alkyl chains between the substrate and molecule have been suggested to rectify without simultaneously engaging both donating and accepting parts of the molecule²⁰⁵. This is due to a profile of electrostatic potential between the electrodes, which is sensitive to the position of the electroactive parts of the molecule, relative to the electrodes. Further theoretical analysis of the molecular

quantum dot (the phenyl ring), asymmetrically placed between two identical electrodes, seemed to confirm these speculations²⁰⁶. The asymmetrical coupling of the molecular π -orbital to the electrodes *via* tunnelling barriers should cause asymmetrical current flow, as the electrostatic potential drops much more rapidly along the barriers than along the conjugated system. Thus, different values of bias voltage, depending on the polarisation of the electrodes, are required to reach resonance with the LUMO on the phenyl ring. The potential of rectification for such a mechanism was claimed to be very high, but only when operated at temperatures close to 0 K. It was also calculated that the maximum rectification values, reaching 500, were achievable only at very high bias voltages of *ca.* ± 3 V. The *AR* at ± 1.3 V was found to be 4 – 10. Later calculations have shown that these values were highly overestimated and there should be no significant rectification observed at ± 1 V under standard measurement conditions for such systems, and other molecular rectifiers²⁰⁷. The latest predictions were also partially supported by experimental observations²⁰⁸.

Despite the evident strength of the Aviram and Ratner concept, it is very difficult to realise it practically. There are several inconveniences, which arise from the instability of molecular systems²⁰⁹:

- 1) in resonance conditions, the molecules are charged and may undergo irreversible reactions;
- 2) thermal effects at high voltages tend to cause decomposition of the molecules;
- 3) sufficiently high electric fields can induce conformational changes of the molecules, which strongly affects their electronic structure.

The last effect that can cause different forms of rectification, such as field-induced rectification, has recently been discussed theoretically by A.Troisi and M.A. Ratner²¹⁰. Such off-resonant molecular rectifiers have been claimed to approach an *AR* of *ca.* 100 at voltages below ± 1.5 V.

3 *Experimental*

This part of the thesis includes basic information about the studied materials, chemical synthesis and analytical procedures, which have been treated briefly. This chapter has been divided into seven major parts, and is organised as follows: the first and the second provide basic information about the materials used (Section 3.1) and systems investigated (Section 3.2); the next three sections show the sequence of sample preparation, which includes wet synthesis of new compounds (Section 3.3), preparation of surfaces for the self-assembly process (Section 3.4) and novel techniques of *in-situ* creation of complex molecular structures (Section 3.5); Section 3.6 presents a unique method of the two-terminal molecular wire formation inside a pre-fabricated solid skeleton structure, used for electrical testing of the molecular wires; Section 3.7 describes operational parameters of the analytical equipment that have been applied for structural and electrical characterisation of the systems and raw materials.

3.1 *Components for the experiments*

The materials that have been used for the project are shown in Table 3.1-1 and Table 3.1-2. The molecules from Table 3.1-1 were employed to create linear conjugated azomethines, attached to gold *via* sulfur groups. The compounds from Table 3.1-2 were applied to form and modify oligo(phenylene-ethynylene) type structures. Reactants: M1 – M9, M15 and M16, were purchased from *Sigma-Aldrich Chemical Co.* (Gillingham, UK). M10 – M12 were synthesised from M1, M2, M5, M8 as part of the project (see Section 3.3). M13 was synthesised by Ch. Wang from Durham University (UK).

Solvents (HPLC grade): methanol, ethanol, chloroform, acetone, diethyl ether, were provided by *Surechem Products Ltd.* (Needham Market, UK). Acetic and hydrochloric acids were purchased from *Sigma-Aldrich Chemical Co.* The type I ultra-pure water (resistivity: 18.2 M Ω cm at 298 K) was produced directly before experiments from a *Millipore Direct-Q 3* system with 185 and 254 nm UV lamps.

Table 3.1-1 Compounds used for preparing the structures from Table 3.2-1 and 3.2-2.

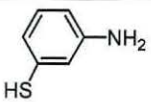
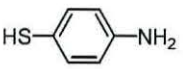


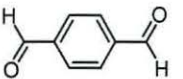
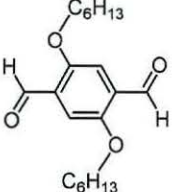
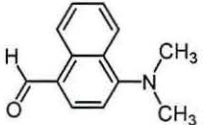
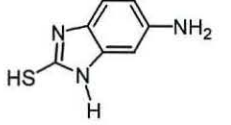
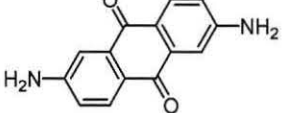
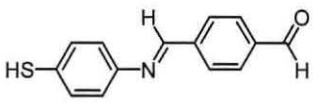
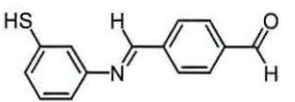
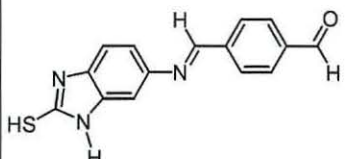
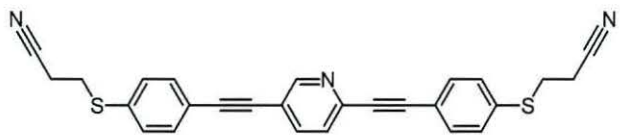
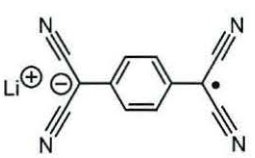
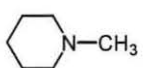
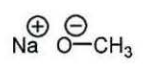
Code	Compound		Molecular mass	
M1		3-Aminobenzenethiol	C_6H_7NS	125.19
M2		4-Aminobenzenethiol	C_6H_7NS	125.19
M3		1,4-Benzenediamine	$C_6H_8N_2$	108.14
M4		4-Nitrophenylamine	$C_6H_6N_2O_2$	138.12
M5		Terephthalaldehyde	$C_8H_6O_2$	134.13
M6		2,5-Bis(hexyloxy)-terephthalaldehyde	$C_{20}H_{30}O_4$	334.45
M7		4-Dimethylamino-1-naphthaldehyde	$C_{13}H_{13}NO$	199.25
M8		6-Amino-1H-benzimidazole-2-thiol	$C_7H_7N_3S$	165.22
M9		2,6-Diaminoanthra-9,10-quinone	$C_{14}H_{10}N_2O_2$	238.24
M10		4-[(4-Mercaptophenylimino)-methyl]-benzaldehyde	$C_{14}H_{11}NOS$	241.31
M11		4-[(3-Mercaptophenylimino)-methyl]-benzaldehyde	$C_{14}H_{11}NOS$	241.31
M12		4-[(2-Mercapto-3H-benzimidazol-5-ylimino)-methyl]-benzaldehyde	$C_{15}H_{11}N_3OS$	281.33

Table 3.1-2 Compounds used for preparing the structures from Table 3.2-3.

Code	Compound	Molecular mass	
M13	 3-{4-{5-[4-(2-Cyano-ethylsulfanyl)-phenylethynyl]-pyridin-2-ylethynyl}-phenylsulfanyl}-propionitrile	$C_{27}H_{19}N_3S_2$	449.59
M14	 Lithium salt of 7,7',8,8'-tetracyanoquinodimethane ($Li^+TCNQ^{\bullet-}$)	$C_{12}H_6N_4^-$ Li^+	206.20 6.94
Reaction assisting compound			
M15	 1-Methylpiperidine	$C_6H_{13}N$	99.17
M16	 Sodium salt of methanol (sodium methoxide)	$Na^+CH_3O^-$	54.02

3.2 Studied systems

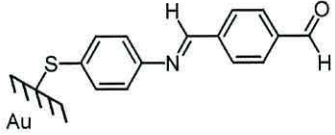
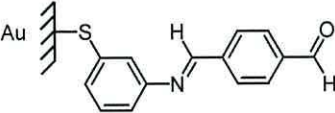
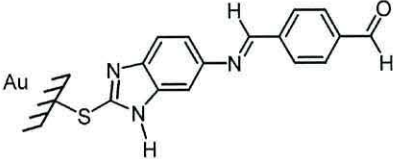
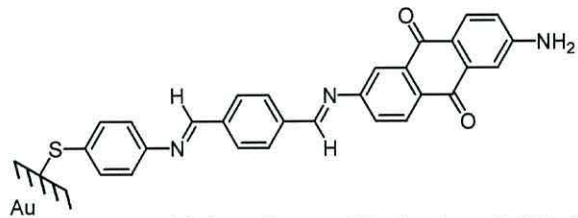
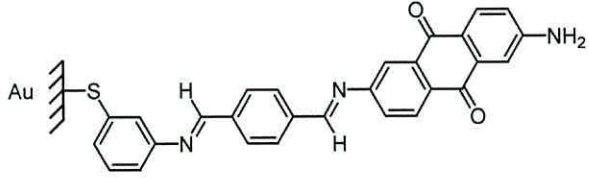
Structures from the first group of studied systems, azomethine thiolates (AT) on gold (Table 3.2-1), were expected to provide very effective electron tunnelling paths along the molecular chains in both or just one direction. In the second case asymmetrical current transmission were to be due to incorporating appropriate electron-donating and electron-accepting components from Table 3.1-1 into the AT chains according to the Aviram – Ratner concept of the molecular rectification (see Section 2.3.5). Very similar structures, oligo(phenylene-vinylenes), had previously been found to provide efficient

electronic coupling between two reservoirs of electrons attached to their chain ends¹⁸¹. However the main advantage of AT systems over oligo(phenylene-vinylenes) is reasonably simple and efficient synthesis of these structures, occurring at room temperature (see Section 3.3 and Section 4.1.2). This enabled an *in-situ* extension of such molecular wires together with an introduction of active components into the molecular backbones.

The studied AT systems were intentionally prepared to vary in: geometry for the attachment to the substrate, length and distribution of functional elements along the chain. Different arrangements on the gold surface were believed to be provided by the variant substitution of the thiol terminal group of M10, M11 and M12. The molecular conformation was also a major factor in determining the successful formation of the structures shown in Table 3.2-2 from M11 and M9. Finally, both structural and electronic properties of the AT systems were in the range of interest.

M13 was used for preparing the thiolate form of 2,5-di(phenylethynyl)-4'-mercapto) pyridine (PeMP), which was further modified *in-situ* to obtain the systems shown in Table 3.2-3. Oligo(phenylene-ethynylenes), had previously been reported to effectively transmit electrons¹⁸², and they are currently the most widely studied molecular wires. The idea behind inserting a pyridine ring into the core oligo(phenylene-ethynylene) structure was to monitor conductivity changes upon the chemical modification of this reactive part of the molecule. From the point of view the molecular electronics, the most interesting was to compare the current transmissions of a neutral molecular wire and an equivalent system with an excess charge localised in the central part of the core structure. Further transformation of this system was based on creating electrically active adlayers on top of the self-assembled monolayers of modified PeMP (see Table 3.2-3) in order to obtain the high molecular rectification.

Table 3.2-1 Studied AT systems (continued on page 50).

	Code	Chemical formula, name of thiolates and molecular mass
1	AT1	 <p>Thiolate form of 4-[(4-mercaptophenylimino)-methyl]-benzaldehyde (240.30)</p>
2	AT2	 <p>Thiolate form of 4-[(3-mercaptophenylimino)-methyl]-benzaldehyde (240.30)</p>
3	AT3	 <p>Thiolate form of 4-[(2-Mercapto-3<i>H</i>-benzoimidazol-5-ylimino)-methyl]-benzaldehyde (280.32)</p>
4	AT1-A	 <p>Thiolate form of 2-Amino-6-{4-[(4-mercaptophenylimino)-methyl]-benzylidene}-amino}-anthraquinone (460.53)</p>
5	AT2-A	 <p>Thiolate form of 2-Amino-6-{4-[(3-mercaptophenylimino)-methyl]-benzylidene}-amino}-anthraquinone (460.53)</p>

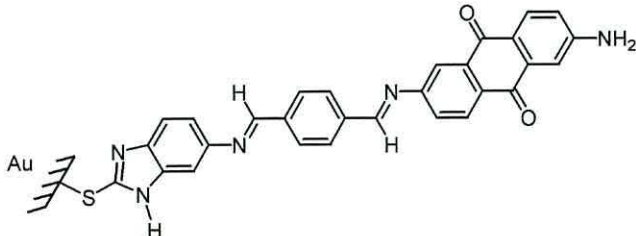
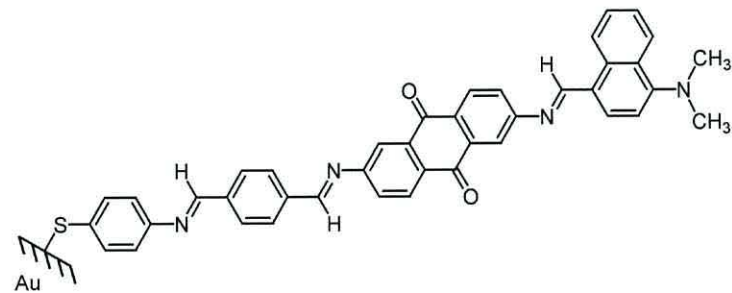
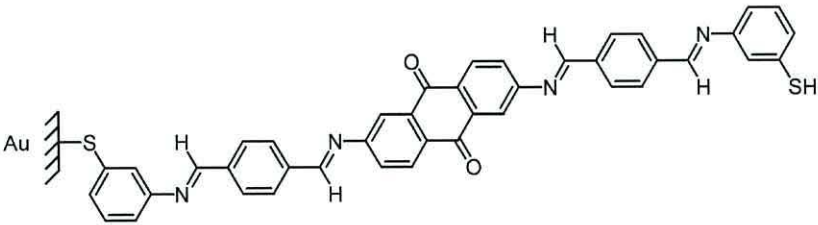
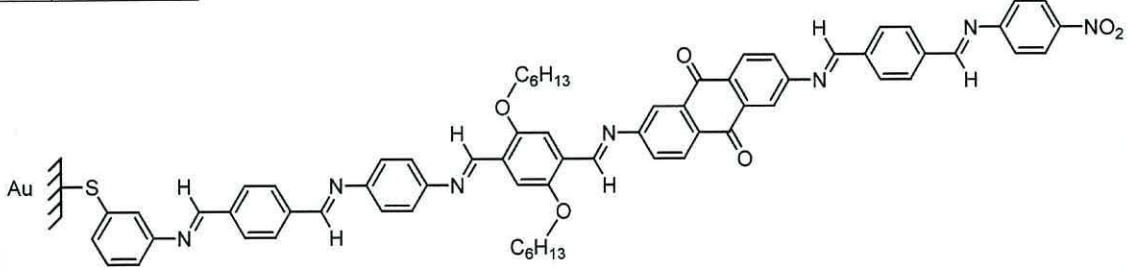
6	AT3-A	 <p>Thiolate form of 2-Amino-6-{{4-[(2-mercapto-3<i>H</i>-benzimidazol-5-ylimino)-methyl]-benzylidene}-amino}-anthraquinone (500.55)</p>
7	AT1-AD	 <p>Thiolate form of 2-[(4-Dimethylamino-naphthalen-1-ylmethylene)-amino]-6-{{4-[(4-mercapto-phenylimino)-methyl]-benzylidene}-amino}-anthraquinone (641.76)</p>
8	AT2-AS	 <p>Thiolate form of 2,6-Bis-{{4-[(3-mercaptophenylimino)-methyl]-benzylidene}-amino}-anthraquinone (683.82)</p>
9	AT2-L	 <p>Thiolate form of 2-{{2,5-Bis-hexyloxy-4-{{4-{{4-[(3-mercaptophenylimino)-methyl]-benzylidene}-amino}-phenylimino}-methyl]-benzylidene}-amino}-6-{{4-[(4-nitrophenylimino)-methyl]-benzylidene}-amino}-anthraquinone (1103.31)</p>

Table 3.2-2 Structures incorporated into the testing platform described in Section 3.7.

	Code	Thiolate forms of AT2 attached to the opposite gold electrodes (1) Dithiolate form of AT2-AS trapped between gold electrodes (2)
1	AT2-g-AT2	
2	AT2-A-AT2	

Table 3.2-3 Studied PeMP systems.

	Code	Thiolate form of 2,5-Di(phenylethynyl)-4'-mercapto)pyridine on gold and derivatives of this thiolate (modified <i>in-situ</i>)	Molecular mass
1	PeMP-a		342.46
2	PeMP-b		378.92
3	PeMP-c		549.67
4	PeMP-d		549.67 + 99.17

3.3 Synthesis of molecules

Three related compounds: M10, M11 and M12 were synthesised using the same type of reaction between amines and aldehydes (see Fig. 3.3-1). The synthesis of M10 was performed as follows: M2 (0.71 cm^3 , 6.68 mmol) and M5 (4.5 g, 33.5 mmol) were refluxed in ethanol (70 cm^3) for three hours at room temperature. A yellow product was obtained (1.42 g, 88 % yield) by rotary evaporation, then washed with ethanol, filtered to remove starting materials and recrystallised from various solvents in the following sequence: diethyl ether – chloroform – acetone. After each recrystallisation step, the product was also washed with ethanol and filtered in order to improve the purity. Amounts of starting materials used for the synthesis of 0.37 g (87 % yield) M11 were: 0.22 g (1.76 mmol) M1 and 1.08 g (8.05 mmol) M5. Similarly, for the synthesis of 0.62 g (73 % yield) M12 these amounts were: 0.50 g (3.03 mmol) M8 and 2.58 g (15.6 mmol) M5. In both cases, as well as for the synthesis of M10, an excess of M5 (*ca.* $\times 3$) was used in order to ensure monosubstitution with M1, M2 and M8.

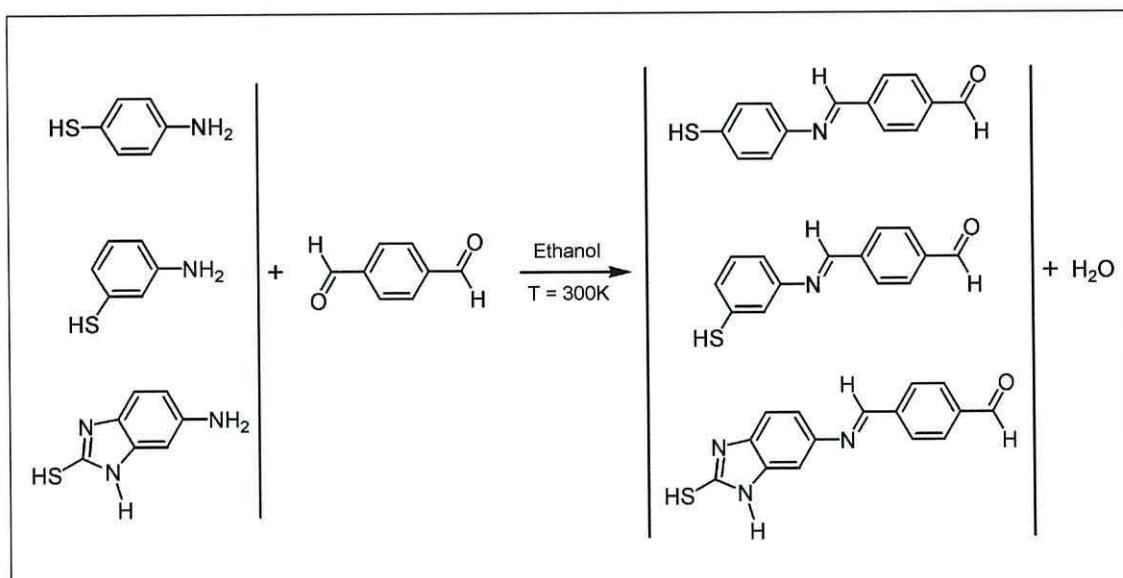


Fig. 3.3-1 Scheme of M10, M11 and M12 synthesis.

3.4 Preparation of gold substrates

Depending on the experimental requirements, three different substrates were used. A short description of each kind of substrate and the methods of their preparation for further molecular deposition are given in this section.

3.4.1 Gold on quartz crystal

Gold covered quartz crystals, adapted to monitor the amount of molecules attached to gold surfaces, according to the description given in Section 2.2.2, were purchased from the *International Crystal Manufacturing Co.* (Oklahoma City, US). Both sides of the AT-cut quartz crystals were pre-coated with 10 nm of an adhesion chromium layer to provide a mechanically stable surface for gold deposition. The layers of gold, *ca.* 100 nm thick, were deposited onto chromium and polished to achieve a smooth surface and the required nominal vibration frequency.

Prior to deposition, the crystals were rinsed with acetone and treated with nitrogen plasma for 2 minutes in *Plasma Prep 2* manufactured by *Gala Instrumente* (Bad Schwalbach, Germany). This procedure guarantees that the gold surface is free of any chemisorbed organic moieties and other residual contaminants from the manufacturing steps²¹¹. Apart from measuring the surface coverage *via* QCM, these substrates were further adapted for STM-STS electrical testing of the deposited molecules in order to compare the results with those obtained for the molecules on other substrates.

3.4.2 Atomically flat gold on mica

Crystalline Au(111) on mica substrates were purchased from *Structure Probe Inc.* (West Chester, US). These structures were manufactured *via* an epitaxial growth of 150 nm layer of gold onto freshly cleaved, *ca.* 50 μm thick, high-quality muscovite mica wafers (chemical formula: $\text{K}_2\text{O}\cdot\text{Al}_2\text{O}_3\cdot\text{SiO}_2$) in high vacuum, followed by annealing. This method provided gold surfaces composed of atomically flat crystalline terraces, typically larger than 100 nm across.

The structures were freshly reconstructed *via* hydrogen flame annealing before delivery and sealed to prevent any permanent contamination. Thus, the molecular layers were deposited without any additional purification procedure. These substrates were employed for XPS experiments and STM high-resolution imaging.

3.4.3 Gold on crystalline graphite

The highly oriented pyrolytic graphite wafers (HOPG) for further gold coating were purchased from *Structure Probe Inc.* The substrates were freshly cleaved prior to deposition. 99.99 % Au (*Sigma-Aldrich Chemical Co.*) was thermally evaporated onto the HOPG wafers in an *Auto 306 EM* unit manufactured by *Edwards Ltd.* This instrument was provided with rotary and diffusion pumps, generating a vacuum of 1.8×10^{-6} Torr. Gold deposition was carried out at the constant rate of *ca.* 0.1 nm/s, until the 100 nm metallic layer was obtained. The gold layer thickness was monitored *via* QCM.

These substrates for molecular self-assembly required no further cleaning, as they were immersed immediately after being removed from the ultra-high vacuum chamber. The whole procedure described above was performed in a clean-room environment (class 1000). Samples with smooth polycrystalline gold surfaces on HOPG were used for the experiments where structural disorder of the molecular adlayers was advantageous, *i.e.* for the conductivity and the current asymmetry measurements of the molecular structures.

3.5 Preparation of molecular structures on gold

Self-assembly was the primary method used to form the molecular structures on gold. Both SAM formation, and *in-situ* modifications of the monolayers were carried out from freshly prepared solutions at room temperature. The concentration of the molecular compounds in solution was 0.5 mM. Initially, the self-assembly of each compound was proceeded on the QCM sensors, described in Section 3.4.1, and the time of deposition to yield a complete monolayer was monitored. To ensure full coverage of

the other substrates, they were immersed in the thiolate solutions for the time needed to cover the QCM gold electrodes.

3.5.1 *AT molecular wires*

Molecules: M10, M11 and M12 were self-assembled from acetone solutions onto gold substrates to form AT1, AT2 and AT3 systems. These substrates were rinsed with pure solvent after deposition to remove molecules, which were not chemisorbed to the gold surface, and then left to dry for *ca.* 1 min. The influence of environmental conditions of the self-assembly process on the final composition of the adlayers and the surface coverage was studied for M10 and M11. However, no correlation was found between the structural properties of the monolayers and the following factors: solvent type, oxygen presence in the solutions, and temperature of the process. Thus, details of these experiments were omitted.

Further extension of the aldehyde-terminated moieties: AT1, AT2 and AT3 was achieved *via* interfacial reactions of these SAMs with molecules containing amino groups: M9 and M3. Reactions of AT1, AT2 and AT3 with M9 resulted in the systems: AT1-A, AT2-A and AT3-A respectively. M3 was used for the second step of building-up the AT2-L molecular wire. For all these reactions, the substrates with the first molecular adlayers were immersed in *ca.* 2 mM ethanol solutions of the reactants. To increase the rate of these reactions acetic acid was added to obtain an acidification of *ca.* 2 %.

The same procedure was repeated to attach the following parts of the investigated structures, using the aldehyde-terminated components: M7 (for AT1-AD) and M11 (for AT1-AS). In the case of the AT2-L structure, after attaching M3 in the second step, the other reactions occurred in the following sequence: M6 – M9 – M5 – M4.

3.5.2 PeMP systems

Self-assembly of M13 required solution mixing for the effective preparation of PeMP-a monolayers. The chloroform solution of M13 was mixed with the *ca.* 5 mM M16 methanol solution; the ratio was *ca.* 2 : 1 (volumetric scale). In this case, M16 facilitated the removal of the cyanoethyl protecting terminal groups from M13. During self-assembly, substrates were taken out of solution at *ca.* 30 min intervals and immersed in pure methanol for *ca.* 5 min in order to remove adsorbed M16, which tend to passivate gold surfaces. After this time, samples were rinsed with chloroform prior to immersion in the solution mixture.

Protonation of PeMP-a in order to obtain PeMP-b structures was performed in hydrogen chloride fumes for *ca.* 1 min. Extension of this time was found to be destructive to the QCM, as it caused corrosion of its metallic parts. The samples were rinsed with ultra-pure water, methanol, then chloroform and left to dry.

PeMP-c structures were created by immersion of PeMP-b in *ca.* 10 mM M14 ethanol solution for three days. During that time an ionic exchange reaction between Cl^- and tetracyanoquinodimethane radical anion ($\text{TCNQ}^{\bullet-}$) occurred. This was predicted to occur due to the excess presence of the $\text{TCNQ}^{\bullet-}$ anion in solution. Positioning of $\text{TCNQ}^{\bullet-}$ on top of PeMP-b was highly probable in those areas of the sample where the SAMs were dense enough to prevent $\text{TCNQ}^{\bullet-}$ from diffusing inside the monolayer structure.

The idea behind using the M15 molecule was to deprotonate PeMP-c. However, immersion of the substrates with PeMP-c in *ca.* 10 mM M15 ethanol solution for up to six days did not give the expected results. Surprisingly, further studies revealed exceptional electrical properties of these samples, which were treated according to the described procedure (see Section 4.4.2) and thus, this molecular system was denoted as PeMP-d.

3.6 Molecular wires inside nano-sized electrode gap

The silicon platforms containing gold electrodes separated by a distance of a few nanometers (which are referred to as Si-DEV), were fabricated by C.J. Bartlett and P.D. Buckle from QinetiQ PLC (Malvern, UK). A diagram of single Si-DEV and photographs of their assembly on a silicon wafer are shown in Fig. 3.6-1. Microscopic images of a central core of Si-DEV are shown in Fig. 3.6-2. The preparation of these structures involved the following steps:

- 1) electron beam evaporation of gold bottom electrodes onto a Si/SiO₂ substrate;
- 2) metalorganic vapour phase epitaxy (MOVPE) of *ca.* 6 µm diameter Si₃N₄ layers on top of the gold and Si₃N₄ pads on either side of the bottom electrodes;
- 3) deposition of SiO₂ domes on the Si₃N₄ layer above the bottom electrode *via* low-energy plasma sputtering;
- 4) deposition of a thin gold layer on top of each SiO₂ dome *via* sputtering;
- 5) electroplating of top contacts to connect central structures attached to the bottom electrodes with separate bond pads;
- 6) wet etching with buffered hydrofluoric acid to wash out the uncovered Si₃N₄ layer plus some additional fraction of this insulator in order to create narrow gold rims around the periphery of the SiO₂ domes, and establish top attachment regions for further molecular self-assembly.

This method offers the possibility of controlling the distance between top and bottom contacts down to single nanometers, whilst maintaining high robustness and mechanical stability of the structure.

Molecular wires linking the electrodes of Si-DEV were created *in-situ* using the method described in Section 3.5.1. Primarily, M11 was self-assembled simultaneously on the top and bottom electrodes to form AT2-g-AT2. In the next step, the aldehyde-terminated groups of AT2 from lower and upper electrodes were linked together by M9. This resulted in the two-terminal molecular wire structures denoted as AT2-A-AT2.

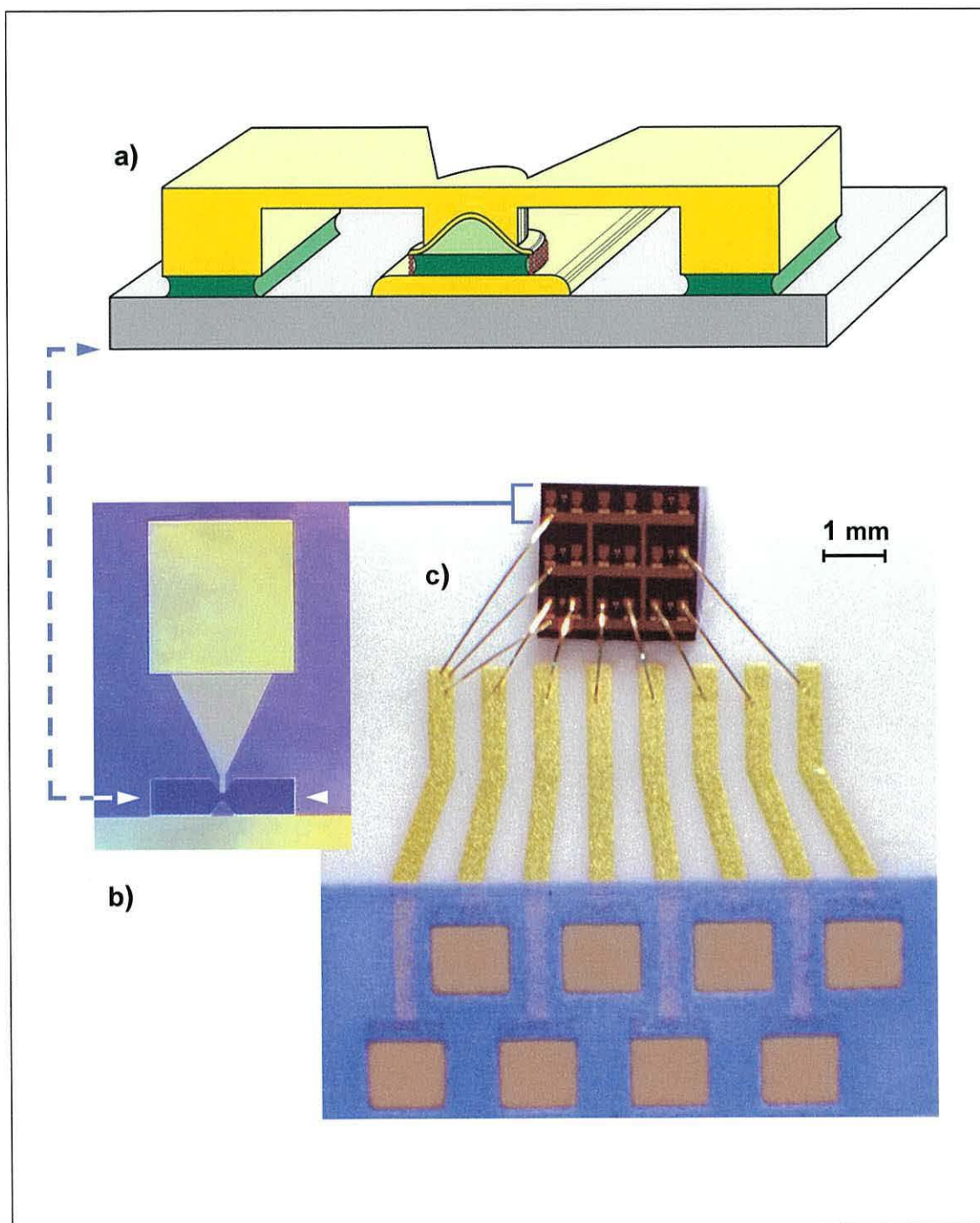


Fig. 3.6-1 a) Cross-section of Si-DEV composed of: bottom and top electrodes (yellow) on a silicon wafer (gray), insulated by Si_3N_4 layers (dark green) and SiO_2 dome (light green), and connected by molecular wires (red) inserted *via* a series of *in-situ* reactions;
 b) Photograph of external terminals of single Si-DEV;
 c) Photograph of an array of 18 autonomic Si-DEV on a testing platform.

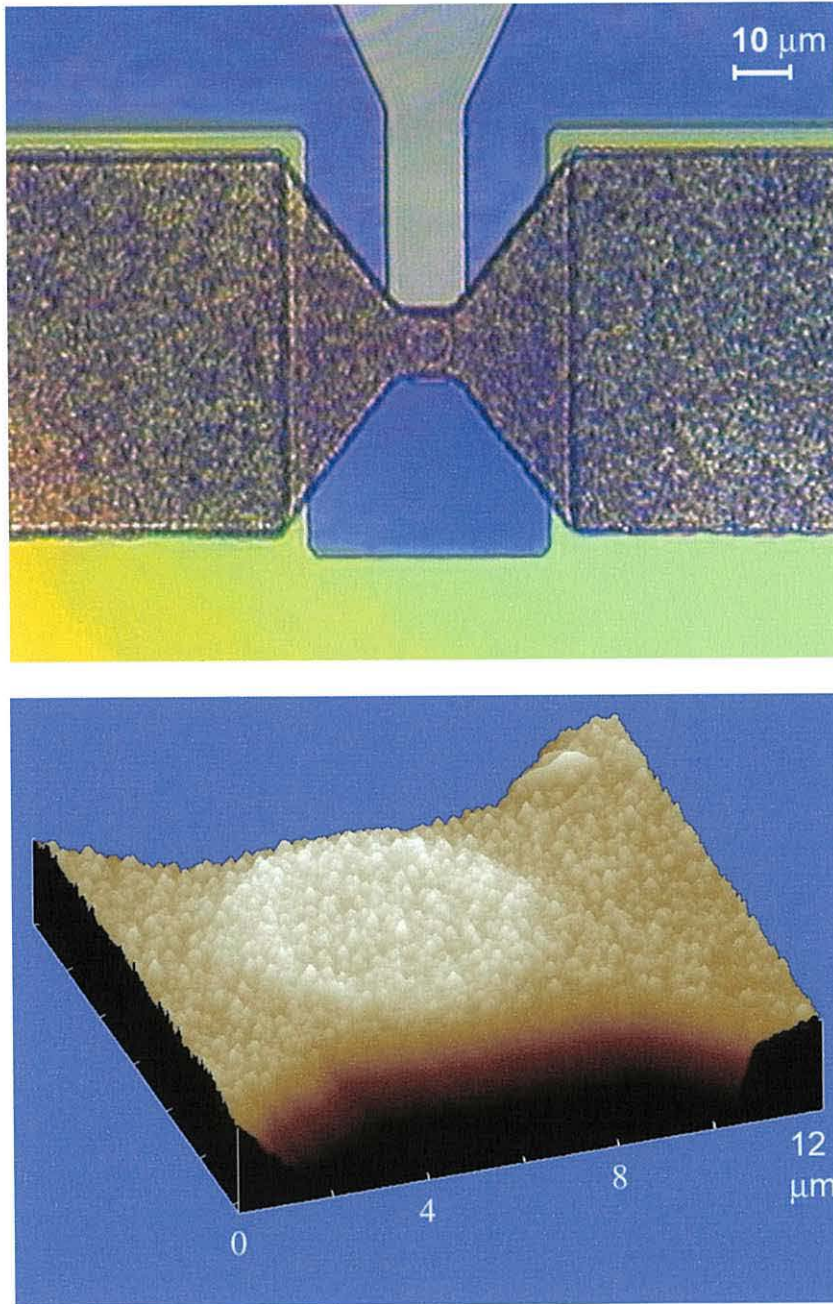


Fig. 3.6-2 Top-view of the central part of Si-DEV *via* optical microscope (top picture), and AFM deflection mode image of the core of the top electrode (bottom picture).

3.7 Analytical equipment

The main analytical techniques and the equipment used for the characterisation of the materials and properties of the created structures are described in this section. Other auxiliary apparatus and basic laboratory equipment have been omitted or treated briefly. A molecular modelling method that was used as an additional supportive technique is mentioned.

3.7.1 Identification and characterisation of new materials

In order to identify the reaction products, thin layer chromatography (TLC) and UV-Vis spectrometry were used. TLC plates with silica-based adsorbent layers were purchased from *Sigma-Aldrich Chemical Co.* UV-Vis spectra of the materials dissolved in acetone solutions were obtained *via* a *Super Aquarius 9000* series spectrometer, in the wavelength range of 190 – 800 nm.

Solid products were also identified *via* a *Research Series* FT-IR (fourier transform infrared spectrometer), which measured spectra in the wavenumber range of 400 – 4000 cm^{-1} . Upon sample preparation, the crystalline solids were dispersed into fine KBr powder and compressed by a high-pressure press to form disks of *ca.* 0.1 mm thickness. The infrared spectra were recorded using *WinFIRST* software.

The purity of the reaction products and the temperatures of their phase transitions were found *via* thermal analysis using *Mettler-Toledo 822^e* differential scanning calorimeter (DSC), supported by *STARe Version 7.01* software. 1 mg samples were scanned at a temperature increase rate of 0.1 K/s.

Mass spectra of the synthesised compounds were obtained in order to confirm the final products. They were performed *via* electrospray ionisation (ESI) by the *EPSRC National Mass Spectrometry Service Centre in Swansea*.

3.7.2 Quartz crystal microbalance

Monitoring the rate of self-assembly and the interfacial reaction yields was performed *via* 10 MHz QCM. The total mass of molecules on the gold electrodes of each crystal was calculated from the vibration frequency changes of the crystals, using Eqn 2.2.2-1 and 2.2.2-2.

A schematic setup for QCM measurements is shown in Fig. 3.7.2-1. The quartz crystals were excited with a *Thandar* TS3021S power supply, providing a DC current of 0.01 A and 9 V. The crystals oscillations were driven by an oscillator circuit, which was made in-house according to the literature description ²¹². The frequency was measured by a *Hewlett Packard* 53131A – 225Hz universal counter. The frequency was measured by a *Hewlett Packard* 53131A – 225Hz universal counter.

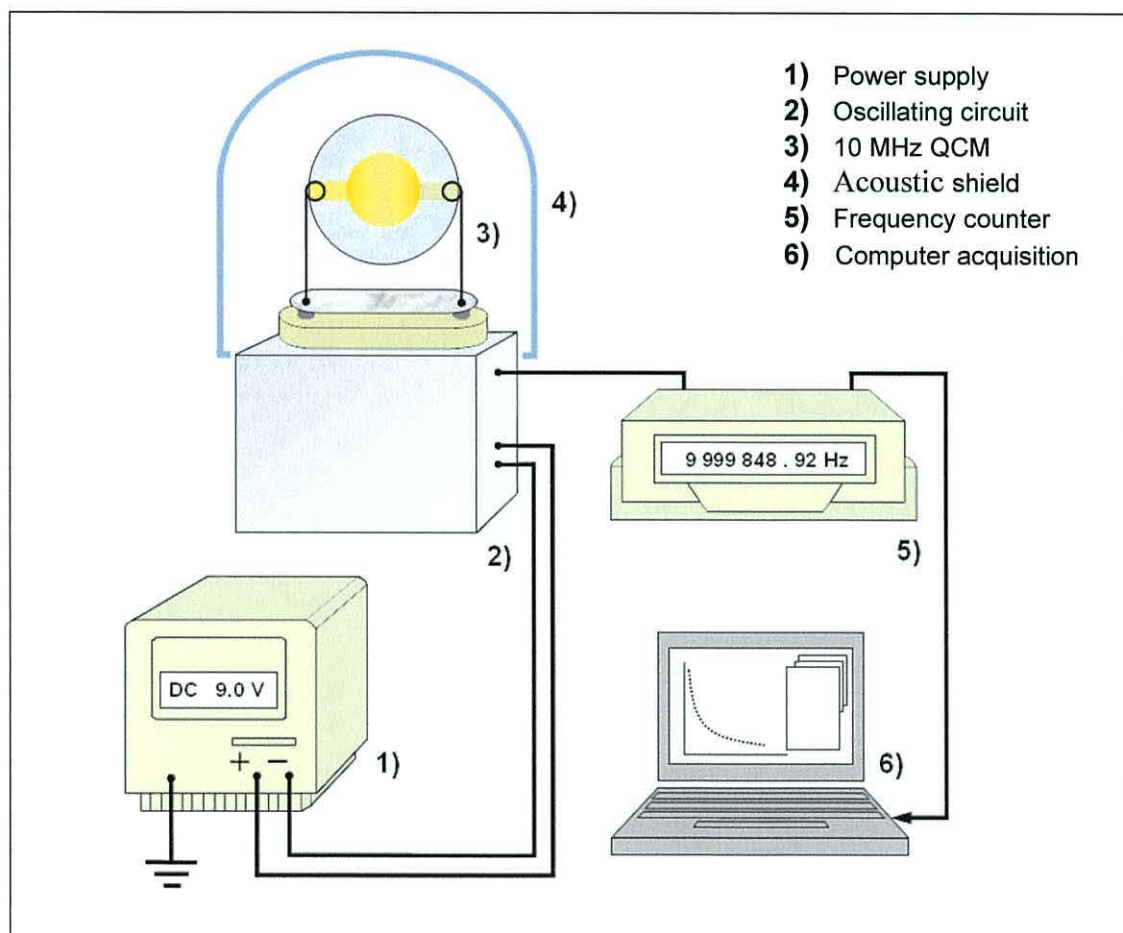


Fig. 3.7.2-1 Experimental setup for QCM measurements.

The nominal vibration frequency of each crystal was checked prior to SAM deposition, after surface preparation. A reference crystal, immersed in pure solvent was also used for longer depositions to monitor any anomalous vibration changes, which arose from the temperature variations, or power supply electrical fluctuations. The frequency measurement procedure included:

- 1) rinsing a sample with pure solvent,
- 2) drying metal electrical contacts of the sensor,
- 3) mounting the sample into a holder of the oscillating circuit for *ca.* 30 s to let the rest of solvent evaporate and settle the resonant frequency,
- 4) taking readings,
- 5) immersing the sample into solution.

3.7.3 X-ray photoelectron spectroscopy

The XPS analyses were performed on an *AXIS Ultra* unit with a monochromatic Al X-ray source at 150 W, manufactured by *Kratos Analytical Co.* Spectra were acquired at 90° take-off angles. Each analysis started with a survey scan from 0 to 1200 eV with a dwell time of 100 ms, pass energy of 160 eV at steps of 1 eV (with 1 sweep). For the higher-resolution scans, the pass energy was lowered to 80, 40, or 20 eV (depending on the intensity of the peaks) at steps of 400, 200, and 100 meV respectively. The dwell time was also changed to 250 ms and the number of sweeps was increased to 5. The spectra of SAMs on gold were referenced to the Au 4f_{7/2} line at 84.0 eV. Data was collected using *CasaXPS Version 1.1* software.

The quantitative calculations were preceded by subtraction of a linear background from the separated peaks. The intensity of the peaks was a count-rate of the signal at a given binding energy per second (CPS units). This was followed by fitting and deconvolution procedures to separate signal characteristics for certain positions of each element in the studied molecule, and finally, integration of an area of the peak. To obtain the required atomic concentrations, the calculated row peak areas (also in CPS units) were divided by atomic relative sensitivity factors (RSF), shown in Table 3.7.3-1 for selected elements.

Table 3.7.3-1 RSF for selected elements.

C 1s	0.278
N 1s	0.477
S 2p	0.668
O 1p	0.780
Cl 2p	0.891
Au 4f	6.25

Quantitative analysis was undertaken using the *Jandel PeakFit Version 4.0* software package, which enabled a type of fitting function to be selected and allowed specific parameters, a_n , to be fixed or varied accordingly. Peaks were fitted by using the Lorentz-Gauss cross-product function:

$$f(x) = \frac{a_0}{1 + a_3 \left(\frac{x - a_1}{a_2} \right)^2} e^{\left(\frac{1 - a_3}{2} \right) \left(\frac{x - a_1}{a_2} \right)^2} \quad \text{Eqn 3.7.3-1}$$

3.7.4 Scanning probe microscopy and spectroscopy

Nano-scale surface images and I - V characteristics of SAMs on planar surfaces were obtained using *Multimode NanoScope IV* and *NanoScope E* sets, both made by *Digital Instruments (Veeco Metrology Group)*. An active ground vibration isolation, model TS-150, made by *Table Stable Ltd.* (Zwillikon, Switzerland), and acoustic wave attenuators were applied during measurements. Gold tips, made by precise angle cut of \varnothing 0.2 mm, 99.99 % gold wire, purchased from *Agar Scientific Ltd.* (Stansted, UK), plasma-cleaned prior to experiment, were used. These Au tips enabled atomic resolution with the STM probing techniques, and provided the possibility of temporal junction formation when contacting thiol-terminated self-assembled molecules.

The substrates described in Section 3.4 were attached to metal conducting plates by a layer of synthetic adhesive material. The metal discs with the samples were mounted directly to a magnetic part of the STM head. In the case of HOPG or mica substrates, electrical contact between Au surfaces and the metal plates was established by silver paint, purchased from *Sigma-Aldrich Chemical Co.* Quartz crystals were also adapted for the electric measurements by using high-k, adhesive material. Electric contact from the top electrode of the crystal to the STM head was *via* a thin wire originally attached to the electrode, which was connected to the metal plate.

Data was collected and processed using *Multimode NanoScope Control, Version 5.12r3* software (*Veeco Instruments*). Initial settings used for the surface scans, when the electrons tunnelled between tip and sample, are shown in Table 3.7.4-1. These parameters allowed a precise tip engagement at a safe distance from the sample, therefore preventing tip or surface damages. They were modified afterwards to meet specific sample features, especially roughness and conductivity, and were re-adjusted with measurement condition changes.

Table 3.7.4-1 STM tip engaging parameters.

Bias voltage	100 mV
Current set-point	0.3 – 2 nA
Scan size	1 μm
Tip velocity	4 $\mu\text{m/s}$
Proportional gain	1.5
Integral gain	1
Tip – sample separation limit	1 μm

STS measurements of I - V characteristics were performed with feedback at both positive and negative bias in order to ascertain that the registered current flow asymmetries were real molecular effects. For transparency, the plots presented in this thesis were registered using the feedback at +1024 mV. The polarity of the bias voltage was defined in the conventional way as representing the voltage on the substrate. This means that the positive bias was attributed to electron transport from tip to substrate. All scans were performed at a scanning rate of up to 8 Hz. To measure I - V and I - t characteristics, the initial bias and the tip – sample separation limit were gradually decreased, which enabled reduction of the distance between tip and sample (s). For I - t scans, a 2 nA current set point was used, and the feedback loop was disabled. Deactivated feedback at sufficiently low current and low voltage enabled a slow drift of the tip toward the sample without changing V . A separate STS mode, built into the software, was used for registering I - s characteristics.

Lateral distance calibration for surface imaging was made using HOPG as a reference (see Fig 3.7.4-1). Measured distances between neighbouring atoms of graphite lattice were compared with the literature crystallographic data and the correction was made before obtaining images of molecular arrays. Recorded images were processed using *Multimode NanoScope Control* software in order to remove noise without losing any topographic information.

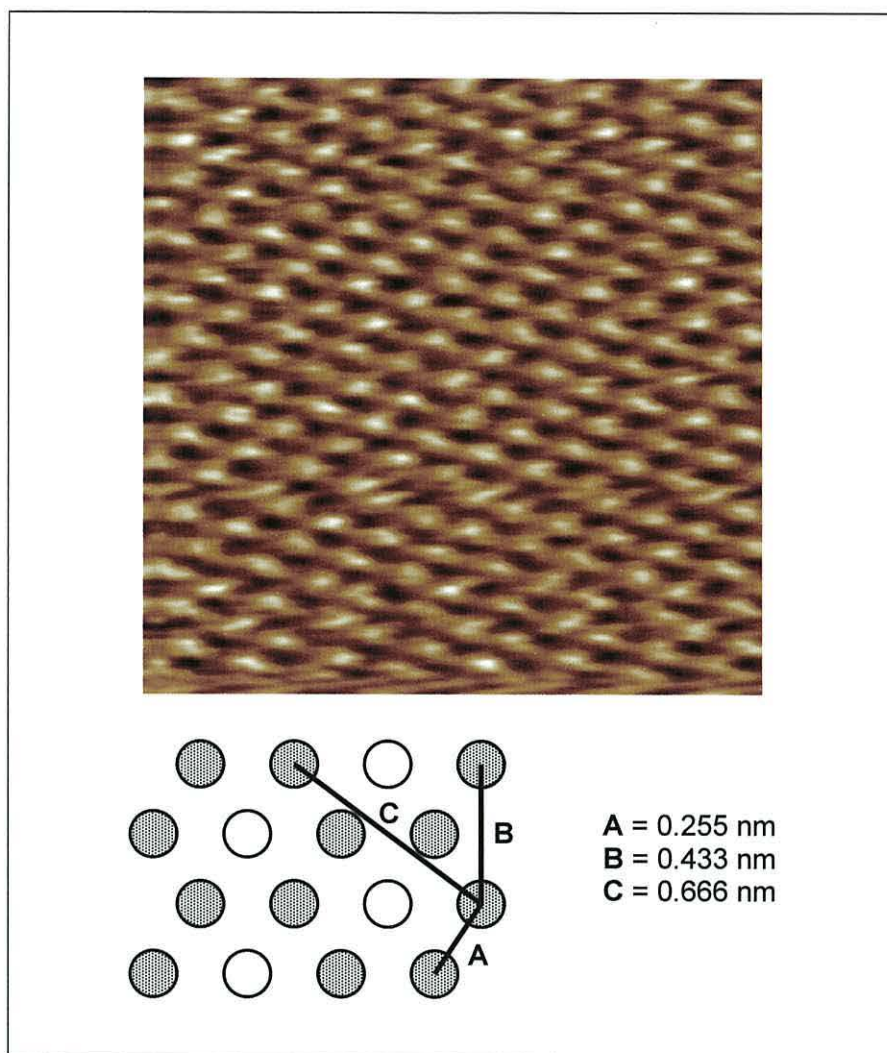


Fig. 3.7.4-1 $3 \times 3 \text{ nm}^2$ constant current STM image of HOPG and schematic structure of HOPG lattice.

3.7.5 Electrical testing of molecular junctions inside silicon platform

In order to measure I - V characteristics of Si-DEV molecular junctions, a simple testing platform was built (see Fig. 3.7.5-1). This enabled quick and accurate contact of external terminals of Si-DEV to testing circuitry. *Keithley Instruments Inc.*, model 6430 *Sub-Femtoamp* source meter, supported by a dedicated signal pre-amplifier containing sensitive feedback elements, was used for the measurements. The signal pre-amplifier was connected to 30 mm, \varnothing 0.2 mm gold wire probing tips *via* a 150 mm protective

shield CAP-31 triax cable (Keithley Instruments Inc.). All possible precautions to eliminate electromagnetic noise and leakage currents, according to information found in the literature on low current measurements^{213,214}, resulted in the complete lack of current offset. I - V measurements were also performed in the dark to avoid photoemission of electrons from the gold electrodes of Si-DEV. The entire setup was controlled by a PC with *LabTracer*, Version 2.42 software.

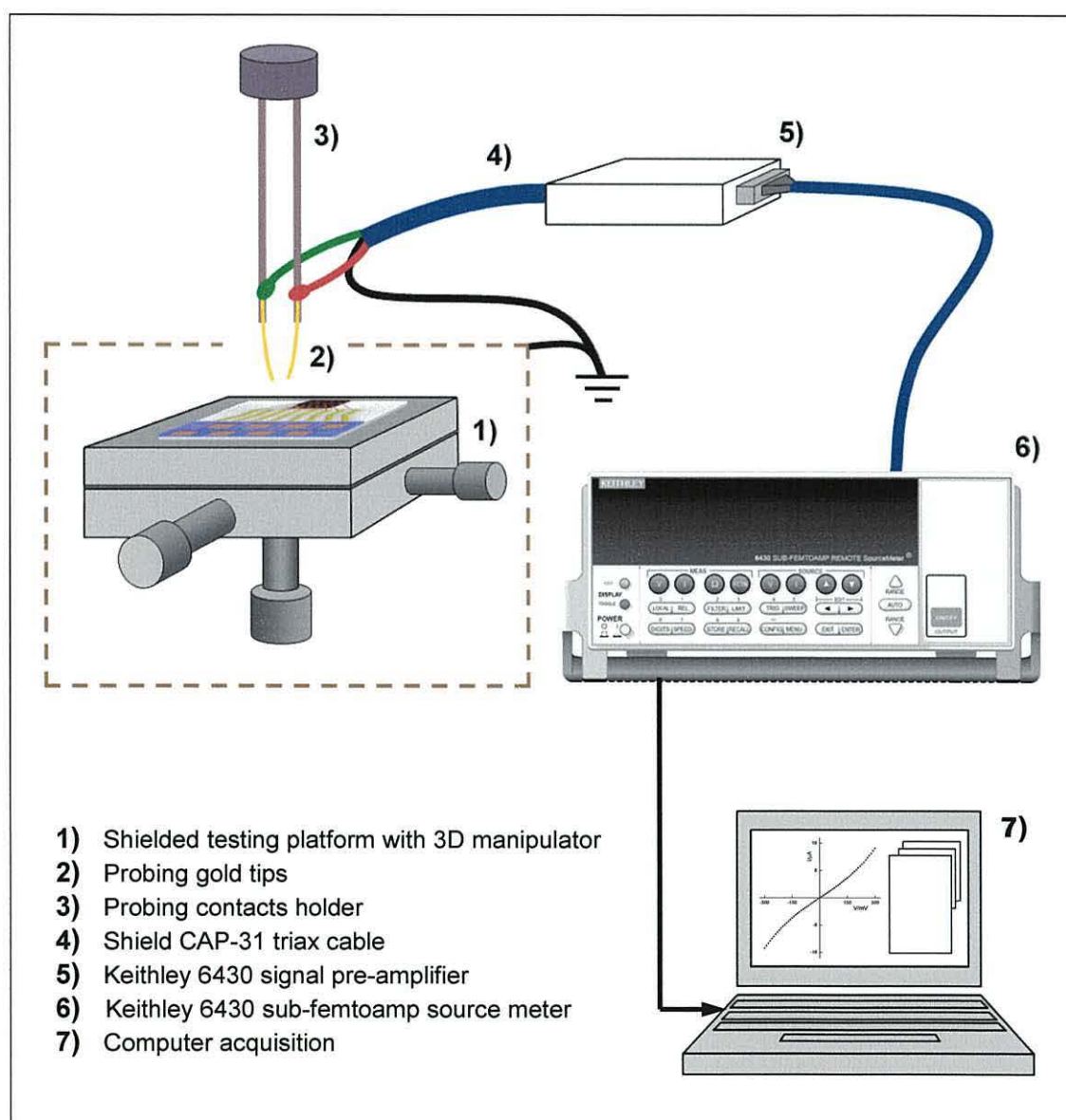


Fig. 3.7.5-1 Experimental setup for I - V measurements of Si-DEV molecular junctions.

3.7.6 *Molecular modelling*

Molecular calculation and visualisation package: *Modelling Studio 4.1* (Cerius Software, Accelrys, Cambridge) was employed in order to:

- 1) provide information about the tendency of molecules to form certain geometries, which was required at the planning stage of the research project;
- 2) localise the frontier molecular orbitals on these molecules;
- 3) estimate the length of molecules and angles, which supported experimental studies on the molecular arrangement on Au and inside Si-DEV.

Molecular geometry optimisation was performed using MOPAC, which is a general-purpose, semiempirical molecular orbital program²¹⁵ and *Austin Model 1* (AM1) calculation method²¹⁶. This method was found to give satisfying results for the aromatic systems, which agreed with experimental observations²¹⁷⁻²²⁰.

4 Results and discussion

Regarding the chemistry of the sample preparation, and various physicochemical features of the prepared systems, this chapter is divided into four major sections. Section 4.1 and 4.2 reveal structural properties of AT systems and PeMP monolayers respectively. Sections 4.3 and 4.4 concern the electrical characterisation of the created molecular wires.

4.1 Structural studies of AT systems

The physicochemical characterisation of the molecular wires, based on an azomethine backbone, focused on the most important aspects of the composition and molecular arrangement of these systems. Detailed analysis concerned only the molecules which had been considered as being useful for further electrical studies. This section is divided into sub-sections in such a way as to describe the analysis of azomethine systems chronologically, at each stage of their preparation. This includes characterisation of the synthesised materials (Section 4.1.1) and structural studies on the molecular monolayers using QCM (Section 4.1.2), XPS (Section 4.1.3) and STM imaging, supported by molecular structures modelling (Section 4.1.4).

4.1.1 Synthesised azomethines

The three products: M10, M11 and M12 were previously analysed *via* TLC, UV-Vis and DSC (after recrystallisation at room temperature). Using these methods, no starting materials or other compounds were identified among the purified final products. Melting point temperatures (MP) of M10 – M12, shown in Table 4.1.1-1, vary from those, observed for M1, M2, M5 and M8. Single UV-Vis absorption peaks at a wavelength maxima in the range of 340 – 384 nm (see Table 4.1.1-1), were responsible for the yellowish colours of these compounds.

Table 4.1.1-1 UV-Vis absorption maxima and MPs of synthesised compounds.

	Wavelength at the maximum of the adsorption peak (nm)	MPs (K)
M10	356	488
M11	340	500
M12	384	514

Mass spectrometry analysis revealed intense peaks at $M = 241$ for M10 and M11, and at $M = 281$ for M12. Accurate mass measurements of M10, using perfluorotributylamine as a reference, enabled determination of the exact values of $M = 241.0552$ vs. calculated $M = 241.0556$.

According to the FT-IR spectra, all three solids absorbed radiation at $2870 - 2860 \text{ cm}^{-1}$ (aldehyde C–H stretching vibrations), and strongly at $1699 - 1694 \text{ cm}^{-1}$ (C=O and C=N stretching vibrations). No sharp absorption at $3370 - 3360 \text{ cm}^{-1}$ (responsible for N–H stretching vibrations) was detected, which confirmed the lack of any significant amounts of M1, M2 and M8 among the respective products.

X-ray absorption peaks for each element of M11 are shown in Fig. 4.1.1-1, for comparison with further studies of AT2 and AT2-A. The core electron binding energies for the elements of M11 and M12 were referenced to the main C 1s peak at 284.7 eV, estimated for SAMs of these compounds (see Table 4.1.3-1). This method enabled tracing changes of binding energies for S and N elements upon chemical reactions and environmental changes.

XPS quantitative analysis of M11 was performed independently by the author and by K. Ford from the University of Queensland (Brisbane, Australia). Analysis of M12 was performed entirely by K. Ford. Calculated ratios of elements, denoted in Fig. 4.1.1-2 for M11 and in Fig. 4.1.1-3 for M12, compared to the theoretical values are shown in Table 4.1.1-2 and Table 4.1.1-3 respectively. Elements, labelled by the same numbers, were considered to be in equivalent chemical environments.

Averaged experimental ratios of the total amounts of C, S, N, and O for M11 were very close to the theoretical ratios expected for these elements, which again proved the chemical purity of these products. Analysis of M12 also revealed exceptional agreement of the experimental ratios with the theoretical ones, generally confirming the high efficiency of the purification method used. The precision of distinguishing the amounts of particular carbon elements in different environment was significantly lower than for different elements of the same compound. This was due to the very high degree of overlap between the peaks which made the resolving procedure problematic. Other small deviations could be due to low accuracy of estimating the baseline when subtracting the background from the separated peaks prior the calculations of their intensities.

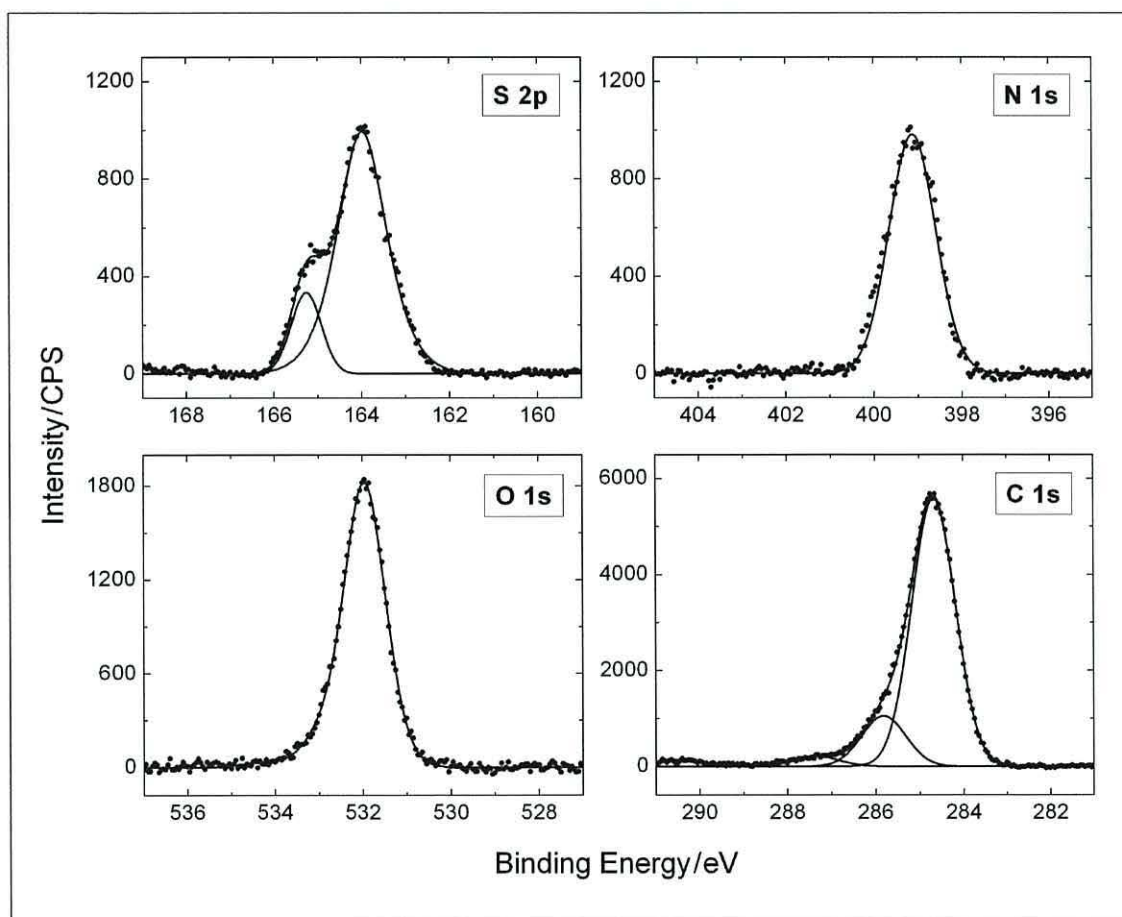


Fig. 4.1.1-1 X-ray absorption peaks of the M11 elements, labelled in the top-right corner of each plot.

Table 4.1.1-2 Results of the XPS elemental analysis of M11. Two values of the elemental ratio were given for each element: the first is for the analysis performed by the author (*PW*) and the second by K. Ford (*KF*).

Element	Chemical environment	Binding energy (eV)	Experimental elemental ratio			Theoretical elemental ratio
			<i>PW</i>	<i>KF</i>	Average	
O 1s	O¹=C	532.0	1.17	0.87	1.02	1
N 1s	C=N²-C	399.1	1.15	1.07	1.11	1
C 1s	C-C³=O	287.2	0.86	0.84	0.85	1
	Aryl-C ⁴ =N Aryl-C ⁵ -N	285.8	2.12	2.22	2.17	2
	Aryl C ⁶ Aryl-C ⁷ -S	284.7	10.6	11.4	11.0	11
S 2p	C-S⁸	164.0 165.3	1.12	0.89	1.00	1

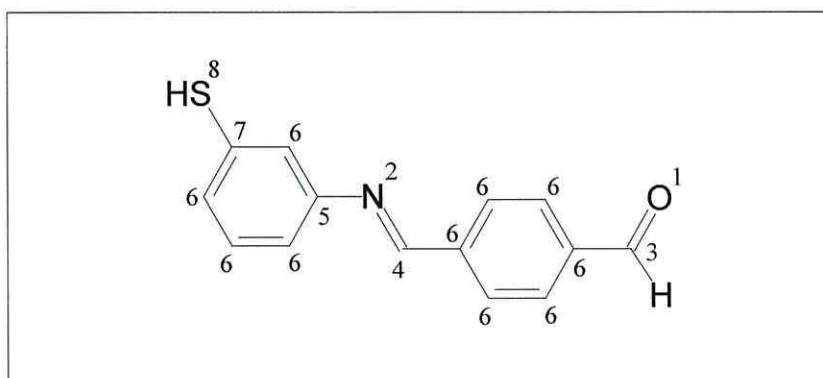
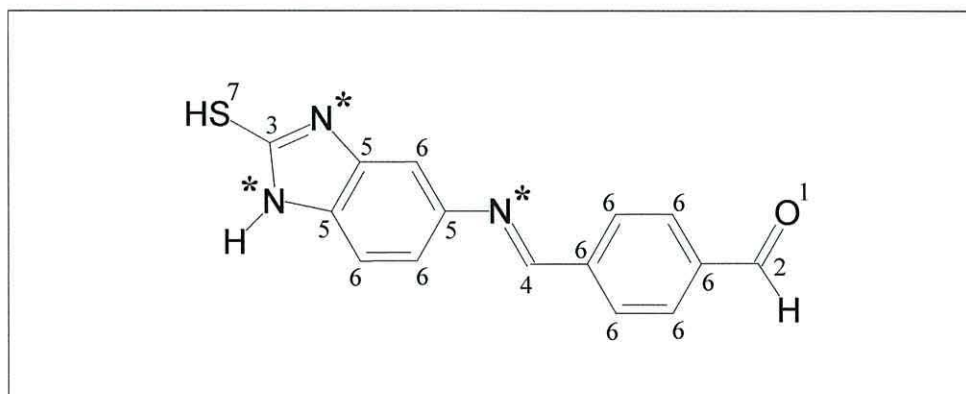


Fig. 4.1.1-2 M11 molecule with numerical labelling, denoting equivalent elements.

Table 4.1.1-3 Results of the XPS elemental analysis of M12 (by K. Ford).

Element	Chemical environment	Binding energy (eV)	Experimental elemental ratio	Theoretical elemental ratio
O 1s	O ¹ =C	531.8	0.90	1
N 1s	N [*]	400.4	2.27	2 [*]
	N [*]	398.7	1.06	1 [*]
C 1s	C–C ² =O	287.5	1.18	1
	N=C ³ –S	287.0	0.93	1
	Aryl–C ⁴ =N Aryl–C ⁵ –N	285.6	3.94	4
	Aryl C ⁶	284.7	8.54	9
S 2p	C–S ⁷	163.4 164.7	0.92	1

* – reliable matching of the detected peaks to the particular nitrogen elements of M12 is impossible at this stage of research due to the lack of literature information about the core electron binding energies for N in this chemical environment.

**Fig. 4.1.1-3** M12 molecule with numerical labelling, denoting equivalent elements.

4.1.2 Self-assembly and interfacial reactions – QCM

Prior to the synthesis of M10, M11 and M12, attempts at forming a well-organised monolayers of M1 and M2 were undertaken. However, the results obtained were very inconsistent. The molecular adlayers were also easily removed by intense rinsing of the QCM electrodes with various solvents. Physisorption, rather than chemical binding of these molecules to gold, was assumed to dominate in these cases. For the small planar molecules the non-upright configuration on gold substrates can not be excluded due to the low intermolecular interactions and considerable affinity of amino groups and phenyl rings to gold surface. Additionally, there is the possibility of disulfides forming which also makes sulfur – gold chemisorption less energetically favourable. As interactions between molecular rings stabilise monolayers, inhibiting close-packing, longer azomethines were synthesised. The replacement of the amino terminal group with an aldehyde group was also expected to promise gold – thiolate formation. Thus M10, M11 and M12 were thought to form densely packed, high-ordered and stable SAMs.

Initially, self-assembly of these molecules was monitored *via* QCM. Results of these measurements, the adsorption isotherms, revealed average areas per molecule (see Eqn 2.2.2-3) *vs.* deposition time. Figure 4.1.2-1 contains such adsorption isotherms for all three systems. Each point in these plots is an average of five independent measurements, obtained for different samples, prepared using the same procedure. The dispersion, treated here as a difference between two extreme readings for each deposition check-points, was also shown by error bars. The area per molecule for maximum surface coverage (*APM*) has been the main reference for molecular packing during these studies. *APM* was reached for deposition times of *ca.* 4, 7 and 24 hours for M10, M11 and M12 respectively. Further depositions of the monolayers of these molecules on other substrates were adequately extended to assure the maximum possible coverage.

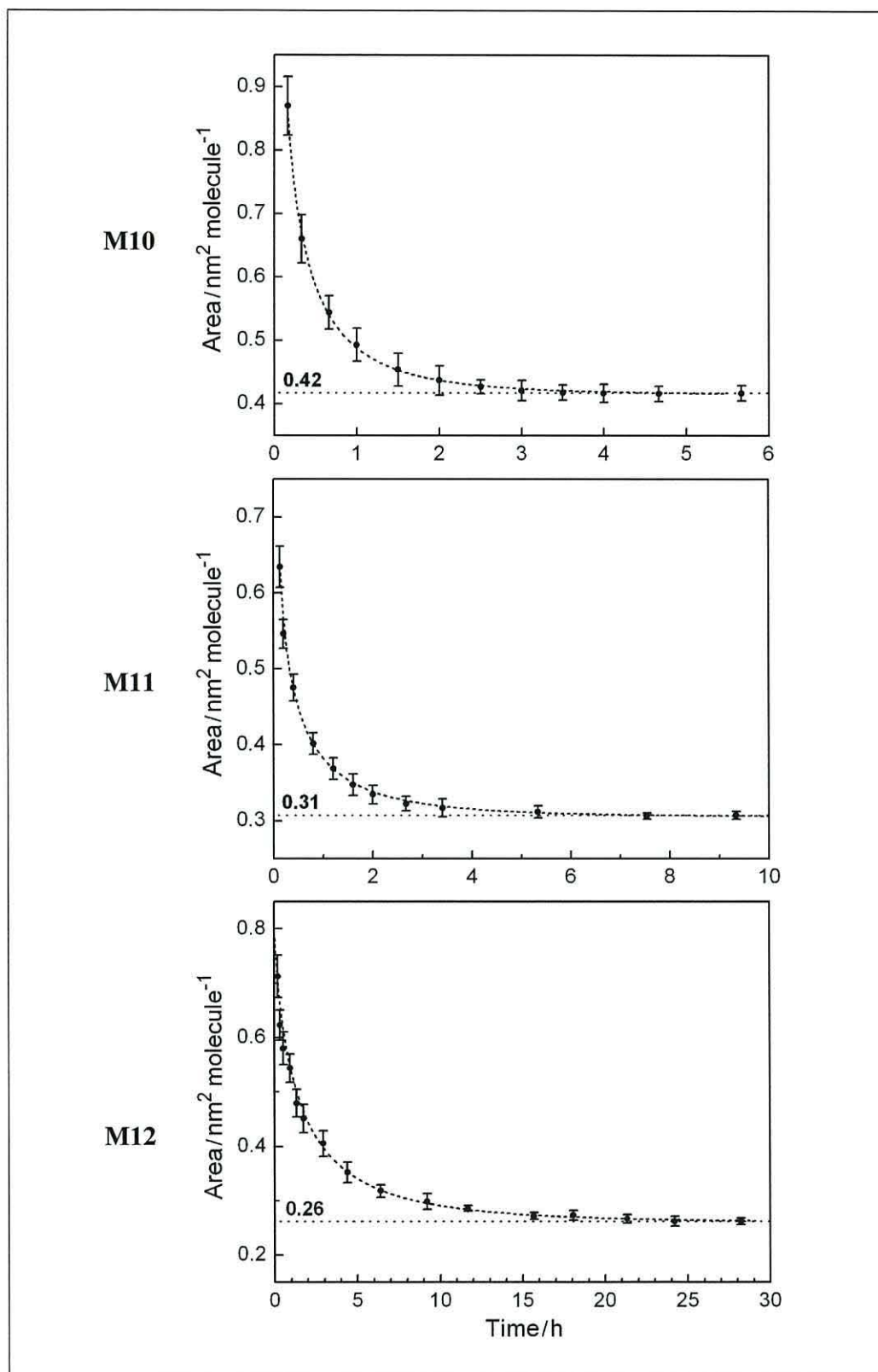


Fig. 4.1.2-1 Adsorption isotherms of M10, M11 and M12 on QCM electrodes.

An exponential dependence of the adsorption isotherms for M10, M11 and M12 matched that observed for diffusion-limited processes (see Section 2.1.2). The QCM data was fitted using a modified Eqn 2.1.2-2, which was adapted to a graphic representation of the adsorption isotherms used in this thesis (see dashed lines in Fig 4.1.2-1):

$$\text{area/molecule} = APM + A e^{-ck_{LD}\sqrt{t}} \quad \text{Eqn 4.1.2-1}$$

Here, A is a scaling factor. The best fittings were obtained for: $k_{LD} = 600 \text{ dm}^3 \text{ mol}^{-1} \text{ s}^{-1/2}$ (M10), $k_{LD} = 320 \text{ dm}^3 \text{ mol}^{-1} \text{ s}^{-1/2}$ (M11), and $k_{LD} = 172 \text{ dm}^3 \text{ mol}^{-1} \text{ s}^{-1/2}$ (M12).

Interfacial reactions of AT1, AT2 and AT3 with M9 or M3, and the following reactions were also monitored *via* QCM. The results, represented by the amount of molecules attached to the previous SAM upon single *in-situ* reaction events, were compared (see Table 4.1.1-3). The amount of molecules involved in each reaction, $\Delta n \text{ (mol)} = \Delta m W^{-1}$, were calculated from Δm , obtained directly from the QCM data, which indicated the maximum surface coverage. Table 4.1.1-3 was divided into four parts, each showing the quantitative characterisation of a different molecular wire structure formation. Three to five samples of each system were tested and analysed to confirm reproducibility of the data.

Presented results indicate a very high yield for most of the interfacial reactions, except the case in which the bulky M6 molecules were involved. However, calculated $APM = 0.79 \text{ nm}^2$ for the AT2-L system was considered as reasonable due to the presence of the hexyloxy side chains in the monolayer. This APM is also consistent with the values reported for other SAMs of linear molecular systems containing these side groups²²¹.

The other tendency was observed for SAMs when reacted with M9. An excess of this compound was detected for 9 of the total 16 samples studied. The highest excess was found for the cases in which the depositions were extended further beyond an average reaction time. Thus, only the samples with stoichiometrically correct amounts of M9 were used for AT1-AD and AT2-AS system formation.

Table 4.1.2-1 The amounts of M10, M11 and M12 deposited onto QCM electrodes, and the amounts of molecules attached *in-situ* to the self-assembled systems, given in $\Delta n (\times 10^{-10} \text{ mol})$ units.

Molecule attached (System created)	Sample 1	Sample 2	Sample 3	Sample 4	Sample 5
M10 (AT1)	1.62	1.68	1.58	1.60	1.64
M9 (AT1-A)	1.54	1.80	1.57	1.79	1.53
M7 (AT1-AD)	1.12	—	1.33	—	1.16
M11 (AT2)	2.25	2.20	2.19	2.17	2.23
M9 (AT2-A)	3.25	2.37	2.15	1.99	2.08
M11 (AT2-AS)	—	—	1.62	1.93	1.79
M12 (AT3)	2.50	2.61	2.67	—	—
M9 (AT3-A)	3.28	2.50	2.72	—	—
M11 (AT2)	2.45	2.45	2.54	—	—
M3 —	2.85	2.75	2.36	—	—
M6 —	0.68	1.18	1.25	—	—
M9 —	0.85	1.19	1.47	—	—
M5 —	0.78	0.90	1.29	—	—
M4 (AT2-L)	0.78	0.80	0.99	—	—

4.1.3 Self-assembly and interfacial reactions – XPS

Samples containing AT2 and AT3 on Au(111) were studied *via* XPS to confirm self-assembly of M11 and M12, and to obtain information about the quality of these SAMs. AT2-A and AT3-A systems were analysed to provide evidence of *in-situ* imino link formation.

Prior to SAM analysis, an air-exposed gold surface was examined in order to study impurities. Traces of C at 284.1 eV and O at 532.7 eV were detected, which was expected according to information found in the literature (see Section 2.1.1). The ratios of C : Au and O : Au were 1 : 3 and 1 : 11. There were no other impurities found on the bare gold surface, apart from these two species. The total absence of S and N elements was also confirmed by the high-resolution scans of S 2p and N 1s regions of the spectrum. As the impurities involved in SAM formation remain unknown, only the amounts of S and N are meaningful for the XPS studies. Thus, the quantitative analysis was limited to these two elements.

X-ray absorption peaks for S and N elements of AT2 and AT2-A are shown in Fig. 4.1.3-1. The binding energies of these elements were referenced to the Au 4f peak at 84.0 eV. Compared to the spectra of powdered thiols, a significant shift in the position of the S 2p doublet towards lower binding energies was distinctive of the direct gold to thiolate sulfur bonding. The peaks: S 2p_{3/2} at 162.0 eV and S 2p_{1/2} at 163.7 eV, detected for the studied SAMs, confirmed dense packing of thiolates in the monolayers²²². The nitrogen peak for AT2 experienced only a minor shift of 0.2 eV towards lower energies.

In the case of M12 self-assembly, the AT3 monolayer formation caused a complete structural reorganisation of the two N 1s peaks. The more intense peak at 400.4 eV, detected for the compound in the solid state, was shifted to 400.1 eV, and the lower intense peak at 398.7 eV remained at the same position. Additionally, the intensity of these two peaks became reversed, as shown in Table 4.1.3-1.

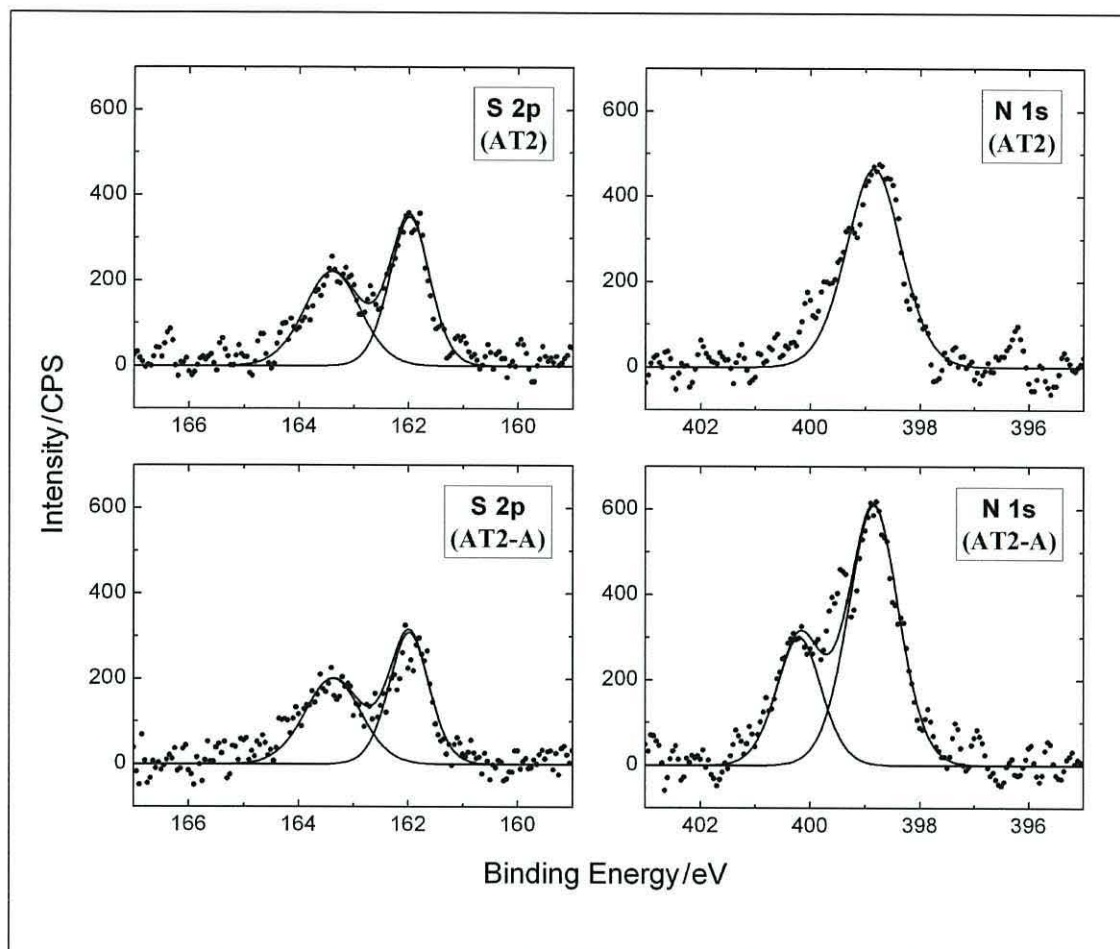


Fig. 4.1.3-1 S 2p and N 1s regions XPS spectra of AT2 and AT2-A, labelled in the top-right corner of each plot.

A quantitative analysis of the XPS adsorption spectra of AT2 and AT3 confirmed the expected S : N ratio to be 1 : 1, and 1 : 3 respectively (see Table 4.1.3-1). The comparison between S : Au ratios, which was 1 : 7.9 for AT2, and 1 : 5.7 for AT3, indicated 38 % higher monolayer density of AT3. The same calculations for the total amount of carbon revealed 29 % higher density of AT3 on the surface. However, both percentage values could be slightly over- or underestimated. This is due to a major limitation of the constant angle XPS technique, which is a decrease in the sensitivity with an increase in the thickness of the SAMs. The presence of any carbonaceous impurities could have also altered the estimation of exact carbon quantities.

A sample of AT2 on gold-coated HOPG was also tested using XPS in order to compare the amount of molecules on polycrystalline gold with that on Au(111). The measured S : Au ratio was 1 : 7.8 in this case, which was comparable to the ratio obtained for AT2 on crystalline gold surfaces.

The evidence of *in-situ* imino link formation, proving interfacial reactions of SAMs and reactant from Table 3.1-1, was also obtained from XPS experiments involving AT2-A. The comparison of N 1s spectra for AT2 and AT2-A (see Fig. 4.1.3-1) indicated differences in intensities of the peaks at 398.9 eV, characteristic of the imino nitrogen, and the presence of another peak at 400.2 eV, which corresponds to the amino nitrogen. Intensities of the peaks at 398.9 eV, measured for AT2 and AT2-A, were 476 and 716 CPS respectively, which suggests a 50 % reaction yield. The intensity of the peak at 400.2 eV was 315 CPS, which (compared to the intensity of the peak at 398.9 eV for this system) gives a 66 % yield. Similarly to the aforementioned analysis for the sulfur element, the sensitivity of the XPS instrument for the in-depth localisation of the particular nitrogen elements reduces the precision of this quantification method.

Table 4.1.3-1 RSF-corrected signal intensities for a total number of the equivalent elements of AT2 and AT3, related to the signal intensity for Au 4f.

Element	Main peak position (eV)	Elemental intensity/Au intensity	
		AT2	AT3
Au 4f	84.0	1	1
S 2p	162.0	0.14	0.18
C 1s	284.7	2.14	2.96
N 1s	398.7	-	0.37
	398.9	0.16	-
	400.1	-	0.19

4.1.4 Molecular geometry and arrangement

STM imaging of the AT1 monolayer and modelling of molecular geometries were performed to gain information regarding the character of the molecular arrangement and the packing density of the respective SAMs.

Figure 4.1.4-1a shows a high-resolution image of the AT1 arrangement on an atomically flat gold surface. A parallel arrangement of the phenyl rings, separated by an average distance of two Au(111) interatomic spacings (0.2884 nm) in parallel, and about four in series (estimating from the central point of the rings), was found to be characteristic for this monolayer (see Fig. 4.1.4-1b). This arrangement suggests the $c(4 \times 2)$ lattice, which contains one molecule per unit cell. However, the absolute confirmation of the molecular arrangement was impossible in this case, due to the lack of information about conformations of the closely packed gold-bonded molecules. The calculated *APM* for the observed AT1 formation was 0.57 nm².

Thermodynamically optimised geometries of the isolated M10, M11 and M12 molecules, resolved using the semiempirical AM1 method, are shown in Figure 4.1.4-2. According to these calculations, each of the studied molecules is twisted along the imino bond. Calculated torsion angles between the two phenyl rings are: 38°, 34° and 33° for M10, M11 and M12 respectively. Such a conformation can also be expected for the molecules in SAMs. Presence of the steric hindrance of these molecules in monolayers is partially supported by the observation of the parallel arrangement of the phenyl rings, which enables the maximum packing density.

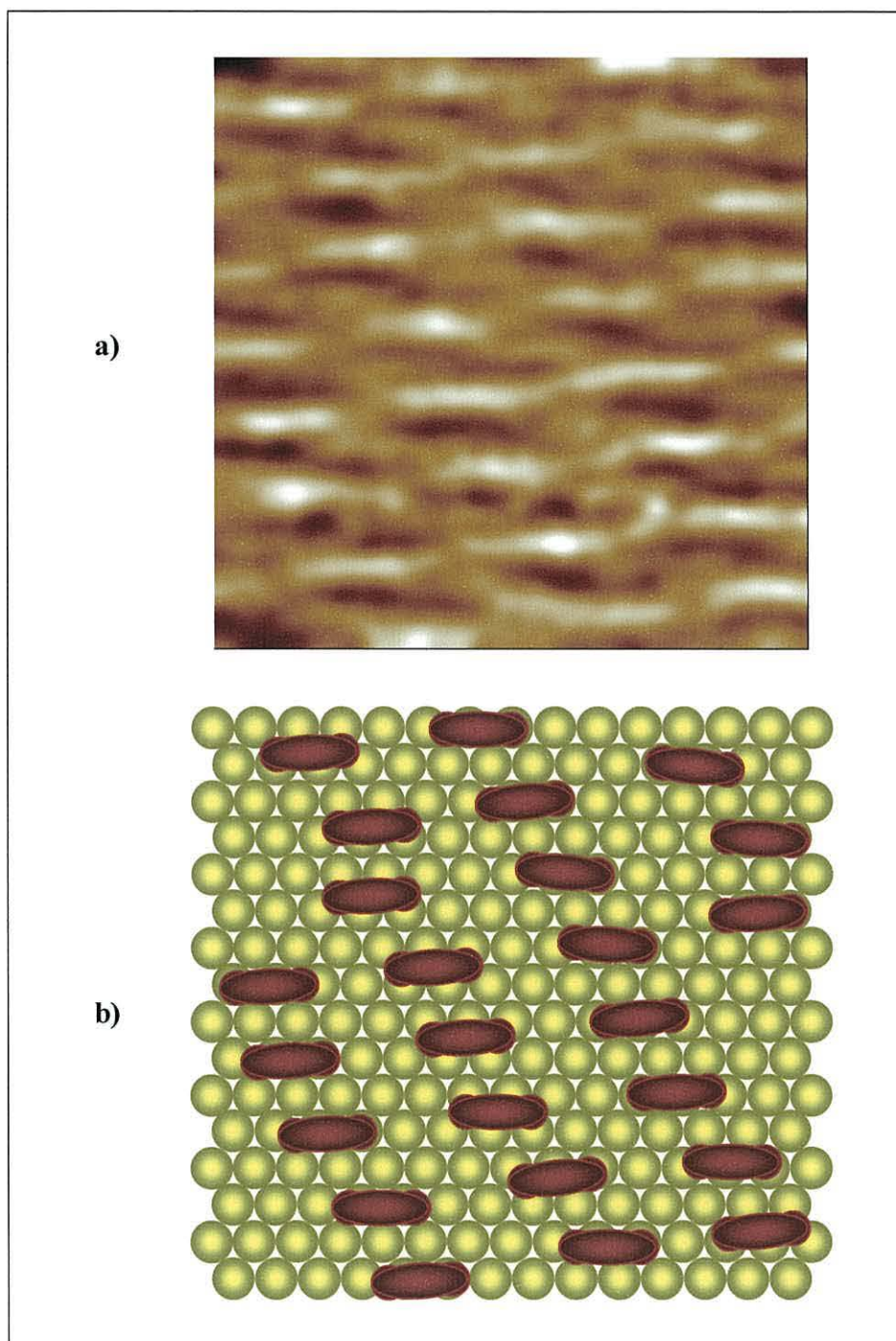


Fig. 4.1.4-1 a) High-resolution $4 \times 4 \text{ nm}^2$ constant current STM image of AT1 on Au (111) surface;
b) Schematic diagram of the presumptive upper phenyl rings map taken from the top image and placed on Au (111) model surface.

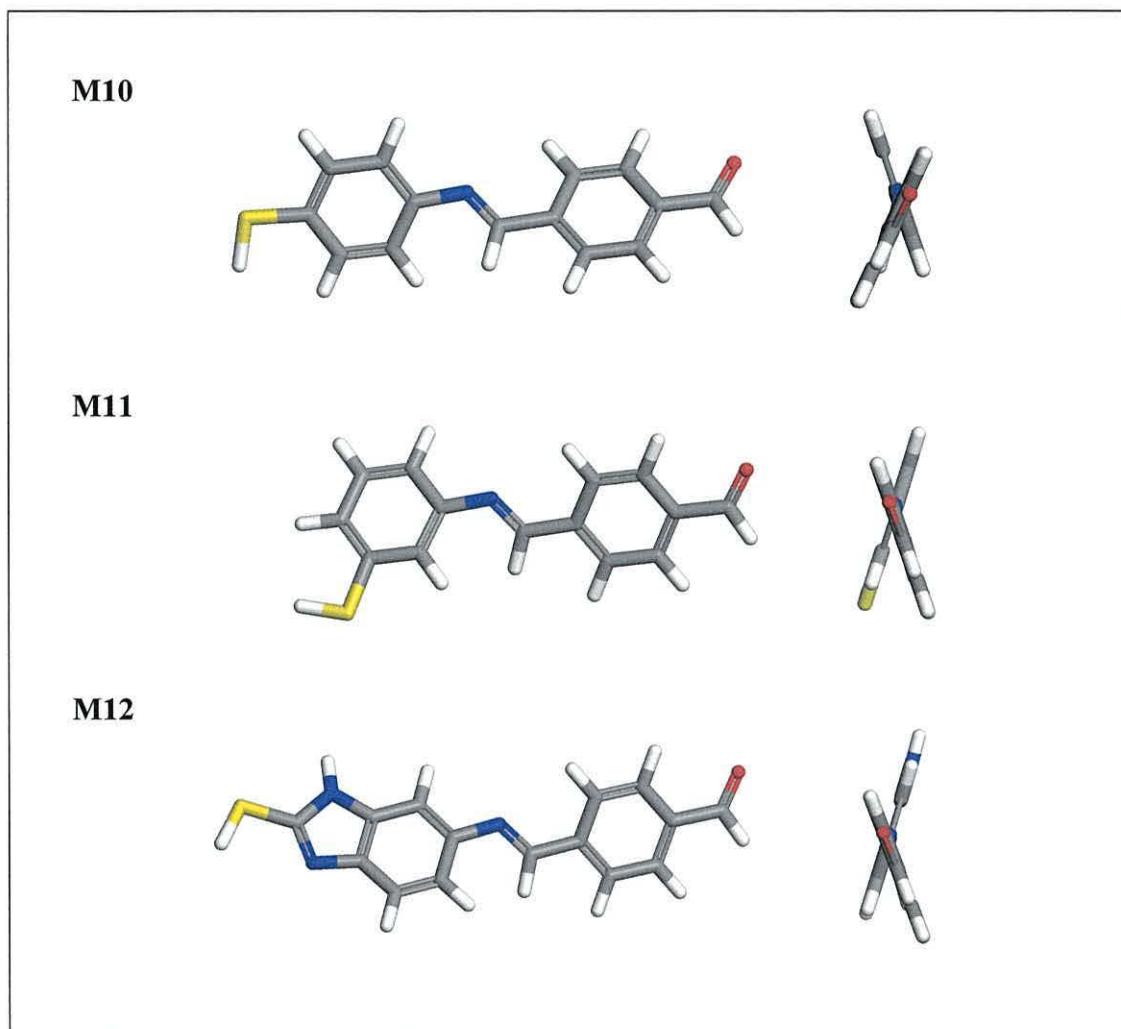


Fig. 4.1.4-2 Side and top views of thermodynamically optimised geometry of the isolated M10, M11 and M12 molecules, resolved using semiempirical AM1 molecular orbitals calculations.

4.1.5 Summary of AT systems preparation

Three molecular systems: M10, M11 and M12, which form SAMs that can be used as starting materials for further *in-situ* reactions, were synthesised. The purity of the materials was proven *via* XPS and confirmed by thermodynamic (DSC) and spectroscopic (UV-Vis, IR) analysis of these compounds.

Strong evidence of S–Au bonding, obtained *via* XPS for AT2 and AT3, proved self-assembly of the synthesised molecules. The core electron binding energies of the sulfur elements in the studied SAMs: 162.0 eV (S 2p_{3/2}) and 163.7 eV (S 2p_{1/2}), are characteristic for densely packed monolayers. XPS quantitative studies confirmed the expected composition of the monolayers.

Dense and highly ordered formations of the AT1 system on an atomically flat gold surface were revealed *via* STM. $APM = 0.57 \text{ nm}^2$ was found for the observed arrangement. This value is slightly higher than that detected for the monolayers of AT1 *via* QCM ($APM = 0.42 \pm 0.02 \text{ nm}^2$). However, the QCM does not possess a “perfect” gold surface on the electrodes. As the calculations of the area per molecule consider the substrate to be perfectly flat, the obtained APM values were probably underestimated. Higher surface coverage was observed *via* QCM for the monolayers of AT2, where $APM = 0.31 \pm 0.01 \text{ nm}^2$, and AT3, where $APM = 0.26 \pm 0.01 \text{ nm}^2$. The lower steric hindrance might be one of the possible reasons for the denser arrangements of AT2 and AT3. This would agree with the AM1 calculations of the isolated molecules geometry. The higher packing density of AT3, which was confirmed by XPS analysis, could have been caused by stronger intermolecular interactions due to N...H–N hydrogen bonding formation. This conclusion was supported by the evident changes in chemical environment of the N elements upon M12 self-assembly, which were detected *via* XPS.

A confirmation of *in-situ* imino bonding formation was obtained *via* XPS studies of the N 1s peaks at 398.9 eV, characteristic for imino bonding, and the peak at 400.2 eV. The second peak arose from the adsorption of radiation by the amino group, which was introduced by the M9 molecules. Further evidence of the *in-situ* reactions was obtained from the QCM measurements. These studies strongly suggest that the reaction yield was determined by the cross-section of the molecules being attached to the previously formed SAMs.

4.2 Structural studies of PeMP systems

Evaluation of the experimental methods for SAM analysis, presented in Section 4.1.5, led to the conclusion that XPS and QCM were sufficient tools for the confirmation of monolayer composition and packing density of the studied systems. Thus, these two methods were applied to analyse PeMP systems.

4.2.1 Self-assembly and interfacial reactions – QCM

Five different samples were used for the study of monolayers of PeMP-a. Each sample was prepared by self-assembly of M13 from a freshly prepared solution, according to the procedure described in Section 3.5.2. Experimental data, representing a calculated area per molecule *vs.* time of deposition are shown in Figure 4.2.1-1, yielded an $APM = 0.28 \pm 0.02 \text{ nm}^2$. Strong dispersion of the rate constant of this process was observed and is represented by error bars in the plot. The existence of two rate constants, or a more complex model of adsorption can not be excluded, as the dependence varies from that observed for the diffusion-limited Langmuir model. The first three experimental data points from Figure 4.2.1-1 were fitted using Eqn 4.1.2-1, characteristic for the diffusion-limited model in order to highlight these differences (see dashed line in Figure 4.2.1-1). These deviations are believed to be connected with the observation of tarnished gold electrodes upon deposition. This was probably caused by M16 extraction from the chloroform/methanol solution mixtures and condensation of this compound onto the surface, effectively blocking the deprotected M13 from being chemisorbed. This adlayer of M16 was periodically removed by rinsing the samples with ultra-pure methanol, as described in Section 3.5.2.

Effects of protonation of PeMP-a to obtain PeMP-b can not be confirmed directly *via* QCM. Any possible changes of the molecular mass on gold, due to the presence of protons being attached to the pyridine ring of the PeMP-a system, and chlorine anions, are below the resolution of this technique. However, an indirect confirmation of this process was obtained during further reaction of PeMP-b with M14.

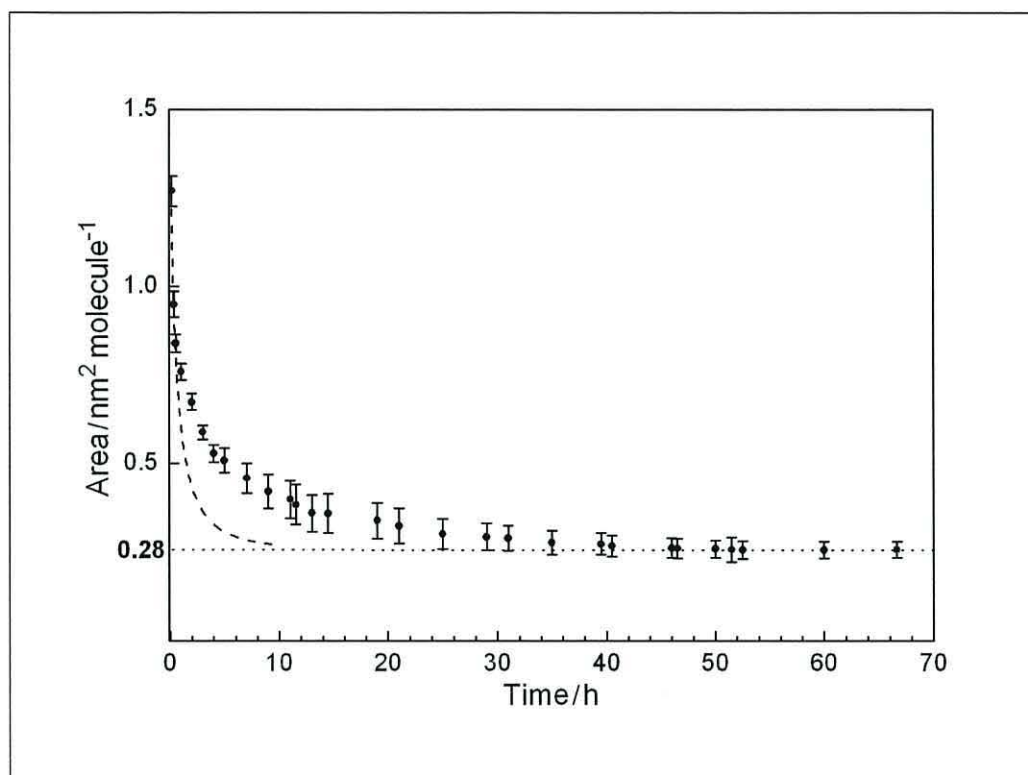


Fig. 4.2.1-1 Kinetics of M16 SAM formation on gold (black dots with error bars) and a theoretical isotherm for the diffusion limited process, calculated for the first three points, representing the initial stage of the self-assembly (dash line).

The QCM results for PeMP-b and PeMP-c samples revealed the presence of a dense adlayer of $\text{TCNQ}^{\bullet-}$ with an average $APM = 0.32 \pm 0.04 \text{ nm}^2$. A stoichiometric PeMP-b : $\text{TCNQ}^{\bullet-}$ ratio between 1 : 0.75 and 1 : 1 was confirmed (see Table 4.2.1-1). This indicated a high efficiency of both: protonation of PeMP-a, and Cl^- replacement by $\text{TCNQ}^{\bullet-}$.

Since tight packing of PeMP-b was confirmed *via* QCM, the $\text{TCNQ}^{\bullet-}$ moieties have been expected not to intermix with the self-assembled molecules, but reside on top of the PeMP-b monolayer. The most convincing proof of this theory was provided with the STS-STM experiments (see Section 4.4.2), where exceptional electrical properties of this system were observed and can only be explained when the $\text{TCNQ}^{\bullet-}$ adlayer formation takes place.

Table 4.2.1-1 Amounts of PeMP-b on gold, TCNQ^{•-} molecules reacted *in-situ* with PeMP-b (forming PeMP-c), and M15 interacting with PeMP-c; all given in Δn ($\times 10^{-10}$ mol) units. The calculated *APM* values (nm^2) are also given.

Molecule/system		Sample				
		1	2	3	4	5
PeMP-b	Amount of mol.	2.18	2.62	2.50	2.57	2.44
	<i>APM</i>	0.312	0.260	0.272	0.265	0.279
TCNQ ^{•-}	Amount of mol.	2.03	2.44	2.64	1.95	1.89
	<i>APM</i>	0.336	0.279	0.258	0.349	0.360
M15	Amount of mol.	1.19	0.73	1.01	-	-
	<i>APM</i>	0.573	0.930	0.677	-	-

According to the QCM studies on PeMP-d, the attempts at deprotonating the pyridine rings of PeMP-c failed. Contrary to the expected removal of TCNQ^{•-} from the system upon deprotonation, an increase in the mass on the QCM was observed for each sample studied (see Table 4.2.1-1). The excess of molecular mass was present in the system, even after intense rinsing of the QCM electrodes with various solvents. There could be two possible reasons for the observed effect. The first is a partial assimilation of M15 by PeMP-c SAMs, and the second is some chemical reaction between M15 and components of the PeMP-c system. The precision of these measurements is reduced due to the low weight of M15 molecules. Thus, definite evidence of M15 present in the PeMP-d system can not be achieved using the QCM technique.

4.2.2 Self-assembly and interfacial reactions – XPS

Samples of PeMP-a, PeMP-b and PeMP-c on Au(111) were studied *via* XPS in order to confirm self-assembly of PeMP-a and to gain information regarding the efficiency of the chemical transformation of this system into PeMP-b, and further into PeMP-c. An analysis of PeMP-d was not undertaken as M15 consists of a very small number of elements, when compared to the total number of elements in PeMP-d. There are no characteristic elements present in M15 that could be easily distinguished and identified.

Processed X-ray absorption peaks for S and N elements of PeMP-a, PeMP-b and PeMP-c are shown in Fig. 4.2.2-1. Binding energies of these elements were referenced to the Au 4f peak at 84.0 eV. The binding energies of the most intense sulfur doublet (S 2p_{3/2} at 163.7 eV and S 2p_{1/2} at 164.9 eV peaks) are characteristic for the thiol group sulfur. The less intense doublet (S 2p_{3/2} at 161.9 eV and S 2p_{1/2} at 163.2 eV peaks) indicated the presence of gold-bound thiolate sulfur in a dense arrangement. There were also shake-up peaks resolved for all three systems at: 167.4 eV and 168.9 eV for PeMP-a, 167.7 eV and 168.6 eV for PeMP-b, and 167.9 eV, 169.3 eV and 170.6 eV for PeMP-c. These changes in the position and the structure of the shake-up peaks confirmed the transformation of the HOMO and LUMO energy levels of PeMP-a upon protonation, and PeMP-b upon ion exchange. However, detailed analysis of the electronic structures of these systems were difficult due to insufficient resolution of the spectra. The N 1s spectra of PeMP-a and PeMP-b consisted of two peaks: the main peak at 399.6 eV, and a shake-up peak, located at 401.8 eV for PeMP-a, which was shifted to 402.1 eV upon protonation. The N 1s spectrum of PeMP-c, apart from these two peaks, also contained a set of peaks with a maximum absorption at 399.8 eV, the shape of which is characteristic for the TCNQ^{•-} nitrogen. The Cl 2p peak was only detected at 198.2 eV for PeMP-b and was included in the quantitative analysis. The high-resolution scans at the binding energies in the range of 192 – 205 eV for PeMP-a and PeMP-c confirmed the absence of chlorine in these systems.

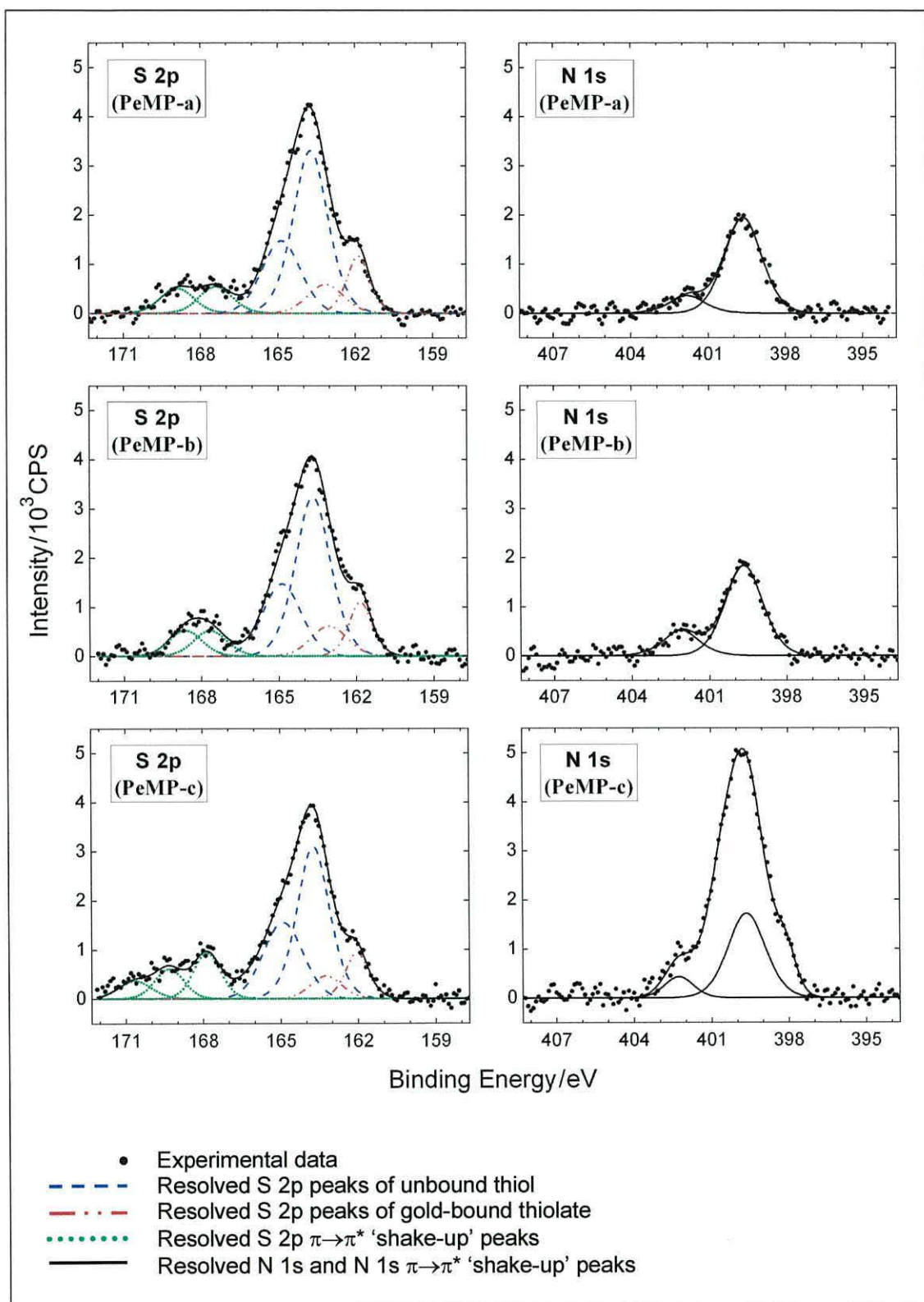


Fig. 4.2.2-1 S 2p and N 1s regions XPS spectra of PeMP-a, PeMP-b and PeMP-c, labelled in top-left corner of each plot.

Table 4.2.2-1 RSF-corrected signal intensities for the total number of PeMP-b and PeMP-c elements, related to the pyridine ring N 1s signal intensity.

Element	Main peak position (eV)	Elemental intensity / N ^(pyridine) 1s intensity	
		PeMP-b	PeMP-c
N 1s	399.6	1	3.10
Cl 2p	198.2	0.58	0
S 2p	163.7 161.9	2.06	1.99

The quantitative analysis included N 1s, S 2p and Cl 2p peaks of PeMP-b and PeMP-c systems (see Table 4.2.2-1). These calculations were only approximations as the sensitivity of the XPS method decreases with the depth of such densely packed systems. This was observed directly for the two S 2p double peaks, which should have had equal intensities if the two sulfur elements had been situated at the same depth. The registered spectra clearly proved the presence of the gold thiolate sulfur characteristic for dense SAMs, and the thiol sulfur on the outer side of the monolayer, as the peak doublet at 163.7 eV and 164.9 eV was much more intense than the thiolate sulfur doublet. The same analysis also proved the existence of a nitrogen somewhere in the middle of the monolayer thickness, as the N 1s peak intensity was half that of the S 2p peak intensity. The signal intensity of the chlorine anion, which should be situated in direct proximity to the pyridine nitrogen, can be reliably referenced to the intensity of the N 1s signal. The comparison of these two peaks suggests 58 % efficiency of the protonation process. A similar value was obtained from a calculation of TCNQ^{•-} nitrogen in the PeMP-c system, which revealed slightly more than one TCNQ^{•-} per two dechlorinated PeMP-b, after anion replacement.

4.2.3 Summary of PeMP systems preparation

Self-assembly of PeMP-a was confirmed *via* XPS by detection of gold-bound thiolate sulfur and nitrogen of the aromatic system, with the correct ratio of these two elements. The dense arrangement of PeMP-a SAMs was proven *via* QCM. The calculated value of $APM = 0.28 \pm 0.02 \text{ nm}^2$ was low, compared to the other systems studied, which was expected for the rigid linear molecules with the small cross-section of a single phenyl ring. The presence of a dense vertical formation was also supported by the observed strong depth profile dependence of the XPS signal.

The transformation of PeMP-a into PeMP-b, studied *via* XPS, revealed a time of *ca.* 1 min to be insufficient for total protonation of PeMP-a pyridine rings, which occurred under the experimental conditions described in Section 3.5.2. This conclusion was based on the compared intensities of XPS signal for the chlorine anions of PeMP-b and the TCNQ^{•-} nitrogens of PeMP-c related to the nitrogen peak of the PeMP-b system. The calculated protonation efficiency was 58 %. A higher reaction yield (> 75 %) was suggested by the QCM data. Moreover, TCNQ^{•-} was found to completely replace the chlorine anions of PeMP-b when immersed in a concentrated solution of M14. Thus, the PeMP-c system contained more than one TCNQ^{•-} per two dechlorinated PeMP-b molecules from the densely packed monolayer. Such a ratio was considered to be sufficient for further studies of the electrical properties of these systems.

Three attempts at proton removal, situated on the pyridine ring of PeMP-c, using M15 were unsuccessful. However, QCM measurements revealed an excess of molecular mass present after PeMP-c immersion into a solution of M15. Structural and elemental analysis of PeMP-d was hindered due to the lack of experimental techniques for such studies. The small molar weight of M15 and a lack of specific chemical composition, distinguishing this molecule from the environment, disallowed the use of XPS and QCM. Further studies on the transformation of PeMP-c into PeMP-d are required, as they would help to identify the composition of PeMP-d, which revealed unique electrical properties (see Section 4.4.2).

4.3 Electronic properties of AT systems

Studies on the electronic properties of AT systems have focused on two major aspects of current flow through *quasi*-one-dimensional molecular structures: efficiency and directional asymmetry of electronic transmission. As yet, there has been no reliable technique for permanently trapping asymmetric molecules between two metal electrodes, so STM remains the major tool for studying asymmetry of current flow through these systems. However, this introduces the problem of tip – molecule separation, whose impact on the shape of observed I - V characteristics has not been identified unambiguously. This problem is a priority for future studies on current rectification in molecular systems and is the primary focus of this investigation (Section 4.3.1).

The second part of these studies (Section 4.3.2) concerns the possibility of obtaining significant rectifying properties from AT systems. The method of *in-situ* extension of AT structure length, studied in Section 4.1.2 and 4.1.3, enables one to introduce electron-accepting and electron-donating molecular components into the conjugated AT chain of the final product. Depending on the distribution of these functional units along the molecular chain of the created system, the direction of rectification could be different. This effect was accurately investigated and compared with other studies on rectification in π -bridge separated donor – acceptor complexes.

Finally, the characterisation of the first rigid, mass-producible platform for studies of molecular conductivity was carried out (Section 4.3.1). The electric properties for each stage of molecular structure formation inside the electrode gap were demonstrated through electrical characterisation of the AT2-A-AT2 molecular wire at different stages of its formation. Next, the benefits of the Si-DEV usage for examining electronic transmission through two-terminal molecular systems were studied. This was done by comparison of the I - V characteristic of AT2-A-AT2 obtained for Si-DEV studies, I - t STS measurements and theoretical calculations.

4.3.1 Statistical studies on I - V characteristics.

Separate I - V characteristics registered using the STM-STs method provide much information about the local electrical properties of an investigated sample. However, this information is distorted by the presence of an air gap between the tip and the sample, which the electrons have to tunnel through. The larger the tip – sample separation, the higher the deviation from the shape of the I - V curves recorded for the maximum tip – sample electronic overlapping. Thus, selective analysis of the separate characteristics makes such studies unreliable. For this reason, accurate estimation of the influence of an air gap potential barrier on the shape of the I - V characteristics is essential for further studies on conductivity and asymmetry of current transmission through organic thin films.

Statistical studies can provide an understanding of the electron tunnelling between the tip and the substrate and, as discussed further in this section, distinguish the measurements being taken at constant tip – sample separation. This method also allows one to group the I - V characteristics according to the decreasing tip – sample separation and trace evolution of the fine structures of these curves in order to find the processes which affect tunnelling through the air gap. Thus, the detailed statistical analysis of the processed I - V characteristics enable very accurate interpretation of the electrical properties of the studied materials, as instrumental response to the electron scattering due to the potential barrier of the air gap can be extracted from such analysis.

Introduction to the statistical analysis

The studies of electronic transmission dependence on tip – substrate separation distance (d) presented here were performed mainly to investigate the influence of an air gap potential barrier on the asymmetry of I - V characteristics, observed *via* STS technique. A novel statistical approach to this problem is demonstrated. This includes comparison of the following dependences:

- 1) **asymmetry – current** [$A_a(V_n) - I_a(V_n)$, where a is the measurement index of each consecutive reading] at two or more characteristic values of tip – substrate bias voltage, V_n , taken from I - V curves, registered at various tip – molecule spatial coordinates:
 - a) when d could vary slightly, but averaged tip – substrate separation distance vs. a remained constant $\{\langle d(a) \rangle = \text{const}\}$,
 - b) when d was slowly and gradually decreasing $\{d(a) = [d_a, \dots 0]\}$;
- 2) **asymmetry – voltage** (A - V), calculated for separate I - V curves, registered at various d ;
- 3) **conductance – voltage** (dI/dV), for I - V curves, registered at various d .

The parameter a can be related to the time of each measurement, as the following I - V curves were taken with approximately constant time intervals of 1 s. This method of analysis was applied on the basis of STS measurements on AT1, and results were used as references for further studies on molecular rectification in other systems on gold.

In order to perform the analysis on AT1, according to the above mentioned procedure, a flat area of gold substrate, where a densely packed molecular arrangement was observed (see Fig. 4.1.4-1), was probed by an STM gold tip. The I - V characteristics were registered with the maximum scan rate of 14 Hz. Primarily, the constant feedback loop at + 1024 mV was used, which maintained $\langle d(a) \rangle = \text{constant}$ conditions. When a statistically significant amount of data was collected, the feedback loop was deactivated, which enabled slow drift of the tip toward the substrate.

STS studies for $\langle d(a) \rangle = \text{constant}$

The two boundary examples of I - V curves for AT1 measurements are presented in Fig. 4.3.1-1. A slight asymmetry was observed at high voltages (Fig. 4.3.1-1a), whereas in the low-voltage range, all characteristics were found to be roughly symmetrical (Fig. 4.3.1-1b). Considering this difference, $A_a(V_n)$, where $a = [1, 2, \dots 100]$, for $V_1 = \pm 1024$ mV and $V_2 = \pm 300$ mV, were calculated from the registered I - V curves and included in further analysis. Prior to the calculations of $A_a(V_2)$, the I - V curves were

smoothed, using an adjacent averaging method, to reduce the error caused by thermal noise (as shown in Fig. 4.3.1-1b).

The values of $I_a(V_1)$ and $I_a(V_2)$, taken from a hundred sequentially measured I - V characteristics, using the constant feedback loop at +1024 mV, were plotted in Fig. 4.3.1-2 and Fig. 4.3.1-3 respectively. These figures also contain $A_a(V_1)$ and $A_a(V_2)$ values, which correspond to $I_a(V_1)$ and $I_a(V_2)$ data. Fig. 4.3.1-2 shows that the applied feedback loop at $V = +1024$ mV kept $I_a(+V_1)$ fairly stable and thus $A_a(V_1)$ is, with a good approximation, linearly proportional to $I_a(-V_1)$. This linear dependence is distinctive in Fig. 4.3.1-4a, where the $A_a(V_1)$ - $I_a(V_1)$ characteristic is presented. The typical current asymmetry at this voltage was in the range between 1 and 2. It temporarily increased to a maximum value of $A_{max}(V_1) = 4.0$. On the other hand, the same I - V characteristics revealed strong variations of $I_a(V_2)$, simultaneously at positive and negative currents (see Fig. 4.3.1-3). The local changes of $I_a(V_2)$, however, did not induce any significant current asymmetry at this voltage. The highest asymmetry at low voltage, $A_{max}(V_2) = 2.8$, was registered for the minimum value of $I_a(V_2)$. However, the lack of a linear relation between the values of $A_a(V_2)$ and $A_a(V_1)$, calculated for the same a , was significant for this data. It can be observed more clearly in Fig. 4.3.1-4b, where a strong dispersion of the data points of $A_a(V_2)$ - $I_a(V_2)$, compared to the linear relation of the equivalent dependence for V_1 (see Fig. 4.3.1-4a), is shown.

The comparison of $A_a(V_n)$ - $I_a(V_n)$ characteristics for V_1 and V_2 indicates that there are at least two competing phenomena, which affect current transmission in the studied voltage range. One of them is dominant at lower, and the other, at higher voltages.

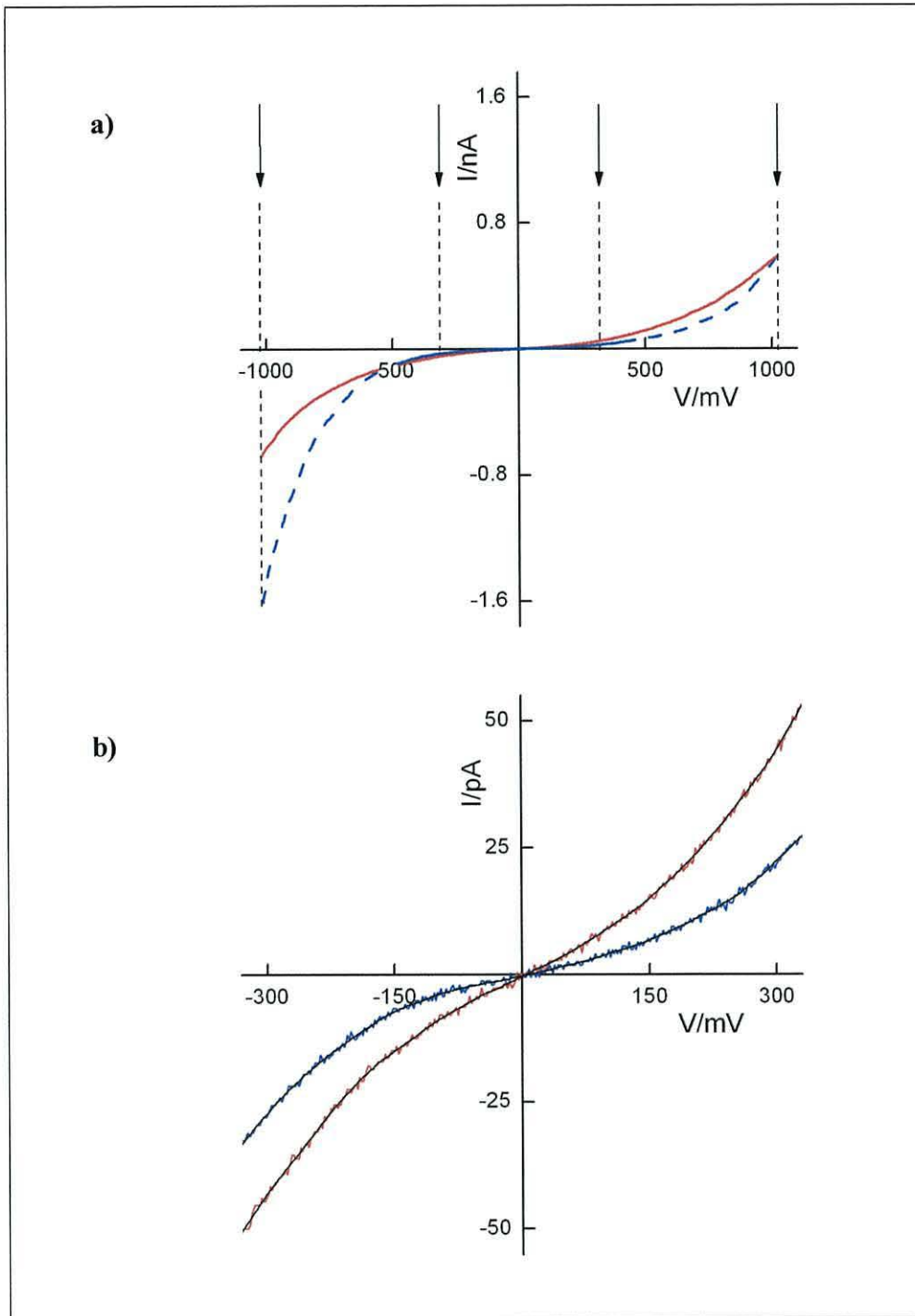


Fig. 4.3.1-1 Examples of symmetrical (red solid lines) and asymmetrical (blue long-dash line) I - V characteristics of AT1 at two voltage ranges: $[-1024; +1024]$ (a), and $[-300; +300]$ (b); dash lines and arrows indicate the values of V_n (± 300 mV and ± 1024 mV) used for the calculations of $A_a(V_n)$; curves were smoothed at lower V for better accuracy of measurements (black solid lines).

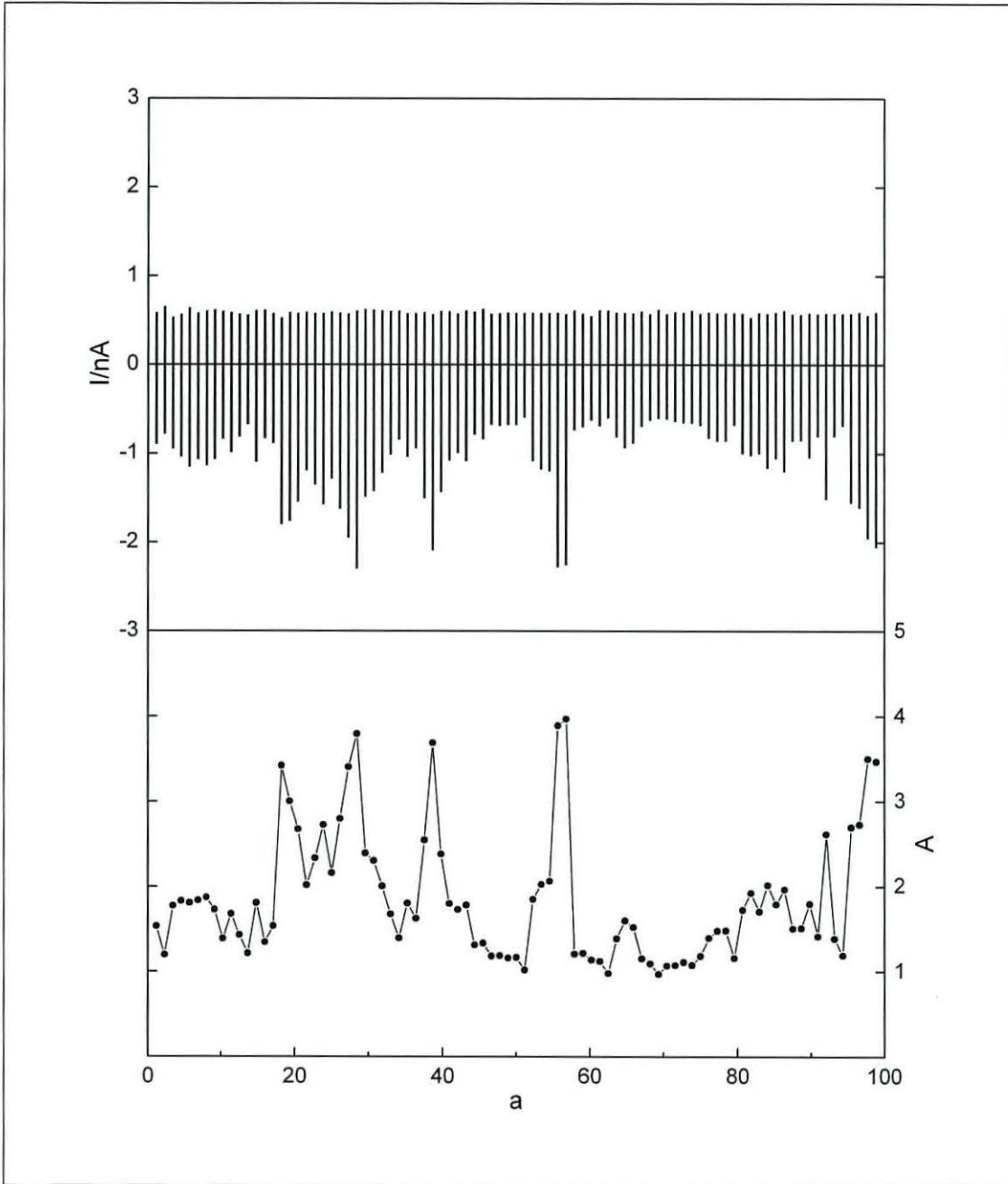


Fig. 4.3.1-2 The values of $I_a(V_1)$, for: $V_1 = \pm 1024$ mV and $a = [1, 2, \dots, 100]$, obtained with constant feedback loop at +1024 mV (top plot), and $A_a(V_1)$, calculated from $I_a(V_1)$ values of the top plot (bottom plot); the original sequence of measurements (X-axis) was maintained.

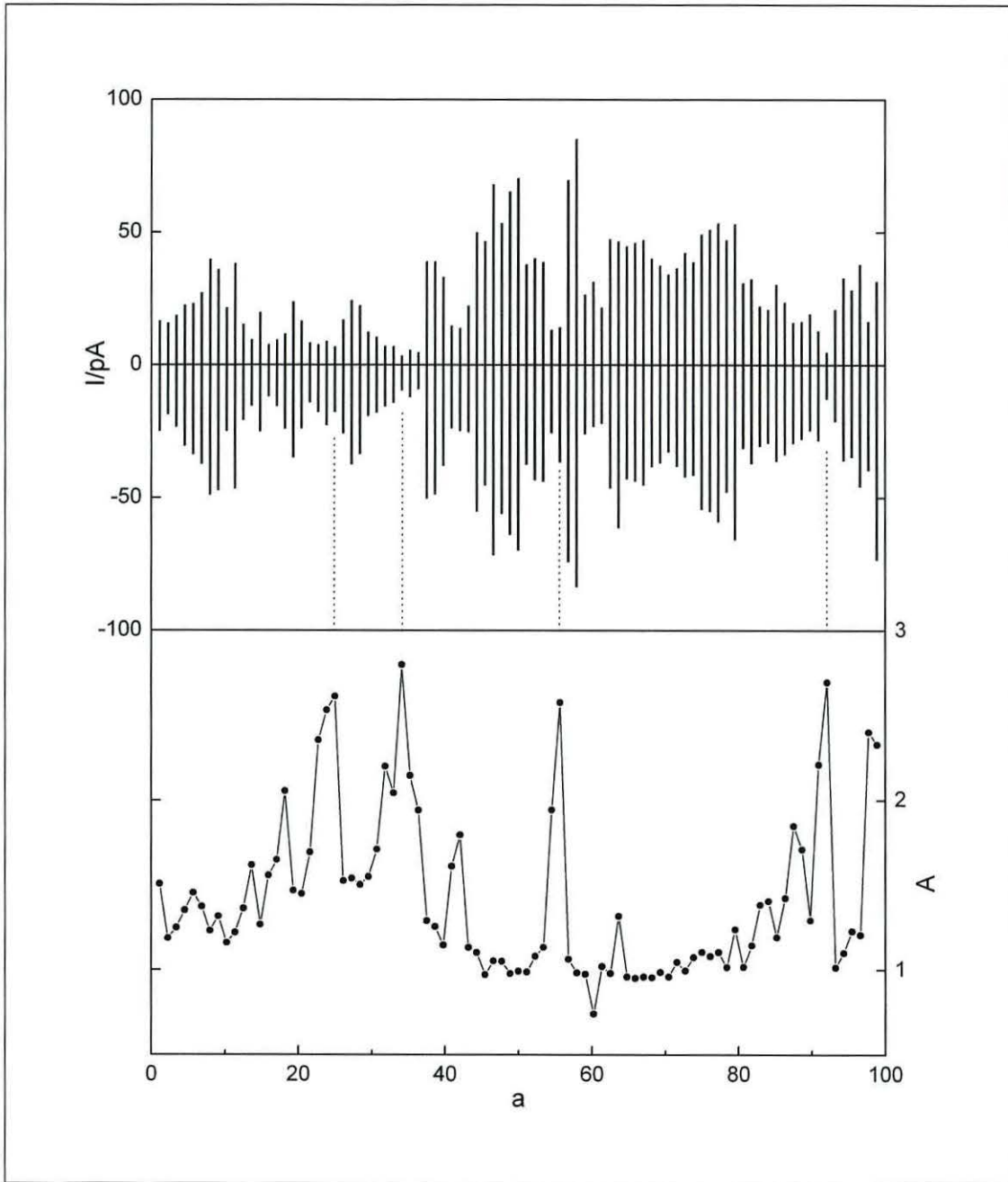


Fig. 4.3.1-3 The values of $I_a(V_2)$, for: $V_2 = \pm 300$ mV and $a = [1, 2, \dots, 100]$, obtained with constant feedback loop at +1024 mV (top plot), and $A_a(V_2)$, calculated from $I_a(V_2)$ values of the top plot (bottom plot); the original sequence of measurements (X-axis) was maintained.

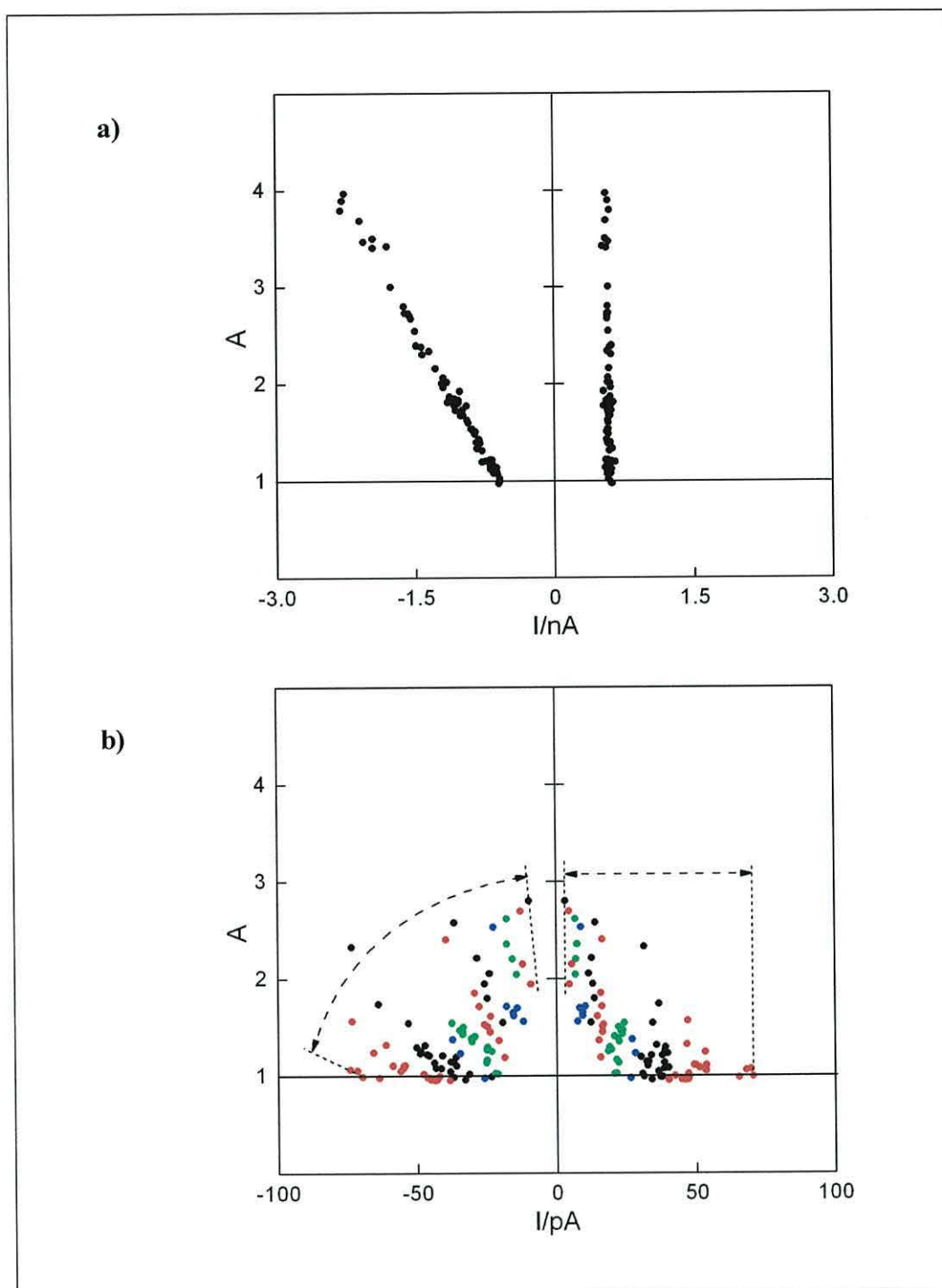


Fig. 4.3.1-4 The comparison of $A_a(V_n)-I_a(V_n)$ characteristics for V_1 (a) and V_2 (b), calculated from data presented on Fig. 4.3.1-2 and Fig. 4.3.1-3 respectively; different colours, for representation of data points on (b) were used in order to distinguish equivalence of $A_a(V_2)-I_a(-V_2)$ and $A_a(V_2)-I_a(+V_2)$ points; the ranges of $A_a(V_2)-I_a(-V_2)$ and $I_a(+V_2)$ dispersions were also indicated on (b).

The comparison of a statistically significant number of $A_a(V_1)$ and $A_a(V_2)$, provided a reference for further studies on asymmetry. On the other hand, the calculations of the complete A - V profiles allowed comparison of asymmetries over the whole range of bias voltages applied during I - V characteristic measurements.

Fig. 4.3.1-5a shows the correlation of $A_a(V_1)$ and $A_a(V_2)$ values for 40 sequentially measured I - V curves $\{a = [1, 2, \dots, 40]\}$. It was found that when $A_a(V_1)$ reached its maximum, $A_a(V_2)$ typically dropped to values which are close to unity. For other I - V measurements, the changes in $A_a(V_2)$ seemed to follow $A_a(V_1)$ variations, or even reach very similar values. The two boundary A - V relations, corresponding to $A_a(V_1)$ and $A_a(V_2)$ values, denoted on Fig. 4.3.1-5a, are shown in Fig. 4.3.1-5b. The fully convex shape of the A - V dependences (see curve 1 in Fig. 4.3.1-5b) was characteristic for these I - V measurements, for which a direct proportionality was found between $A_a(V_1)$ and $A_a(V_2)$ values (*i.e.* where an increase in $A_a(V_2)$ followed an increase in $A_a(V_1)$). The different shaped A - V profiles (see curve 2 in Fig. 4.3.1-5b), corresponded to most asymmetrical I - V characteristics (*i.e.* for which $A_a(V_1)$ reached maximal values).

The important element of the studies on I - V asymmetries was the analysis of the fine structure of these characteristics. The calculations of dI/dV provided very important information in this field. Small peaks were observed at the same voltages for these dI/dV characteristics that corresponded to I - V curves of the same asymmetry and shape. However, it was found that the position on the voltage scale changed with variations in asymmetry and current on I - V curves. The dI/dV characteristics, calculated from two I - V curves (shown in Fig. 4.3.1-6), which slightly varied in shape, were presented in Fig. 4.3.1-7. Small distortions of I - V curves, highlighted in Fig. 4.3.1-6b, could be easily recognised as peaks in the dI/dV characteristics. All the peaks, observed for the more symmetrical curve, were shifted towards higher voltages, as compared to their equivalents in the more asymmetrical characteristic. As this regularity was also found for other I - V curves, the physical phenomenon responsible for this effect can be considered to be independent of bias voltage. This observation strongly suggests that the aforementioned effect was caused by the electron energy losses upon passing the potential barrier of the air gap. Such dissipative tunnelling was studied theoretically by S. Braig and K. Flensberg²²³.

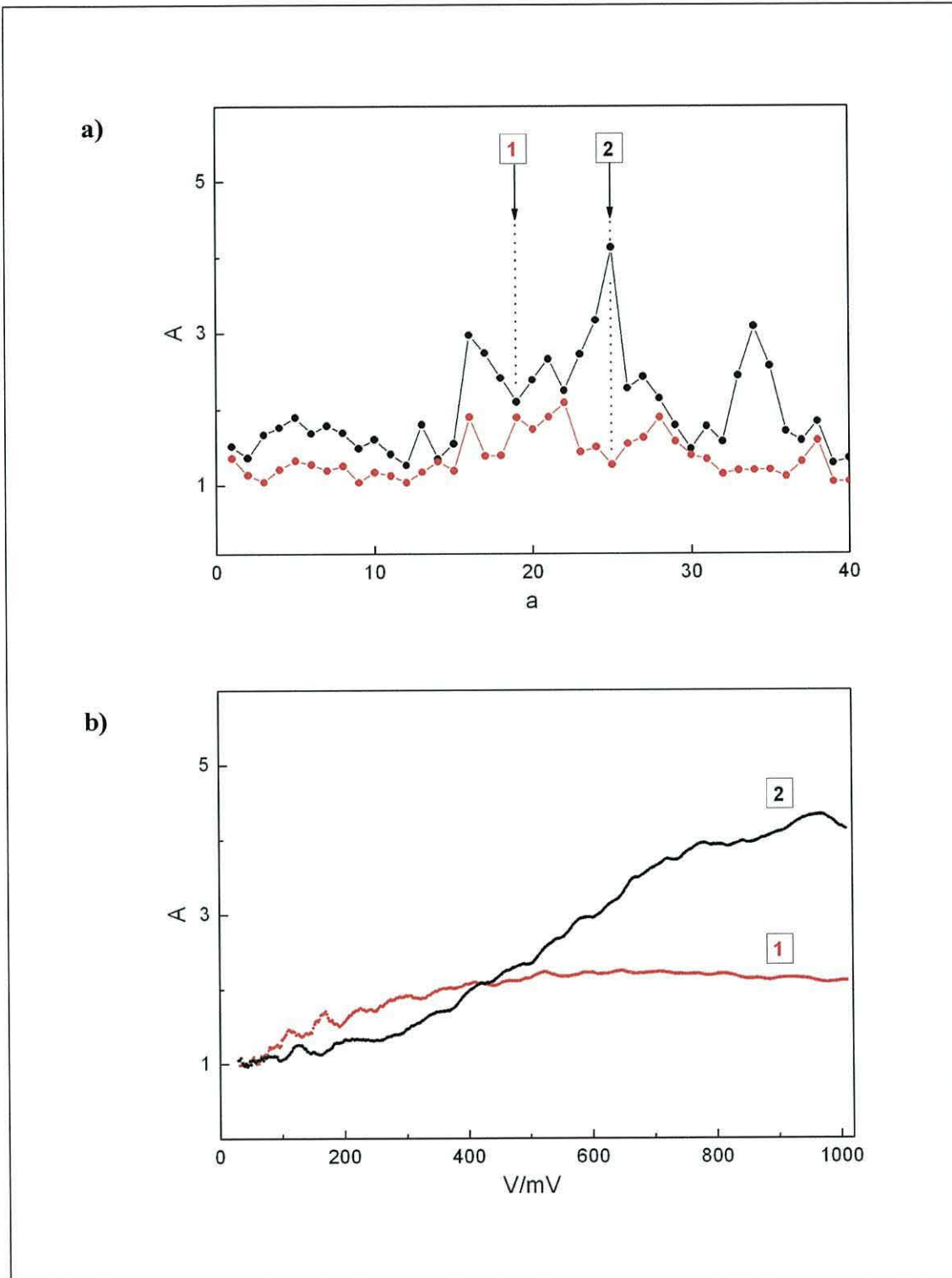


Fig. 4.3.1-5 a) Comparison of 40 typical values of $A_a(V_1)$ – black dots, and $A_a(V_2)$ – red dots $\{a = [1, 2, \dots, 40]\}$;
b) A - V characteristics, corresponding to $A_{22}(V_n)$ and $A_{25}(V_n)$ data point.

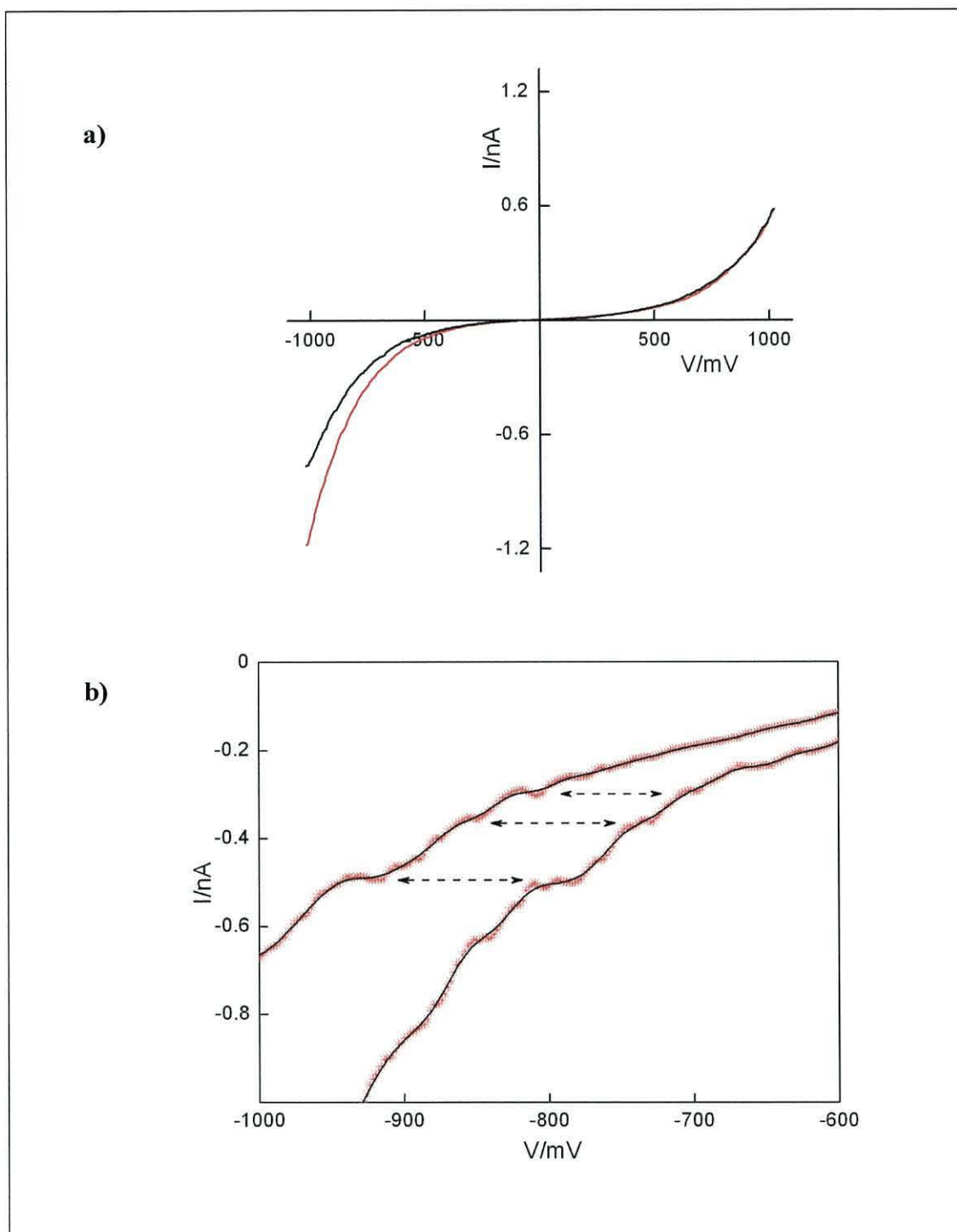


Fig. 4.3.1-6 a) The two I - V curves, which were used for calculation of the dI/dV characteristics, shown in Fig. 4.3.1-7;
b) Small distortions of these I - V curves were distinguished and denoted by dash arrows.

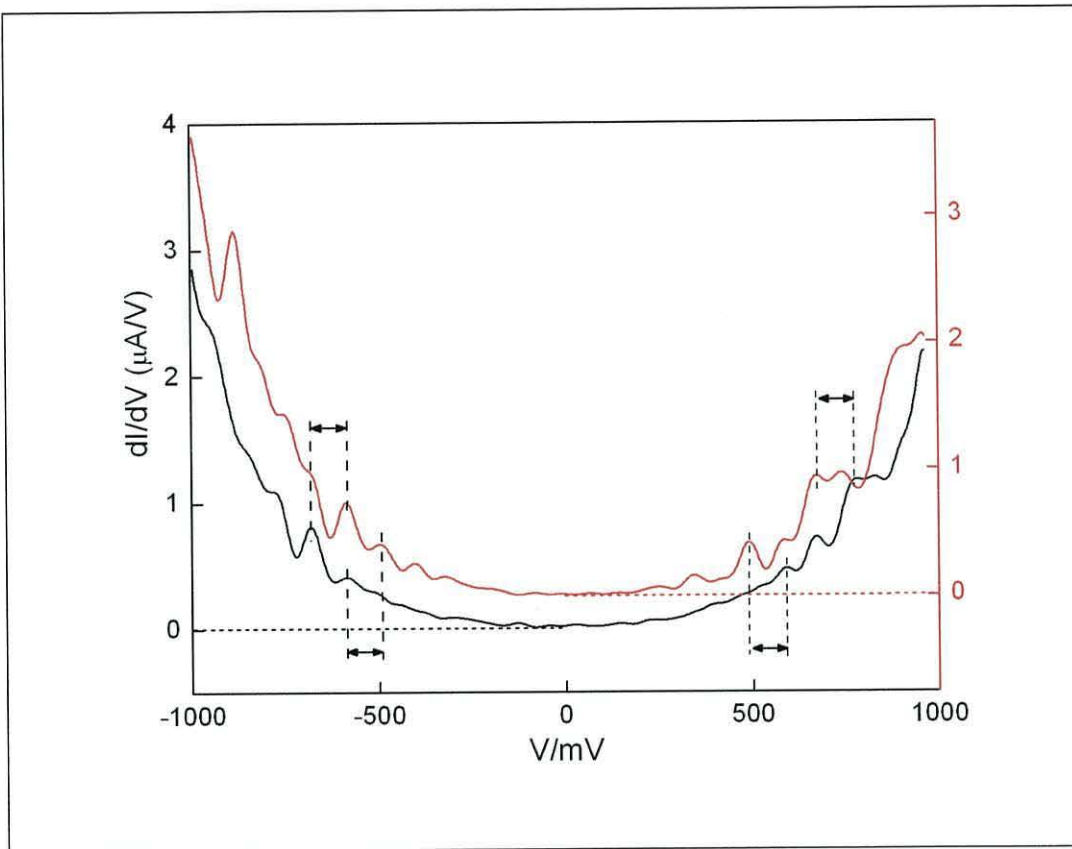


Fig. 4.3.1-7 dI/dV characteristics, calculated from I - V curves, presented in Fig. 4.3.1-6 (black curve corresponds to the more symmetrical I - V dependence); black arrows indicate shifts of the most characteristic peaks.

STS studies for $d(a) = [d_a, \dots, 0]$

Similarly to previous studies, $A_a(V_n)$, for $V_1 = \pm 1024$ mV and $V_2 = \pm 300$ mV were calculated from the registered I - V curves. In this case $a = [1, 2, \dots, 69]$, as this was limited by the time of STM tip drift towards the substrate. Fig. 4.3.1-8 shows the values of $I_a(V_1)$ and $A_a(V_1)$, and Fig. 4.3.1-9 the values of $I_a(V_2)$ and $A_a(V_2)$, presented according to the sequence of I - V characteristic measurements. After deactivating the feedback loop, a slow and continuous increase in current for the whole voltage range was detected (see Fig. 4.3.1-10). The largest current increase was observed for higher values of negative voltage, which caused a rapid growth of $A_a(V_1)$, until it reached $A_{max}(V_1) = 6$ at $a = 24$. Then, $A_a(V_1)$ dropped immediately and fluctuated around values slightly higher than one. No significant increase in $A_a(V_2)$ was observed. However, there was a lower amplitude of fluctuation in asymmetries for $a > 24$, than for other $A_a(V_n)$. This was observed for the whole voltage range. An I - V characteristic, typical for $a > 24$, is shown in Fig. 4.3.1-11a. The shape of this curve is different from the *quasi*-symmetrical characteristics observed for $a < 24$, and also for I - V measurements, for which the feedback loop was used. The reversal in direction of asymmetry at the lowest voltages after reaching $a = 36$ was unusual. This effect could be seen as $A_a(V_2) < 1$ in Fig. 4.3.1-9 and Fig. 4.3.1-10b. There was no clear relation found between $A_a(V_1)$ - $I_a(V_1)$ and $A_a(V_2)$ - $I_a(V_2)$ dependences. The only ordered behaviour of data points was observed for $A_a(V_2)$ - $I_a(V_2)$ dependence, for $a < 38$ and $a > 59$.

Another interesting I - V curve was observed at $a = 69$, directly before the STM tip contacted the surface of the gold substrate (see Fig. 4.3.1-11b). The S-shape characteristic, similar to that shown in Fig. 4.3.1-11a, was registered for: $|V| < 380$ mV. At $V_B \approx \pm 380$ mV, conductivity reached the value of $g_0 \equiv dI/dV \approx (12.9 \text{ k}\Omega)^{-1}$, distinctive for ballistic electron transport. Then, it dropped rapidly, and for higher voltages remained below $(12.9 \text{ k}\Omega)^{-1}$, oscillating around $g \approx (27 \text{ k}\Omega)^{-1}$ for $|V| > 420$ mV. Similar relations were observed for both: forward scan ($+1024 \text{ mV} \rightarrow -1024 \text{ mV}$), and reverse scan ($-1024 \text{ mV} \rightarrow +1024 \text{ mV}$), which means that this effect was observed at $d = \text{const}$.

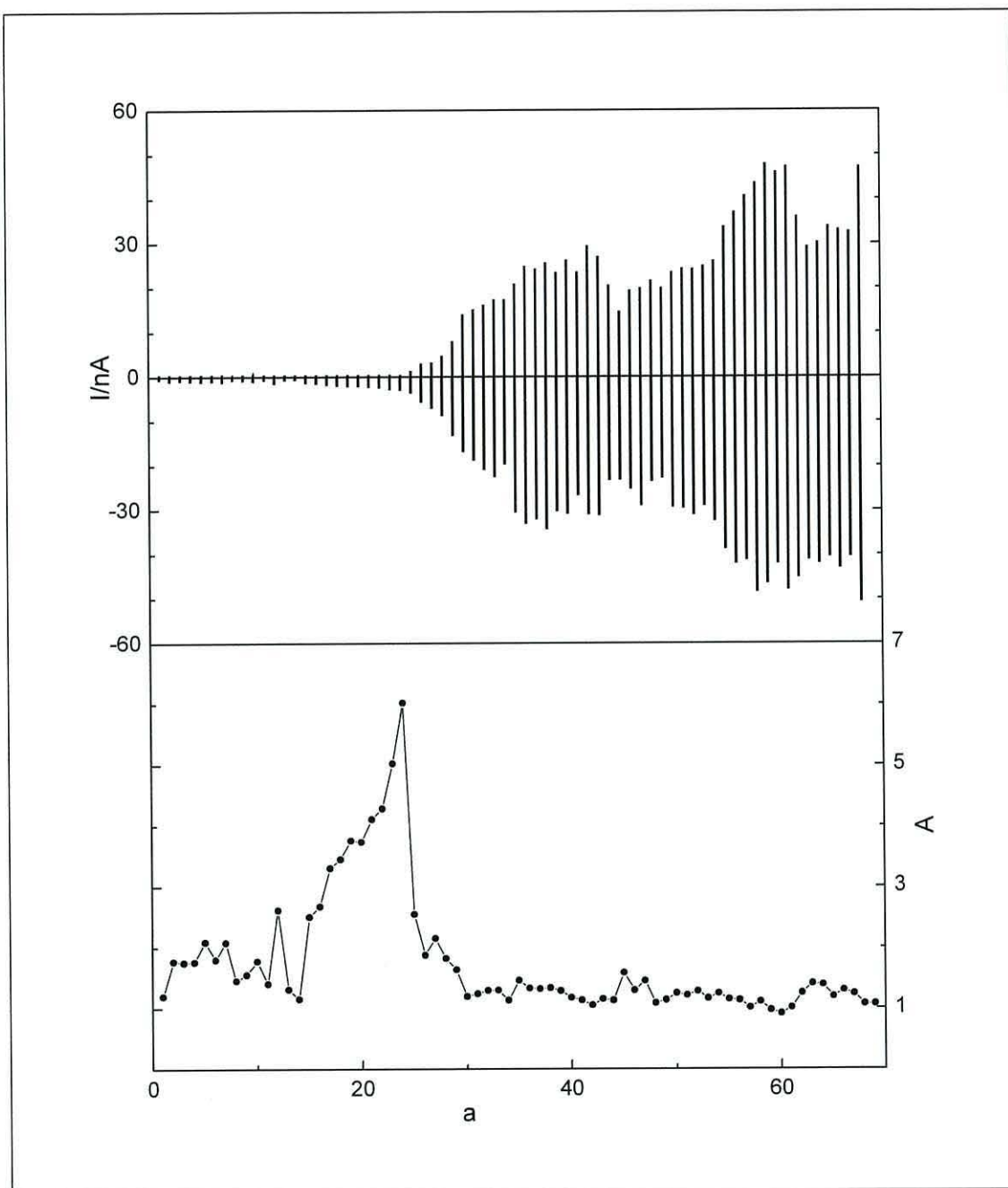


Fig. 4.3.1-8 The values of $I_a(V_1)$, for $V_1 = \pm 1024$ mV and $a = [1, 2, \dots, 69]$, obtained during slow drift of the STM tip towards substrate, after deactivating feedback loop (top plot), and $A_a(V_1)$, calculated from $I_a(V_1)$ values of the top plot (bottom plot); the original sequence of measurements (X-axis) was maintained.

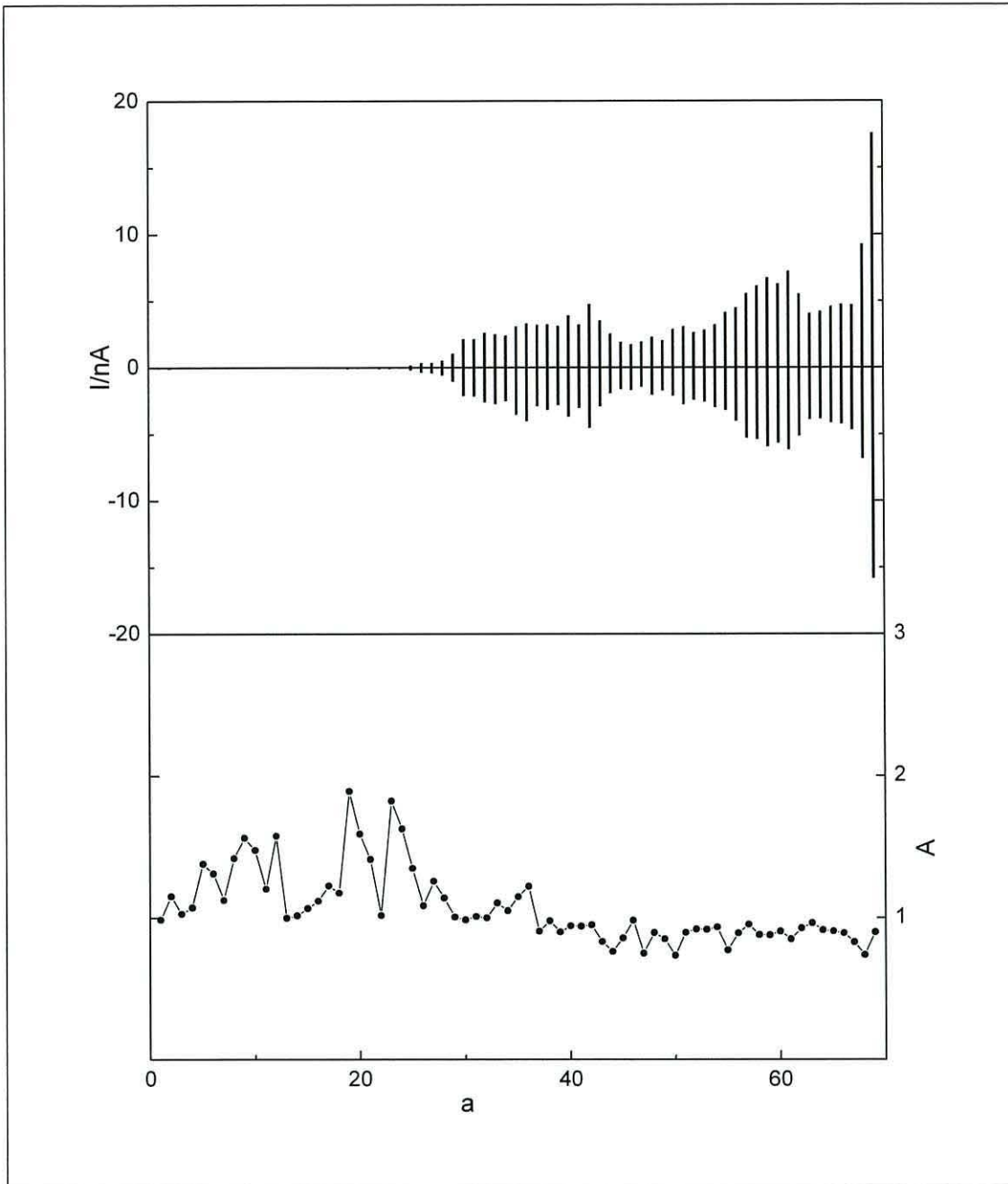


Fig. 4.3.1-9 The values of $I_a(V_2)$, for $V_2 = \pm 300$ mV and $a = [1, 2, \dots, 69]$, obtained during slow drift of the STM tip towards substrate, after deactivating feedback loop (top plot), and $A_a(V_2)$, calculated from $I_a(V_2)$ values of the top plot (bottom plot); the original sequence of measurements (X-axis) was maintained.

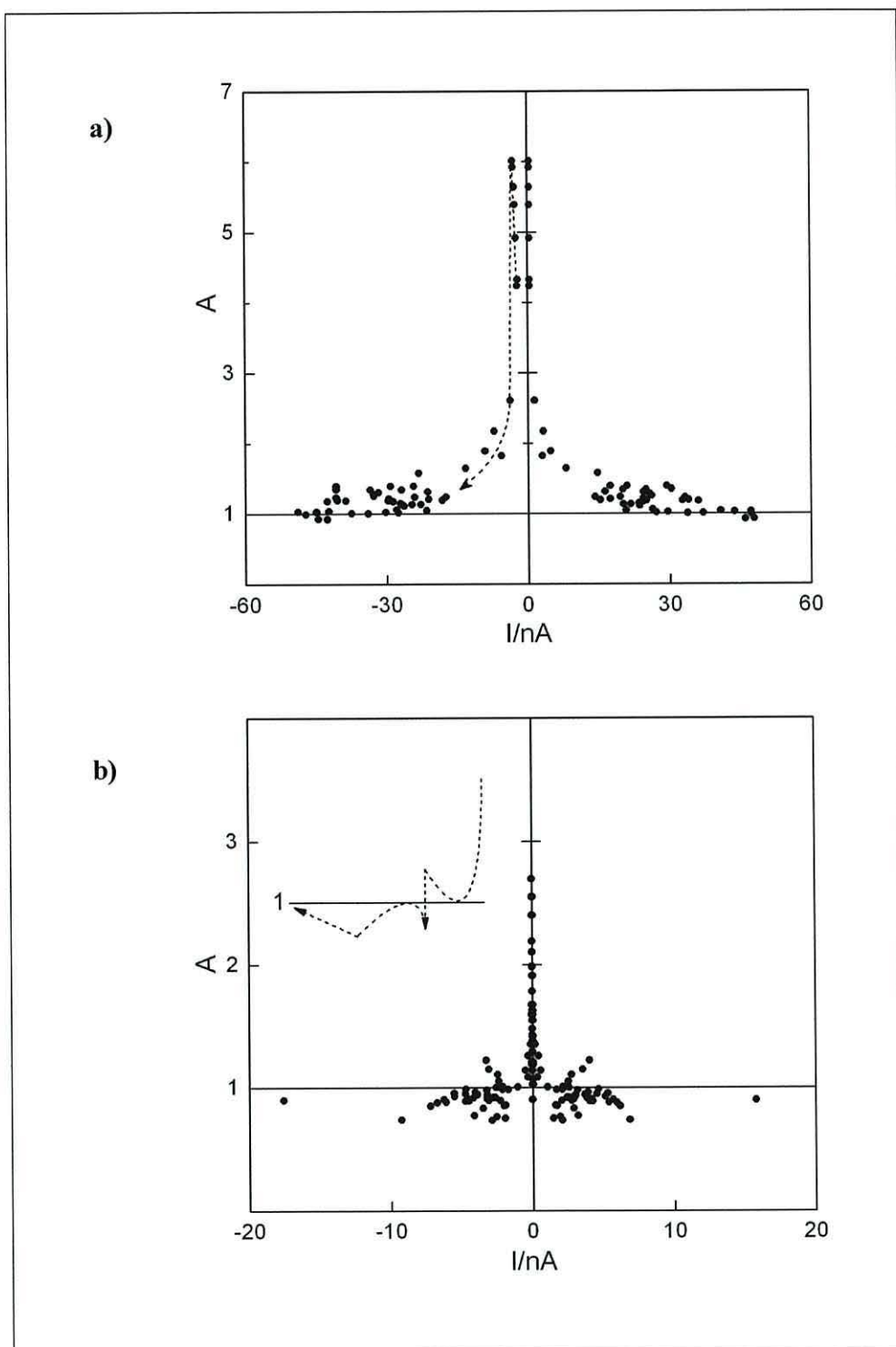


Fig. 4.3.1-10 The comparison of $A_a(V_n)-I_a(V_n)$ characteristics for (a) V_1 and (b) V_2 ; dash arrows represent the general trend, describing the sequence of measurements.

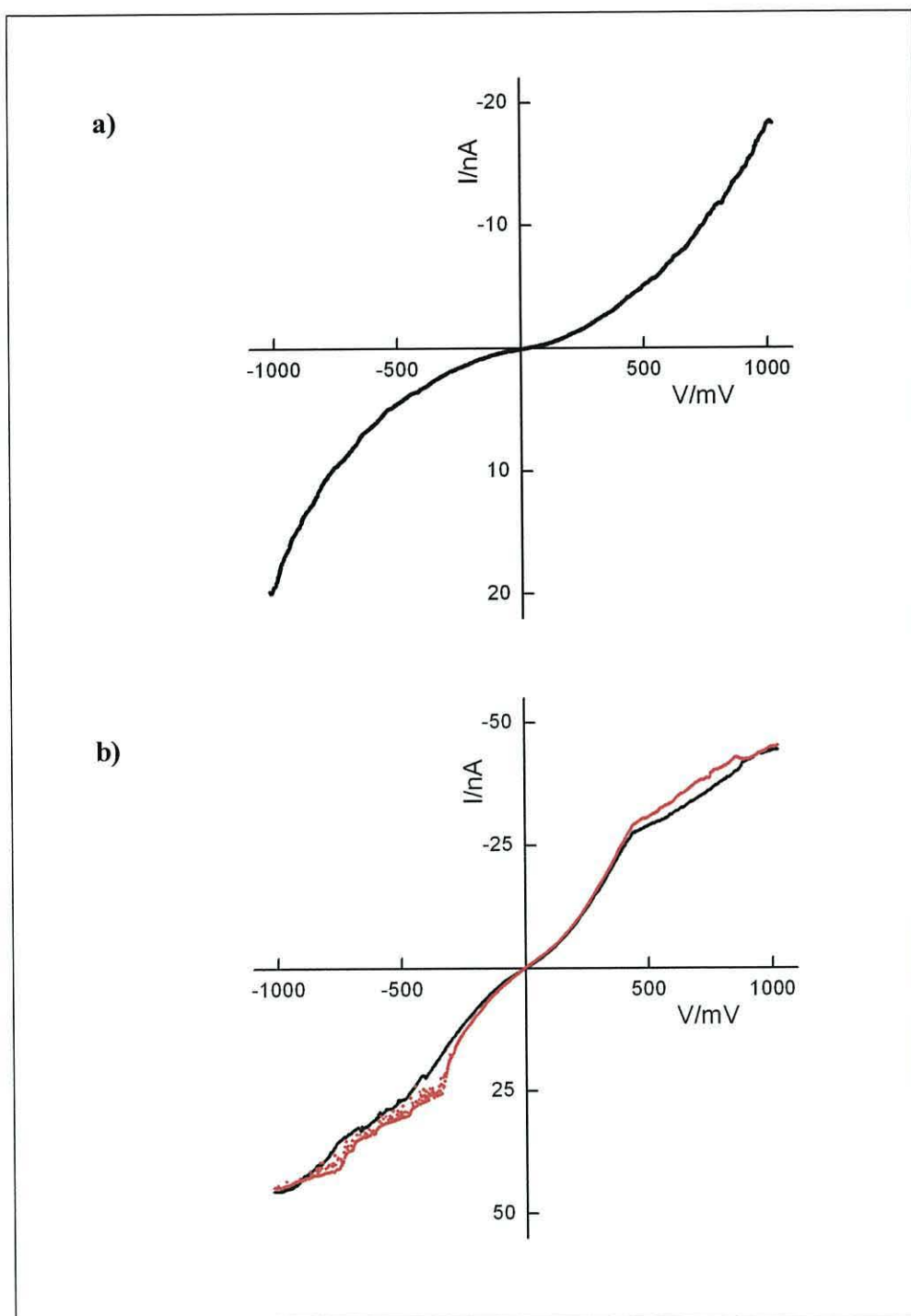


Fig. 4.3.1-11 $I-V$ characteristics observed for: (a) $a = 50$ and (b) $a = 69$; forward scan ($+1024$ mV \rightarrow -1024 mV) is represented by a black line, and reverse (-1024 mV \rightarrow $+1024$ mV) by a red line.

The results presented so far in this section, provide strong proof that the atomically sharp STM tip, which previously probed the molecular layer of AT1, penetrated this layer and contacted the gold substrate. The point at which $a = 24$ can be identified as the moment at which an AT1 aldehyde terminal group and the tip were in closest proximity. The arguments for this conclusion are:

- 1) significant increase in current at $a = 24$;
- 2) the maximum value of asymmetry achieved for $a = 24$, which was most probably caused by the lower energy dissipation by coupling with the environment during electron tunnelling through the potential barrier of the air gap;
- 3) abrupt drop in $A_a(V_1)$ at $a = 25$, and stabilising of this parameter at values close to unity for $a = [30, 31, \dots 69]$;
- 4) the permanent reverse in the direction of low-voltage asymmetry at $a = 36$; the origin of this phenomenon remains unknown, however this behaviour was not observed for the tip position above the molecular level of the sample.

The atomic sharpness of the STM tip was confirmed when direct imaging of the monolayer was successfully performed. And secondly, when the conductance characteristic for a single-point contact was measured, just before the tip hit the gold substrate.

Due to the arguments presented above, the analysis of the I - V characteristics at $a = [1, 2, \dots 24]$ was crucial for further studies on molecular rectification. Fig. 4.3.1-12 shows the A - V profile changes, calculated from I - V curves, taken for $a = [5, 18, 22, 24]$. The A - V characteristic for $a = 5$ was similar to curve 2 from Fig. 4.3.1-5. Here, asymmetry was close to unity for $V < 500$ mV, and was increasing continuously for higher V , and finally stabilised at a value slightly higher than 2 for $V > 850$ mV. As the tip approached the molecule, the asymmetry for $V < 800$ mV started to increase consistently. The increase in A with decreasing d was less regular for $V > 850$ mV.

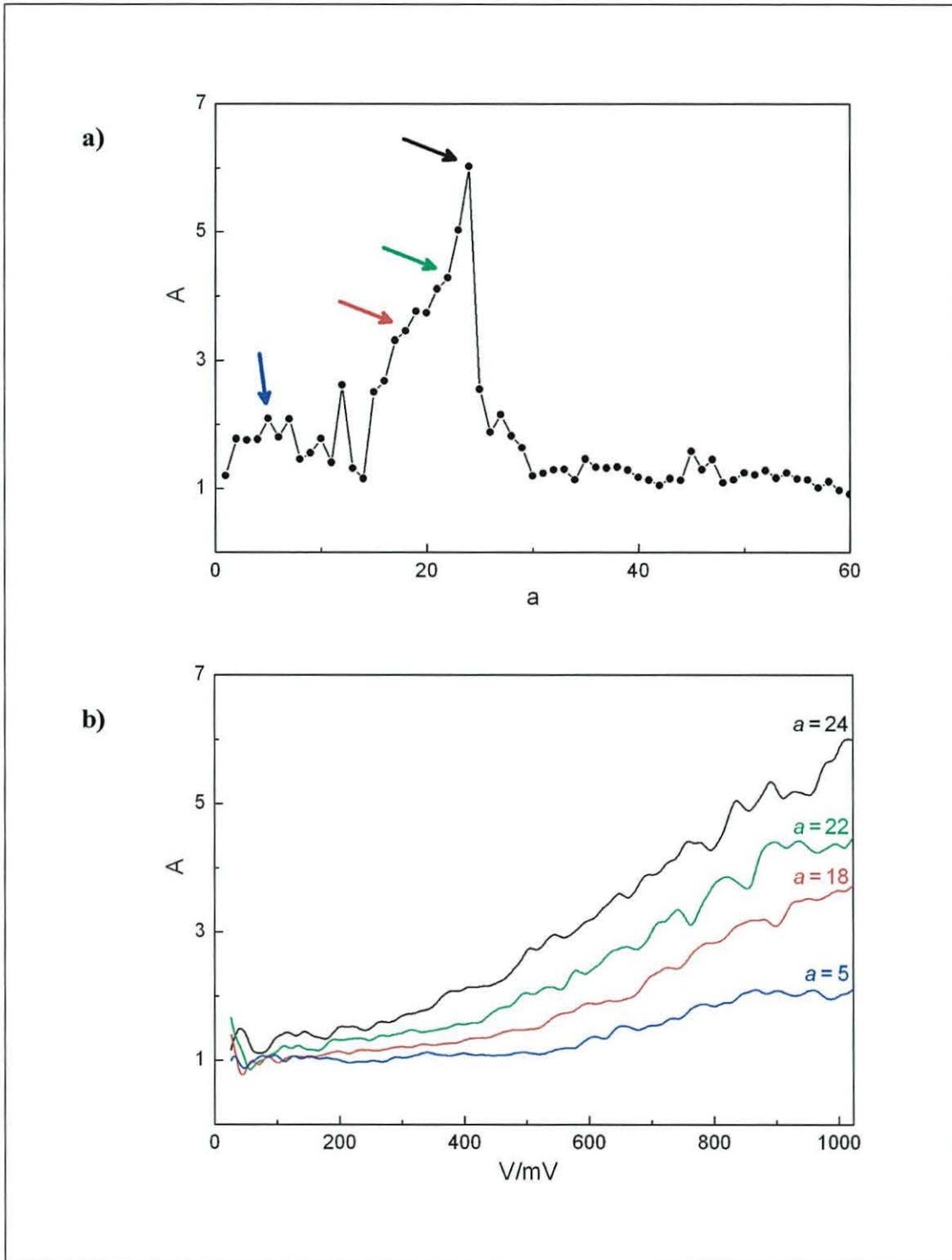


Fig. 4.3.1-12 The values of $A_a(V_1)$ (a) for $a = [1, 2, \dots, 40]$, with indicated data points: $a = [5, 18, 22, 24]$, for which A - V profiles (b) were calculated.

The fine structure of the presented A - V profiles should be noted, as distortions of these curves change their positions in an organised manner, similar to that observed for dI/dV . When d increased, the A - V curves became shifted by a constant factor towards lower voltages. This effect is distinctive for I - V curves, with $A_{max} > 2.5$, for $V > 400$ mV, where strong variations in A were observed.

Analysis of the conductivity changes vs. voltage for these curves showed the same regularities, as observed for A - V profiles. It also confirmed the previous assumptions, made after studying dI/dV for I - V measurements upon $\langle d(a) \rangle = \text{constant}$ conditions. Fig. 4.3.1-13 shows the three dI/dV characteristics, corresponding to the measurements performed at $a = [12, 17, 22]$. A consequent shift of the most distinctive peak towards lower voltages in accordance with the decrease in d was significant. These shifts were measured, as shown in Fig. 4.3.1-13, and used for scaling I - V characteristics: $a = 12$ and $a = 17$ along X-axis, in order to confirm that the shape of the scaled curves matched the reference curve: $a = 22$. As shown in Fig. 4.3.1-14, this procedure gave very good results, and scaled curves: $a = 12$ and $a = 17$ exactly overlaid the original curve: $a = 22$.

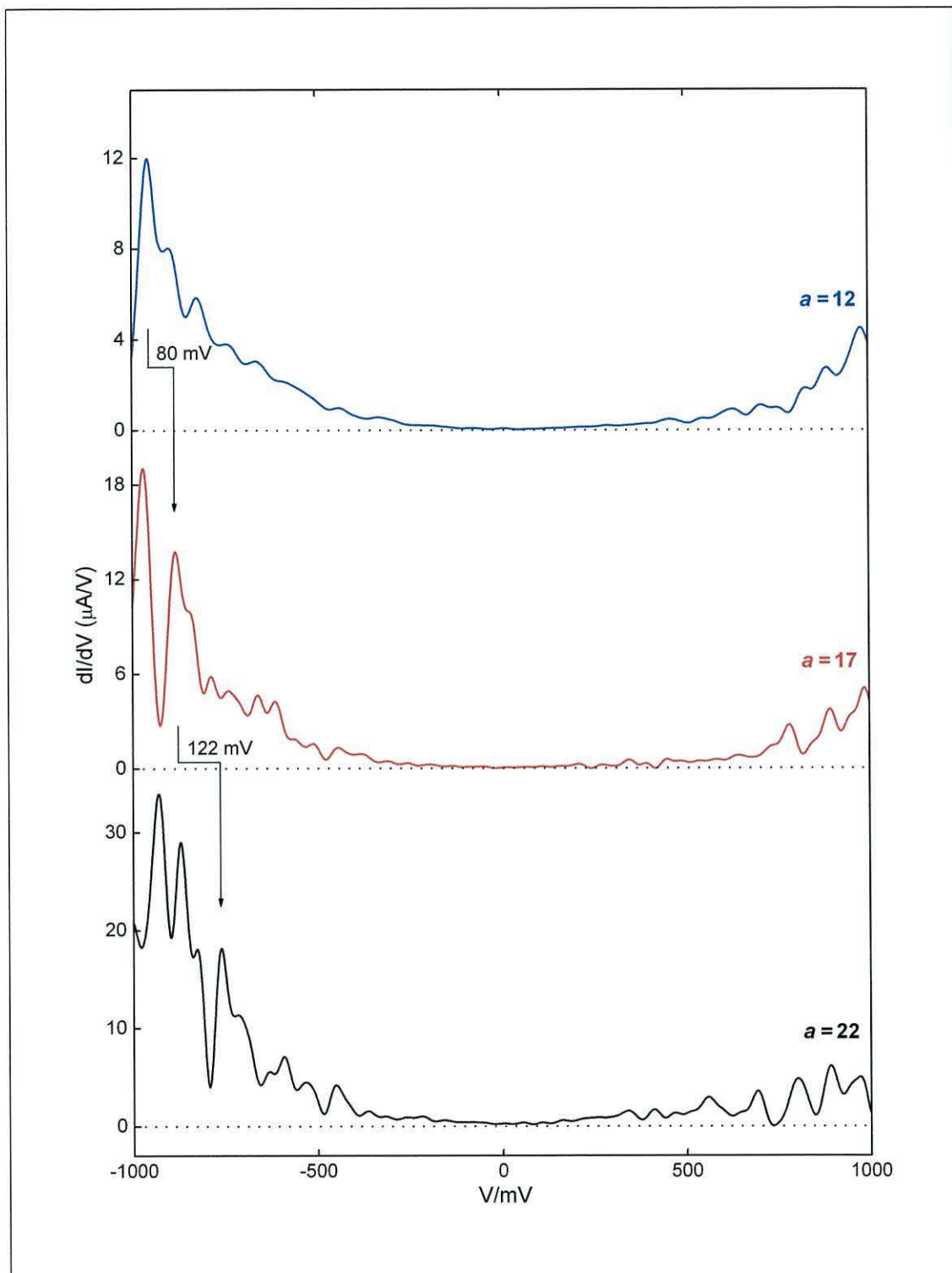


Fig. 4.3.1-13 dI/dV characteristics for $a = [12, 17, 22]$; the position of the most characteristic double peak was monitored (see arrows).

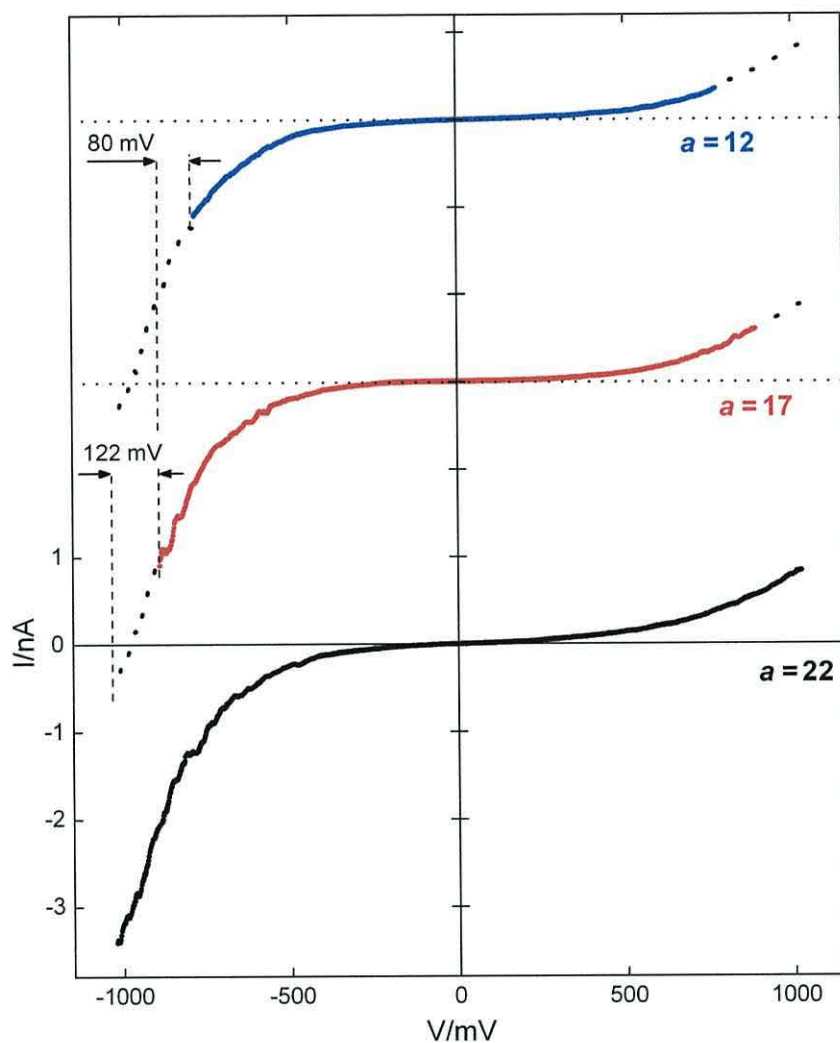


Fig. 4.3.1-14 The three I - V curves registered for $a = 22$ (black solid curve, and dot curves above), $a = 17$ (red solid curve), and $a = 12$ (blue solid curve); the last two were scaled along the voltage scale, according to the shift in peaks of corresponding dI/dV characteristics shown in Fig. 4.3.1-13.

Discussion

The presented analysis has proven that observation of current transmission asymmetry strongly depends on the thickness of the potential barrier between the medium (which demonstrates rectifying properties) and the probing electrode (STM tip). Thus, optimal rectifying features of molecules should only be measured when the gap between tip and molecule is minimal. Increasing this distance always causes attenuation of the real molecular effect, which can be observed by comparing dI/dV and A - V characteristics, calculated from I - V measurements at different d .

These studies also provide evidence that more than one process determines I - V curves asymmetry in the voltage range: $|V| < 1$ V, which is distinctive when comparing $A_a(V_n)$ - $I_a(V_n)$ characteristics for different V_n . Local electronic features of the probed molecules must be involved in the asymmetry changes, as for the same tunnelling current and voltage, different $A_a(V_n)$ could have been observed. Recently, A. Riposan and G. Liu²²⁴ also demonstrated that similar rules apply to STM imaging, providing complex studies of LDOS and tip – termini separation dependence on topography images using STM. They observed systematic, reversible, and reproducible contrast transitions with bias and current variations. It was concluded that these contrast transitions were caused by probing the corresponding LDOS upon variation of the tunneling conditions, and not by the reorientation of the molecules during scanning.

A simplified picture, neglecting the fine character of LDOS distribution, which partially explains current asymmetry in AT systems, was presented by J. Rosink *et al.*²²⁵. Their model considered an AT molecule acting as a potential barrier to electron transmission without resonances at least up to 1.5 V bias. Thus, electrons tunnelled at energies in the gap between orbitals: HOMO and LUMO. In such a case, the shape of the barrier is the only determinant of the total current and its asymmetry, when any differences in molecule – electrode coupling are neglected. This shape was strongly affected by differences in energy of the HOMO, the LUMO, their localisation on the molecule, and Fermi levels of the substrate and the tip. These factors cause the asymmetry of the AT1 molecular barrier, whose model shape was approximately trapezoidal. The asymmetry can be estimated by measuring the dipole moment of the molecule and the tunnelling current.

On the other hand, the consideration that tunnelling electrons are a significant distance away from resonance with any molecular orbital, does not explain the existence of sharp, well-defined peaks in the dI/dV characteristics. These were observed consistently at negative voltages above 750 mV. The smaller peaks at lower voltage could be associated with vibrational modes of the molecules^{173,226-229}. However, organic molecules do not absorb energy above 0.4 eV so intensively and selectively, in order to affect the electronic transmission as observed in dI/dV characteristics. Another effect, the origin of which is not clear, is the shape of the $I-V$ curves. The stepwise character of the angle of inclination changes along the voltage scale was particularly difficult to explain on the basis of the presented theories. There are also significant distortions in the linear character of these studies above 750 mV, unusual for off-resonant electronic transmissions. Considering these two observations, the electronic transmission through AT systems should be assumed to be affected by the LDOS of at least one of the molecular orbitals, under an applied bias $V > 750$ mV.

A more precise description, including calculations in the LDOS of the HOMO and the LUMO of AT1 and other AT systems, was provided by A.I. Onipko *et al.*²³⁰. They found that, depending on which molecular atom was probed by the STM tip, the current response to the positive and negative tip – sample bias should be substantially different. Both electronic coupling of the gold atoms of the tip apex with different molecular atoms and the LDOS distribution of the molecule were included in the analysis. They also considered the electronic structure of the STM tip. However, in this case, any asymmetry due to the tip sharpness could be ruled out since it would have resulted in a stronger electric field at the tip and enhanced transmission from the tip to the sample. This is in opposition to the trend found here. Any mechanically tip-induced effects, which could have caused dynamic molecular geometry changes affecting electronic structure, were also neglected, as they should be accompanied by significant current variations alternately in both directions. Thus, the most probable reasons for the current asymmetry variations are: lateral drift of the tip through different LDOS of a molecular layer, and the aforementioned alternate changes of the tip – sample separation. The chance of asymmetry arising from the second effect increased with strengthened molecule – tip electronic coupling as the distance between them decreased.

4.3.2 Rectifying behaviour of functionalised SAMs

The studies on the rectifying properties of AT systems were performed in order to validate the influence of HOMO and LUMO electronic states on the transmission of current under external bias voltage in the range of $-1\text{ V} < V < +1\text{ V}$. Localisation of electron-accepting and electron-donating molecular components, separated by the imino linking groups of the AT backbone structure, and the geometry of these systems were considered as having a major influence on the rectification. Measurements and data analysis were performed according to the information gained during the statistical studies of AT1 I - V characteristics asymmetry, described in Section 4.3.1.

Analogous to AT1, the I - V curves observed for AT2 and AT3 were slightly asymmetrical, with higher current transmission from substrate to STM tip (the negative quadrant of the I - V characteristics). The maximum asymmetries at $\pm 1\text{ V}$, typically observed for the minimal tip – molecule separation, detected for AT2 and AT3 were: $A_{\max} \approx 4$. The shape of the I - V curves, for which A_{\max} were observed, was also very similar for all three systems. Elongating AT1, AT2 and AT3 by the strongly electron-accepting M9 units caused inversion of the asymmetry. The A_{\max} values at $\pm 1\text{ V}$ were different for each system. The lowest values were observed for AT2-A: $A_{\max} \approx 7$, and AT3-A: $A_{\max} \approx 4.5$ (see Fig. 4.3.2-2). The highest values were commonly registered for AT1-A: $A_{\max} \approx 11$ (see the top plot in Fig. 4.3.2-3), and this system was further extended by the M7 unit to form AT1-AD. As a consequence of introducing the strongly donating M7 components the asymmetry was reversed again and $A_{\max} \approx 10.5$ was detected (see the bottom plot in Fig. 4.3.2-3).

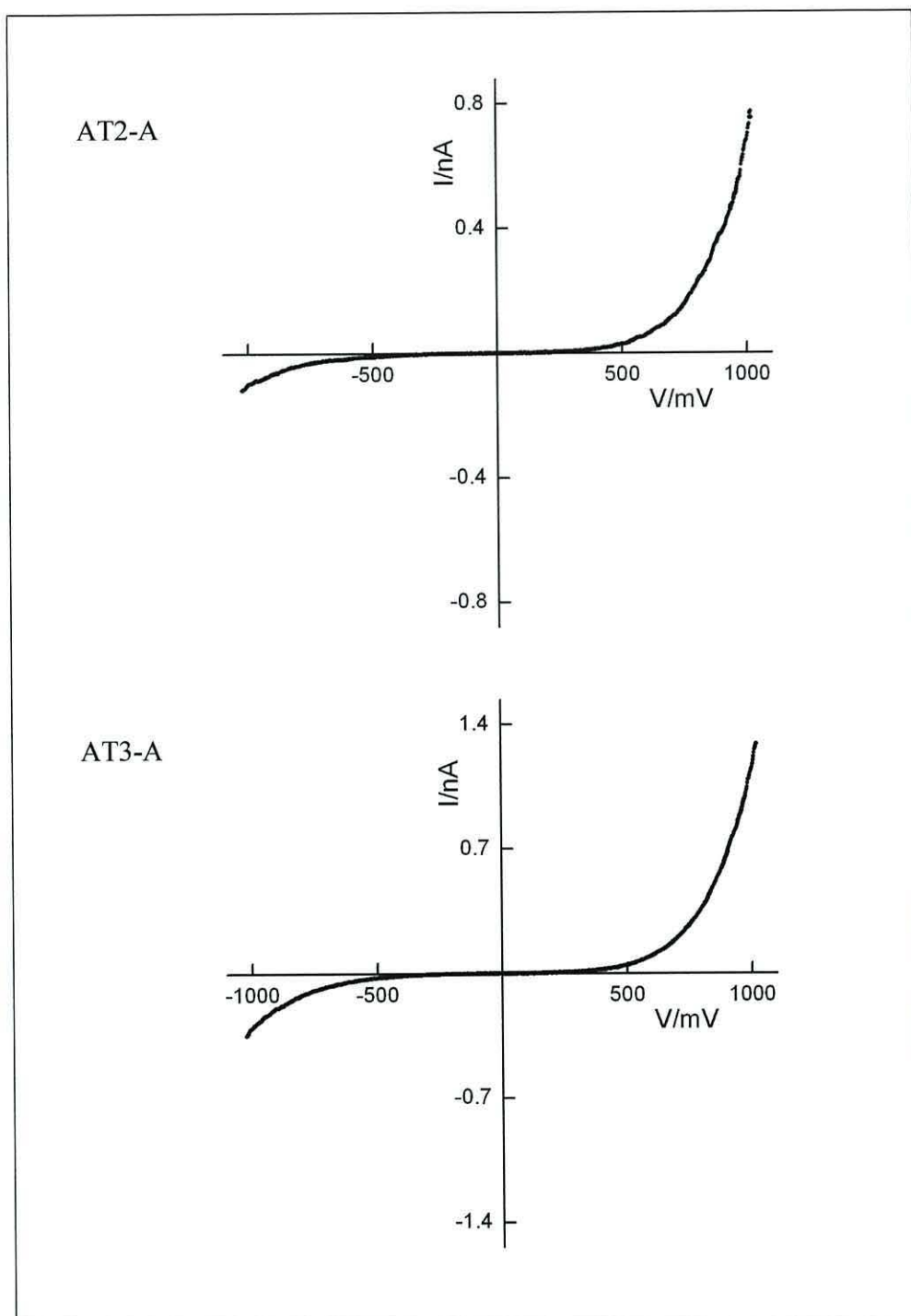


Fig. 4.3.2-2 *I-V* characteristics of AT2-A and AT3-A, registered for the minimum tip – molecule separation.

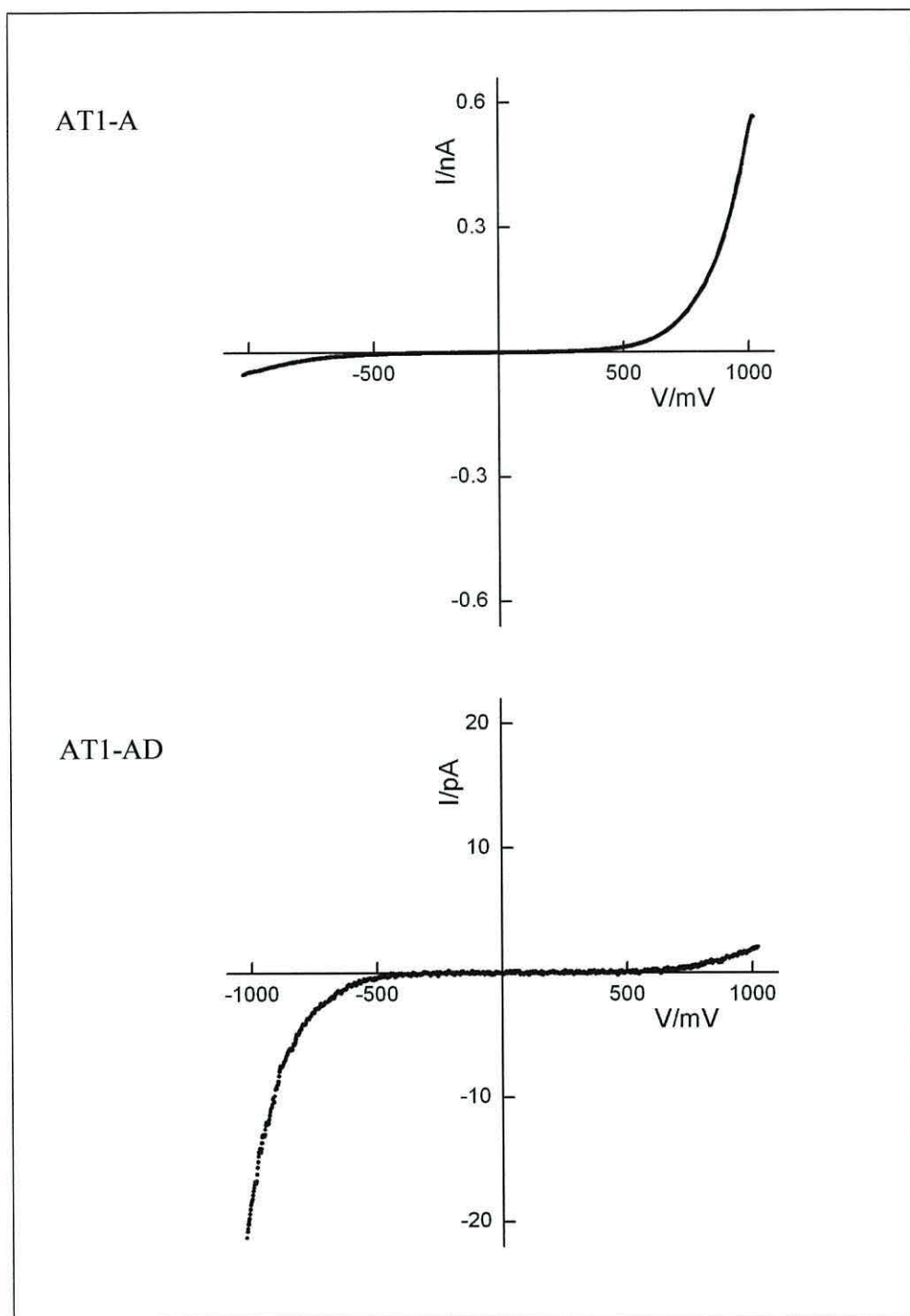


Fig. 4.3.2-3 I - V characteristics of AT1-A and AT1-AD, registered for the minimum tip – molecule separation.

The weakly rectifying behaviour of these systems can be explained by considering that the LDOS of the HOMO and the LUMO states of the molecules affect the electronic transmission. Thus, the electron-donating and the electron-accepting components, separated by the imino π -bridges, which twist the backbone molecular structure slightly, cause some permanent polarisation of the systems. Even if the molecular orbitals do not participate in the electronic transmission directly, the shape of the potential barrier for tunnelling electrons is highly unsymmetrical, and facilitates current flow in the direction of the permanent molecular dipole moment. This effect was extensively studied by Dhirani *et al.*²³¹. The profile of such barriers depends mainly on energy levels of the frontier molecular orbitals and intermediate bridging states, their localisation on the molecules, and also on the geometries of the molecules. The molecular geometry affects overlapping of the molecular orbitals, which reduces or increases isolation of the functional molecular elements.

The HOMO and LUMO of the isolated AT1-A and AT1-AD systems, calculated using the AM1 method, the localisation of which explains the rectifying properties of these molecules, are shown in Fig. 4.3.2-4. The LUMO of AT1-A is situated on the M9 unit, as the central part of this component is a strong electron acceptor. The HOMO was found to be localised on the thiophenyl ring. Thus, the polarisation of the AT1-A system should be towards the substrate, as the gold surface is electron-donating relative to the molecular thiolate groups (see Section 2.1.2), and is expected to increase the total dipole moment of this system. This analysis agrees with the reported STS results for AT1-A, AT2-A and AT3-A, which can be generally treated as $\text{Au} | \text{Au}-(\text{D})-\pi-(\text{A})$ systems.

In the case of AT1-AD, the LUMO is also situated on the M9 unit, and was almost the same shape as the LUMO of AT1-A. However, the HOMO of the isolated AT1-AD system was on the M7 component. The location of this strongly electron-donating element inversed the permanent polarisation, relative to that observed for AT1-A. The thiolate bonding probably attenuated the total dipole moment of AT1-AD. However, its predicted direction remain unchanged, as the I - V characteristic of this system revealed the highest current in the negative quadrant. Thus, the electronic structure of this system can be described as $\text{Au} | \text{Au}-\pi-(\text{A})-\pi-(\text{D})$.

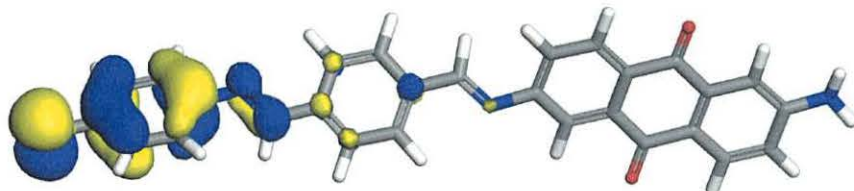
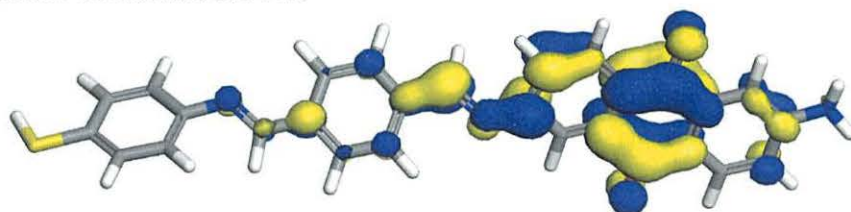
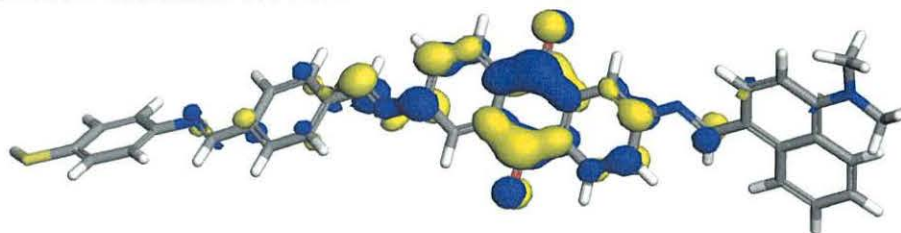
HOMO of isolated AT1-A**LUMO** of isolated AT1-A**HOMO** of isolated AT1-AD**LUMO** of isolated AT1-AD

Fig. 4.3.2-4 Molecular orbitals: HOMO and LUMO of isolated AT1-A and AT1-AD, calculated using semiempirical AM1 method.

The twist along the imino components (linking electron-donating and electron-accepting units) was confirmed to be sufficient to maintain the separation of HOMO and LUMO states. As shown in Fig. 4.3.2-4, the resolved frontier molecular orbitals are not strongly delocalised along the studied molecules. Calculated torsion angles between aromatic rings of the electron-donating and the electron-accepting units were 34° and 31° for AT1-A and AT1-AD respectively. An increase of the twist along imino π -spacers should cause a decrease of the effective overlapping between the π -orbitals of donating and accepting units. The correlation between these angles and the rectification ratio was observed by Ashwell *et al.*²⁰² for other systems, described as $\text{Au} | \text{Au}-\sigma-(\text{A})-\pi-(\text{D})$. Moreover, $\text{Au} | \text{Au}-\sigma-(\text{A})-\pi-(\text{D})$ systems, for which the AM1 resolved twist along the π -spacer was 31° , revealed rectification ratios of 11 – 18 at $\pm 1\text{V}$ ^{202,220}. These values are very similar to the maximum rectification detected for AT1-AD, with the same twist along the π -spacer. Slightly stronger rectifying behaviour was found for similar systems, containing the same $(\text{A})-\pi-(\text{D})$ segments as AT1-AD in which the π -spacer between Au and the acceptor was replaced by the short σ -spacer²³². This was probably due to the lack of the electron-donating thiophenyl part of AT1-AD, which attenuated the electron-donating features of the opposite segment of this molecule.

Much stronger rectifying properties were obtained for a more extended molecular wire: AT2-L (see Fig. 4.3.2-5). Due to a combination of two electron-donating components on the substrate side of the molecular system, and two electron-accepting units on the opposite side, which led to the $\text{Au} | \text{Au}-(\text{D})-\pi-(\text{D})-\pi-(\text{A})-\pi-(\text{A})$ system, an A_{max} value of *ca.* 44 was achieved. Comparison of this system with AT2-A shows that the rectification could be improved over 6 times by inserting the M6 strong electron donor between the thiolate donating part of AT2-A and the first accepting M9 unit, and also another acceptor, M4, at the end of the system. The presence of M3 and M5 spacers might also contribute to the final value of the current asymmetry by increasing the effective barrier between the outer donating and accepting components.

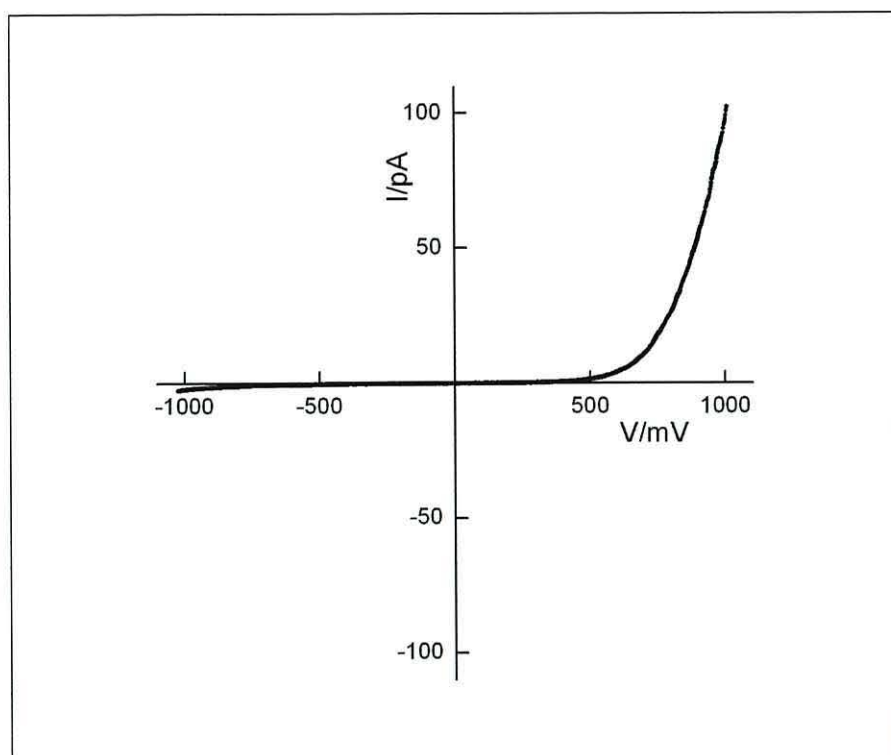


Fig. 4.3.2-5 *I-V* characteristic of AT2-L, registered for the minimum tip – molecule separation.

4.3.3 Electron transport through two-terminal AT molecular wires

Two techniques were used in order to characterise electrical properties and determine the off-resonance conductivity of the symmetrical AT2-A-AT2 molecular wire. The first method involved the prefabricated Si-DEV, described in Section 3.6, for determining the general shape of *I-V* characteristics for a dense arrangement of these molecules, both ends of which were contacted to gold electrodes. The second experiment used the STM-STS technique to scan a mono-thiolate version of AT2-A-AT2, which was spontaneously bound to the STM tip, and to measure the current transmission through the separate molecular systems. Results of two these experiments were compared with theoretical calculations of the conductivity through AT2-A-AT2, performed by Dr Christopher M. Finch and Dr Ian R. Grace of the Lancaster University (UK).

Prior to the characterisation of the AT2-A-AT2 system, the tunnelling current between gold electrodes of an empty Si-DEV was measured. Contrary to expectations, the I - V characteristics of the empty Si-DEV were unsymmetrical (see Fig. 4.3.3-1a). The origin of this effect remains unknown. However, a possible difference in the roughness of top and bottom electrodes could have been a reason for the different electronic work functions of these electrodes. As the gap between the electrodes was estimated to be *ca.* 3.6 nm, such a difference seemed to have a major influence on asymmetric features of the tunnelling process. Deposition of M11 molecules, simultaneously on the top and bottom electrodes (AT2-g-AT2 systems), caused an increase in current of more than 40 times, but the shape of the I - V curves mimicked that of the empty Si-DEV (see Fig. 4.3.3-1b).

I - V characteristics of the AT2-A-AT2 arrangement inside Si-DEV demonstrated an increase in current of three orders of magnitude compared to AT2-g-AT2; their shape was perfectly symmetrical (see the top plot of Fig. 4.3.3-2). Symmetrical I - V curves were also commonly observed during STS scans of a mono-thiolate version of this system, formed on a planar gold substrate using a three-step synthetic process. When the scans were performed under low-resistance conditions (current set-point of 0.5 nA at 10 mV) the tip occasionally contacted separate molecules, presumably forming temporal tip – thiolate bondings. This was detected as abrupt increases in current. A typical I - V curve, observed when the two-terminal AT2-A-AT2 system was formed during the STS experiment, is shown in the bottom plot of Fig. 4.3.3-2. The shape of this curve exactly matches the characteristic observed for AT2-A-AT2 inside Si-DEV.

The spontaneous thiolate bonding formation between the tip and AT2-A-AT2 was studied in detail *via* I - t STS measurements at $V = +300$ mV. This bias was commonly used by other authors^{196,233} to obtain comparative values of I , which characterise the off-resonant current transmission through single molecules. An example of one of most commonly observed current jumps, indicating a single adsorption – desorption act, is shown in Fig. 4.3.3-3a. The duration of such an event was typically 20 – 80 ms and caused an average current increase of 0.55 ± 0.05 nA. Very few current jumps that could be related to simultaneous multiple adsorptions were detected, which suggests a loosely packed arrangement of at least the outer thiol-terminated component, attached during the last step of *in-situ* reaction (see Fig. 4.3.3-3b).

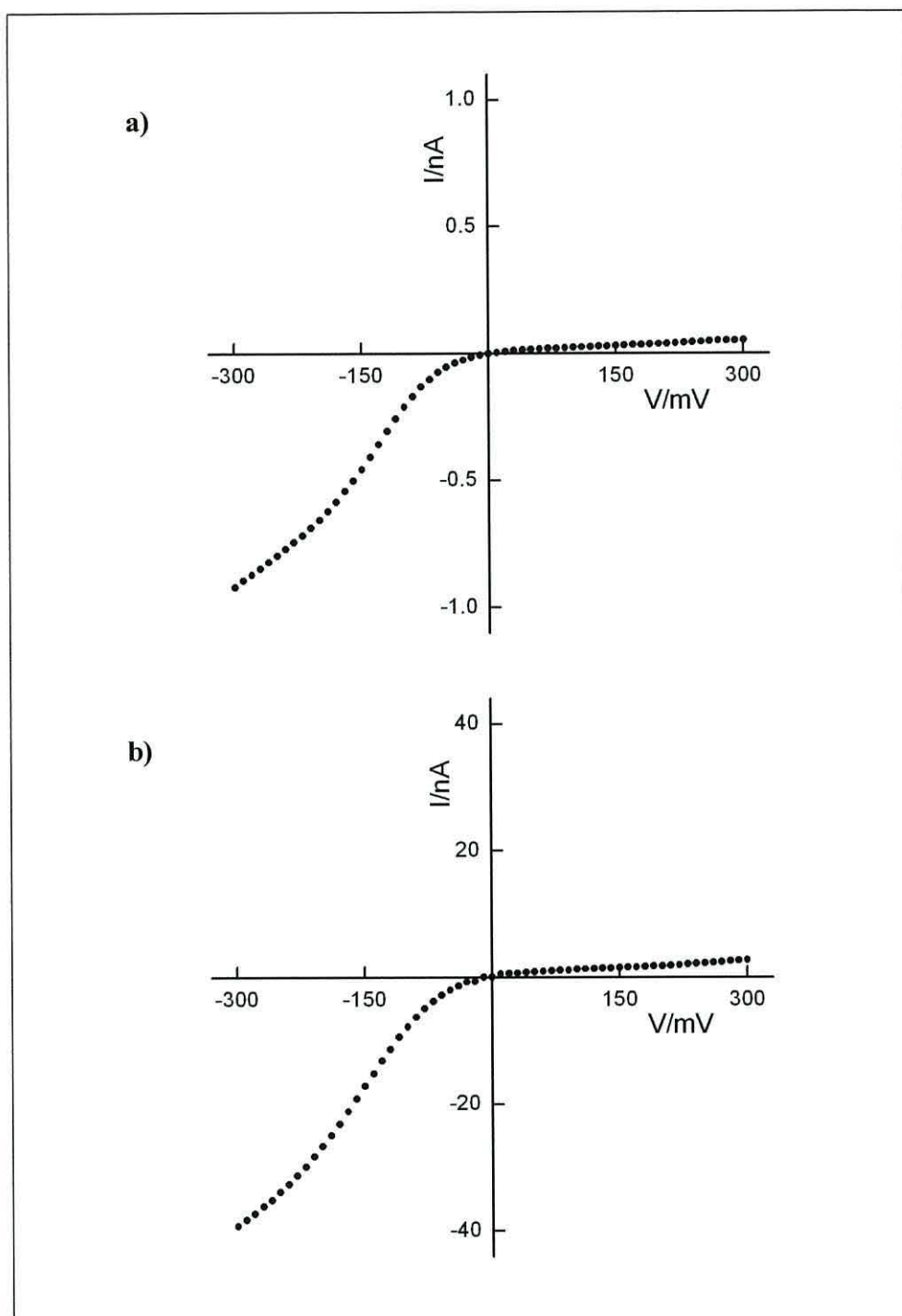


Fig. 4.3.3-1 I - V characteristics of (a) an empty Si-DEV and (b) AT2-g-AT2 system inside Si-DEV, both measured in the dark.

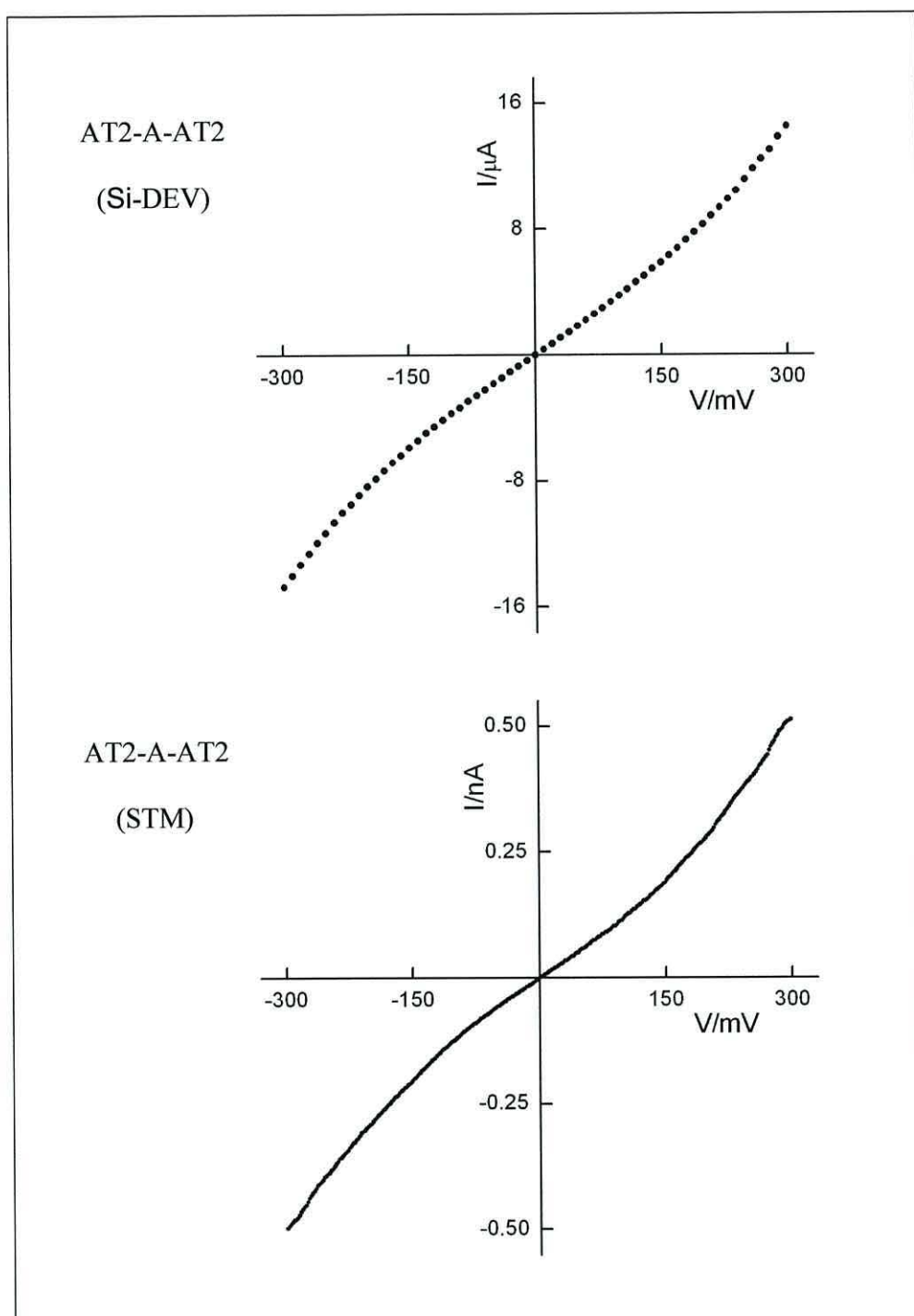


Fig. 4.3.3-2 *I-V* characteristics of the AT2-A-AT2 system inside Si-DEV, and substrate – molecule – STM tip assembly.

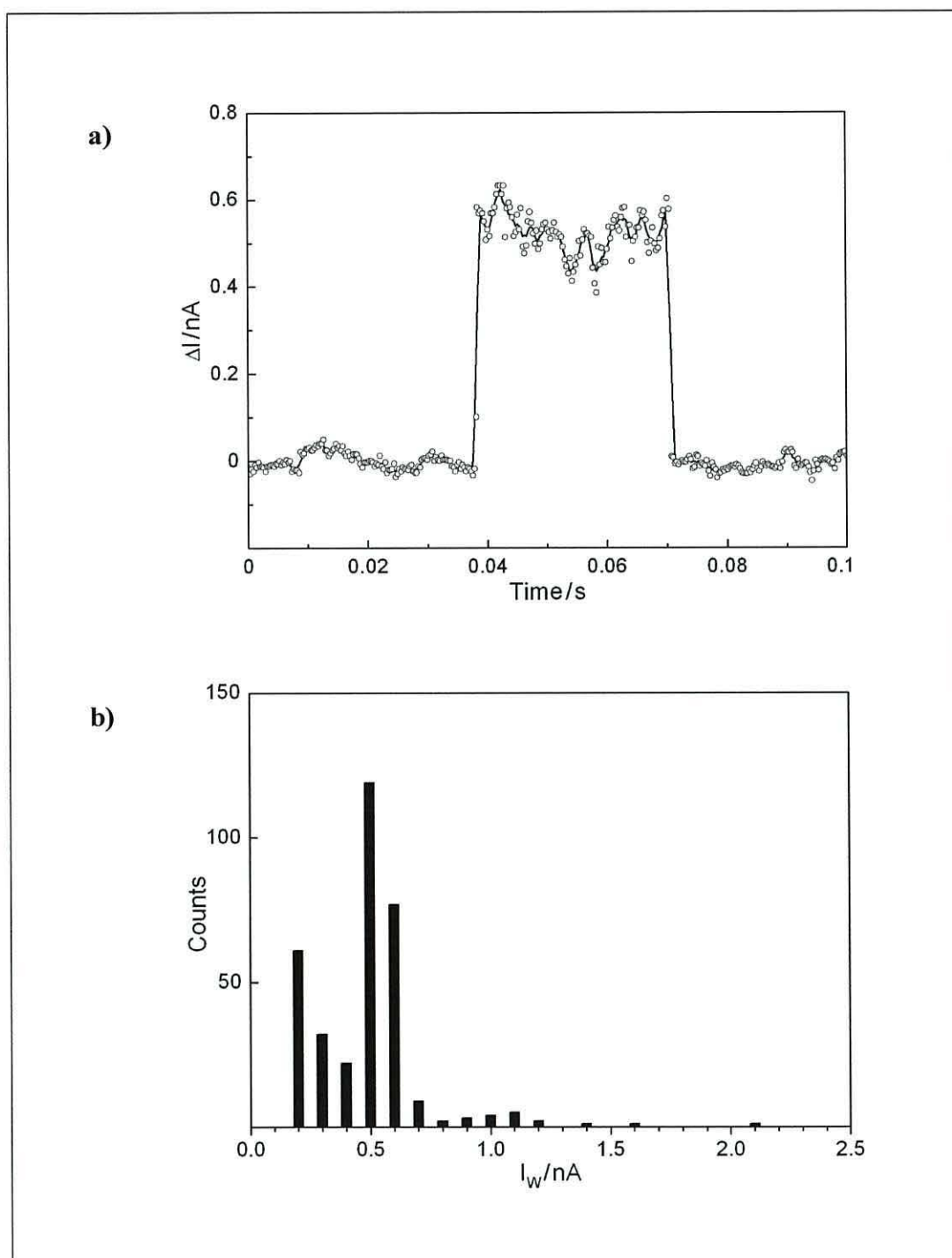


Fig. 4.3.3-3 a) Typical current jump at 300 mV bias voltage observed during I - t STS scans of the mono-thiolate version of AT2-A-AT2 on gold; b) Histogram of 340 current jump registered for this system.

The transmission coefficient for electron transfer through the AT2-A-AT2 molecular junction (see Fig. 4.3.3-4) was calculated by Ch.M. Finch and I.R. Grace (see Fig. 4.3.3-5a). They used the SIESTA density functional theory package²³⁴ to minimise free energy of the model molecular configuration. The relaxed molecule was provided with partial leads, each containing five Au(111) layers of fifteen gold atoms. This large surface area was found to be necessary to fully describe the coupling between the gold surfaces and the molecular wire, vertically aligned between the contacts. Then, a modified DFT package was used to find the Hamiltonian and overlap matrices of the system, describing charge transfer effects at the lead – molecule interface. Finally, the SMEAGOL code, which is a hybrid of DFT and non-equilibrium Green's function techniques²³⁵, was applied to compute zero-bias $T(E)$. This data was used to calculate a model I - V characteristic for AT2-A-AT2 system, shown in Fig. 4.3.3-5b, from Eqn 2.3.3-2.

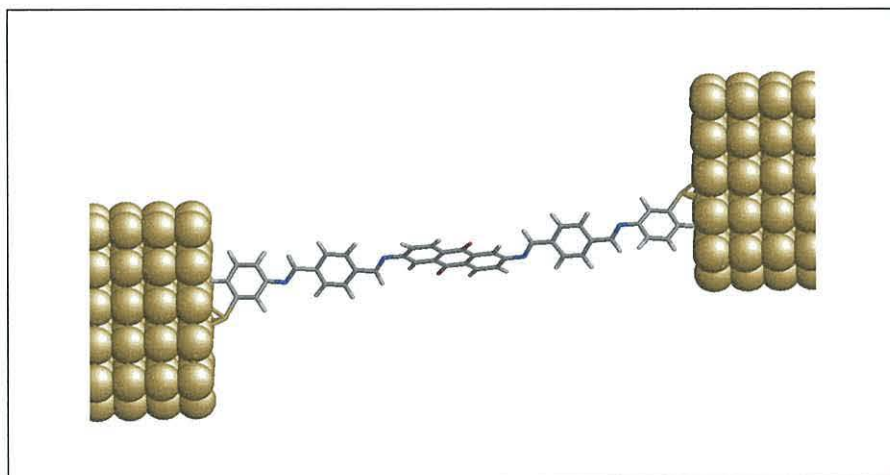


Fig. 4.3.3-4 Relaxed AT2-A-AT2 geometry for $T(E)$ computation.

The theoretical data displayed typical off-resonant current due to the broadened HOMO and LUMO resonance tails. The profile of the computed I - V curve was similar to those obtained from STS experiments and Si-DEV measurements. The theoretically predicted current of *ca.* 0.2 nA at 300 mV is also in reasonable agreement with the measured single molecule current at the same bias.

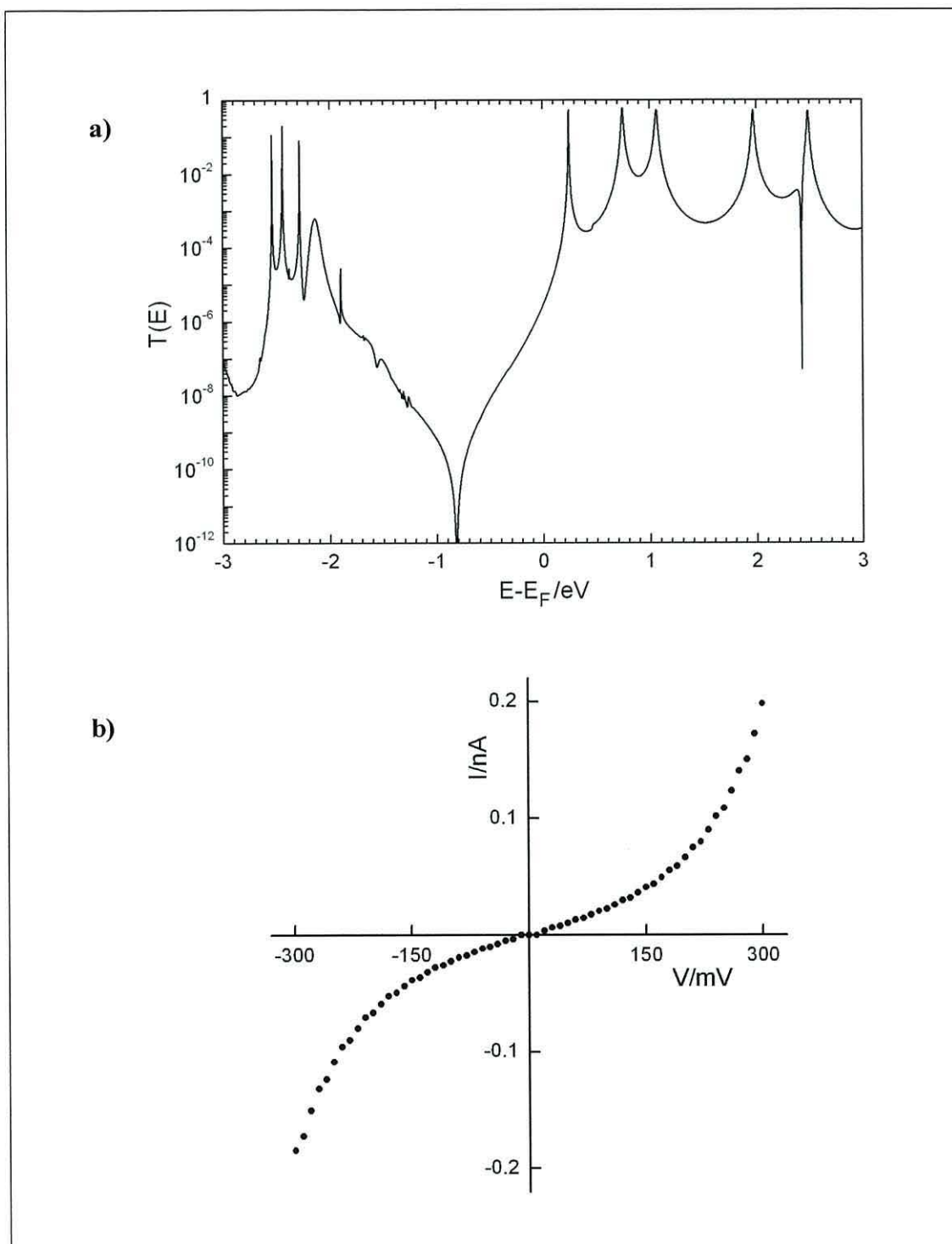


Fig. 4.3.3-5 a) Zero-bias electronic transmission coefficient as a function of energy, computed by Ch.M. Finch and I.R. Grace for relaxed AT2-A-AT2 system; b) Theoretical $I-V$ characteristic, calculated from the molecular Landauer formula using $T(E)$.

4.3.4 Summary of electronic properties of AT systems

A novel statistical approach to the analysis of current flow asymmetry resulted in development of the first reliable method for precise estimation of STS operational parameters, for which the minimum tip – sample separation could be achieved. In order to recognise which I - V characteristics represented current transmission under the strongest tip – molecule coupling conditions, histograms of $A_a(V_n)$ parameters were plotted. These parameters are calculated from I - V characteristics registered when the tip – substrate separation was decaying to zero $\{d(a) = [d_a, \dots 0]\}$. Next, A - V and dI/dV dependences for the most characteristic points of the $A_a(V_n)$ histograms were compared and analysed.

More detailed studies of $A_a(V_n)$ - $I_a(V_n)$ characteristics, calculated from I - V curves taken at different feedback voltages, can also lead to better understanding the influence of LDOS on the observed I - V curves asymmetries. This has been impossible using standard STM-STS analysis. The presented experimental results prove that the electronic transmission between tip and substrate was strongly attenuated by electron energy dissipation effects upon tunnelling through the air gap. Coexistence of these competing phenomena, when each affects the current asymmetry in a different way, complicates the analysis of separate I - V curves. However, the proposed method of $A_a(V_n)$ - $I_a(V_n)$ characteristic analysis, gives new opportunities of obtaining complete lists of factors causing the asymmetry of current flow through particular molecular systems.

The described method of current asymmetry analysis was applied for studying current rectifying properties of AT structures. The following systems: AT1-A, AT2-A and AT3-A revealed low-rectifying properties, and can be generally treated as $\text{Au} | \text{Au}-(\text{D})-\pi-(\text{A})$ systems. Different values of the maximum current asymmetry were detected for these systems. The rectification was inversed by attaching a strong electron-donating units to AT1-A to form AT1-AD with $\text{Au} | \text{Au}-\pi-(\text{A})-\pi-(\text{D})$ type electronic structure. According to preliminary expectations, the strongest rectifying properties were observed for AT2-L, containing two sets of electron donors and acceptors. The electronic structure of this system was described as $\text{Au} | \text{Au}-(\text{D})-\pi-(\text{D})-\pi-(\text{A})-\pi-(\text{A})$.

The rectification ratio of *ca.* 44 at $\pm 1\text{V}$, found for this system, is the highest value reported for stable monolithic π -conjugated molecular wire structures.

Methods of the step-by-step *in-situ* molecular wire synthesis, reported here and by other research groups²³⁶⁻²⁴⁰, was found to be very useful for manufacturing two-terminal molecular devices for prospective future technological applications. Previous attempts of bridging two electrodes in Si-DEV by long and rigid dithiol molecules had failed, which revealed major difficulties in forming stable electrical contacts with both metallic terminals simultaneously. The step-by-step approach enabled one to achieve this target. Monolayers of small, conjugated molecules onto both electrodes of Si-DEV can be formed *via* self-assembly. The following step enables the reactive terminal groups of the self-assembled molecules to be bridged with functional units, the length of which can be precisely selected to fit the gap between the self-assembled components. This technique has four major advantages:

- 1) self-assembly of short molecules separately onto both electrodes guarantees a relaxed geometry and dense molecular arrangements, which leads to:
 - a) the strongest substrate – molecule electronic coupling, minimising the barrier for electronic transmission;
 - b) high symmetry of the final two terminal structures, demonstrated by perfectly symmetrical *I-V* characteristics of AT2-A-AT2 system;
- 2) length of molecular systems can be precisely adjusted *via* preliminary computer modelling of the junction architecture;
- 3) electrostatic interaction between molecules can be limited, as:
 - a) the molecules form a ring around the central insulating core of the device;
 - b) density of the central linking components can be controlled by introducing molecular side groups acting as electrically neutral spacers;
- 4) time-consuming and expensive process of synthesising long molecular systems *via* standard wet chemical methods was replaced by efficient *in-situ* synthesis using cheap and commercially available components.

4.4 Electronic properties of PeMP systems

Studies of PeMP systems were undertaken in order to determine the conductivity of these molecular wires. In particular, attention was paid to the method of improving the conductivity by introducing a positive charge to the central aromatic ring of the self-assembled molecule (Section 4.4.1). The second part of these studies (Section 4.4.2) concerns the functionalisation of PeMP-b monolayers by *in-situ* ion exchange reactions, to create hybrid “sandwich-type” structures, which can be described as $\text{Au} | \text{Au}-\pi-(\text{A}^+)-\pi | (\text{D}^-)-\pi$ systems. Such a counter-ionic system was expected to reveal strong rectifying properties due to large energetic differences between the energy levels of the frontier molecular orbitals of the donor and acceptor, and effective separation of these components.

4.4.1 Electron transport through two-terminal PeMP molecular wires

Two STS techniques, *I-s* and *I-t*, were applied for characterising the off-resonant current transmission through PeMP-a and PeMP-b at $V = 300$ mV. Results of these experiments were compared with theoretical *I-V* characteristics for these systems, calculated from $T(E)$, which were computed by Finch and Grace of the Lancaster University.

Most of the *I-V* curves observed for both forms of the system: neutral and protonated, were highly symmetrical. The most commonly seen *I-V* characteristics registered for these systems are shown in Fig. 4.4.1-1. The typical current jumps registered for PeMP-a and PeMP-b, using both STS methods, are shown in Fig. 4.4.1-2 and Fig. 4.4.1-3 respectively. The multiple jumps, indicating adsorption of more than one molecule at a time, were also recorded using the *I-t* technique, which suggested a dense molecular arrangement. Duration of the periodic tip – molecule contacting events during the experiment was relatively short (10 – 60 ms) when compared to other data¹⁹⁶, which was expected for very rigid molecular systems.

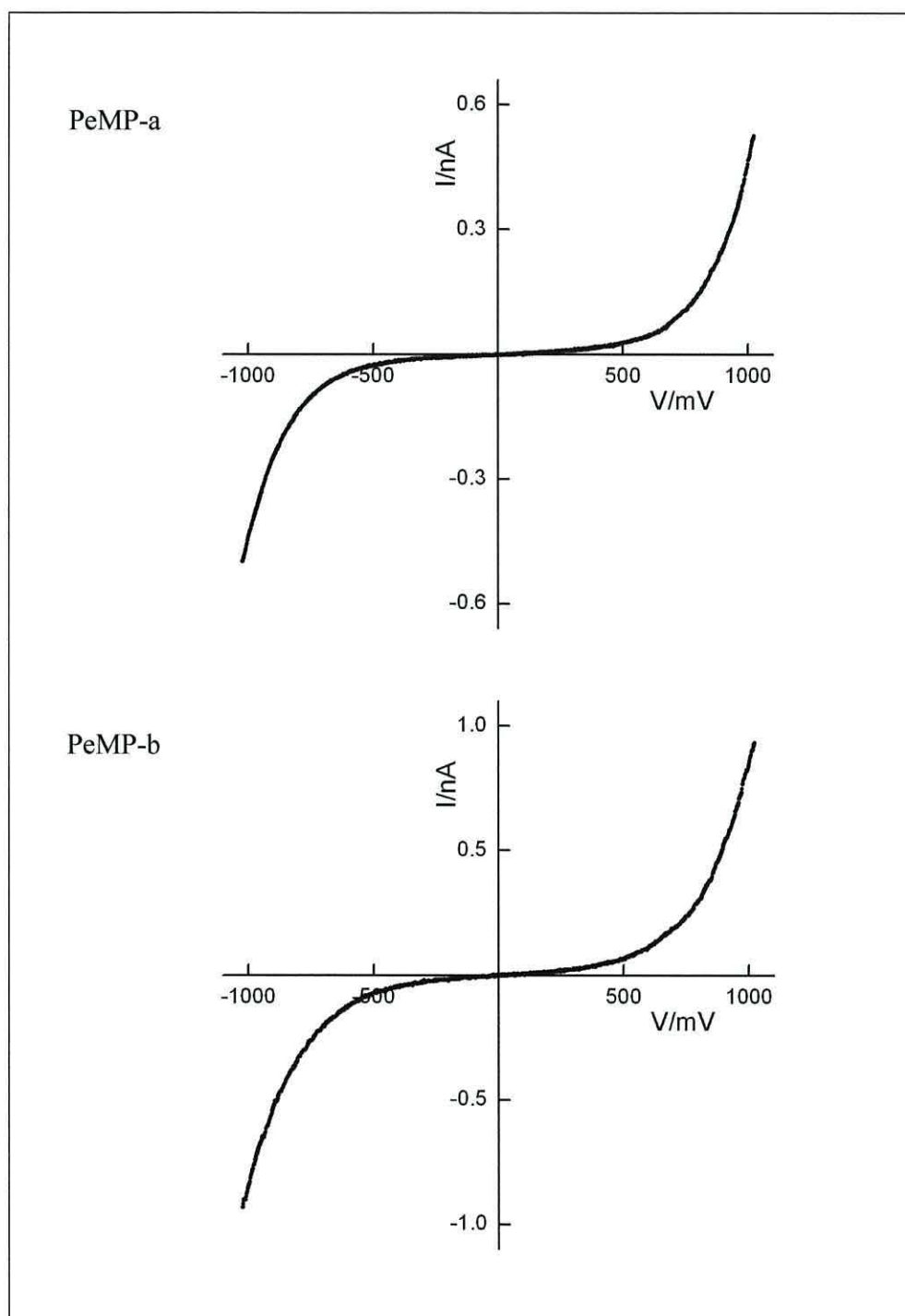


Fig. 4.4.1-1 Typical I - V characteristics observed for PeMP-a and PeMP-b.

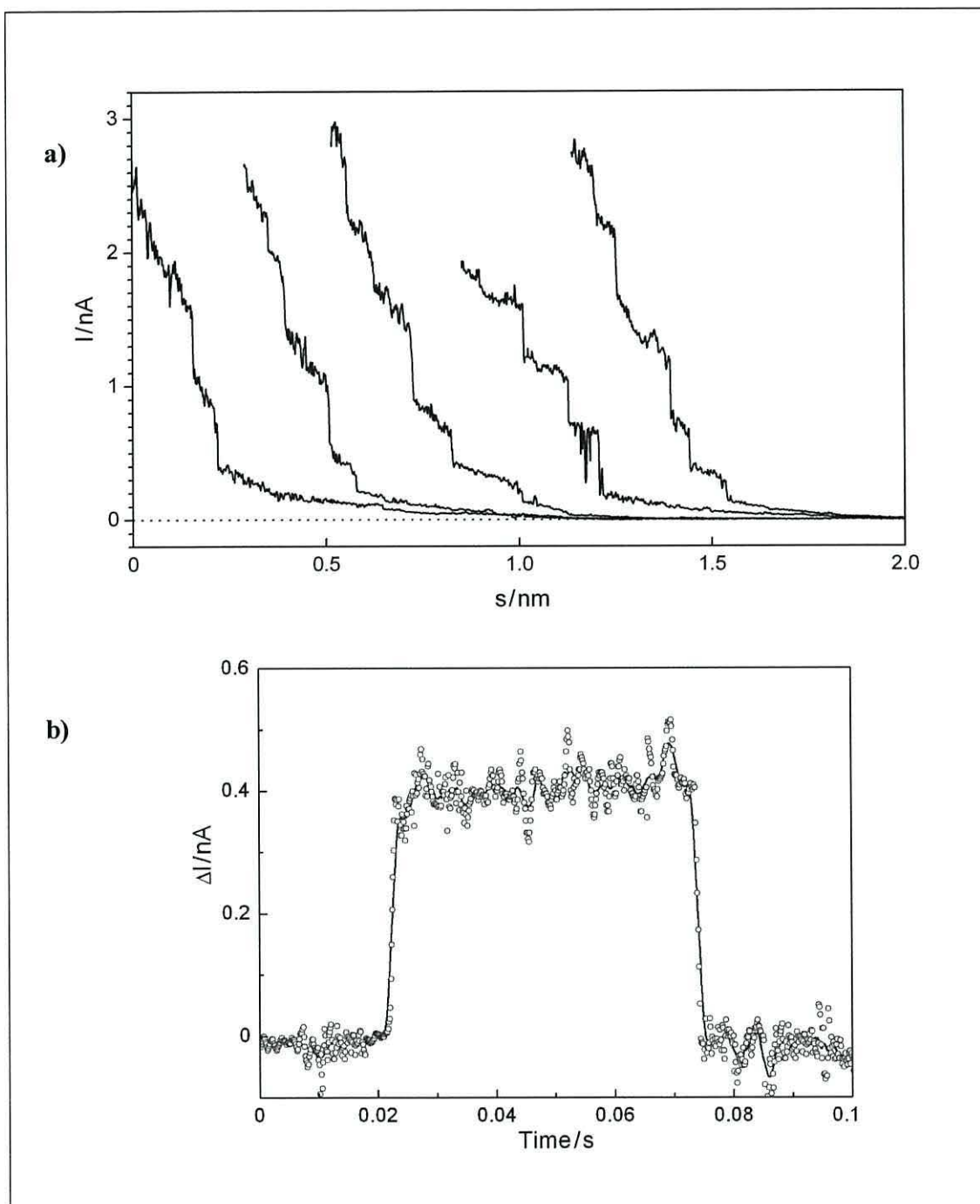


Fig. 4.4.1-2 Typical current jumps recorded at $V = 300$ mV for PeMP-a via (a) I - s and (b) I - t STS scans (the four I - s curves on the right in (a) were shifted along X-axis for clarity).

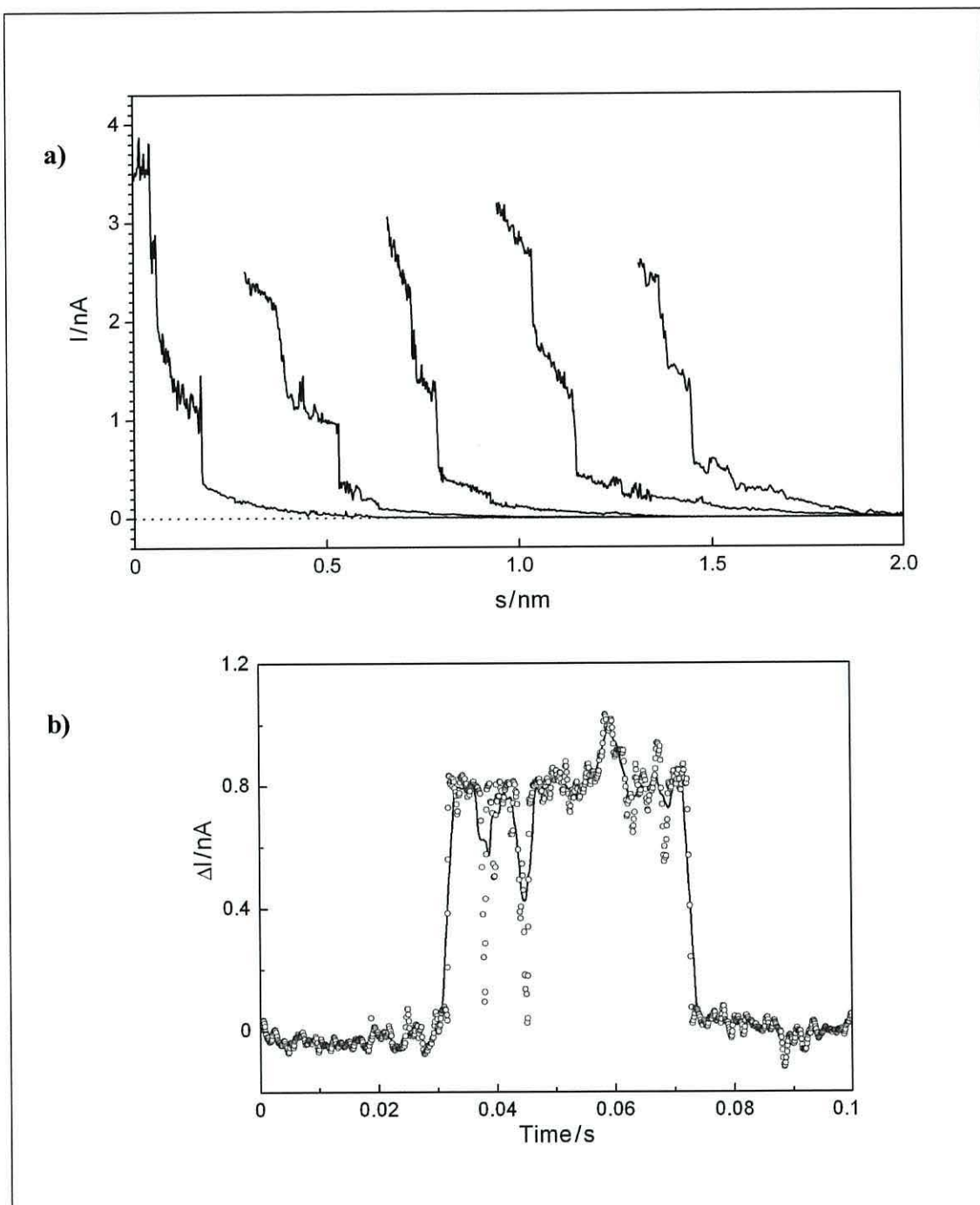


Fig. 4.4.1-3 Typical current jumps recorded at $V = 300$ mV for PeMP-b via (a) I - s and (b) I - t STS scans (the four I - s curves on the right in (a) were shifted along X-axis for clarity).

Major peaks in histograms of the current jumps, registered *via* the STS *I-s* and *I-t* techniques for PeMP-a, indicated a tunnelling current of 0.40 ± 0.05 nA at 300 mV (see Fig. 4.4.1-4). The equivalent histograms for the PeMP-b system revealed two different values of the current, which could have been observed with equal probability: $I_1 = 0.40 \pm 0.05$ nA, and $I_2 = 0.80 \pm 0.05$ nA (see Fig. 4.4.1-5). It is believed that the peaks at lower current can be assigned to transmission mediated by PeMP-a, and the peaks at higher current are associated with transmission through PeMP-b system. This would agree with the previous XPS quantitative studies on PeMP-b and PeMP-c, which suggested the PeMP-a systems protonation yield to be *ca.* 58 %.

Zero-bias electronic transmission coefficients as functions of energy were computed for the relaxed PeMP-a and PeMP-b geometries attached to partial leads, containing five Au(111) layers of nine gold atoms each (see Finch and Grace calculations in Fig. 4.4.1-6). Profiles of the theoretical *I-V* characteristic, calculated from the molecular Landauer formula using computed $T(E)$, are shown in Fig. 4.4.1-7. The theoretical data for PeMP-a display typical off-resonant currents in the studied range of $V = [-1V, 1V]$. A profile of the computed *I-V* curve for this system was similar to that obtained from the STS experiment. However, the theoretically predicted current of *ca.* 50 nA at 300 mV (see red curve in Fig. 4.4.1-7) was two orders of magnitude higher than that detected during *I-s* and *I-t* measurements. The results of $T(E)$ calculations for PeMP-b revealed a resonance at *ca.* 0.24 eV, which would give rise to a strong current increase at *ca.* 480 mV (see blue curve in Fig. 4.4.1-7). This effect was not observed during STS *I-V* scans, which was most probably due to the lack of strong tip – molecule electronic coupling and the electron's energy dissipation at the air gap potential barrier (see Section 4.3.1). However, according to theory, the off-resonant electronic transmission in the voltage range of $V = [-300\text{mV}, 300\text{mV}]$ was very weakly affected by the presence of a proton on the central aromatic ring of the self-assembled molecule (see Fig. 4.4.1-7b). This corresponds well to the experimental STS *I-s* and *I-t* results at 300 mV.

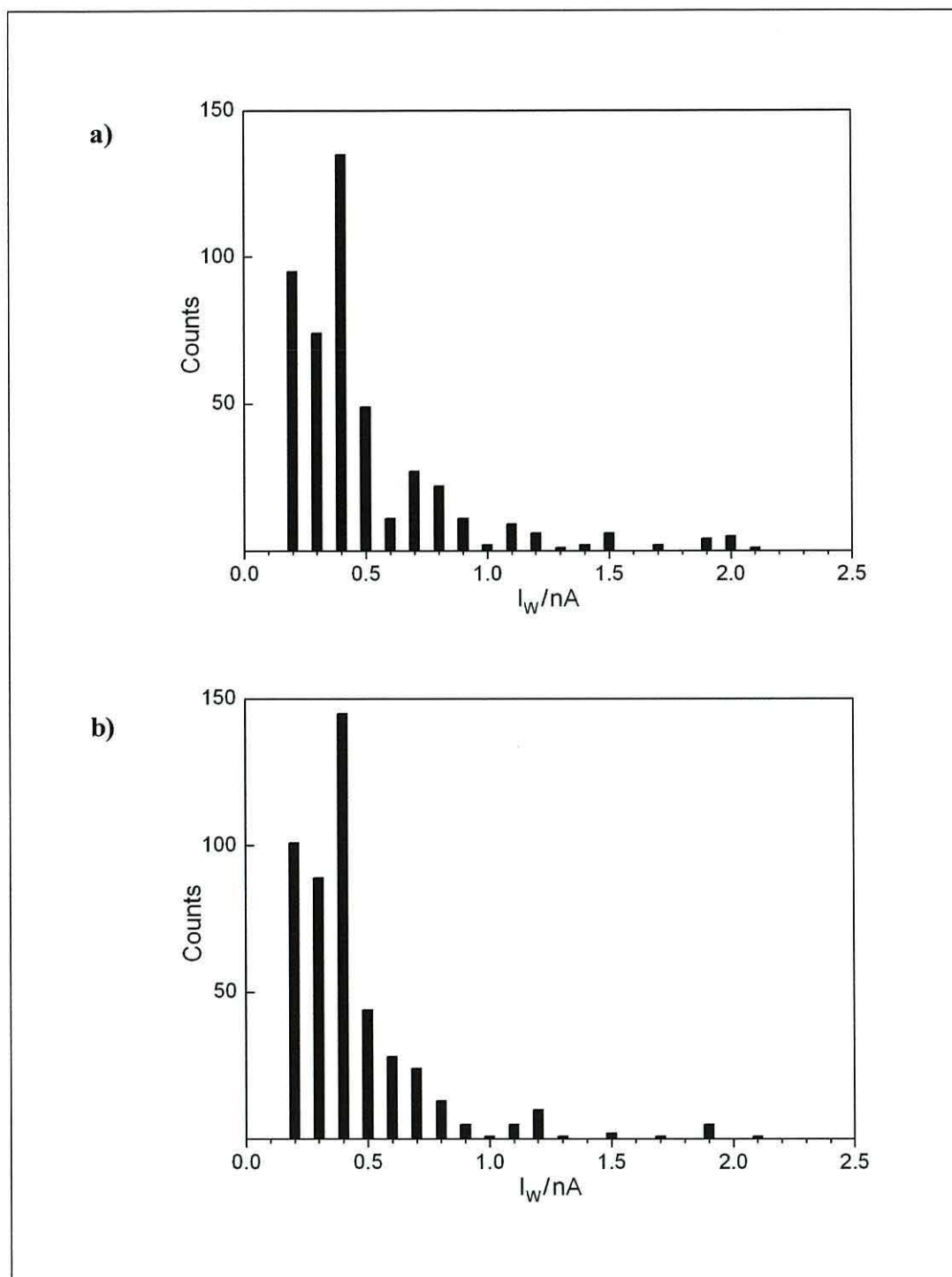


Fig. 4.4.1-4 Histograms of (a) 462 current jumps registered at $V = 300$ mV via $I-s$ and (b) 475 jumps registered via $I-t$ STS technique for PeMP-a.

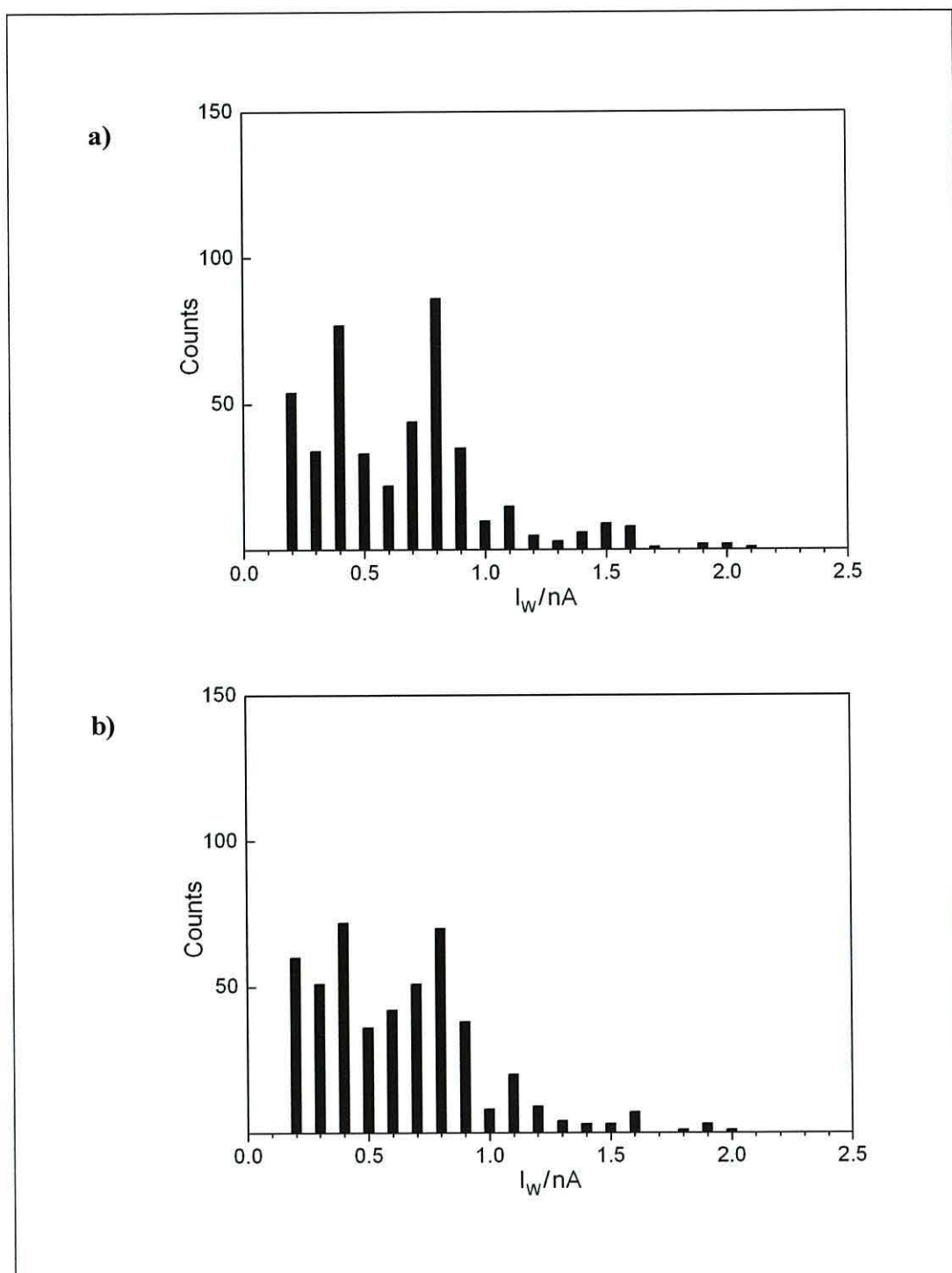


Fig. 4.4.1-5 Histograms of (a) 447 current jumps registered at $V = 300$ mV via $I-s$ and (b) 479 jumps registered via $I-t$ STS technique for PeMP-b.

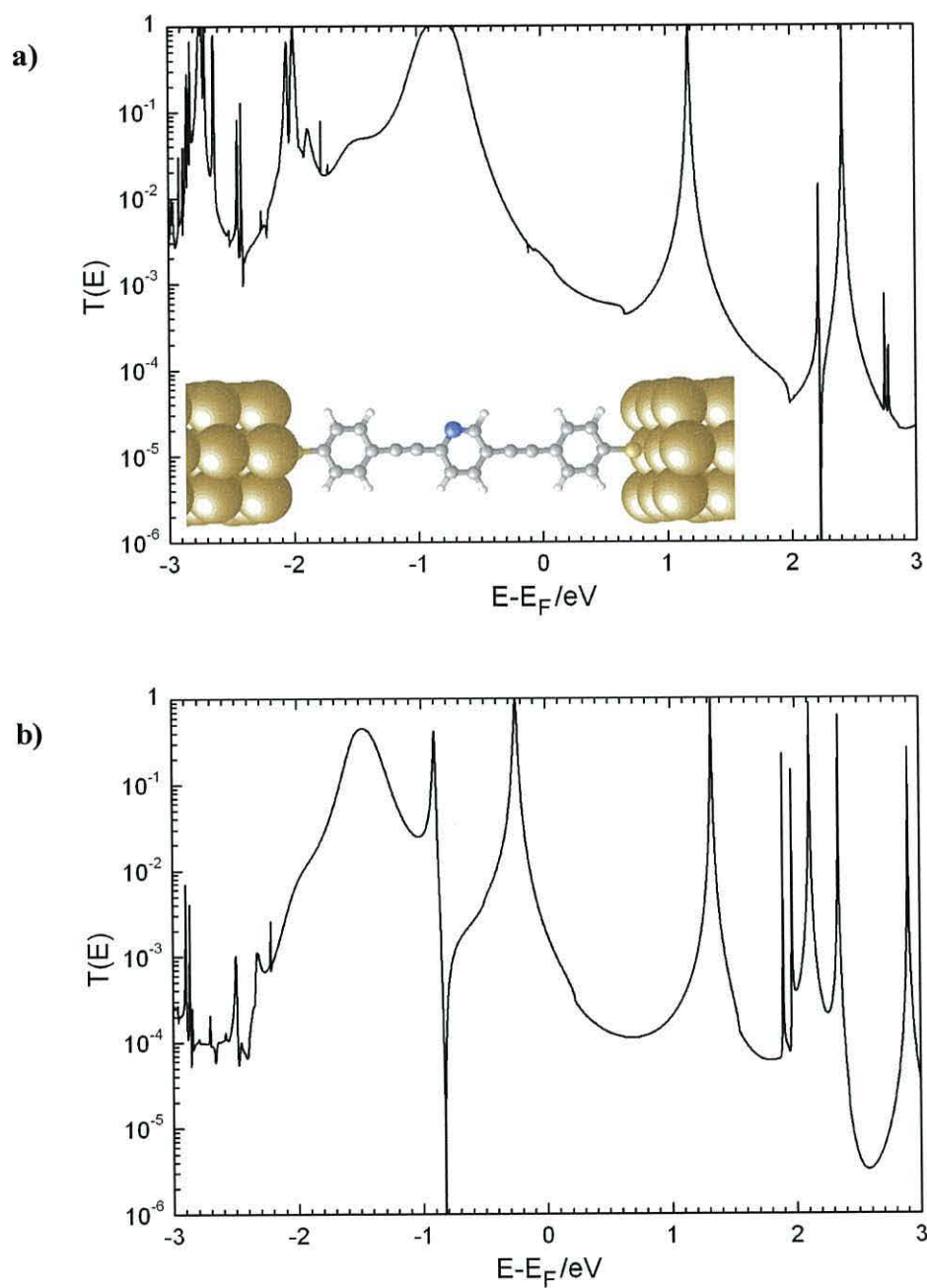


Fig. 4.4.1-6 Zero-bias $T(E)$ computed by Ch.M. Finch and I.R. Grace for relaxed (a) PeMP-a geometry (shown in the bottom left corner of the plot) and (b) PeMP-b geometry, which resembled that from plot (a).

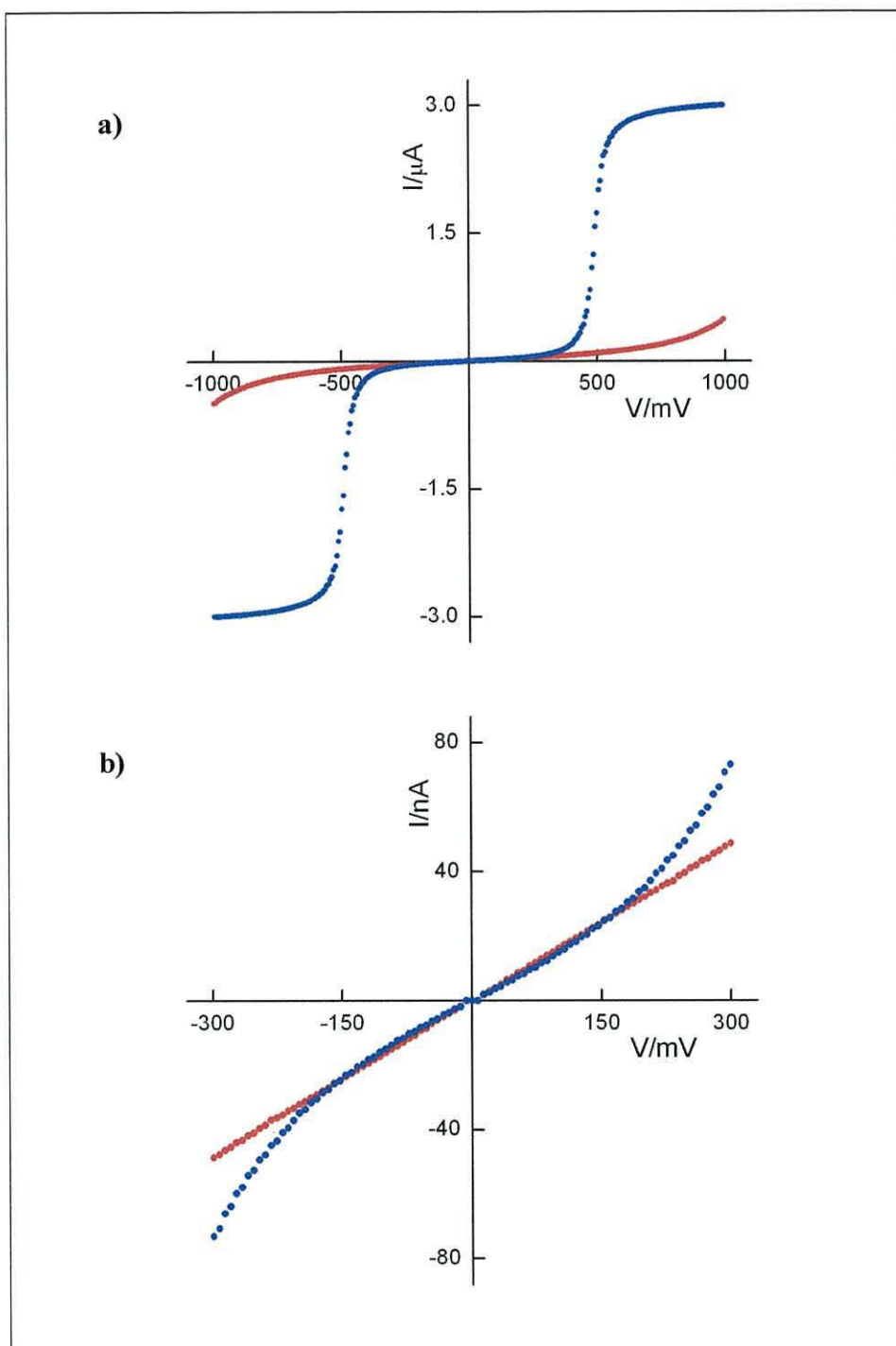


Fig. 4.4.1-7 Theoretical I - V characteristics for PeMP-a (red line) and PeMP-b (blue line) in the voltage range of **(a)** $V = [-1\text{V}, 1\text{V}]$ and **(b)** $V = [-300\text{mV}, 300\text{mV}]$, calculated from the molecular Landauer formula using zero-bias $T(E)$ shown in Fig.4.4.1-6.

The electrical studies of PeMP-a and PeMP-b systems indicated that the measurements agreed with theory about the small difference in off-resonant conductivity between these two systems, but they also revealed a strong disagreement about the exact quantity. The very similar values of the tunnelling current at $V = 300$ mV were obtained by B. Urasinska for compounds with a similar backbone structure, but different side groups attached to the central aromatic rings²²¹. Depending on the nature of the side groups, current varied between 0.2 and 0.5 nA. This indicates a very weak dependence of oligo(phenylene-ethynylene) systems molecular structure on the tunnelling current in normal environmental conditions. This regularity may also apply to other *quasi*-linear conjugated molecular systems such as AT2-A-AT2 (Section 4.3.3), and longer conjugated systems up to 7 nm in length^{221,233}. The current registered *via* STS at $V = 300$ mV varied between 0.1 and 0.8 nA for all these systems, including PeMP-b, where the highest value was observed.

There can be several reasons for the differences observed between the measured tunnelling current and the theoretical values, calculated for separate molecules:

- 1) lateral interaction between molecules in SAMs, which can attenuate charge transfer per molecule (even by a few orders of magnitude), compared to the theoretically analysed separate molecular system:
 - a) electrostatic interactions, discussed by Y. Xue and M.A. Ratner²⁴¹;
 - b) various thermal effects, observed by Y. Selzer²⁴², which arose from the presence of neighbouring molecules;
- 2) presence of small molecules from the atmosphere (mainly H₂O) in direct proximity of SAMs, which can affect molecular conductivity in a similar way as the neighbouring molecules forming SAMs do; this was studied by C. Lambert²⁴³;
- 3) real geometry of a gold – molecule interface determining the electric terminals – molecule electronic coupling, which is different from that theoretically predicted;
- 4) molecular response under applied bias can be significant, and was not included in the theoretical analysis; this may be especially important for π -conjugated molecules revealing high polarisabilities, as this effect can strongly influence the shape of the tunnelling barrier.

4.4.2 Rectifying behaviour of modified PeMP SAMs

According to the previous studies of PeMP-b and PeMP-c systems, the TCNQ^{•-} electron-donating moieties successfully replaced all Cl⁻ ions during the ionic exchange reaction described in Section 4.2.2. Due to a dense molecular arrangement of PeMP-b systems, the bulky TCNQ^{•-} radical anions were assumed to form an adlayer on top of the self-assembled cationic PeMP-b molecules, rather than diffusing inside the monolayers. As the protonation yield for the applied method was estimated to be higher than 50 %, the radical anions (the cross-section of which is higher than for the molecules in the monolayer) could have formed a uniform and sufficiently dense adlayer. Thus, the expected arrangement of PeMP-c molecular layers, shown in Fig. 4.4.2-1, was treated as Au | Au- π -(A⁺)- π | (D⁻)- π .

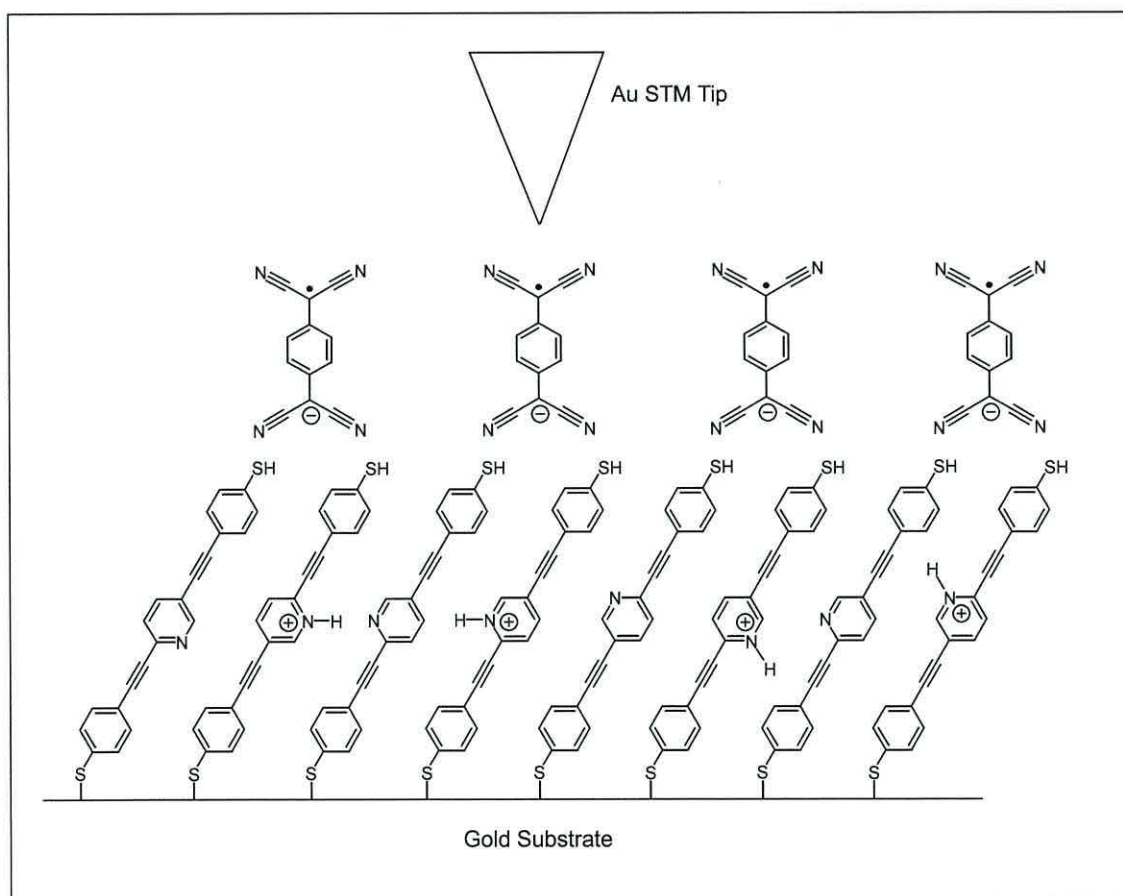


Fig. 4.4.2-1 Schematic image of the molecular arrangement expected for PeMP-c.

STS measurements of PeMP-c and PeMP-d were conducted according to the methods given in Section 4.3.1. Strong rectification up to *ca.* 200 at ± 1 V was consistently observed during scanning of the PeMP-c samples (see. Fig. 4.4.2-2). This has proven the preliminary assumptions about the structure of the molecular bilayer and has also revealed the great potential of the ionically coupled π -conjugated molecules.

Current rectification of 20 – 30 at ± 1 V for $\text{Au} | \text{Au}-\sigma-(\text{A}^+) | \text{TCNQ}^{\bullet-}$ molecular systems was previously reported by Ashwell *et al.*²⁴⁴. Rectification increased to 60 – 100 at ± 1 V when $\text{TCNQ}^{\bullet-}$ was replaced by the bulky copper phthalocyanine, $\text{CuPc}(\text{SO}_3^-)_4(\text{Na}^+)_n$, where $1 \leq n \leq 2$ ²⁴⁵. Soon afterwards, the highest rectification reported to date for ionically coupled non-conjugated systems (> 1000 at ± 1 V) was found for $\text{Au} | \text{Au}-\sigma-(\text{A}^+)-\pi-\text{D} | \text{CuPc}(\text{SO}_3^-)_4(\text{Na}^+)_n$, also by Ashwell *et al.*²⁴⁶. The only studies on rectification by ionically coupled π -conjugated systems were performed for self-assembled 7 nm long molecular wires with $\text{CuPc}(\text{SO}_3^-)_4(\text{Na}^+)_n$ deposited on top of the monolayer, which was reported by Ch. Wang *et al.*²⁴⁷. The structure of this system can be described as $\text{Au} | \text{Au}-\pi-(\text{A}^+)_{2-\pi} | \text{CuPc}(\text{SO}_3^-)_4(\text{Na}^+)_n$, whose structure is very similar to that studied by the author. However, despite using double electron-accepting groups on the molecular wires and the very strong copper phthalocyanine electron donors, the rectification obtained was relatively weak (< 50 at ± 1 V). Much higher rectification, found for the PeMP-c system, in which the weaker donating and accepting components were used, could be due to higher packing density of the molecular wires, which guaranteed high uniformity of the electron-donating adlayer. This could have resulted in a very high permanent dipole moment for the bilayer.

An estimation of the final structure of PeMP-d was found to be a complex problem, which could not have been solved with the available experimental methods. For this system rectification inversion relating to PeMP-c was observed (see Fig. 4.4.2-2b). This high rectification ratio of up to 65 at ± 1 V (in the negative quadrant of the I - V plot) was consistently observed for all three samples of PeMP-d. However, due to the lack of information about the PeMP-d composition, further studies in this field are required in order to find the origin of the observed effect.

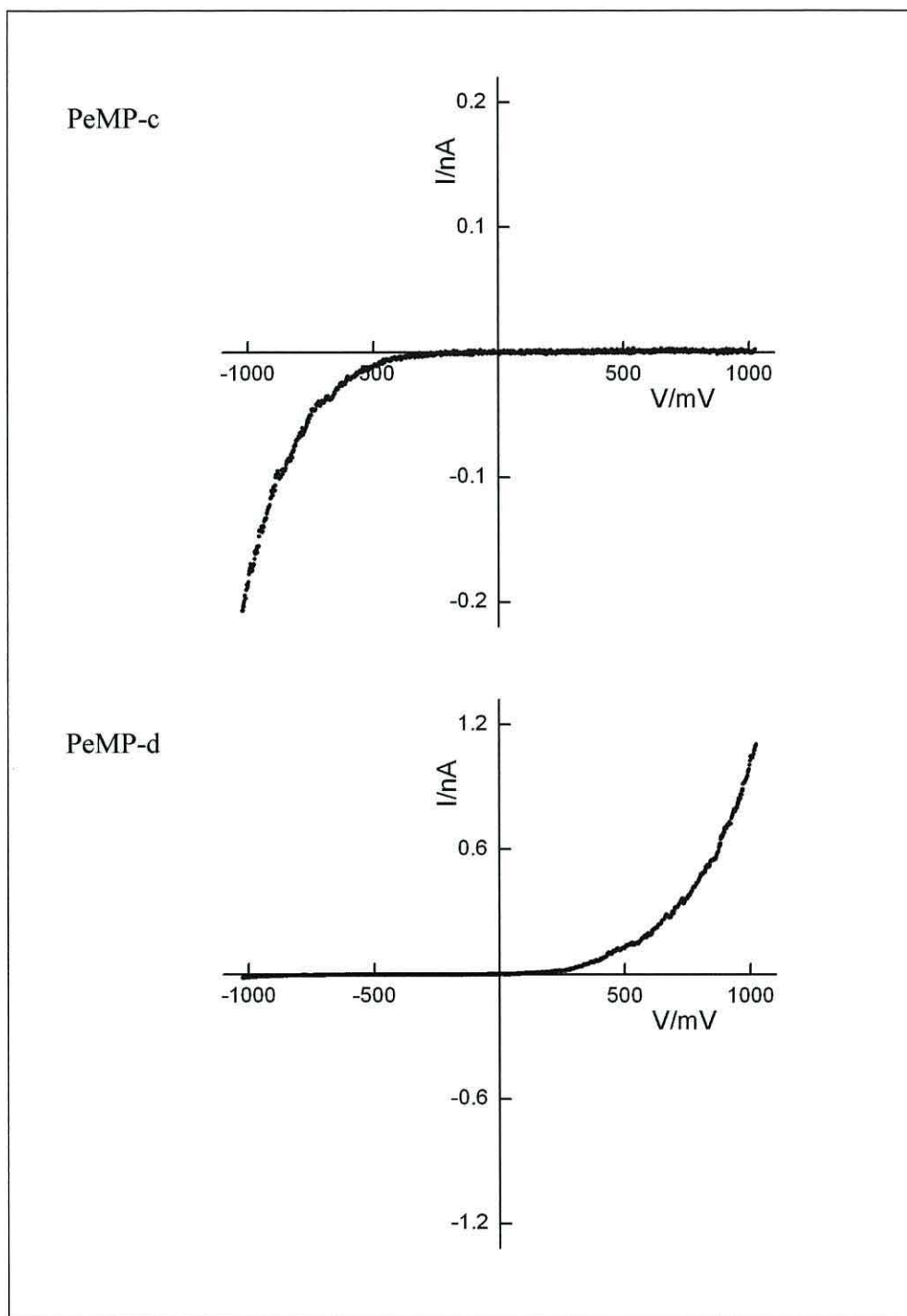


Fig. 4.4.2-2 Typical I - V characteristics observed for PeMP-c and PeMP-d.

4.4.3 Summary of electronic properties of PeMP systems

Studies of the conductivity of PeMP-a and PeMP-b systems proved that tunnelling current through the junctions (formed after contacting the thiol groups with the STM tip), did not differ significantly from the off-resonant current of other conjugated moieties in monolayers. Theoretical calculations, which predicted a tunnelling current two orders of magnitude higher, concerned separate molecules in a vacuum with ideally symmetrical leads. However, this did not include the effect of electric field on the molecules, which is a very unrealistic situation. Due to the much better agreement of theory and experiment for the AT2-A-AT2 system, the arrangement in which the monolayer was less dense, it is highly probable that intermolecular interactions had a major limiting influence on the current transmission through the junctions. This close-packing effect was also proved by other authors^{241,242}. On the other hand, the theory correctly predicted the difference in the tunnelling current between PeMP-a and PeMP-b.

The densely packed SAMs, based on the PeMP core structure, could be easily modified and functionalised in order to obtain the desired rectifying properties, which to date were not observed for any other conjugated systems. The electronic structure of the PeMP-c system, described as $\text{Au} | \text{Au}-\pi-(\text{A}^+)-\pi | (\text{D}^-)-\pi$, provides a rectification ratio of up to *ca.* 200 at $\pm 1\text{V}$. The chemical method of reversing this rectification, and obtaining a value of *ca.* 65 at $\pm 1\text{V}$ in the opposite direction was also found. The origin of this effect is unknown, but such a strong evolution of the electronic properties is most probably associated with a redistribution of charge upon some fundamental structural transformations of the system. Thus, resolving the chemical structure of PeMP-d is essential for understanding the unique properties of this system and should be the topic of further research.

5 Conclusions

The current rectifying features of the extended molecular wires, formed from multiple-stage *in-situ* synthesis, confirmed the significance of the step-by-step method. It provides complex conjugated molecular systems, the structural and electronic properties of which can be precisely controlled by incorporating functional units into the backbone architecture. This method is very simple, efficient and relatively fast, compared to standard wet chemical synthetic procedures. This is also economically favourable, which is promising for further commercial applications. Its usefulness has been demonstrated by connecting the electrode of a prefabricated silicon-based platform with *ca.* 3.6 nm long molecular wires. This rigid hybrid structure enables precise monitoring of electronic conductivity of molecular systems, and can be useful for development of future cutting-edge electronic technologies. It can also be considered as a prototype of a two-terminal molecular electronic device. A great number of such structures can be integrated on the same silicon wafer and adapted for mass production.

The method of *in-situ* molecular film functionalisation using ionic interactions for the formation of adlayers was also effective. The densely packed monolayers of ionic molecular wires coupled to counter-ionic molecules of the adlayer demonstrated a very high rectification. The usage of very simple short linear compounds for the creation of such a dual-layer film resulted in high uniformity of the structure and its electronic properties.

A significant contribution was made in the field of STS studies on current asymmetry. The presented statistical approach was found to be very useful, especially when applied for estimating the maximum rectification of studied systems. This method is believed to have great potential for investigating the electron tunnelling effect and should be developed further. This may lead to better understanding of electronic transmission through the STM tip – air gap – molecule – substrate setup and to gain a complete image of energy dissipation and LDOS impact on current asymmetry of self-assembled molecular systems. Further studies in this field should be focused on

correlating trends of $A_a(V_n)$ - $I_a(V_n)$ dependences for $a = [1, 2, \dots, z]$, where $z \geq 1000$, with changes in molecular conductivity, traced on corresponding dI/dV characteristics.

There are several barriers which need to be overcome before molecular electronic devices can be applied. One of the most important prerequisites for designing molecular electronic devices is the complete understanding of electron transport through molecular systems considering all the phenomena affecting this process. This problem is very complex and requires sophisticated theoretical studies of non-equilibrium electronic states on molecules, and interfaces, to be compared with adequate experimental results. The presented results of the conductivity and the current asymmetry measurements have also made a significant contribution in this matter, and can be used as a reference for further studies in this field.

6 Reference list

1. EE Times Europe (12/19/2006), *Analyst Predicts 70% CAGR for Organic Electronics Market*, available at: <http://eetimes.eu/semi/196700767>.
2. Intel, *Moore's Law*, available at: <http://www.intel.com/technology/mooreslaw/index.htm>.
3. Intel News Release (18/09/2007), *Intel Demonstrates Industry's First 32nm Chip and Next-Generation Nehalem Microprocessor Architecture*, available at: http://www.intel.com/pressroom/archive/releases/20070918corp_a.htm.
4. Semiconductor International (12/09/2007), *IBM Alliance Develops 32 Nm High-k/Metal Gate SRAM*, available at: <http://www.semiconductor.net/article/CA6510988.html>.
5. Physorg News (12/04/2007), *IBM Extends Moore's Law to the Third Dimension*, available at: <http://www.physorg.com/news95575580.html>.
6. Keyes, R. W. (2001), 'Fundamental Limits of Silicon Technology', *Proceedings of the IEEE*, Vol. 89, pp. 227-239.
7. Keyes, R. W. (2005), 'Physical Limits of Silicon Transistors and Circuits', *Reports on Progress in Physics*, Vol. 68, pp. 2701-2746.
8. Meindl, J. D., Chen, Q., and Davis, J. A. (2001), 'Limits on Silicon Nanoelectronics for Terascale Integration', *Science*, Vol. 293, pp. 2044-2049.
9. Meindl, J. D., Davis, J. A., Zarkesh-Ha, P., Patel, C. S., Martin, K. P., and Kohl, P. A. (2002), 'Interconnect Opportunities for Gigascale Integration', *IBM Journal of Research and Development*, Vol. 46, pp. 245-263.
10. Taur, Y., Buchanan, D. A., Chen, W., Frank, D. J., Ismail, K. E., Lo, S.-H., Sai-Halasz, G. A., Viswanathan, R. G., Wann, H.-J. C., Wind, S. J., and Wong, H.-S. (1997), 'CMOS Scaling into the Nanometer Regime', *Proceedings of the IEEE*, Vol. 85, pp. 486-504.
11. Wong, H.-S., Frank, D. J., Solomon, P. M., Wann, C. H. J., and Welser, J. J. (1999), 'Nanoscale CMOS', *Proceedings of the IEEE*, Vol. 87, pp. 537-570.
12. Plummer, J. D. and Griffin, P. B. (2001), 'Material and Process Limits in Silicon VLSI Technology', *Proceedings of the IEEE*, Vol. 89, pp. 240-258.
13. Frank, D. J., Dennard, R. H., Nowak, E., Solomon, P. M., Taur, Y., and Wong, H.-S. (2001), 'Device Scaling Limits of Si MOSFETs and Their Application Dependencies', *Proceedings of the IEEE*, Vol. 89, pp. 259-288.
14. Agnello, P. D. (2002), 'Process Requirements for Continued Scaling of CMOS - the Need and Prospects for Atomic-Level Manipulation', *IBM Journal of Research and Development*, Vol. 46, pp. 317-338.
15. Osburn, C. M., Kim, I., Han, S. K., De, I., Yee, K. F., Gannavaram, S., Lee, S. J., Lee, C.-H., Luo, Z. J., Zhu, W., Hauser, J. R., Kwong, D.-L., Lucovsky, G., Ma, T. P., and Öztürk, M. C. (2002), 'Vertically Scaled MOSFET Gate Stacks and Junctions: How Far Are We Likely to Go?', *IBM Journal of Research and Development*, Vol. 46, No. 299-315.

16. Wong, H.-S. (2002), 'Beyond the Conventional Transistor', *IBM Journal of Research and Development*, Vol. 46, pp. 133-168.
17. Nowak, E. J. (2002), 'Maintaining the Benefits of CMOS Scaling When Scaling Bogs Down', *IBM Journal of Research and Development*, Vol. 46, pp. 169-180.
18. Blish, R., Dellin, T., Huber, S., Johnson, M., Maiz, J., Likins, B., Lycoudes, N., McPherson, J., Peng, Y., Peridier, C., Preussger, A., Prokop, G., and Tullos, L. (2003), *Critical reliability challenges for The International Technology Roadmap for Semiconductors (ITRS)*, International SEMATECH, <http://itrs.net/Links/2003ITRS/LinkedFiles/PIDS/4377atr.pdf>.
19. Keyes, R. W. (1988), 'Miniaturization of Electronics and Its Limits', *IBM Journal of Research and Development*, Vol. 32, pp. 24-28.
20. Wada, Y. (2001), 'Prospects for Single Molecule Information Processing Devices', *Current Applied Physics*, Vol. 1, pp. 28-38.
21. Lundstrom, M. (2002), 'Is Nanoelectronics the Future of Microelectronics?', in *Proceedings of the 2002 International Symposium on Low Power Electronics and Design* at Monterey, California; ACM Press, New York, pp. 172-177.
22. Goldhaber-Gordon, D., Montemerlo, M. S., Love, J. C., Opiteck, G. J., and Ellenbogen, J. C. (1997), 'Overview of Nanoelectronic Devices', *Proceedings of the IEEE*, Vol. 85, pp. 521-540.
23. Shaw, D. (1999), *Nanostructure science and technology*, National Science and Technology Council (US), <http://www.whitehouse.gov/WH/EOP/OSTP/NSTC/>.
24. Aviram, A. and Ratner, M. A. (1974), 'Molecular Rectifiers: Conceptual Basis.', *Bulletin of the American Physical Society*, Vol. 19, pp. 341.
25. Aviram, A. and Ratner, M. A. (1974), 'Molecular Rectifiers', *Chemical Physics Letters*, Vol. 29, pp. 277-283.
26. Carroll, R. L. and Gorman, C. B. (2002), 'The Genesis of Molecular Electronics', *Angewandte Chemie - International Edition*, Vol. 41, pp. 4378-4400.
27. Tour, J. M. (2000), 'Molecular Electronics. Synthesis and Testing of Components', *Accounts of Chemical Research*, Vol. 33, pp. 791-804.
28. Paul, F. and Lapinte, C. (1998), 'Organometallic Molecular Wires and Other Nanoscale-Sized Devices. An Approach Using the Organoiron (Dppe)Cp*Fe Building Block', *Coordination Chemistry Reviews*, Vol. 178-180, pp. 431-509.
29. Tour, J. M., Rawlett, A. M., Kozaki, M., Yao, Y., Jagessar, R. C., Dirk, S. M., Price, D. W., Reed, M. A., Zhou, C.-W., Chen, J., Wang, W., and Campbell, I. (2001), 'Synthesis and Preliminary Testing of Molecular Wires and Devices', *Chemistry - a European Journal*, Vol. 7, pp. 5118-5134.
30. Friggeri, A., van Manen, H.-J., Auletta, T., Li, X.-M., Zapotoczny, S., Schonherr, H., Vancso, G. J., Huskens, J., van Veggel, F. C. J. M., and Reinhoudt, D. N. (2001), 'Chemistry on Surface-Confined Molecules: an Approach to Anchor Isolated Functional Units to Surfaces', *Journal of the American Chemical Society*, Vol. 123, pp. 6388-6395.
31. Oh, M., Carpenter, G. B., and Sweigart, D. A. (2004), 'Supramolecular Metal-Organometallic Coordination Networks Based on Quinonoid π -Complexes', *Accounts of Chemical Research*, Vol. 37, pp. 1-11.

32. Ellenbogen, J. C. and Love, J. C. (2000), 'Architectures for Molecular Electronic Computers: 1. Logic Structures and an Adder Designed From Molecular Electronic Diodes', *Proceedings of the IEEE*, Vol. 88, pp. 386-426.
33. Stan, M. R., Franzon, P. D., Goldstein, S. C., Lach, J. C., and Ziegler, M.M. (2003), 'Molecular Electronics: From Devices and Interconnect to Circuits and Architecture', *Proceedings of the IEEE*, Vol. 91, pp. 1940-1957.
34. Fu, L., Cao, L., Liu, Y., and Zhu, D. (2004), 'Molecular and Nanoscale Materials and Devices in Electronics', *Advances in Colloid and Interface Science*, Vol. 111, pp. 133-157.
35. Bigelow, W. C., Pickett, D. L., and Zisman, W. A. (1946), 'Oleophobic Monolayers. Films Adsorbed From Solution in Non-Polar Liquids', *Journal of Colloid and Interface Science*, Vol. 1, pp. 513-538.
36. Nuzzo, R. G. and Allara, A. L. (1983), 'Adsorption of Bifunctional Organic Disulfides on Gold Surfaces', *Journal of the American Chemical Society*, Vol. 105, pp. 4481-4483.
37. Walczak, M. M., Chung, C., Stole, S. M., Widrig, C. A., and Porter, M. D. (1991), 'Structure and Interfacial Properties of Spontaneously Adsorbed *n*-Alkanethiolate Monolayers on Evaporated Silver Surfaces', *Journal of the American Chemical Society*, Vol. 113, pp. 2370-2378.
38. Laibinis, P. E., Whitesides, G. M., Allara, D. L., Tao, Y.-T., Parikh, A. N., and Nuzzo, R. G. (1991), 'Comparison of the Structures and Wetting Properties of Self-Assembled Monolayers of *n*-Alkanethiols on the Coinage Metal Surfaces, Cu, Ag, Au', *Journal of the American Chemical Society*, Vol. 113, pp. 7152-7167.
39. Jennings, G. K. and Laibinis, P. E. (1996), 'Self-Assembled Monolayers of Alkanethiols on Copper Provide Corrosion Resistance in Aqueous Environments', *Colloids and Surfaces A*, Vol. 116, pp. 105-114.
40. Jennings, G. K., Yong, T.-H., Munro, J. C., and Laibinis, P. E. (2003), 'Structural Effects on the Barrier Properties of Self-Assembled Monolayers Formed From Long-Chain ω -Alkoxy-*n*-Alkanethiols on Copper', *Journal of the American Chemical Society*, Vol. 125, pp. 2950-2957.
41. Magnussen, O. M., Ocko, B. M., Deutsch, M., Regan, M. J., Pershan, P. S., Abernathy, D., Grübel, G., and Legerand, J.-F. (1996), 'Self-Assembly of Organic Films on a Liquid Metal', *Nature*, Vol. 384, pp. 250-252.
42. Muskal, N., Turyan, I., and Mandler, D. (1996), 'Self-Assembled Monolayers on Mercury Surfaces', *Journal of Electroanalytical Chemistry*, Vol. 409, pp. 131-136.
43. Stratmann, M. (1990), 'Chemically Modified Metal Surfaces-a New Class of Composite Materials', *Advanced Materials*, Vol. 2, pp. 191-195.
44. Volmer, M., Stratmann, M., and Viehhaus, H. (1990), 'Electrochemical and Electron Spectroscopic Investigations of Iron Surfaces Modified With Thiols', *Surface and Interface Analysis*, Vol. 16, pp. 278-282.
45. Sheen, C. W., Shi, J.-X., Mårtensson, J., Parikh, A. N., and Allara, D. L. (1992), 'A New Class of Organized Self-Assembled Monolayers: Alkane Thiols on Gallium Arsenide(100)', *Journal of the American Chemical Society*, Vol. 114, pp. 1514-1515.
46. Gu, Y., Lin, Z., Butera, R. A., Smentkowski, V. S., and Waldeck, D. H. (1995), 'Preparation of Self-Assembled Monolayers on InP', *Langmuir*, Vol. 11, pp. 1849-1851.

47. Ulman, A. (1991), *An Introduction to Ultrathin Organic Films*, Academic Press, Boston.
48. Ulman, A. (1996), 'Formation and Structure of Self-Assembled Monolayers', *Chemical Reviews*, Vol. 96, pp. 1533-1554.
49. Somorjai, G. A. (1994), *Introduction to Surface Chemistry and Catalysis*, Wiley & Sons, New York.
50. Poirier, G. E., Herne, T. M., Miller, C. C., and Tarlov, M. J. (1999), 'Molecular-Scale Characterization of the Reaction of Ozone With Decanethiol Monolayers on Au(111)', *Journal of the American Chemical Society*, Vol. 121, pp. 9703-9711.
51. Bond, G. C. (2000), 'Relativistic Effects in Coordination, Chemisorption and Catalysis', *Journal of Molecular Catalysis A*, Vol. 156, pp. 1-20.
52. Gottfried, J. M., Schmidt, K. J., Schroeder, S. L. M., and Christmann, K. (2003), 'Adsorption of Carbon Monoxide on Au(110)-(1×2)', *Surface Science*, Vol. 536, pp. 206-224.
53. Kim, J., Samano, E., and Koel, B. E. (2006), 'CO Adsorption and Reaction on Clean and Oxygen-Covered Au(211) Surfaces', *The Journal of Physical Chemistry B*, Vol. 110, pp. 17512-17517.
54. Laiho, T. and Leiro, J. A. (2006), 'Influence of Initial Oxygen on the Formation of Thiol Layers', *Applied Surface Science*, Vol. 252, pp. 6304-6312.
55. Yim, W.-L., Nowitzki, T., Necke, M., Schnars, H., Nickut, P., Biener, J., Biener, M. M., Zielasek, V., Al-Shamery, K., Klüner, T., and Bäumer, M. (2007), 'Universal Phenomena of CO Adsorption on Gold Surfaces With Low-Coordinated Sites', *The Journal of Physical Chemistry C*, Vol. 111, pp. 445-451.
56. Pestryakov, A., Bluhm, H., Hävecker, M., Kleimenov, E., Knop-Gericke, A., Teschner, D. and Schlögl, R. (2005) 'In situ XPS investigations of oxygen species on gold surface', *23rd European Conference on Surface Science, Applied surface science* (Abstract).
57. Steadman, P., Peters, K., Isern, H., Alvarez, J., and Ferrer, S. (2000), 'Interaction of CO With the Reconstructed Au(111) Surface Near Atmospheric Pressures', *Physical Review B*, Vol. 62, pp. 2295-2298.
58. Nowitzki, T., Nickut, P., Deiter, C., Wollschläger, J., Al-Shamery, K., and Bäumer, M. (2006), 'Au Deposits on Graphite: on the Nature of High Temperature Desorption Peaks in CO Thermal Desorption Spectra', *Surface Science*, Vol. 600, pp. 3595-3599.
59. Mills, G., Gordon, M. S., and Metiu, H. (2003), 'Oxygen Adsorption on Au Clusters and a Rough Au(111) Surface: the Role of Surface Flatness, Electron Confinement, Excess Electrons, and Band Gap', *The Journal of Chemical Physics*, Vol. 118, pp. 4198-4205.
60. Schwartz, D. K. (2001), 'Mechanisms and Kinetics of Self-Assembled Monolayer Formation', *Annual Review of Physical Chemistry*, Vol. 52, pp. 107-137.
61. Schreiber, F. (2000), 'Structure and Growth of Self-Assembling Monolayers', *Progress in Surface Science*, Vol. 65, pp. 151-256.
62. Love, J. Ch., Estroff, L. A., Kriebel, J. K., Nuzzo, R. G., and Whitesides, G. M. (2005), 'Self-Assembled Monolayers of Thiolates on Metals As a Form of Nanotechnology', *Chemical Reviews*, Vol. 105, pp. 1103-1169.

63. Rieley, H. and Kendall, G. K. (1999), 'X-Ray Studies of Self-Assembled Monolayers on Coinage Metals. 3. Angularly Resolved Near Edge X-Ray Absorption Fine Structure Determination of the Orientation in 1-Octanethiol SAMs on Ag(111) and Cu(111)', *Langmuir*, Vol. 15, pp. 8867-8875.
64. Evans, S. D. and Ulman, A. (1990), 'Surface Potential Studies of Alkyl-Thiol Monolayers Adsorbed on Gold', *Chemical Physics Letters*, Vol. 170, pp. 462-466.
65. Zhong, C.-J., Woods, N. T., Dawson, G. B., and Porter, M. D. (1999), 'Formation of Thiol-Based Monolayers on Gold: Implications From Open Circuit Potential Measurements', *Electrochemistry Communications*, Vol. 1, pp. 17-21.
66. Schessler, H. M., Karpovich, D. S., and Blanchard, G. J. (1996), 'Quantitating the Balance Between Enthalpic and Entropic Forces in Alkanethiol/Gold Monolayer Self Assembly', *Journal of the American Chemical Society*, Vol. 118, pp. 9645-9651.
67. Standard, J. M., Gregory, B. W., and Clark, B. K. (2007), 'Computational Studies of Copper, Silver, and Gold Alkanethiolates and Alkaneselenates', *Journal of Molecular Structure*, Vol. 803, pp. 103-113.
68. Cometto, F. P., Paredes-Olivera, P., Macagno, V. A., and Patrito, E. M. (2005), 'Density Functional Theory Study of the Adsorption of Alkanethiols on Cu(111), Ag(111), and Au(111) in the Low and High Coverage Regimes', *The Journal of Physical Chemistry B*, Vol. 109, pp. 21737-21748.
69. Grönbeck, H., Curioni, A., and Andreoni, W. (2000), 'Thiols and Disulfides on the Au(111) Surface: the Headgroup-Gold Interaction', *Journal of the American Chemical Society*, Vol. 122, pp. 3839-3842.
70. Lavrich, D. J., Wetterer, S. M., Bernasek, S. L., and Scoles, G. (1998), 'Physisorption and Chemisorption of Alkanethiols and Alkyl Sulfides on Au(111)', *The Journal of Physical Chemistry B*, Vol. 102, pp. 3456-3465.
71. Nuzzo, R. G., Dubois, L. H., and Allara, D. L. (1990), 'Fundamental Studies of Microscopic Wetting on Organic Surfaces. 1. Formation and Structural Characterization of a Self-Consistent Series of Polyfunctional Organic Monolayers', *Journal of the American Chemical Society*, Vol. 112, pp. 558-569.
72. Schlenoff, J. B., Li, M., and Ly, H. (1995), 'Stability and Self-Exchange in Alkanethiol Monolayers', *Journal of the American Chemical Society*, Vol. 117, pp. 12528-12536.
73. Wetterer, S. M., Lavrich, D. J., Cummings, T., Bernasek, S. L., and Scoles, G. (1998), 'Energetics and Kinetics of the Physisorption of Hydrocarbons on Au(111)', *The Journal of Physical Chemistry B*, Vol. 102, pp. 9266-9275.
74. Widrig, C. A., Chung, Ch., and Porter, M. D. (1991), 'The Electrochemical Desorption of *n*-Alkanethiol Monolayers From Polycrystalline Au and Ag Electrodes', *Journal of Electroanalytical Chemistry*, Vol. 310, pp. 335-359.
75. Hasan, M., Bethell, D., and Brust, M. (2002), 'The Fate of Sulfur-Bound Hydrogen on Formation of Self-Assembled Thiol Monolayers on Gold: ¹H NMR Spectroscopic Evidence From Solutions of Gold Clusters', *Journal of the American Chemical Society*, Vol. 124, pp. 1132-1133.
76. Andreoni, W., Curioni, A., and Grönbeck, H. (2000), 'Density Functional Theory Approach to Thiols and Disulfides on Gold: Au(111) Surface and Clusters', *International Journal of Quantum Chemistry*, Vol. 80, pp. 598-608.

77. Nuzzo, R. G., Zegarski, B. R., and Dubois, L. H. (1987), 'Fundamental Studies of the Chemisorption of Organosulfur Compounds on Gold(111). Implications for Molecular Self-Assembly on Gold Surfaces', *Journal of the American Chemical Society*, Vol. 109, pp. 733-740.
78. Trevor, J. L., Lykke, K. R., Pellin, M. J., and Hanley, L. (1998), 'Two-Laser Mass Spectrometry of Thiolate, Disulfide, and Sulfide Self-Assembled Monolayers', *Langmuir*, Vol. 14, pp. 1664-1673.
79. Nishida, N., Hara, M., Sasabe, H., and Knoll, W. (1996), 'Dimerization Process in Alkanethiol Self-Assembled Monolayer on Au(111)', *Japanese Journal of Applied Physics*, Vol. 35, No. 2, pp. 799-802.
80. Nishida, N., Hara, M., Sasabe, H., and Knoll, W. (1996), 'Thermal Desorption Spectroscopy of Alkanethiol Self-Assembled Monolayer on Au(111)', *Japanese Journal of Applied Physics*, Vol. 35, No. 1, pp. 5866-5872.
81. Eberhardt, A., Fenter, P., and Eisenberger, P. (1998), 'Growth Kinetics in Self-Assembling Monolayers: a Unique Adsorption Mechanism', *Surface Science*, Vol. 397, pp. 285-290.
82. Peterlinz, K. A. and Georgiadis, R. (1996), 'In Situ Kinetics of Self-Assembly by Surface Plasmon Resonance Spectroscopy', *Langmuir*, Vol. 12, pp. 4731-4740.
83. Dannenberger, O., Buck, M., and Grunze, M. (1999), 'Self-Assembly of *n*-Alkanethiols: a Kinetic Study by Second Harmonic Generation', *The Journal of Physical Chemistry B*, Vol. 103, pp. 2202-2213.
84. Karpovich, D. S. and Blanchard, G. J. (1994), 'Direct Measurement of the Adsorption Kinetics of Alkanethiolate Self-Assemble Monolayers on a Microcrystalline Gold Surface', *Langmuir*, Vol. 10, pp. 3315-3322.
85. Rahn, J. R. and Hallock, R. B. (1995), 'Antibody Binding to Antigen-Coated Substrates Studied With Surface Plasmon Oscillations', *Langmuir*, Vol. 11, pp. 650-654.
86. Kawasaki, M., Sato, T., Tanaka, T., and Takao, K. (2000), 'Rapid Self-Assembly of Alkanethiol Monolayers on Sputter-Grown Au(111)', *Langmuir*, Vol. 16, pp. 1719-1728.
87. Yamada, R., Wano, H., and Uosaki, K. (2000), 'Effect of Temperature on Structure of the Self-Assembled Monolayer of Decanethiol on Au(111) Surface', *Langmuir*, Vol. 16, pp. 5523-5525.
88. Dannenberger, O., Wolff, J. J., and Buck, M. (1998), 'Solvent Dependence of the Self-Assembly Process of an Endgroup-Modified Alkanethiol', *Langmuir*, Vol. 14, pp. 4679-4682.
89. Bain, C. D., Troughton, E. B., Tao, Y.-T., Evall, J., Whitesides, G. M., and Nuzzo, R. G. (1989), 'Formation of Monolayer Films by the Spontaneous Assembly of Organic Thiols From Solution Onto Gold', *Journal of the American Chemical Society*, Vol. 111, pp. 321-335.
90. Yamada, R., Sakai, H., and Uosaki, K. (1999), 'Solvent Effect on the Structure of the Self-Assembled Monolayer of Alkanethiol', *Chemistry Letters*, pp. 667-668.
91. Schneider, T. W. and Buttry, D. A. (1993), 'Electrochemical Quartz Crystal Microbalance Studies of Adsorption and Desorption of Self-Assembled Monolayers of Alkyl Thiols on Gold', *Journal of the American Chemical Society*, Vol. 115, pp. 12391-12397.
92. Ishida, T., Mizutani, W., Azebara, H., Sato, F., Choi, N., Akiba, U., Fujihira, M., and Tokumoto, H. (2001), 'Adsorption Processes of Self-Assembled Monolayers Made From Terphenyl Thiols', *Langmuir*, Vol. 17, pp. 7459-7463.

93. Franzen, S. (2003), 'Density Functional Calculation of a Potential Energy Surface for Alkane Thiols on Au(111) As Function of Alkane Chain Length', *Chemical Physics Letters*, Vol. 381, pp. 315-321.
94. Maksymovych, P., Sorescu, D. C., and Yates, J. T. (2006), 'Methanethiolate Adsorption Site on Au(111): A Combined STM/DFT Study at the Single-Molecule Level', *The Journal of Physical Chemistry B*, Vol. 110, pp. 21161-21167.
95. Gottschalck, J. and Hammer, B. (2002), 'A Density Functional Theory Study of the Adsorption of Sulfur, Mercapto, and Methylthiolate on Au(111)', *The Journal of Chemical Physics*, Vol. 116, pp. 784-790.
96. Yourdshahyan, Y. and Rappe, A. M. (2002), 'Structure and Energetics of Alkanethiol Adsorption on the Au(111) Surface', *The Journal of Chemical Physics*, Vol. 117, pp. 825-833.
97. Hayashi, T., Morikawa, Y., and Nozoye, H. (2001), 'Adsorption State of Dimethyl Disulfide on Au(111): Evidence for Adsorption As Thiolate at the Bridge Site', *The Journal of Chemical Physics*, Vol. 114, pp. 7615-7621.
98. Yourdshahyan, Y., Zhang, H. K., and Rappe, A. M. (2001), '*n*-Alkyl Thiol Head-Group Interactions With the Au(111) Surface', *Physical Review B*, Vol. 63, pp. 081405-081408.
99. Vargas, M. C., Giannozzi, P., Selloni, A., and Scoles, G. (2001), 'Coverage-Dependent Adsorption of CH₃S and (CH₃S)₂ on Au(111): a Density Functional Theory Study', *The Journal of Physical Chemistry B*, Vol. 105, pp. 9509-9513.
100. Maksymovych, P., Sorescu, D. C., Dougherty, D., and Yates, J. T. (2005), 'Surface Bonding and Dynamical Behaviour of the CH₃SH Molecule on Au(111)', *The Journal of Physical Chemistry B*, Vol. 109, pp. 22463-22468.
101. Shimada, T., Kondoh, H., Nakai, I., Nagasaka, M., Yokota, R., Amemiya, K., and Ohta, T. (2005), 'Structural Study of Hexanethiolate on Au(111) in the 'Striped' Phase', *Chemical Physics Letters*, Vol. 406, pp. 232-236.
102. Roper, M. G., Skegg, M. P., Fisher, C. J., Lee, J. J., Dhanak, V. R., Woodruff, D. P., and Jones, R. G. (2004), 'Atop Adsorption Site of Sulphur Head Groups in Gold-Thiolate Self-Assembled Monolayers', *Chemical Physics Letters*, Vol. 389, pp. 87-91.
103. Kondoh, H., Iwasaki, M., Shimada, T., Amemiya, K., Yokoyama, T., Ohta, T., Shimomura, M., and Kono, S. (2003), 'Adsorption of Thiolates to Singly Coordinated Sites on Au(111) Evidenced by Photoelectron Diffraction', *Physical Review Letters*, Vol. 90, pp. 066102 [1-4].
104. Torrelles, X., Vericat, C., Vela, M. E., Fonticelli, M. H., Millone, M. A. D., Felici, R., Lee, T.-L., Zegenhagen, J., Munoz, G., Martin-Gago, J. A., and Salvarezza, R. C. (2006), 'Two-Site Adsorption Model for the ($\sqrt{3} \times \sqrt{3}$)-R30° Dodecanethiolate Lattice on Au(111) Surfaces', *The Journal of Physical Chemistry B*, Vol. 110, pp. 5586-5594.
105. Zhang, J., Chi, Q., and Ulstrup, J. (2006), 'Assembly Dynamics and Detailed Structure of 1-Propanethiol Monolayers on Au(111) Surfaces Observed Real Time by in Situ STM', *Langmuir*, Vol. 22, pp. 6203-6213.
106. Vericat, C., Vela, M. E., and Salvarezza, R. C. (2005), 'Self-Assembled Monolayers of Alkanethiols on Au(111): Surface Structures, Defects and Dynamics', *Physical Chemistry Chemical Physics*, Vol. 7, pp. 3258-3268.

107. Maksymovych, P., Sorescu, D. C., and Yates, J. T. Jr. (2006), 'Gold-Adatom-Mediated Bonding in Self-Assembled Short-Chain Alkanethiolate Species on the Au(111) Surface', *Physical Review Letters*, Vol. 97, pp. 146103 [1-4].
108. Yu, M., Bovet, N., Satterley, Ch. J., Bengió, S., Lovelock, K. R. J., Milligan, P. K., Jones, R. G., Woodruff, D. P., and Dhanak, V. (2006), 'True Nature of an Archetypal Self-Assembly System: Mobile Au-Thiolate Species on Au(111)', *Physical Review Letters*, Vol. 97, pp. 166102 [1-4].
109. Mazzarello, R., Cossaro, A., Verdini, A., Rousseau, R., Casalis, L., Danisman, M. F., Floreano, L., Scandolo, S., Morgante, A., and Scoles, G. (2007), 'Structure of a CH₃S Monolayer on Au(111) Solved by the Interplay Between Molecular Dynamics Calculations and Diffraction Measurements', *Physical Review Letters*, Vol. 98, pp. 016102 [1-4].
110. Esplandiu, M. J., Carot, M. L., Cometto, V. A., Macagno, V. A., and Patrito, E. M. (2006), 'Electrochemical STM Investigation of 1,8-Octanedithiol Monolayers on Au(111). Experimental and Theoretical Study', *Surface Science*, Vol. 600, pp. 155-172.
111. Stranick, S. J., Parikh, A. N., Allara, D. L., and Weiss, P. S. (1994), 'A New Mechanism for Surface Diffusion: Motion of a Substrate-Adsorbate Complex', *The Journal of Physical Chemistry*, Vol. 98, pp. 11136-11142.
112. Tamada, K., Hara, M., Sasabe, H., and Knoll, W. (1997), 'Surface Phase Behavior of *n*-Alkanethiol Self-Assembled Monolayers Adsorbed on Au(111): an Atomic Force Microscope Study', *Langmuir*, Vol. 13, pp. 1558-1566.
113. Munuera, C., Barrena, E., and Ocal, C. (2005), 'Chain-Length Dependence of Metastable Striped Structures of Alkanethiols on Au(111)', *Langmuir*, Vol. 21, pp. 8270-8277.
114. Xu, S., Cruchon-Dupeyrat, S. J. N., Garno, J. C., Liu, G.-Y., Jennings, G. K., Yong, T.-H., and Laibinis, P. E. (1998), 'In Situ Studies of Thiol Self-Assembly on Gold From Solution Using Atomic Force Microscopy', *The Journal of Chemical Physics*, Vol. 108, pp. 5002-5012.
115. Yamada, R. and Uosaki, K. (1998), 'In Situ Scanning Tunneling Microscopy Observation of the Self-Assembly Process of Alkanethiols on Gold(111) in Solution', *Langmuir*, Vol. 14, pp. 855-861.
116. Schönenberger, C., Jorritsma, J., Sondag-Huethorst, J. A. M., and Fokkink, L. G. J. (1995), 'Domain Structure of Self-Assembled Alkanethiol Monolayers on Gold', *The Journal of Physical Chemistry*, Vol. 99, pp. 3259-3271.
117. Poirier, G. E., Tarlov, M. J., and Rushmeier, H. E. (1994), 'Two-Dimensional Liquid Phase and the $p \times \sqrt{3}$ Phase of Alkanethiol Self-Assembled Monolayers on Au(111)', *Langmuir*, Vol. 10, pp. 3383-3386.
118. Prathima, N., Harini, M., Rai, N., Chandrashekara, R. H., Ayappa, K. G., Sampath, S., and Biswas, S. K. (2005), 'Thermal Study of Accumulation of Conformational Disorders in the Self-Assembled Monolayers of C₈ and C₁₈ Alkanethiols on the Au(111) Surface', *Langmuir*, Vol. 21, pp. 2364-2374.
119. Lay, M. D., Varazo, K., and Stickney, J. L. (2003), 'Formation of Sulfur Atomic Layers on Gold From Aqueous Solutions of Sulfide and Thiosulfate: Studies Using EC-STM, UHV-EC, and TLEC', *Langmuir*, Vol. 19, pp. 8416-8427.
120. Vericat, C., Vela, M. E., Andreasen, G., and Salvarezza, R. C. (2001), 'Sulfur-Substrate Interactions in Spontaneously Formed Sulfur Adlayers on Au(111)', *Langmuir*, Vol. 17, pp. 4919-4924.

121. Rodriguez, J. A., Dvorak, J., Jirsak, T., Liu, G., Hrbek, J., Aray, Y., and González, C. (2003), 'Coverage Effects and the Nature of the Metal-Sulfur Bond in S/Au(111): High-Resolution Photoemission and Density-Functional Studies', *Journal of the American Chemical Society*, Vol. 125, pp. 276-285.
122. Vericat, C., Vela, M. E., Benitez, G. A., Martin Gago, J. A., Torrelles, X., and Salvarezza, R. C. (2006), 'Surface Characterization of Sulfur and Alkanethiol Self-Assembled Monolayers on Au(111)', *Journal of Physics: Condensed Matter*, Vol. 18, pp. R867-R900.
123. Poirier, G. E. (1997), 'Characterization of Organosulfur Molecular Monolayers on Au(111) Using Scanning Tunneling Microscopy', *Chemical Reviews*, Vol. 97, pp. 1117-1127.
124. Dubois, L. H. and Nuzzo, R. G. (1992), 'Synthesis, Structure, and Properties of Model Organic Surfaces', *Annual Review of Physical Chemistry*, Vol. 43, pp. 437-463.
125. Torrelles, X., Barrena, E., Munuera, C., Rius, J., Ferrer, S., and Ocal, C. (2004), 'New Insights in the $c(4 \times 2)$ Reconstruction of Hexadecanethiol on Au(111) Revealed by Grazing Incidence X-Ray Diffraction', *Langmuir*, Vol. 20, pp. 9396-9402.
126. Nuzzo, R. G., Korenic, E. M., and Dubois, L. H. (1990), 'Studies of the Temperature-Dependent Phase Behavior of Long Chain *n*-Alkyl Thiol Monolayers on Gold', *The Journal of Chemical Physics*, Vol. 93, pp. 767-773.
127. Anselmetti, D., Baratoff, A., Güntherodt, H.-J., Delamarche, E., Michel, B., Gerber, Ch., Kang, H., Wolf, H., and Ringsdorf, H. (1994), 'Domain and Molecular Superlattice Structure of Dodecanethiol Self-Assembled on Au(111)', *Europhysics Letters*, Vol. 27, pp. 365-370.
128. Xiao, X., Wang, B., Zhang, C., Yang, Z., and Loy, M. M. T. (2001), 'Thermal Annealing Effect of Alkanethiol Monolayers on Au(111) in Air', *Surface Science*, Vol. 472, pp. 41-50.
129. Noh, J. and Hara, M. (2002), 'Final Phase of Alkanethiol Self-Assembled Monolayers on Au(111)', *Langmuir*, Vol. 18, pp. 1953-1956.
130. Dhirani, A. A., Zehner, R. W., Hsung, R. P., Guyot-Sionnest, P., and Sita, L. R. (1996), 'Self-Assembly of Conjugated Molecular Rods: a High-Resolution STM Study', *Journal of the American Chemical Society*, Vol. 118, pp. 3319-3320.
131. Frey, S., Stadler, V., Heister, K., Eck, W., Zharnikov, M., and Grunze, M. (2001), 'Structure of Thioaromatic Self-Assembled Monolayers on Gold and Silver', *Langmuir*, Vol. 17, pp. 2408-2415.
132. Duan, L. and Garrett, S. J. (2001), 'An Investigation of Rigid *p*-Methylterphenyl Thiol Self-Assembled Monolayers on Au(111) Using Reflection-Absorption Infrared Spectroscopy and Scanning Tunneling Microscopy', *The Journal of Physical Chemistry B*, Vol. 105, pp. 9812-9816.
133. Himmel, H.-J., Terfort, A., and Wöll, Ch. (1998), 'Fabrication of a Carboxyl-Terminated Organic Surface With Self-Assembly of Functionalized Terphenylthiols: the Importance of Hydrogen Bond Formation', *Journal of the American Chemical Society*, Vol. 120, pp. 12069-12074.
134. Kang, J. F., Ulman, A., Liao, S., Jordan, R., Yang, G., and Liu, G.-Y. (2001), 'Self-Assembled Rigid Monolayers of 4'-Substituted-4-Mercaptobiphenyls on Gold and Silver Surfaces', *Langmuir*, Vol. 17, pp. 95-106.
135. Fuxen, C., Azzam, W., Arnold, R., Witte, G., Terfort, A., and Wöll, Ch. (2001), 'Structural Characterization of Organothiolate Adlayers on Gold: the Case of Rigid, Aromatic Backbones', *Langmuir*, Vol. 17, pp. 3689-3695.

136. Leung, T. Y. B., Schwartz, P., Scoles, G., Schreiber, F., and Ulman, A. (2000), 'Structure and Growth of 4-Methyl-4'-Mercaptobiphenyl Monolayers on Au(111): a Surface Diffraction Study', *Surface Science*, Vol. 458, pp. 34-52.
137. Yang, G., Qian, Y., Engtrakul, C., Sita, L. R., and Liu, G.-Y. (2000), 'Arenethiols Form Ordered and Incommensurate Self-Assembled Monolayers on Au(111) Surfaces', *The Journal of Physical Chemistry B*, Vol. 104, pp. 9059-9062.
138. Andrade, J. D. (1985), 'X-Ray Photoelectron Spectroscopy', in Andrade, J. D. (Editor), *Surface and Interfacial Aspects of Biomedical Polymers*, Vol. I, Plenum Press, New York, pp. 105-195.
139. Zeggane, S. and Delamar, M. (1987), 'Composition Depth Information in Organic Materials by Measurement of XPS Background Signal', *Applied Surface Science*, Vol. 29, pp. 411-417.
140. Stanchev, A., Ignatova, V., and Ghelev, Ch. (2000), 'A Novel Approach to Angular-Resolved X-Ray Photoelectron Spectroscopy Depth-Profiling', *Nuclear Instruments and Methods in Physics Research B*, Vol. 166-167, pp. 350-356.
141. Vinodh, M. S. and Jeurgens, L. P. H. (2004), 'Quantitative Analysis of Angle-Resolved XPS Spectra Recorded in Parallel Data Acquisition Mode', *Surface and Interface Analysis*, Vol. 36, pp. 1629-1636.
142. Freude, D. (Leipzig University) (2006), *X-Ray Spectroscopy, Photoelectron Spectroscopy, Auger Spectroscopy*, available at: <http://ingo.exphysik.uni-leipzig.de/study/freude/freuse8.pdf>.
143. Bunde, R. L., Jarvi, E. J., and Rosentreter, J. J. (1998), 'Piezoelectric Quartz Crystal Biosensors', *Talanta*, Vol. 46, pp. 1223-1236.
144. Hlavay, J. and Guilbault, G. G. (1977), 'Applications of the Piezoelectric Crystal Detector in Analytical Chemistry', *Analytical Chemistry*, Vol. 49, pp. 1890-1898.
145. Marx, K. A. (2003), 'Quartz Crystal Microbalance: a Useful Tool for Studying Thin Polymer Films and Complex Biomolecular Systems at the Solution-Surface Interface', *Biomacromolecules*, Vol. 4, pp. 1100-1120.
146. Okahata, Y., Matsuura, K., and Ebara, Y. (1996), 'Gas-Phase Molecular Recognition on Functional Monolayers Immobilized on a Highly Sensitive Quartz-Crystal Microbalance', *Supramolecular Science*, Vol. 3, pp. 165-169.
147. Laricchia-Robbio, L. and Revoltella, R. P. (2004), 'Comparison Between the Surface Plasmon Resonance (SPR) and the Quartz Crystal Microbalance (QCM) Method in a Structural Analysis of Human Endothelin-1', *Biosensors & Bioelectronics*, Vol. 19, pp. 1753-1758.
148. Sauerbrey, G. (1959), 'The Use of Quartz Oscillators for Weighing Thin Layers and for Microweighing', *Zeitschrift Für Physik*, Vol. 155, pp. 206-222.
149. Binnig, G., Rohrer, H., Gerber, Ch., and Weibel, E. (1982), 'Surface Studies by Scanning Tunneling Microscopy', *Physical Review Letters*, Vol. 49, pp. 57-61.
150. Bonnell, D.A. (1993), *Scanning Tunneling Microscopy and Spectroscopy: Theory, Techniques, and Applications*, VCH, New York,
151. Li, B., Wang, H., Yang, J., and Hou, J. G. (2004), 'High-Resolution Scanning Tunneling Microscopy for Molecules', *Ultramicroscopy*, Vol. 98, pp. 317-334.

152. Baski, A. A. (2003), 'Nanoscale and Molecular Level Structures Fabricated and Tested by STM Like Tools', in Morkoç, H. (Editor), *Advanced Semiconductors and Organic Nano-Technologies*, Vol. III, Academic Press, San Diego.
153. Samori, P. (2004), 'Scanning Probe Microscopies Beyond Imaging', *Journal of Materials Chemistry*, Vol. 14, pp. 1353-1366.
154. Ho, W. (2002), 'Single-Molecule Chemistry', *The Journal of Chemical Physics*, Vol. 117, pp. 11033-11061.
155. Tersoff, J. and Hamann, D. R. (1983), 'Theory and Application for the Scanning Tunneling Microscope', *Physical Review Letters*, Vol. 50, pp. 1998-2001.
156. Tersoff, J. and Hamann, D. R. (1985), 'Theory of the Scanning Tunneling Microscope', *Physical Review B*, Vol. 31, pp. 805-813.
157. Lang, N. D. (1986), 'Spectroscopy of Single Atoms in the Scanning Tunneling Microscope', *Physical Review B*, Vol. 34, pp. 5947-5950.
158. Bardeen, J. (1961), 'Tunnelling From a Many-Particle Point of View', *Physical Review Letters*, Vol. 6, pp. 57-59.
159. Stein, J. and Joachim, C. (1987), 'Perturbation Expansion of the Transfer Matrix for Tunnelling Problems', *Journal of Physics A: Mathematical and General*, Vol. 20, pp. 2849-2857.
160. Feuchtwang, T. E. and Cutler, P. H. (1988), 'The Scanning Tunneling Microscope: Which Sample Characteristics Does It Probe?', *Physica Scripta*, Vol. 38, pp. 252-259.
161. Sacks, W. and Noguera, C. (1991), 'Generalized Expression for the Tunneling Current in Scanning Tunneling Microscopy', *Physical Review B*, Vol. 43, pp. 11612-11622.
162. Sacks, W. (2000), 'Tip Orbitals and the Atomic Corrugation of Metal Surfaces in Scanning Tunneling Microscopy', *Physical Review B*, Vol. 61, pp. 7656-7668.
163. Probst, O. M. (2002), 'Tunneling Through Arbitrary Potential Barriers and the Apparent Barrier Height', *The American Journal of Physics*, Vol. 70, pp. 1110-1116.
164. Zahid, F., Paulsson, M., and Datta, S. (2003), 'Conduction Through Nano Tubes- Wires, Molecules: Theory', in Morkoç, H. (Editor), *Advanced Semiconductors and Organic Nano-Technologies*, Vol. III, Academic Press, San Diego.
165. Xue, Y., Datta, S., and Ratner, M. A. (2002), 'First-Principles Based Matrix Green's Function Approach to Molecular Electronic Devices: General Formalism', *Chemical Physics*, Vol. 281, pp. 151-170.
166. Büttiker, M., Imry, Y., Landauer, R., and Pinhas, S. (1985), 'Generalized Many-Channel Conductance Formula With Application to Small Rings', *Physical Review B*, Vol. 31, pp. 6207-6215.
167. Takayanagi, K., Kondo, Y., and Ohnishi, H. (2001), 'Suspended Gold Nanowires: Ballistic Transport of Electrons', *Journal of the Japan Society of Applied Physics - International Edition*, Vol. 3, pp. 3-8.
168. Xu, B. and Tao, N. J. (2003), 'Measurement of Single-Molecule Resistance by Repeated Formation of Molecular Junctions', *Science*, Vol. 301, pp. 1221-1223.

169. Javey, A., Guo, J., Wang, Q., Lundstrom, M., and Dai, H. (2003), 'Ballistic Carbon Nanotube Field-Effect Transistors', *Nature*, Vol. 424, pp. 654-657.
170. Kong, J., Yenilmez, E., Tombler, T. W., Kim, W., Dai, H., Laughlin, R. B., Liu, L., Jayanthi, C. S., and Wu, S. Y. (2001), 'Quantum Interference and Ballistic Transmission in Nanotube Electron Waveguides', *Physical Review Letters*, Vol. 87, pp. 106801 [1-4].
171. Javey, A., Guo, J., Paulsson, M., Wang, Q., Mann, D., Lundstrom, M., and Dai, H. (2004), 'High-Field Quasiballistic Transport in Short Carbon Nanotubes', *Physical Review Letters*, Vol. 92, pp. 106804 [1-4].
172. Wang, W., Lee, T., and Reed, M. A. (2003), 'Mechanism of Electron Conduction in Self-Assembled Alkanethiol Monolayer Devices', *Physical Review B*, Vol. 68, pp. 035416 [1-7].
173. Wang, W., Lee, T., and Reed, M. A. (2005), 'Electronic Transport in Molecular Self-Assembled Monolayer Devices', *Proceedings of the IEEE*, Vol. 93, pp. 1815-1824.
174. Remacle, F. and Levine, R. D. (2006), 'Electrical Transport in Saturated and Conjugated Molecular Wires', *Faraday Discussions*, Vol. 131, pp. 45-67.
175. Kuznetsov, A. M. and Ulstrup, J. (2000), 'Theory of Electron Transfer at Electrified Interfaces', *Electrochimica Acta*, Vol. 45, pp. 2339-2361.
176. Petrov, E. G. and May, V. (2001), 'A Unified Description of Superexchange and Sequential Donor-Acceptor Electron Transfer Mediated by a Molecular Bridge', *The Journal of Physical Chemistry A*, Vol. 105, pp. 10176-10186.
177. Eng, M. P. and Albinsson, B. (2006), 'Non-Exponential Distance Dependence of Bridge-Mediated Electronic Coupling', *Angewandte Chemie - International Edition*, Vol. 45, pp. 5626-5629.
178. Smalley, J. F., Finklea, H. O., Chidsey, Ch. E. D., Linford, M. R., Creager, S. E., Ferraris, J. P., Chalfant, K., Zawodzinski, T., Feldberg, S. W., and Newton, M. D. (2003), 'Heterogeneous Electron-Transfer Kinetics for Ruthenium and Ferrocene Redox Moieties Through Alkanethiol Monolayers on Gold', *Journal of the American Chemical Society*, Vol. 125, pp. 2004-2013.
179. Sakaguchi, H., Hirai, A., Iwata, F., Sasaki, A., Nagamura, T., Kawata, E., and Nakabayashi, S. (2001), 'Determination of Performance on Tunnel Conduction Through Molecular Wire Using a Conductive Atomic Force Microscope', *Applied Physics Letters*, Vol. 79, pp. 3708-3710.
180. Weber, K., Hockett, L., and Creager, S. (1997), 'Long-Range Electronic Coupling Between Ferrocene and Gold in Alkanethiolate-Based Monolayers on Electrodes', *The Journal of Physical Chemistry B*, Vol. 101, pp. 8286-8291.
181. Sikes, H. D., Smalley, J. F., Dudek, S. P., Cook, A. R., Newton, M. D., Chidsey, C. E. D., and Feldberg S.W. (2001), 'Rapid Electron Tunneling Through Oligophenylenevinylene Bridges', *Science*, Vol. 291, pp. 1519-1523.
182. Creager, S., Yu, C. J., Bamdad, C., O'Connor, S., MacLean, T., Lam, E., Chong, Y., Olsen, G. T., Luo, J., Gozin, M., and Kayyem, J. F. (1999), 'Electron Transfer at Electrodes Through Conjugated "Molecular Wire" Bridges', *Journal of the American Chemical Society*, Vol. 121, pp. 1059-1064.
183. Ishida, T., Mizutani, W., Aya, Y., Ogiso, H., Sasaki, S., and Tokumoto, H. (2002), 'Electrical Conduction of Conjugated Molecular SAMs Studied by Conductive Atomic Force Microscopy', *The Journal of Physical Chemistry B*, Vol. 106, pp. 5886-5892.

184. Reimers, J. R., Lü, T. X., Crossley, M. J., and Hush, N. S. (1996), 'Molecular Electronic Properties of Fused Rigid Porphyrin-Oligomer Molecular Wires', *Nanotechnology*, Vol. 7, pp. 424-429.
185. Segal, D., Nitzan, A., Davis, W. B., Wasielewski, M. R., and Ratner, M. A. (2000), 'Electron Transfer Rates in Bridged Molecular Systems 2. A Steady-State Analysis of Coherent Tunneling and Thermal Transitions', *The Journal of Physical Chemistry B*, Vol. 104, pp. 3817-3829.
186. Engelkes, V. B., Beebe, J. M., and Frisbie, C. D. (2004), 'Length-Dependent Transport in Molecular Junctions Based on SAMs of Alkanethiols and Alkanedithiols: Effect of Metal Work Function and Applied Bias on Tunneling Efficiency and Contact Resistance', *Journal of the American Chemical Society*, Vol. 126, pp. 14287-14296.
187. Basch, H., Cohen, R., and Ratner, M. A. (2005), 'Interface Geometry and Molecular Junction Conductance: Geometric Fluctuation and Stochastic Switching', *Nano Letters*, Vol. 5, pp. 1668-1675.
188. Yaliraki, S. N., Kemp, M., and Ratner, M. A. (1999), 'Conductance of Molecular Wires: Influence of Molecule-Electrode Binding', *Journal of the American Chemical Society*, Vol. 121, pp. 3428-3434.
189. Di Ventra, M., Pantelides, S. T., and Lang, N. D. (2000), 'First-Principles Calculation of Transport Properties of a Molecular Device', *Physical Review Letters*, Vol. 84, pp. 979-982.
190. Berlin, Y. A. and Ratner, M. A. (2005), 'Intra-Molecular Electron Transfer and Electric Conductance Via Sequential Hopping: Unified Theoretical Description', *Radiation Physics and Chemistry*, Vol. 74, pp. 124-131.
191. McCreery, R. L. (2004), 'Molecular Electronic Junctions', *Chemistry of Materials*, Vol. 16, pp. 4477-4496.
192. Petrov, E. G., Shevchenko, Y. V., and May, V. (2003), 'On the Length Dependence of Bridge-Mediated Electron Transfer Reactions', *Chemical Physics*, Vol. 288, pp. 269-279.
193. Berlin, Y. A., Burin, A. L., and Ratner, M. A. (2001), 'Charge Hopping in DNA', *Journal of the American Chemical Society*, Vol. 123, pp. 260-268.
194. Lambert, Ch., Nöll, G., and Schelter, J. (2002), 'Bridge-Mediated Hopping or Superexchange Electron-Transfer Processes in Bis(Triarylamine) Systems', *Nature Materials*, Vol. 1, pp. 69-73.
195. Weiss, E. A., Tauber, M. J., Kelley, R. F., Ahrens, M. J., Ratner, M. A., and Wasielewski, M. R. (2005), 'Conformationally Gated Switching Between Superexchange and Hopping Within Oligo-*p*-Phenylene-Based Molecular Wires', *Journal of the American Chemical Society*, Vol. 127, pp. 11842-11850.
196. Haiss, W., Nichols, R. J., van Zalinge, H., Higgins, S. J., Bethell, D., and Schiffrin, D. J. (2004), 'Measurement of Single Molecule Conductivity Using the Spontaneous Formation of Molecular Wires', *Physical Chemistry Chemical Physics*, Vol. 6, pp. 4330-4337.
197. Haiss, W., van Zalinge, H., Higgins, S. J., Bethell, D., Höbenreich, H., Schiffrin, D. J., and Nichols, R. J. (2003), 'Redox State Dependence of Single Molecule Conductivity', *Journal of the American Chemical Society*, Vol. 125, pp. 15294-15295.
198. Haiss, W., van Zalinge, H., Höbenreich, H., Bethell, D., Schiffrin, D. J., Higgins, S. J., and Nichols, R. J. (2004), 'Molecular Wire Formation From Viologen Assemblies', *Langmuir*, Vol. 20, pp. 7694-7702.

199. Metzger, R. M. (1995), 'D- σ -A Unimolecular Rectifiers', *Materials Science and Engineering C*, Vol. 3, pp. 277-285.
200. Ashwell, G. J., Sambles, J. R., Martin, A. S., Parker, W. G., and Szablewski, M. (1990), 'Rectifying Characteristics of Mg | (C₁₆H₃₃Q3CNQ LB Film) | Pt Structures', *Chemical Communications*, pp. 1374-1376.
201. Metzger, R. M. (2003), 'Unimolecular Rectifiers and Proposed Unimolecular Amplifier', *Annals New York Academy of Sciences*, Vol. 1006, pp. 252-276.
202. Ashwell, G. J. and Mohib, A. (2005), 'Improved Molecular Rectification From Self-Assembled Monolayers of a Sterically Hindered Dye', *Journal of the American Chemical Society*, Vol. 127, pp. 16238-16244.
203. Sambles, J. R. and Martin, A. S. (1993), 'Molecular Rectification', *Physica Scripta*, Vol. 49, pp. 718-720.
204. Nguyen, H. Q., Cutler, P. H., Feuchtwang, T. E., Huang, Z.-H., Kuk, Y., Silverman, P. J., Lucas, A. A., and Sullivan, T. E. (1989), 'Mechanisms of Current Rectification in an STM Tunnel Junction and the Measurement of an Operational Tunneling Time', *IEEE Transactions on Electron Devices*, Vol. 36, pp. 2671-2678.
205. Krzeminski, C., Delerue, C., Allan, G., Vuillaume, D., and Metzger, R. M. (2001), 'Theory of Electrical Rectification in a Molecular Monolayer', *Physical Review B*, Vol. 64, pp. 085405 [1-6].
206. Kornilovitch, P. E., Bratkovsky, A. M., and Williams, R. S. (2002), 'Current Rectification by Molecules With Asymmetric Tunneling Barriers', *Physical Review B*, Vol. 66, pp. 165436 [1-11].
207. Larade, B. and Bratkovsky, A. M. (2003), 'Current Rectification by Simple Molecular Quantum Dots: an Ab-Initio Study', *Physical Review B*, Vol. 68, pp. 235305 [1-8].
208. Ashwell, G. J. and Stokes, R. J. (2004), 'Do Alkyl Tunnelling Barriers Contribute to Molecular Rectification?', *Journal of Materials Chemistry*, Vol. 14, pp. 1228-1230.
209. Troisi, A. and Ratner, M. A. (2002), 'Molecular Rectification Through Electric Field Induced Conformational Changes', *Journal of the American Chemical Society*, Vol. 124, pp. 14528-14529.
210. Troisi, A. and Ratner, M. A. (2004), 'Conformational Molecular Rectifiers', *Nano Letters*, Vol. 4, pp. 591-595.
211. Raiber, K., Terfort, A., Benndorf, C., Krings, N., and Strehblow, H.-H. (2005), 'Removal of Self-Assembled Monolayers of Alkanethiolates on Gold by Plasma Cleaning', *Surface Science*, Vol. 595, pp. 56-63.
212. Mecea, V. and Bucur, R. V. (1974), 'The Use of RF Voltage in Quartz Crystal Microbalance Measurements: Application to Nonmetallic Films', *Apparatus and Techniques*, Vol. 7, pp. 348-349.
213. Anonymous (2004), *Low Level Measurements Handbook* (6th edition), Keithley, Cleveland, Ohio.
214. Meyyappa, M. (2007), *Nanotechnology Measurement Handbook* (1st edition), Keithley, Cleveland, Ohio.
215. Stewart, J. J. P. (1990), 'MOPAC: a Semiempirical Molecular Orbital Program', *Journal of Computer-Aided Molecular Design*, Vol. 4, pp. 1-105.

216. Dewar, M. J. S., Zoebisch, E. G., Healy, E. F., and Stewart, J. J. P. (1985), 'AM1: a New General Purpose Quantum Mechanical Molecular Model', *Journal of the American Chemical Society*, Vol. 107, pp. 3902-3909.
217. Welsh, W. J. (2004), 'AM1 Molecular Orbital Studies of the Structures, Conformations, Protonation Energies, and Electronic Properties of Triazine Dihydrofolate Reductase Inhibitors', *Journal of Computational Chemistry*, Vol. 11, pp. 644-653.
218. Freeman, H. S., Lickfield, G. C., Drews, M. J., Polk, M. B., Kumar, S., Hinks, D., Chen, T., Hu, X., Cleveland, L., and Lye, J. (1995), 'A Molecular Orbital Approach to Molecular Design', *National Textile Center Annual Report*, Vol. 22, pp. 283-293.
219. Ashwell, G. J., Hamilton, R., and High, L. R. H. (2003), 'Molecular Rectification: Asymmetric Current-Voltage Curves From Self-Assembled Monolayers of a Donor-(π -Bridge)-Acceptor Dye', *Journal of Materials Chemistry*, Vol. 13, pp. 1501-1503.
220. Ashwell, G. J., Tyrrell, W. D., and Whittam, A. J. (2004), 'Molecular Rectification: Self-Assembled Monolayers in Which Donor-(π -Bridge)-Acceptor Moieties Are Centrally Located and Symmetrically Coupled to Both Gold Electrodes', *Journal of the American Chemical Society*, Vol. 126, pp. 7102-7110.
221. Urasinska, B. (2008), 'Molecular wires and molecular rectification from ionically coupled structures', *PhD thesis*, University of Wales, Bangor.
222. Ishida, T., Choi, N., Mizutani, W., Tokumoto, H., Kojima, I., Azehara, H., Hokari, H., Akiba, U., and Fujihira, M. (1999), 'High-Resolution X-Ray Photoelectron Spectra of Organosulfur Monolayers on Au(111): S(2p) Spectral Dependence on Molecular Species', *Langmuir*, Vol. 15, pp. 6799-6806.
223. Braig, S. and Flensberg, K. (2003), 'Vibrational Sidebands and Dissipative Tunneling in Molecular Transistors', *Physical Review B*, Vol. 68, pp. 205324 [1-10].
224. Riposan, A. and Liu, G.-Y. (2006), 'Significance of Local Density of States in the Scanning Tunneling Microscopy Imaging of Alkanethiol Self-Assembled Monolayers', *The Journal of Physical Chemistry B*, Vol. 110, pp. 23926-23937.
225. Rosink, J. J. W. M., Blauw, M. A., Geerligs, L. J., van der Drift, E., and Radelaar, S. (2000), 'Tunneling Spectroscopy Study and Modeling of Electron Transport in Small Conjugated Azomethine Molecules', *Physical Review B*, Vol. 62, pp. 10459-10466.
226. Kushmerick, J. G., Lazorcik, J., Patterson, Ch. H., and Shashidhar, R. (2004), 'Vibronic Contributions to Charge Transport Across Molecular Junctions', *Nano Letters*, Vol. 4, pp. 639-642.
227. Stipe, B. C., Rezaei, M. A., and Ho, W. (1998), 'Single-Molecule Vibrational Spectroscopy and Microscopy', *Science*, Vol. 280, pp. 1732-1735.
228. Paulsson, M., Frederiksen, T., and Brandbyge, M. (2006), 'Inelastic Transport Through Molecules: Comparing First-Principles Calculations to Experiments', *Nano Letters*, Vol. 6, pp. 258-262.
229. Chen, Y.-C., Zwolak, M., and Di Ventra, M. (2005), 'Inelastic Effects on the Transport Properties of Alkanethiols', *Nano Letters*, Vol. 5, pp. 621-624.
230. Onipko, A. I., Berggren, K.-F., Klymenko, Y. O., Malysheva, L. I., Rosink, J. J. W. M., Geerligs, L. J., van der Drift, E., and Radelaar, S. (2000), 'Scanning Tunneling Spectroscopy on π -Conjugated Phenyl-Based Oligomers: a Simple Physical Model', *Physical Review B*, Vol. 61, pp. 11118-11124.

231. Dhirani, A. A., Lin, P.-H., Guyot-Sionnest, P., Zehner, R. W., and Sita, L. R. (1997), 'Self-Assembled Molecular Rectifiers', *The Journal of Chemical Physics*, Vol. 106, pp. 5249-5253.
232. Gigon, J. (2008), (unpublished PhD thesis), University of Wales, Bangor.
233. Ashwell, G. J., Urasinska, B., Wang, Ch., Bryce, M. R., Grace, I., and Lambert, C. J. (2006), 'Single-Molecule Electrical Studies on a 7 nm Long Molecular Wire', *Chemical Communications*, pp. 4706-4708.
234. Soler, J. M., Artacho, E., Gale, J. G., García, A., Junquera, J., Ordejón, P., and Sánchez-Portal, D. (2002), 'The SIESTA Method for *Ab Initio* Order-*N* Materials Simulation', *Journal of Physics: Condensed Matter*, Vol. 14, pp. 2745-2779.
235. Rocha, A. R., García-Suárez, V. M., Bailey, S., Lambert, C., Ferrer, J., and Sanvito, S. (2006), 'Spin and Molecular Electronics in Atomically Generated Orbital Landscapes', *Physical Review B*, Vol. 73, pp. 085414 [1-22].
236. Rosink, J. J. W. M., Blauw, M. A., Geerligs, L. J., van der Drift, E., Rousseeuw, B. A. C., and Radelaar, S. (1998), 'Growth and Characterisation of Organic Multilayers on Gold Grown by Organic Molecular Beam Deposition', *Optical Materials*, Vol. 9, pp. 416-422.
237. Rosink, J. J. W. M., Blauw, M. A., Geerligs, L. J., van der Drift, E., Rousseeuw, B. A. C., and Radelaar, S. (1999), 'Growth and Scanning Tunneling Spectroscopy of Self-Assembled π -Conjugated Oligomers', *Materials Science and Engineering C*, Vol. 8-9, pp. 267-272.
238. Rosink, J. J. W. M., Blauw, M. A., Geerligs, L. J., van der Drift, E., Rousseeuw, B. A. C., Radelaar, S., Sloof, W. G., and Fakkeldij, E. J. M. (2000), 'Self-Assembly of π -Conjugated Azomethine Oligomers by Sequential Deposition of Monomers From Solution', *Langmuir*, Vol. 16, pp. 4547-4553.
239. Klare, J. E., Tulevski, G. S., and Nuckolls, C. (2004), 'Chemical Reactions With Upright Monolayers of Cruciform π -Systems', *Langmuir*, Vol. 20, pp. 10068-10072.
240. Tang, J., De Poortere, E. P., Klare, J. E., Nuckolls, C., and Wind, S. J. (2006), 'Single-Molecule Transistor Fabrication by Self-Aligned Lithography and in Situ Molecular Assembly', *Microelectronic Engineering*, Vol. 83, pp. 1706-1709.
241. Xue, Y. and Ratner, M. A. (2003), 'Microscopic Study of Electrical Transport Through Individual Molecules With Metallic Contacts. I. Band Lineup, Voltage Drop, and High-Field Transport', *Physical Review B*, Vol. 68, pp. 115406 [1-18].
242. Selzer, Y., Cai, L., Cabassi, M. A., Yao, Y., Tour, J. M., Mayer, T. S., and Allara, D. L. (2005), 'Effect of Local Environment on Molecular Conduction: Isolated Molecule Versus Self-Assembled Monolayer', *Nano Letters*, Vol. 5, pp. 61-65.
243. Lambert, C. J. (Lancaster University) (2007), *Professor* (unpublished results).
244. Ashwell, G. J., Moczko, K., Sujka, M., Chwialkowska, A., and High, L. R. H. (2007), 'Molecular Diodes and Ultra-Thin Organic Rectifying Junctions: Au-S-C_nH_{2n}-Q3CNQ and TCNQ Derivatives', *Physical Chemistry Chemical Physics*, Vol. 9, pp. 996-1002.
245. Ashwell, G. J., Ewington, J., and Robinson, B. J. (2006), 'Organic Rectifying Junctions Fabricated by Ionic Coupling', *Chemical Communications*, pp. 618-620.

246. Ashwell, G. J., Urasinska, B., and Tyrrell, W. D. (2006), 'Molecules That Mimic Schottky Diodes', *Physical Chemistry Chemical Physics*, Vol. 8, pp. 3314-3319.
247. Wang, Ch., Batsanov, A. S., Bryce, M. R., Ashwell, G. J., Urasinska, B., Grace, I., and Lambert, C. J. (2007), 'Electrical Characterization of 7 Nm Long Conjugated Molecular Wires: Experimental and Theoretical Studies', *Nanotechnology*, Vol. 18, pp. 044005 [1-8].